



---

DET NATURVIDENSKABELIGE FAKULTET  
KØBENHAVNS UNIVERSITET

# Investigation of Metastable Magnesium Atoms

by

Kasper T. Therkildsen

Thesis submitted in partial fulfilment  
of the requirements for the degree of  
Doctor of Philosophy

The Niels Bohr Institute  
University of Copenhagen

2009



---

# Preface

The following thesis describes a part of the work I performed during my Ph.d.-study at the Niels Bohr Institute at the University of Copenhagen. The content of my project has changed quite a bit over the course of the three years I have spend on the project. Initially the plan was that I should work on the two experiments in our lab: A sodium BEC experiment under construction and a atomic clock experiment with magnesium atoms in its initial stages. I started out working primarily on the Sodium BEC experiment, where we after 8 months we obtained a BEC. However due to a lack of funding it was necessary to shut down the experiment and a general trend during my ph.d. is that money have been few, but that just challenge your creativity to find unorthodox solutions. During that period of the first 8 months I had also been working on improving the Mg setup where the setup was in need of a major upgrade. When I started the primary laser source for the experiment (a dye laser which generated 285 nm laser light by frequency doubling in a BBO crystal) was placed in the room next door to the vacuum chamber with the magneto-optical trap (MOT). This gave rise to some severe alignment problems since the vacuum chamber and the optics required was mounted on a table that stood directly on the wooden floor in our 4th floor lab. So during my ph.d. the vacuum chamber and the MOT optics have been refitted directly on the concrete and the frequency doubling stage have been moved into the room with the vacuum chamber. The long term goal for the Mg experiment is to construct an atomic optical lattice clock, but in order to reach that goal first a sample of cold Mg atom is needed. The primary focus of my work have been to construct a number of laser sources

which are needed in order to realize this. During my time a number of new laser systems have been added to the lab. A 457 nm laser system have been rebuilt after the laser diode died and a new amplifier have been added, two 383 nm and a 517 nm laser systems have been constructed. Furthermore my fellow ph.d student Brian and I put a lot of work into constructing a source of metastable atoms, with which we experienced some meltdowns, that taught us about different magnesium, aluminum, copper and steel alloys. Also as a part of my ph.d. I have spend 6 months working at a Rb BEC experiment at University of Queensland, been an exercise teacher in statistical mechanics during two terms and the last four months have been spend on writing this thesis.

I have enjoyed the many different experiences that the last three years have provided and I am thankful for having come across people from so many different lines of work. I am also happy with the opportunities I have had to encounter people from so many different cultures and through them have my perspective broadened. A special thanks goes to the people I have worked with in the lab and my supervisor.

Luckily life contains other things than work and the last three years I am glad for the time I have spent with family and friends. Furthermore I am very grateful to my wonderful daughter who have been very cooperative and understanding the last four months where she has not seen her farther as much as she had been used to. I would off course also like to thank my lovely wife who has been extraordinarily patient and supportive and without whom it would not have been possible to finish this thesis.

---

# Contents

<b>Preface</b>	<b>iii</b>
<b>Contents</b>	<b>v</b>
<b>1 Introduction</b>	<b>1</b>
1.1 Properties of Magnesium . . . . .	3
1.1.1 Electronic Structure of Magnesium . . . . .	4
1.2 Frequency Standards and Atomic Clocks . . . . .	6
1.2.1 Possible Drift of Natural Constants . . . . .	10
1.3 Astronomical Applications of Magnesium Transitions . . . . .	12
1.4 Outline of Thesis . . . . .	14
<b>2 Laser Cooling and Trapping</b>	<b>15</b>
2.1 Radiation Pressure . . . . .	16
2.2 Optical Molasses . . . . .	18
2.3 Doppler Limit . . . . .	20
2.4 Magneto Optical Trap . . . . .	22
2.5 Magnetic Trapping . . . . .	26
2.6 Optical Trapping . . . . .	28
<b>3 Experimental Setup</b>	<b>33</b>
3.1 Laser Systems . . . . .	34
3.1.1 Second Harmonic Generation . . . . .	35
3.1.2 Enhancement Cavities . . . . .	38
3.1.3 285 nm Laser System . . . . .	41

3.1.4	457 nm Laser System . . . . .	48
3.1.5	881 nm Laser System . . . . .	57
3.1.6	383 nm Laser Systems . . . . .	57
3.1.7	517 nm Laser System . . . . .	61
3.2	Generation of Metastable Magnesium . . . . .	65
3.2.1	Theory of Metastable Excitation . . . . .	68
3.2.2	Characterization of the Metastable Source . . . . .	71
3.2.3	Frequency Stabilization . . . . .	75
3.3	MOT Setup . . . . .	77
3.3.1	Detection . . . . .	79
3.3.2	MOT Characteristics . . . . .	81
<b>4</b>	<b>Experiments with the Metastable Source</b>	<b>87</b>
4.1	Spectroscopy of the $^3P_{0,1} - ^3S_1$ Transitions . . . . .	87
4.1.1	Experimental Setup . . . . .	88
4.1.2	Results and Discussion . . . . .	89
4.1.3	Conclusion . . . . .	93
4.2	Spectroscopy of the $^3P_{0,1,2} - ^3D_{1,2,3}$ Transitions . . . . .	94
4.2.1	Experimental Setup . . . . .	94
4.2.2	Results and Discussion . . . . .	95
4.2.3	Conclusion . . . . .	98
<b>5</b>	<b>Experiments with the MOT</b>	<b>99</b>
5.1	Measurement of the Spin-forbidden Decay Rate $(3s3d)^1D_2 \rightarrow$ $(3s3p)^3P_{2,1}$ in $^{24}\text{Mg}$ . . . . .	100
5.1.1	The Optical Bloch Equations for the Three Level System	100
5.1.2	Leaks to Metastable States . . . . .	103
5.1.3	Experimental Results . . . . .	110
5.1.4	Conclusion . . . . .	113
5.2	Lifetime of the $^3P_1$ State . . . . .	114
5.2.1	Introduction . . . . .	114
5.2.2	Theory of the Experiment . . . . .	115
5.2.3	Experimental setup . . . . .	118

---

5.2.4	Experimental Results and Discussion . . . . .	121
5.2.5	Conclusion . . . . .	126
<b>6</b>	<b>Outlook</b>	<b>127</b>
6.1	Outlook . . . . .	127
6.1.1	Determination of the Magic Wavelength . . . . .	127
6.1.2	Optical Trapping . . . . .	128
6.1.3	Expected Performance of a Mg Atomic Clock . . . . .	130
	<b>Appendix: Publications</b>	<b>133</b>
	<b>References</b>	<b>163</b>



---

---

# CHAPTER 1

---

## Introduction

Laser cooling of neutral atoms and ions was first suggested by Hänsch and Schawlow [1] for neutral atoms and for ions by Wineland and Dehmelt [2] in 1975. The field of laser cooling of neutral atoms and ions have experienced a rapid development which has lead to the possibility of investigating confined samples of neutral atoms in the  $\mu\text{K}$  regime and ions in the Lamb-Dicke regime.

For neutral atoms a series of experimental breakthroughs lead the way in the eighties: the first observation of the slowing of a neutral atomic beam in 1982 [3], followed by 3D-cooling of neutral atoms in 1985 [4], optical dipole trapping in 1986 [5], magnetic trapping [6] and finally the development of the first magneto-optical trap (MOT) [7] in 1987.

The first obvious applications of laser cooling was high precision spectroscopy and in high precision measurements of frequency and time [8], [9], [10], [11]. This was essentially due to the reduction of the Doppler effect by many orders of magnitude compared to spectroscopy in a vapor or thermal beam.

A myriad of new cooling mechanisms were discovered and explained (for a review see e.g. [12], [13], [14] and references therein) while new elements of the alkali group and noble gasses were rapidly added to the family of laser cooled atomic species, culminating with the achievement of the Bose-Einstein Condensation (BEC) in dilute gases Rb [15], Na [16] and Li [17].

For the first time, a macroscopic quantum object, which was easy to manipulate, was at disposal in laboratory for experimental investigations. This has led to an entirely new class of experiments and theoretical investigations. An increasing number of research groups has begun to work in this exciting field, adding more elements to the list of atoms that have been trapped and condensed (H [18], K [19], He [20], Cs [21], Yb [22], Cr [23]). Laser cooling and trapping have found applications in many fields of atomic physics, from the study of cold, ultracold collisions [24], molecular photo-association [25], atomic interferometry [26], degenerate fermi gases [27], molecular BECs [28], [29] and in general in precision measurements of physical quantities. Molecules and elements from different families than the alkali group began to attract the attention of the growing scientific community, leading to an increasing number of elements being laser cooled and trapped.

Alkali-earth atoms (Be, Mg, Ca, Sr, Ba, Ra) and alkali-earth like atoms (Yd, Hg) have shown their potential as workhorses of the ion trapping and cooling field with the development of ultra-precise ion clocks thanks to the cancelation of the Doppler effect [30] or in playing a remarkable role in quantum information [31], [32].

It is only recently that the interest for neutral earth alkali like atoms has increased dramatically. The electronic structure of the two-electrons atoms with a singlet-triplet structure features many interesting properties. The simple electronic structure and the fact that the ground state lacks fine and in some cases hyperfine structure make the earth alkali like atoms attractive for experimental and theoretical studies of many atomic processes such as cold collisions [33], molecular photo-association [34], [35], [36], atomic dipole moments [37], [38], high precision spectroscopy [39] and the Doppler theory of laser cooling itself [40].

High resolution spectroscopy of earth alkali atoms is favored by the presence of long living triplet states with narrow optical transition lines connecting the singlet ground state to the triplet states. Narrow optical transitions are the backbone in the optical clocks which now have proven to be a very effi-

cient class of atomic clocks compared to the microwave Cs atomic clocks [41].

The alkali earth like atoms possess transitions with high quality factors due to the singlet-triplet structure. As a consequence of this the alkali-earth atoms with the exception of Be, have been laser cooled and trapped by a number of research groups [42], [43], [44], [45], [46], [47], [48], [49] and high-precision spectroscopy has been achieved [50], [51], [52]. A first example of an optical atomic clock on the  $^1S_0 - ^3P_0$  transition of  $^{87}\text{Sr}$  has been realized [53] and has been followed by other similar experiments in strontium [54], [55] (and in  $^{174}\text{Yb}$  [56] and for  $^{88}\text{Sr}$  [57]) which has led to the acceptance of Sr as a secondary frequency reference.

In the following, a brief introduction to atomic clocks and their applications to determine possible changes in natural constants will be given, followed by a description of the properties of Magnesium relevant for this thesis, ending with an outline of this thesis.

## 1.1 Properties of Magnesium

Magnesium is a fairly strong, silvery-white, light-weight metal (two thirds the density of aluminium). Magnesium can be compared with aluminium and since it is strong and light, it is used in several high volume part manufacturing applications including car and truck components. Magnesium is the third most commonly used metal in industry following steel and aluminium. As a metal the principal use of magnesium is as an alloying additive to aluminium used mainly for beverage cans.

The properties of magnesium relevant for this thesis, is mainly the electronic structure, which will be described in the following section.

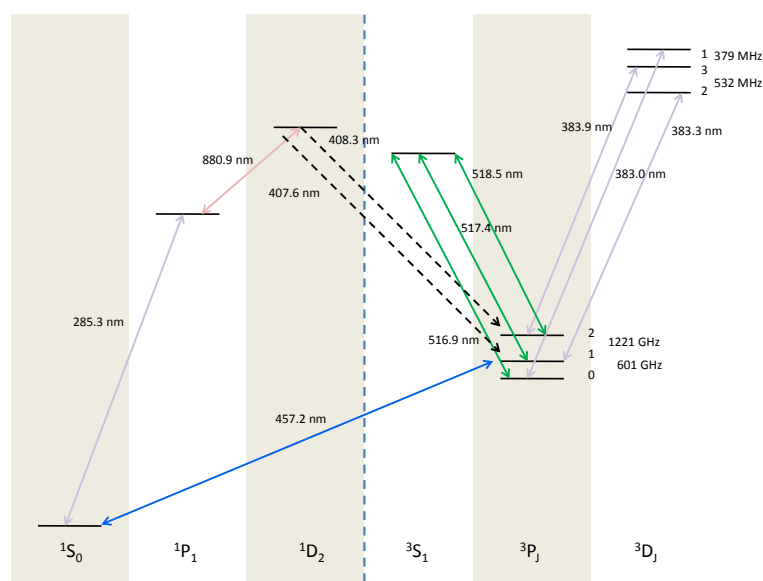


**Figure 1.1:** Level diagram for  $^{24}\text{Mg}$  showing transitions relevant for this thesis. The states are organized horizontally by their electronic spin. The dashed line indicates the separation between the singlet and triplet spin states originating from the dipole selection rule,  $\Delta S = 0$ . Note that for  $^{25}\text{Mg}$  hyperfine structure is also present.

### 1.1.1 Electronic Structure of Magnesium

The alkaline earth atoms, located in group two of the periodic table, have two valence electrons. The presence of a second valence electron creates a rich mixture of electronic states divided into spin singlet (opposite spin of the two valence electrons  $S = 0$ ) and spin triplet (same spin of the two valence electrons  $S = 1$ ) states. An electronic structure similar to the alkaline earth atoms are found in elements such as ytterbium, zinc, cadmium, and mercury. The energy level diagram for Magnesium is shown in Figure 1.1. While details of the energy level structure are different for each alkaline earth atom, many features are shared among them. The ground state is a  $^1\text{S}_0$  state with no fine or hyperfine structure. Strong dipole allowed transitions exist from the ground state to  $^1\text{P}_1$  states. For Magnesium and several other alkaline earth

atoms the very first excited state is a triplet state  $^3P$ , with allowed dipole transitions to a variety of  $^3S$  and  $^3D$  states. No electric dipole transitions are allowed between the spin singlet and spin triplet states due to the electric dipole selection rule  $\Delta S = 0$ . As a consequence, the level diagrams of alkaline earth atoms are divided into a singlet and triplet part isolated from each other except for a set of weaker multipole couplings connecting them. One notable exception to the lack of dipole couplings between the singlet and triplet states is between the ground  $^1S_0$  and the excited  $^3P_1$  states. As a result of  $L \cdot S$  interaction among the excited states, the  $^3P_1$  state is mixed slightly with the  $^1P_1$  state, and a weak  $^1S_0 - ^3P_1$  transition exists [58]. The main difference between magnesium and the heavier alkaline earth atoms is the  $^1D_2$  state. For the alkaline earth atoms, which are heavier than magnesium the  $^1D_2$  state lies below the  $^1P_1$  state resulting in a decay channel from  $^1P_1$  to  $^1D_2$  and from there further down to the  $^3P_1$  and  $^3P_2$  states. For magnesium the  $^1D_2$  state lies above the  $^1P_1$  state making the  $^1S_0 - ^1P_1$  transition an almost perfect two level system.

There are three stable isotopes of magnesium:  $^{24}\text{Mg}$ ,  $^{25}\text{Mg}$  and  $^{26}\text{Mg}$ . The stable isotopes and their natural abundance are found in Table 1.1 [59].

Isotope	$^{24}\text{Mg}$	$^{25}\text{Mg}$	$^{26}\text{Mg}$
Abundance	78.99%	10.00%	11.01%

**Table 1.1:** *Abundances of stable magnesium isotopes [59].*

Due to spin pairing of the nucleons, the isotopes with even atomic numbers  $Z$  and an even atomic mass number  $A$  have a nuclear spin  $I = 0$  [60]. This is the case for the even isotopes of magnesium, which have  $Z = 12$ . The odd isotope  $^{25}\text{Mg}$  has  $I = 5/2$  and the presence of nuclear spin allows the hyperfine interaction to perturb the  $^3P$  states shown in figure 1.1. The hyperfine interaction weakly mixes levels with the same  $F$ , but different  $J$  in this case  $^3P_0$   $F = 5/2$  mixes with the  $^1P_1$   $F = 5/2$  and  $^3P_1$   $F = 5/2$  states thus changing the frequency and the intensity of the transition components. Consequently,  $^3P_0$  acquires a very weak coupling (although much weaker than  $^3P_1$ ) to  $^1S_0$ . The ground state  $^1S_0$  has three noteworthy tran-

sitions each with very different strengths. The diversity in these transitions facilitate their use for a variety of atomic manipulations. The  $^1S_0 - ^1P_1$  transition is strong (lifetime  $\tau = 2$  ns) and the lowest  $^1P_1$  state has no decay rates to states other than  $^1S_0$ . As a result, this transition is well-suited for traditional laser cooling, permitting a thermal beam of dilute Mg gas to be cooled to mK temperatures and collected in a magneto optical trap with lifetimes up to several seconds. The  $^1S_0 - ^3P_1$  transition is weaker ( $\tau = 4.4$  ms) and is a closed transition. Unfortunately this transition is too weak to permit further cooling since the cooling force cannot sustain the atoms in the gravitational field. For  $^{25}\text{Mg}$ , the  $^1S_0 - ^3P_0$  transition is extremely weak and is therefore suitable as an atomic transition for an optical frequency standard. It has two important qualities: a narrow linewidth and weak sensitivity to perturbations. The blackbody radiation shift for magnesium is the lowest of the earth alkali atoms and is one order of magnitude smaller than for Sr [61]. Together with other properties discussed later in this text, Mg is a very favorable candidate for a high performance optical frequency standard. Many laboratories around the world are actively developing standards based on alkaline earth atoms where Sr has taken the lead [41]. The hope for alkaline earth optical frequency standards along with other optical frequency standards, is to reach inaccuracies of  $1 \cdot 10^{-18}$  or approximately 100 times smaller than the expected limit of the Cs standard inaccuracy.

## 1.2 Frequency Standards and Atomic Clocks

Of all measurement quantities, frequency represents the one that can be determined with by far the highest degree of accuracy. The progress in frequency measurements achieved, allows one to perform measurements of other physical and technical quantities with unprecedented precision, whenever they could be traced back to a frequency measurement. It is now possible to measure frequencies that are accurate to 5 parts in  $10^{17}$  [62]. In order to compare and link the results to those that are obtained in different fields, at

different locations, or at different times, a common base for the frequency measurements is necessary. Frequency standards are devices which are capable of producing stable and well known frequencies with a given accuracy and provide the necessary references over the huge range of frequencies of interest for science and technology.

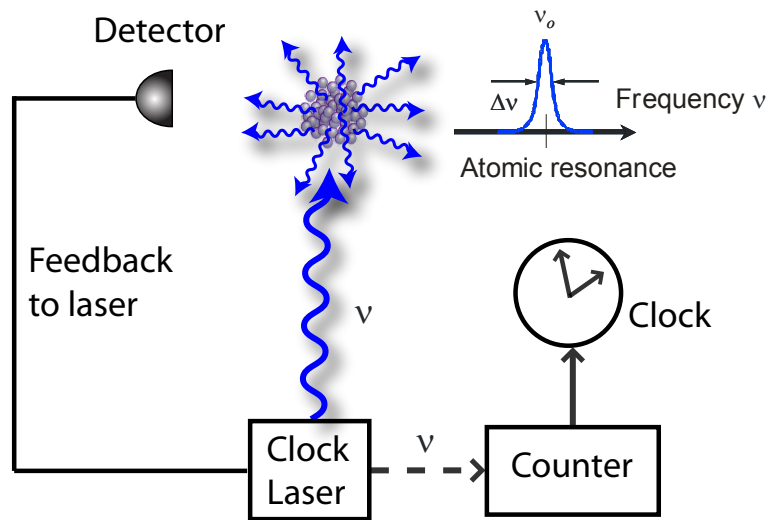


**Figure 1.2:** *Illustration of a frequency standard and atomic clock. An atomic sample is interrogated by a clock laser. The response of the atoms is detected and used as feedback to the clock laser. The frequency of the clock laser is transferred to a clockwork consisting of a counter and a clock.*

A frequency standard consists of a device with a sensitivity to a frequency, see figure 1.2. Such a frequency reference may be based on microscopic quantum systems like an ensemble of atoms. When interrogated by a suitable oscillator, the frequency dependence of the frequency reference may result in an absorption line with a minimum of the transmission at the resonance frequency  $\nu_0$ . The absorption signal can be used to generate a servo signal. The servo signal acting on the servo input of the oscillator is supposed to tune the frequency  $\nu$  of the oscillator as close as possible to the frequency  $\nu_0$  of the reference. With a closed servo loop the frequency  $\nu$  of the oscillator is stabilized close to the reference frequency  $\nu_0$  and the device can be used as

a frequency standard.

The two properties that characterize the quality of an atomic clock are accuracy and stability. The accuracy of an atomic clock is determined by how well the uncertainty of the measured frequency is known. The accuracy will depend on the atomic species used and how well it can be isolated from environmental effects during interrogation.

The performance of atomic frequency standards is characterized by the stability and accuracy and is given by:

$$\nu_{clock} = \nu_0(1 + \varepsilon + y(t)) \quad (1.1)$$

where  $\nu_0$  is the unperturbed frequency of the atomic reference transition,  $\varepsilon$  is the relative displacement of the frequency and  $y(t)$  is the fluctuations of the relative frequency.

The precision of the clock is more commonly referred to as the stability (or instability), which represents the repeatability of the measured clock frequency over a given averaging time  $\tau$ . The stability is typically expressed by an approximate form of the Allan deviation [63], given by:

$$\sigma_y(\tau) \simeq \frac{\Delta\nu}{\nu_0} \frac{1}{S/N} \sqrt{\frac{T_c}{\tau}} \quad (1.2)$$

where  $\Delta\nu$  is the linewidth at the transition frequency  $\nu_0$ ,  $S/N$  is the signal to noise ratio of the measurement,  $\tau$  is the measurement time and  $T_c$  is the cycle time used for preparation and interrogation of the atoms. For a system with the same signal to noise ratio and the same ratio of interrogation to cycle time, an optical transition can have a several orders of magnitude higher quality factor  $Q = \frac{\nu_0}{\Delta\nu}$ , compared to a microwave transition.

In order for a stable frequency source to constitute a frequency standard it is furthermore necessary that the frequency  $\nu$  is known in terms of absolute units. In the international system of units (SI) the frequency is measured in units of Hertz representing the number of cycles in one second (1 Hz = 1/s). So only by tracing the frequency of a device back to the frequency

of a primary standard used to realize the SI unit, the device represents a frequency standard.

A frequency standard can be used as a clock if the frequency is suitably divided in a clockwork device and displayed. As an example consider the case of a wrist watch where a quartz resonator defines the frequency of the oscillator at 32768 Hz that is used with a divider to generate the pulses that drives the second of the watch.

The problem with optical clock schemes has always been in the readout of the optical frequency. In the microwave atomic clocks, the clock frequency is accessible with conventional electronics making measurement and distribution of the clock signal relatively straight forward. Optical frequencies on the other hand are very difficult to measure since the oscillation is orders of magnitude faster than electronics can measure. The traditional method for measuring optical frequencies was to develop complex frequency chains which essentially divide the optical frequency in steps by comparison with a number of other oscillators [64]. This approach was expensive and labor intensive so that only major national standards laboratories could realistically pursue high accuracy optical frequency measurements. In the last decade, the development of octave spanning fs-comb lasers has revolutionized the field of optical frequency metrology [39], [65, 66, 67]. The principle behind can be described briefly as follows: In the frequency domain the output of a femtosecond (fs) laser consists of a large number of lasing modes which are evenly spaced by the frequency at which pulses are emitted from the laser known as the repetition rate  $f_{rep}$ . Owing to dispersion inside the fs-laser, the frequencies of the comb modes are not exact harmonics of the repetition frequency, instead the entire comb is offset in frequency by a small (microwave) frequency  $f_o$ . If  $f_{rep}$  and  $f_o$  are known, then the frequency of the n'th comb mode is given by  $\nu_n = nf_{rep} + f_o$  meaning that the optical frequency  $\nu_n$  can be expressed in terms of two microwave frequencies and an integer n. With all the comb mode frequencies precisely known, an optical clock frequency can be measured via heterodyne beat with the nearest comb mode as  $\nu_{clock} = \nu_n + f_{beat}$ , meaning that the optical frequency is completely determined by microwave frequencies and an integer. This means that the fs-laser

provides a coherent link between the optical and microwave regions of the electromagnetic spectrum providing a greatly simplified system for measuring optical frequencies with traditional microwave technology and thereby opening the field of optical frequency standards with earth alkali atoms as magnesium.

### 1.2.1 Possible Drift of Natural Constants

The question of whether fundamental constants, such as the fine structure constant  $\alpha$ , are really constant or vary with time, was raised as early as in 1937 by Dirac [68] in his large number hypothesis. Today Dirac's large-number hypothesis can be ruled out by experimental data. There are however other theories that require the fundamental constants to change with time. Such a temporal variation of the non-gravitational fundamental constants is excluded by the equivalence principle of General Relativity. Theories attempting to unify gravitation and other interactions may violate this principle. In the concept of string theory as well as in the Kaluza-Klein theories that use extra spatial dimensions [69] new fields namely the scalar dilaton field or moduli fields are proposed as partners of Einstein's tensor field  $g_{\mu\nu}$ . These fields couple to matter and might lead to time-varying fundamental constants [70], [71]. These ideas have attracted new interest from the report of frequency shifted absorption spectra from distant quasars [72] that were interpreted as evidence for the evolution of the fine structure constant  $\alpha$  on a cosmological timescale. There are experimental bounds that limit these violations. From the Lunar Laser Ranging experiment [73] the Earth and the Moon fall towards the Sun with a constant acceleration measured to better than 1 part in  $10^{12}$ . Nuclear data together with the Oklo phenomenon, astrophysical data and clock comparisons, introduce even more stringent limits.

The Oklo phenomenon is attributed to the existence of a natural fission reactor moderated by water in Gabon (Western Africa). The evidence that this fission reactor operated about two billion years ago for about a million years has been derived from ores of the Oklo mine that contained much less  $^{149}\text{Sm}$ ,  $^{151}\text{Eu}$ ,  $^{155}\text{Gd}$  and  $^{157}\text{Gd}$  than the usual natural abundancy. This

phenomenon has been investigated by the French Commissariat à l’Energie Atomique and it is believed that the missing isotopes like the  $^{149}\text{Sm}$  isotope, which is a good neutron absorber, were burned up by the neutron flux from the uranium fission. From the  $^{149}\text{Sm}/^{147}\text{Sm}$  ratio one can deduce a maximal variation of the position of the resonance from the time when the reactor was operational until today. This places an upper limit to a possible variation of  $\alpha$  as has been pointed out in [74]. The data have been re-evaluated in [75] who have imposed stringent limits for  $\dot{\alpha}/\alpha < 5 \cdot 10^{-17}/\text{year}$ .

Another completely different source for the determination of any possible time dependence of the fundamental constants is given by the absorption lines from quasar spectra. The large distance to these quasi-stellar objects of up to  $10^{10}$  light years, means that the measured absorption spectra contained the information about the value of a fine structure constant  $10^{10}$  years ago. A possible shift of these lines with respect to the corresponding absorption spectra obtained at the present time in the laboratory may be buried in the huge red shift of the radiation from the quasars. Comparing the spectra of heavy and light atoms from the same quasi-stellar objects or the gross structure with the fine structure of the same element allows one to surpass this difficulty. Evaluations of the spectra of Fe and Mg with respect to the relativistic correction were performed in [76], [77], [78].

The rapid progress in the development of clocks allows one to investigate possible variations of fundamental constants by comparing the frequencies of clocks based on different physical principles or transitions. The sensitivity of such clock rate comparisons to a variable fine structure constant results from the fact that the relativistic contributions of the hyperfine splitting are a function of  $\alpha$  times the nuclear charge  $Z$  which increases for heavier atoms or ions. The frequencies of a Cs and a Rb fountain clock have been compared over about five years and yielded  $\dot{\alpha}/\alpha = (0.4 \pm 16) \cdot 10^{-16}/\text{year}$  [79]. A measurement of the optical  $^{199}\text{Hg}^+$  standard with respect to the hyperfine transition of the Cs atomic clock over a two year duration in [80] yielded an upper bound for  $|\dot{\alpha}/\alpha| < 1.2 \cdot 10^{-15}/\text{year}$ . A recent comparison between two optical frequency standards  $^{199}\text{Hg}^+$  and  $^{27}\text{Al}^+$  over a period of a year sets a constraint on the fine structure constant of  $\dot{\alpha}/\alpha = (-1.6 \pm 2.3) \cdot 10^{-17}/\text{year}$

[62], the to date strongest constraint on the fine structure constant.

### 1.3 Astronomical Applications of Magnesium Transitions

The key to understanding the evolution of galaxies including our own galaxy, the Milky Way, is through measurements of the abundances of the chemical elements. The chemical compositions of galaxies change as different generations of stars form, evolve and later burn out. At the end of their lives sufficiently massive stars eject newly synthesized elements into the gaseous interstellar medium of their host galaxy. New stars form from this gas reservoir with a composition enriched by heavy elements compared to previous stellar generations. By measuring the diverse compositions of the stars in a galaxy it is possible to determine its evolutionary history.

Amongst the elements whose abundances can be measured, two are particularly important: magnesium (Mg) and iron (Fe). Iron is the final product of exothermic nuclear burning, and is produced in two sites: the cores of massive stars preceding their collapse into supernovae of type SN Ib, Ic and II, and in the fireballs that become the low-mass supernovae of type SN Ia [81]. Magnesium is also produced by massive stars that later become core-collapse supernovae but it is produced much earlier in the stars evolution and under much more calm conditions in the non-explosive burning of neon. Massive stars are the sole source of Mg whereas Fe is produced in the supernovae of high- and low-mass stars. From observational and theoretical studies of stars in the Milky Way astronomers have discovered that the abundance ratio of Mg/Fe is an important diagnostic of galaxy evolution. The ratio reduces during later stages of galaxy evolution due to the late onset of Fe production in SN Ia. Hence observations of Mg and Fe together constrain the lifetimes of the stellar populations that make up galaxies and their star-formation histories. This is seen both in our own Galaxy where star-by-star measurements of the Mg/Fe ratio is possible [82] and in more distant elliptical galaxies [83]

where the combined light of many stars shows a higher value of the Mg/Fe ratio than in the Sun. The Mg/Fe ratio also provides very important information on the mechanism of the SN II explosion. Although this certainly involves the collapse of the core of a massive star, astronomers have been unable to calculate where in the core the imploding and the exploding layers divide the location of the so-called mass cut. This in turn leaves uncertainty of the fate of the compact remnant i.e. whether it becomes a neutron star or a black hole and the amount of newly synthesized material that escapes to enrich the interstellar medium and future generations of stars. The Mg/Fe ratio can shed light on this situation. Mg is produced well outside the core of the precursor of the SN II, whereas Fe is produced in the region of the mass cut. Observations of the Mg/Fe abundance ratio in stars that have formed from gas ejected by SN II therefore show how much of the Fe core has been ejected compared to the amount of Mg produced earlier in its evolution. Variations in this ratio from one SN II to another, for example as a result of different precursor masses, can also be estimated from an observational analysis of the range of Mg/Fe ratios preserved in later generations of stars. For reasons associated with the uncertainty of Fe production many astronomers would prefer to use Mg as the usual standard for measuring the overall heavy-element content of a star, whereas Fe is used currently because of the greater ease of measuring that atomic species.

In order to make reliable measurements of the Mg abundances of stars it is necessary to have accurate values for each of the observable transitions. As stars vary widely in temperature and Mg content, the strengths of the Mg spectral lines also vary greatly such that lines that are easily measured and analyzed in one star may be unsuitable for the task in another. For this reason it is vital that accurate values are available for a wide range of observable transitions. An experiment with cold Mg atoms makes it possible to determine these values.

## 1.4 Outline of Thesis

- **Chapter 2** contains a brief introduction to laser cooling, optical and magnetic trapping.
- **Chapter 3** is a description of the experimental setup and contains information about the different laser systems generated for the experiment together with a description of the 285 nm MOT and a source of metastable atoms used for frequency stabilization of some of the lasers described in this chapter.
- **Chapter 4** deals with different spectroscopic measurements using a metastable beam line.
- **Chapter 5** describes the measurements of the spin-forbidden decay rate  $(3s3d)^1D_2 \rightarrow (3s3p)^3P_{2,1}$  in  $^{24}\text{Mg}$  and the  $^3P_1$  lifetime.
- **Chapter 6** contains the outlook and describes some future experiments with the Mg setup.

---

---

## CHAPTER 2

---

# Laser Cooling and Trapping

This chapter is dedicated to the quick review of laser cooling and trapping of neutral atoms in connection with the experimental investigation of magnesium. The chapter is organized as follows: the scattering force will be introduced followed by the optical molasses configuration leading to the magneto-optical trap (MOT). Finally magnetic and optical trapping are described.

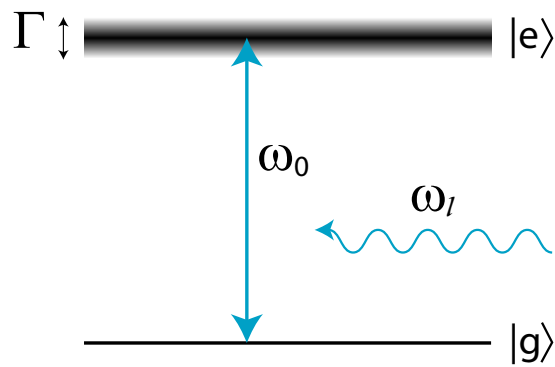


**Figure 2.1:** *A laser beam interacting with a two-level atom*

## 2.1 Radiation Pressure

The basic theory of laser cooling is derived by considering a simple two level atom. As mentioned, magnesium is among the few atoms, where this assumption is correct to a large extent. Therefore consider a neutral two level atom with a ground state  $|g\rangle$  and excited state  $|e\rangle$  with an energy difference of  $\hbar\omega_0$  as illustrated in figure 2.1. The atom is traveling at a velocity  $v$  in a coherent electromagnetic field generated by a laser. For now let the movement of the atom be restricted to one dimension along the line of the laser beam. If the laser is set on resonance with the transition, the atom will eventually absorb a photon from the light field and due to conservation of momentum receive the momentum  $\hbar k$  along the path of the photon. The excited atom will eventually decay to its ground state and emit a photon. If the photon is emitted by stimulated emission, the atom receives a momentum of  $\hbar k$  and no net momentum is transferred in the process. On the other hand, if the photon is emitted by spontaneous decay, the atom receives either  $\hbar k$  or  $-\hbar k$ . This results in a net momentum transfer of either 0 or  $2\hbar k$ , both equally probable. The process is sketched in figure 2.2. When repeating this procedure many times, it is easily seen that the atom on average receives a net transfer of momentum per absorption/emission cycle given by:

$$\Delta\bar{p}_a = \hbar\bar{k} \quad (2.1)$$

The atom is therefore pushed in the direction of the laser beam.

For intensities much lower than the saturation intensity<sup>1</sup>, spontaneous emission is dominant compared to stimulated emission. In the following, the intensity of the light is assumed to be so low that the stimulated emission can be neglected. The average time for one absorption/emission cycle is given by the lifetime  $\tau$  of  $|e\rangle$ . Denoting the average occupancy of  $|e\rangle$  by

<sup>1</sup>The saturation intensity is given by [14] as  $I_0 = \frac{\pi\hbar c}{2\lambda^3\tau}$  and is defined as the intensity at which a monochromatic beam excites the transition at a rate equal to one half of its natural line width

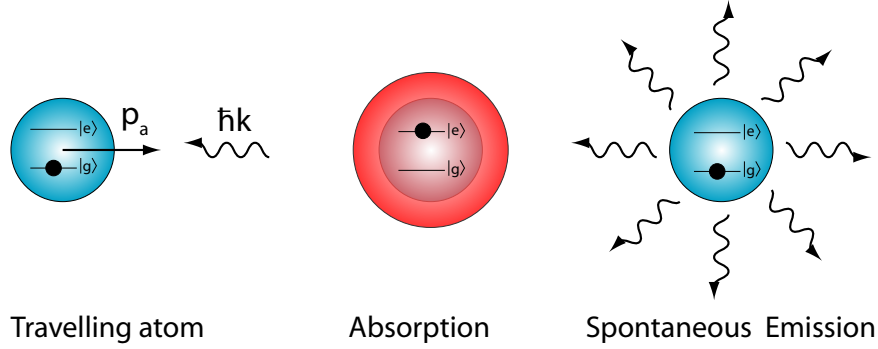


**Figure 2.2:** (Left) A photon and a two level atom traveling with momentum  $p_a$ . (Middle) The atom absorbs the photon leaving it in an excited state. (Right) By spontaneous decay the photon is emitted in a random direction.

$\rho_{ee} = N_e/N$ , the mean force exerted on the atom is given by:

$$\langle \bar{F} \rangle = \frac{\Delta \bar{p}_a}{\Delta t} = \hbar \bar{k} \Gamma \rho_{ee} \quad (2.2)$$

where  $\Gamma = \tau^{-1}$  is the natural line width of the excited state. The density  $\rho_{ee}$  is easily calculated by solving the two level optical Bloch equations and is given by:

$$\rho_{ee} = \frac{1}{2} \frac{s_0}{1 + s_0 + 4 \left( \frac{\delta}{\Gamma} \right)^2} \quad (2.3)$$

where  $\delta = \omega_l - \omega_0$  is the detuning of the laser and  $s_0 = I/I_0$  is the on-resonance saturation parameter with  $I_0$  being the saturation intensity. The momentum transfer will inevitably change the resonance condition of the laser light due to the Doppler shift. To account for the Doppler shift a correction of  $-\bar{k} \cdot \bar{v}$  is added to  $\delta$ . Inserting this into equation 2.2 results in an average force:

$$\langle \bar{F} \rangle = \hbar \bar{k} \frac{\Gamma}{2} \frac{s_0}{1 + s_0 + 4 \left( \frac{\delta - \bar{k} \cdot \bar{v}}{\Gamma} \right)^2} \quad (2.4)$$

This force is called the scattering force or radiation pressure force and can be used to slow or deflect for example atomic neutral beams. It is seen that  $\rho_{ee}$  converges toward  $1/2$  for  $s_0 \rightarrow \infty$  resulting in an optical force from a single beam of  $\hbar k \frac{\Gamma}{2}$ . For  $^{24}\text{Mg}$  the  $^1S_0 \rightarrow ^1P_1$  transition at 285 nm (2 ns lifetime)  $a_{max} \sim 10^6 m/s^2$ . However the impressive acceleration will only last for a very short time as the atom quickly is pushed out of resonance due to the Doppler shift. Moreover since the system is shifted out of resonance by the slowing action, the efficiency of the slowing on atomic thermal beam with this technique is indeed limited. Consequently, a number of techniques have been developed to keep a certain velocity class of the slowing atoms in resonance with the radiation, where the most common are Zeeman slowing [84] and chirp cooling [85]. Magnesium slowed on the 285 nm transition has a large radiative force which grants enough slowing force to capture a usable amount of atoms even without a slowing beam or a Zeeman slower.

## 2.2 Optical Molasses

In 1975, Hänsch and Shawlow [1] proposed a configuration with two counter propagating laser beams for laser cooling. A technique known as optical molasses. If both lasers are red detuned, it is more likely that a moving atom absorbs a photon from the laser beam which is propagating in the opposite direction of the atoms itself. Consequently the contribution of both lasers can build up a force opposed to the atomic motion reducing the overall kinetic energy i.e. slowing the sample down. Since the atoms are kept in resonance with the transition thanks to the Doppler effect, the energy of the sample is dragged away by the field due to  $\omega_l - \omega_0 < 0$ .

In the case concerning low intensity of each beam, the force in first approx-

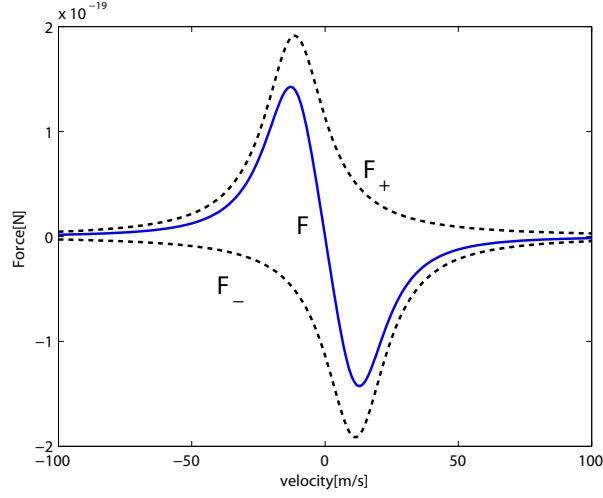


**Figure 2.3:** Total force acting on an atom as function of the velocity for an optical molasses configuration together with the scattering forces created by the single laser beam

imation can be simply written as the sum of the scattering forces originating from the two laser beams, while the population in the excited state is calculated considering the sum of the intensities of each laser. The average net force exerted on the atom in one dimension is [13]:

$$\begin{aligned}
 \langle \bar{F}_{om} \rangle &= \langle \bar{F}_+ \rangle + \langle \bar{F}_- \rangle \\
 &= \hbar \bar{k} \frac{\Gamma}{2} \left( \frac{s_0}{1 + 2s_0 + 4 \left( \frac{\delta - \bar{k} \cdot \bar{v}}{\Gamma} \right)^2} - \frac{s_0}{1 + 2s_0 + 4 \left( \frac{\delta + \bar{k} \cdot \bar{v}}{\Gamma} \right)^2} \right) \\
 &= \hbar \bar{k} \frac{\Gamma}{2} s_0 \frac{16\delta \frac{\bar{k} \cdot \bar{v}}{\Gamma^2}}{\left[ 1 + 2s_0 + 4 \frac{\delta^2}{\Gamma^2} + 4 \frac{\bar{k} \cdot \bar{v}}{\Gamma^2} \right]^2 - \left[ 8\delta \frac{\bar{k} \cdot \bar{v}}{\Gamma^2} \right]^2} \quad (2.5)
 \end{aligned}$$

As shown in figure 2.3 the force is almost linear around  $v = 0$ . For very low velocities ( $v \ll \Gamma/k$ ) the terms including  $\left( \frac{\bar{k} \cdot \bar{v}}{\Gamma} \right)^2$  and higher orders can be neglected in 2.5 and one finds

$$\langle \bar{F}_{om} \rangle \approx 8\hbar k^2 \frac{\delta}{\Gamma} \frac{s_0}{[1 + 2s_0 + (\frac{2\delta}{\Gamma})^2]^2} \bar{v} \equiv \alpha \bar{v} \quad (2.6)$$

For red detuning ( $\delta < 0$ ) one finds  $F_{om} = -\alpha \bar{v}$ , which represents a friction force. The force is a damping force which is active for all atomic velocities. As a result of the Doppler effect, atoms moving with a velocity  $\bar{v}$  are more resonant with the counter-propagating beam as compared to the co-propagating beam. As a consequence, the atom is decelerated by the viscous damping in the red detuned near-resonant light field [4], [86]. By adding two more couples of counter propagating beams for each direction, the motion is damped in all the degrees of freedom thanks to the viscous force known as the optical molasses [4]. Nevertheless, due to the finite size of the laser beams, only atoms with a velocity below the capture velocity  $v_c$  can be slowed before leaving the interaction area.

## 2.3 Doppler Limit

One might expect the residual motion of the atoms to gradually decrease so that the atoms come to rest and reach a temperature  $T = 0$ . This clearly nonphysical result does not take into account that even an atom at rest would absorb and emit photons. The recoil energy transferred to each atom during the absorption process of  $+\frac{\hbar^2 k^2}{2m}$  and the emission process of  $-\frac{\hbar^2 k^2}{2m}$  leads to heating which in total corresponds to a mean increase in the kinetic energy per particle by  $\frac{2\hbar^2 k^2}{2m}$  (in the one dimensional case). In equilibrium

$$\dot{E}_{heat} = \dot{E}_{cool} \quad (2.7)$$

holds. The heating rate  $\dot{E}_{heat}$  for each of the two beams due to the rate of the recoil transfers is proportional to the fraction of atoms in the excited state  $\rho_{ee}$  and to the decay rate  $\Gamma = 1/\tau$ . Hence the heating rate is

$$\dot{E}_{heat} = 2 \frac{(\hbar k)^2 \Gamma_{bb}}{2m} \frac{2s_0}{1 + 2s_0 + 4 \left(\frac{\delta}{\Gamma}\right)^2} \quad (2.8)$$

where we have assumed that the on-resonance saturation parameter in the two counterpropagating beams is  $2S_0$ . The cooling rate due to the loss of kinetic energy resulting from the damping is calculated from

$$\dot{E}_{cool} = \frac{\partial}{\partial t} \frac{p^2}{2m} = \dot{p} \frac{p}{m} = F(v)v = -\alpha v^2 \quad (2.9)$$

Combining this with equations 2.6, 2.8 in equation 2.7 and replacing  $v^2$  with its mean value  $\langle v^2 \rangle$  leads to:

$$m \langle v^2 \rangle = \frac{\hbar \Gamma}{4} \frac{1 + 2s_0 + \left(\frac{2\delta}{\Gamma}\right)^2}{2 \frac{\delta}{\Gamma}} \quad (2.10)$$

Using  $\frac{1}{2}m \langle v^2 \rangle = \frac{1}{2}k_B T$  this gives a temperature of

$$T = \frac{\hbar \Gamma}{4k_B} \frac{1 + 2s_0 + \left(\frac{2\delta}{\Gamma}\right)^2}{2 \frac{\delta}{\Gamma}} \quad (2.11)$$

The temperature has a minimum for  $\delta = \gamma/2$  in the limit of  $s_0 \rightarrow 0$  also known as the Doppler limit or Doppler temperature:

$$T_D = \frac{\hbar \Gamma}{2k_B} \quad (2.12)$$

The Doppler limit in three dimensions is derived similarly [86]. It suffices to note that the cooling rate is the same as in the one-dimensional case but the heating rate is three times higher if six beams are used rather than two. However, the three degrees of freedom result in  $m \langle v^2 \rangle_{3D}/2 = 3k_B T/2$  and the Doppler limit in three dimensions is the same as in 2.12.

For the  $^1S_0 - ^1P_1$  transition in magnesium ( $\lambda = 285nm, \gamma = 78MHz$ ) the Doppler limit is 1.9 mK. The velocity corresponding to the Doppler limit is 80 cm/s.

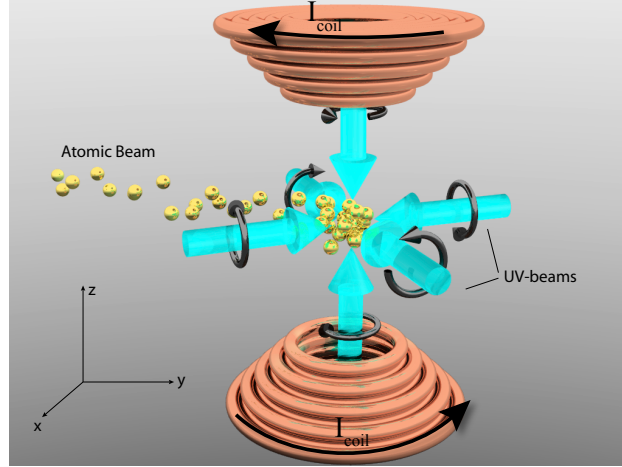


**Figure 2.4:** *Illustration of a magneto optical trap (MOT) with three orthogonal pairs of counter propagating beams together with the copper coils in the anti Helmholtz configuration*

## 2.4 Magneto Optical Trap

In optical molasses atoms are decelerated to very low velocities. However there is only a damping force but no force that confines the atoms to a particular point in space. Such a force can be generated using an inhomogeneous magnetic field in a magneto optical trap (MOT). Consider an atom with a ground state with total angular momentum  $J = 0$  and an excited state with  $J = 1$ , which is the case of magnesium. In a magnetic field, the energy of the ground state is not affected whereas the energy level of the excited state is split into three magnetic sub-states, known as Zeeman splitting. The  $m_J = 0$  sub-state is unaffected of the magnetic field whereas the energies of the two other sub-states ( $m_J = \pm 1$ ) vary linearly but with opposite signs with an applied magnetic field. The energy shifts in a weak magnetic field are found

by treating the interaction of the magnetic field as a small perturbation. The corresponding Zeeman shift of the energy of the excited state become [87]:

$$\Delta E_B = g_J m_J \mu_B B \quad (2.13)$$

where  $\mu_B = \frac{e\hbar}{2m_e}$  is the Bohr magneton and

$$g_J = 1 + \frac{j(j+1) + s(s+1) - l(l+1)}{2j(j+1)} \quad (2.14)$$

is the Landé-factor.

The magnetic field is created by setting up two coils in an anti-Helmholtz configuration with  $z$  being the axis of symmetry, as shown in figure 2.4.

The strength of the field is found from Biot-Savart's law:

$$B_z(z) = \frac{\mu_0 \mathcal{I} N}{2} \left( \frac{a^2}{((z-b)^2 + a^2)^{3/2}} - \frac{a^2}{((z+b)^2 + a^2)^{3/2}} \right) \quad (2.15)$$

and

$$B_x(x) = \frac{\mu_0 \mathcal{I}}{4\pi} \int_0^{2\pi} 2ab \cos \theta \left( (x - a \cos \theta)^2 + a^2 \sin^2 \theta + b^2 \right)^{-3/2} d\theta \quad (2.16)$$

where  $b$  is the distance from one coil to the center,  $a$  is the radius of the coils,  $N$  is the number of windings and  $\mathcal{I}$  is the current. Due to symmetry  $B_y(y)$  is the same as 2.16.

Restricting the attention to positions close to the center, the field is approximated with the first order Taylor expansion:

$$B_z(z) = \frac{\partial B}{\partial z} z \quad (2.17)$$

Due to Maxwell's equations, where  $\nabla \cdot \mathbf{B} = 0$ , it is seen that

$$B_x(x) = \frac{\partial B}{\partial x}x = -\frac{1}{2} \frac{\partial B}{\partial z}x \quad (2.18)$$

and likewise for the y-component.

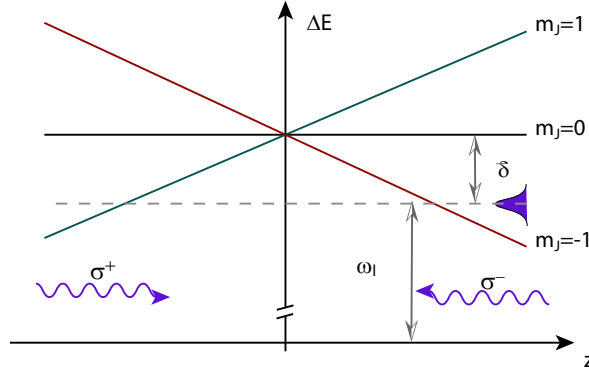


**Figure 2.5:** Zeeman splitting as a function of spatial position. The Zeeman splitting depends linearly on the magnetic field, which is proportional to the distance from the center. For a negative detuning of the laserbeam, an atom positioned at  $z > 0$  is pushed towards the center by the  $\sigma^-$ -beam, while for  $z < 0$  it is pushed towards the center by the  $\sigma^+$ -beam.

The linear relation between position and field results in a linear relationship between position and energy shift due to equation (2.13). This relationship is illustrated in figure 2.5 for all three sub-states along the  $z$ -axis.

According to the atomic selection rules, circularly polarized light  $\sigma^+/\sigma^-$  can in the electric dipole approximation [87] only induce transitions between the ground state and the state with  $(m_J = +1)/(m_J = -1)$  respectively. This is exploited for creating a trap.

Each pair of orthogonal beams are prepared in such a way that one is right-hand polarized  $\sigma^+$  and the other is left-hand polarized  $\sigma^-$ . From figure 2.5 it is seen that by choosing the right polarization, an atom at a position  $z > 0$  is closer to resonance with the left-hand polarized beam ( $\sigma^-$ ) than with the right-hand polarized beam ( $\sigma^+$ ) resulting in a net force towards the center of the magnetic field. An atom at  $z < 0$  would result in an oppositely directed force still towards the center.

Inserting the Zeeman shift into equation 2.5:

$$\begin{aligned} \langle F_{MOT,z} \rangle = & \hbar k \frac{\Gamma}{2} \left( \frac{s_0}{1 + 2s_0 + 4 \left( \frac{\delta - \bar{k} \cdot \bar{v} - \frac{g_{J\mu_B}}{\hbar} \frac{\partial B}{\partial z} z}{\Gamma} \right)^2} \right. \\ & \left. - \frac{s_0}{1 + 2s_0 + 4 \left( \frac{\delta + \bar{k} \cdot \bar{v} + \frac{g_{J\mu_B}}{\hbar} \frac{\partial B}{\partial z} z}{\Gamma} \right)^2} \right) \end{aligned} \quad (2.19)$$

The force  $\langle \bar{F}_{MOT} \rangle$  can be Taylor expanded around  $(x=0, v=0)$  to the first order leading to:

$$\langle F_{MOT,z} \rangle \approx \alpha \bar{v} - \kappa z \quad (2.20)$$

where

$$\kappa = 8k\mu_B \frac{\partial B}{\partial z} \frac{\delta}{\Gamma} \frac{s_0}{[1 + 2s_0 + (\frac{2\delta}{\Gamma})^2]^2} \quad (2.21)$$

The force on the atoms in a MOT shows that they undergo a damped oscillatory motion in the MOT region. The extension of this scheme to a three-dimensional MOT is straightforward [7] when for each spatial dimension a pair of laser beams with the proper circular polarisation is employed (figure 2.4). A magnetic field that vanishes at the center of the trap and increases approximately linearly with the distance from the center can be generated by a pair of anti-Helmholtz coils.

## 2.5 Magnetic Trapping

The Stern-Gerlach experiment in 1924 first demonstrated the influence of inhomogeneous magnetic fields on neutral atoms having a magnetic moment. The principle behind has since been used for focusing and state selection of atomic beams. The first experimental realization of a magnetic trap for neutral atoms was achieved for the first time in 1985 [6] in a quadruple magnetic trap.

The trapping potential felt by an atom in a magnetic trap is generated by the interaction of the atoms magnetic dipole moment  $\bar{\mu}$  with the magnetic fields  $\bar{B}$  of the trap. A classical magnetic dipole interacting with a magnetic field has a potential energy  $U_m = -\bar{\mu} \cdot \bar{B} = \mu B \cos(\theta)$ . Quantum mechanically, the energy levels in a magnetic field are  $E(m_F) = g_J m_J \mu_B B$ , where  $g$  is the Landé g-factor and  $m_J$  is the quantum number of the z-component of the angular momentum. The classical term  $\cos(\theta)$  can be related to the quantum mechanical quantity  $m_J/J$ . A dipole can lower its energy by moving to a lower field, or by changing its orientation such that it is more closely aligned with the magnetic field.

The angle  $\theta$  between the dipole moment and the magnetic field is constant when an atom is exposed to a homogeneous field ( $\mu$  simply precesses around the magnetic field at constant angle  $\theta$ ). As a dipole moves through an inhomogeneous field, it experiences a local magnetic field which is changing in both magnitude and direction. An isolated atom moving slowly enough through an inhomogeneous magnetic field feels a conservative potential simply proportional to the magnitude of the field. To trap atoms in such a potential, a local minimum of the magnetic potential energy  $E(m_J)$  must be created. For  $g_J m_J > 0$  (weak-field seeking states) this requires a local magnetic field minimum. Strong-field seeking states ( $g_J m_J < 0$ ) cannot be trapped by static magnetic fields, since a magnetic field maximum in free space is not allowed by Maxwells equations [88], [89].

The ground state of  $^{24}\text{Mg}$  cannot be magnetically trapped due to the lack of a magnetic moment. However the  $^3P_{1,2}$  states are possible to trap magnet-

ically. In this case  $g_J = 3/2$  is positive, and  ${}^3P_1 m_J = 1$  and  ${}^3P_2 m_J = 1, 2$  are the trapped states. The trapping magnetic field in the experiment is the MOT quadrupole magnetic field generated by the coils in the anti-helmholtz configuration. The magnetic field close to the center can be approximated by:

$$\bar{\mathbf{B}}(x, y, z) = A(x\hat{\mathbf{x}} + y\hat{\mathbf{y}} - 2z\hat{\mathbf{z}}) \quad (2.22)$$

where  $A = \frac{\partial B}{\partial x} = \frac{\partial B}{\partial y} = -\frac{1}{2} \frac{\partial B}{\partial z}$  is the magnetic field gradient.

The trap depth can be estimated by calculating the Zeeman shift in the  $z$  direction. For the  ${}^3P_1 m_J = 1$  state a trap depth of  $100.8\mu\text{K}/\text{gauss}$  is obtained. Combined with the experimental gradient of approximately  $170$  gauss/cm, this results in a trap depth of  $1.7$  mK/mm. Meaning that a MOT-sample at temperature of  $5$  mK can be trapped in a reasonable small trap of  $3$  mm in radius.

## 2.6 Optical Trapping

The Stark shift,  $\Delta\nu$ , of an energy level  $i$  in the presence of an electric field with amplitude  $E$  is given by [90]:

$$h\Delta\nu = -\frac{1}{2}\alpha_i|E|^2 \quad (2.23)$$

where  $\alpha_i$  is the polarizability of the atomic state  $i$ .

In the presence of a laser field of frequency  $\omega_L$ , the dynamic dipole polarizability of a state  $i$  involves the sum over the dipole interaction between state  $i$  and excited states  $k$  given as [87]

$$\alpha_i(\omega_L) = 2e^2 \sum_k \frac{\hbar\omega_{ik} |\langle\phi_k|\mathbf{D}|\phi_i\rangle|^2}{\hbar^2(\omega_{ik}^2 - \omega_L^2)} \quad (2.24)$$

where  $e$  is the electron charge,  $\omega_{ik}$  is energy difference between states  $i$  and  $k$ ,  $\omega_L$  is the energy of a laser photon and with  $\mathbf{D} = -e\mathbf{r}$  representing the electric dipole operator. The dipole matrix element  $|\langle\phi_k|\mathbf{D}|\phi_i\rangle|^2$  can be written in terms of transition rates  $A_{ik}$  using the fact that

$$A_{ik} = \frac{e^2}{4\pi\epsilon_0} \frac{4\omega_{ik}^3}{3\hbar c^3} |\langle\phi_k|\mathbf{D}|\phi_i\rangle|^2 \quad (2.25)$$

Combining equations 2.24 and 2.25 and including a term which contains the selection rules, gives

$$\alpha_i = 6\pi\epsilon_0 c^3 \sum_{k,m'} \frac{A_{ik}(2J_k + 1)}{\omega_{ik}^2(\omega_{ik}^2 - \omega_L^2)} \begin{pmatrix} J_i & 1 & J_k \\ m_i & p & -m' \end{pmatrix}^2 \quad (2.26)$$

which depends only on the laser frequency, the transition rates between states  $i$  and  $k$ , and their corresponding energy difference  $\hbar\omega_{ik}$ . The expres-

sion in large parentheses denotes a Wigner 3- $j$  symbol. It describes the selection rules and relative strengths of the transitions depending on the involved angular momenta  $J$ , their projections  $m$ , and the polarization  $p$  of the laser. Then only the measured  $A_{ik}$  values and state energies are needed for performing the calculation. Using data from [91], the polarizability can be calculated. For a 1D optical lattice geometry, the optical potential experienced by the atoms is described by a longitudinal standing wave with a gaussian distribution in the radial dimension, given by [92]

$$U(r, z) = 4U_m e^{\frac{-2r^2}{w(z)^2}} \cos^2(2\pi z/\lambda_L). \quad (2.27)$$

Where  $U_m = P\alpha_i/(\pi c\epsilon_0 w(z)^2)$ ,  $P$  is the average laser power of the incoming beam,  $w(z)$  is the beam waist at a longitudinal distance  $z$  from the focus of the beam,  $r$  is the radial distance from the beam center, and  $\lambda_L$  is the laser wavelength.

In figure 2.6 the maximum Stark shift as a function of wavelength can be seen. The different curves correspond to different states of  $^{24}\text{Mg}$  for different polarizations of the trap laser in a 1D lattice configuration with an incoming power of 600 mW and a beam waist of 60  $\mu\text{m}$ . In the calculation, hyperfine structure has not been included, so the  $^1\text{S}_0$  and  $^3\text{P}_0$  states only have a  $m_J = 0$  state and  $^3\text{P}_1$  has  $m_J = -1, 0, 1$ . Inclusion of the hyperfine structure is discussed in [93], [94] and is relevant for an operating clock, however for locating the magic wavelength<sup>2</sup>, the shifts induced by the hyperfine interaction are negligible. The inset in figure 2.6 show the region of interest which contains crossings (and thereby magic wavelengths) between the  $^1\text{S}_0$  ground state and an excited  $^3\text{P}$  state. For the  $^3\text{P}_0$  state the magic wavelength is found at 464 nm in agreement with [95]. For the  $^3\text{P}_1$  state crossings are found at 452 nm and 433 nm. At these wavelengths it is difficult to generate high power lasers and it is necessary to use external cavities for frequency doubling. However the calculation of the magic wavelength is not better than the information

---

<sup>2</sup>The magic wavelength is the wavelength at which the Stark shift of the ground and excited state cancel.

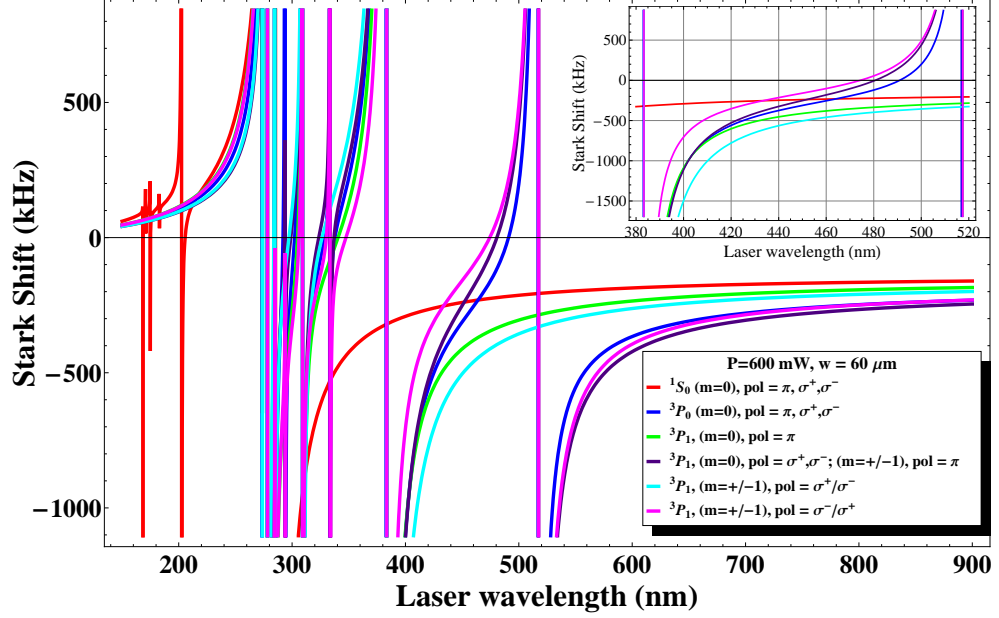


**Figure 2.6:** Stark shift of different states in  $^{24}\text{Mg}$  and different polarizations of trap laser in a 1D lattice configuration with an incoming power of 600 mW and a beam waist of 60  $\mu\text{m}$ . Inset show the region of interest which contains crossings (and thereby magic wavelengths) between the  $^1S_0$  ground state and an excited  $^3P$  state. For the  $^3P_0$  state the magic wavelength is found at 464 nm.

available on the different lines and line strengths involved and especially important are the states closest to the  $^1S_0$  and  $^3P_0$  states, meaning the  $^1P_1$ ,  $^3S_1$  and  $^3D_1$  states. Unfortunately these levels are not very well determined for Mg and a rather large uncertainty in the magic wavelength is expected. In the original paper proposing the optical lattice clocks [93] the magic wavelength calculated for Sr later turned out to be more than 10 nm off [96]. A 10% error in the value for the linewidth of one of the three most important levels ( $(3s^2)^1P_1$ ,  $(3s4s)^3S_1$ ,  $(3s3d)^3D_1$ ) for magnesium will lead to a shift of

up to 6 nm in the calculation of the magic wavelength.

The parameters used in figure 2.6 (600 mW incoming power and a beam waist of  $60 \mu\text{m}$ ) give a trap depth of  $44 \mu\text{K}$ . This is a very shallow trap compared to the Doppler temperature of the 285 nm MOT of 1.9 mK. The lattice clocks realized for Sr or Yb have the option of a second stage cooling on the intercombination line resulting in a much lower temperature (down to  $1 \mu\text{K}$ ) of the Yb or Sr MOT sample that is loaded into the optical lattice. This option is not available for Mg since the cooling force of the intercombination line is too weak to sustain the atoms in the gravitational field. Other cooling schemes have been suggested for Mg (e.g. quench cooling [45] and two-color cooling [97]), however none have proven to be capable of reducing the temperature of Mg below 1 mK. As an alternative to reducing the temperature of the atom, one could instead increase the trap depth of the optical lattice and load the atoms directly from the MOT into the optical lattice as demonstrated in [98]. In order to reach a significant loading rate, the trap depth has to be comparable to the temperature of the atoms. It requires an intensity of  $120 \text{ kW/cm}^2$  to reach a trap depth of 0.5 mK. This can be realized by generating 200 mW of 464 nm light by frequency doubling and coupling it into an enhancement cavity with a build up of 70 and a beam waist of  $60 \mu\text{m}$ . The scattering rate at this intensity is 0.07 photons per second which is considered insignificant. Different strategies for confining a sample of Mg atoms in an optical lattice at the magic wavelength will be discussed later.



---

## CHAPTER 3

---

# Experimental Setup

In this chapter an overview of the experimental setup is presented. A general overview of the different parts of the experiment can be seen in figure 3.1. The focus will initially be on the many different light sources involved in the experiments and their frequency stabilization. Furthermore the MOT-setup is described including the different detection schemes used, and to conclude is a section about the generation of metastable magnesium atoms.

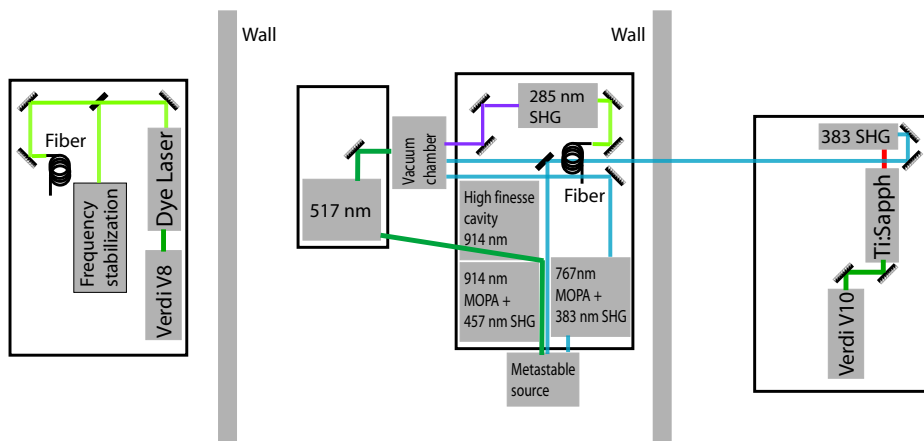


**Figure 3.1:** General overview of experimental setup. The different elements will be described in the following chapter.

### 3.1 Laser Systems

In this experimental work six different light sources have been used to address a similar amount of magnesium transitions, see figure 3.2. All of these light sources except two are frequency doubled and therefore a section giving a brief introduction to second harmonic generation and enhancement cavities have been included before describing the different laser systems.

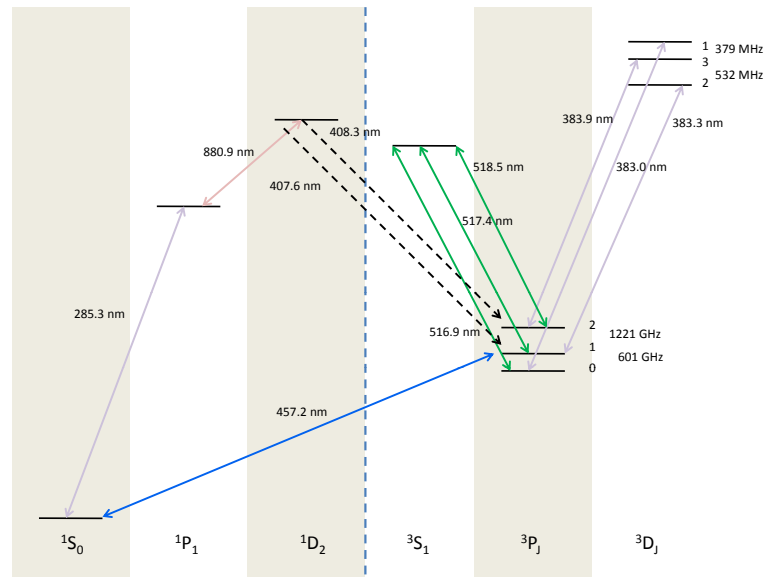


**Figure 3.2:** Level diagram for  $^{24}\text{Mg}$  showing transitions relevant for this thesis. The different laser systems described in this section are used for addressing the transitions shown here.

### 3.1.1 Second Harmonic Generation

Optical second harmonic generation (SHG) is a technique which provides the means for extending laser radiation to shorter wavelengths of the optical spectrum. The main objective is to convert a large fraction of power at the fundamental frequency to that at the second harmonic frequency. SHG is either performed with single pass through a nonlinear crystal or in a nonlinear crystal placed in an enhancement cavity. SHG in an external resonator for the fundamental light is usually chosen when no laser source is available at the desired wavelength. The most obvious motivation for employing an external resonator is to enhance the fundamental light intensity and hence the conversion efficiency in the nonlinear crystal. Another reason for this choice is the fact that the integration of a doubling cavity into a laser setup helps to make the system all-solid-state with obvious advantages related to maintenance and compactness. In general, SHG in an external resonator is preferred, when any disturbance to the laser action, as a result of placing a nonlinear optically active crystal in the laser cavity, must be prevented. The first experiment in nonlinear optics consisted of generating the second harmonic of a ruby laser beam at 694 nm that was focused on a quartz crystal [99]. The conversion efficiency of this first experiment was about  $\sim 10^{-8}$  which since has been improved to a point where about 90 percent conversion has been observed in cw second harmonic generation from  $\text{LiNbO}_3$  inside a linear standing wave cavity [100].

Second harmonic generation is a process where a nonlinear optical process produces laser light which has twice the frequency of the input beam. The generated power at twice the fundamental frequency in a nonlinear medium is given by [101]:

$$P_{2\omega} = 2 \left( \frac{\mu_0}{\epsilon_0} \right)^{3/2} \frac{\omega^2 d_{eff}^2 l^2 P_\omega^2}{n^3 A} \frac{\sin^2(\frac{\Delta kl}{2})}{(\frac{\Delta kl}{2})^2} \quad (3.1)$$

Here  $d_{eff}$  is the effective second-order susceptibility, which depends on the direction of propagation in the medium,  $\omega$  is the angular frequency of

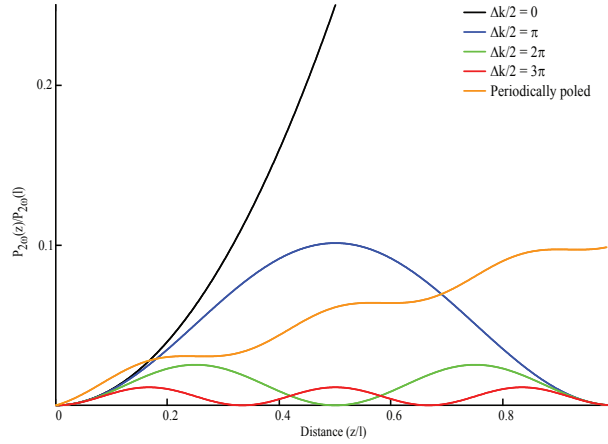


**Figure 3.3:** Normalized SHG output as function of normalized distance in a nonlinear optical crystal for different amounts of phase velocity mismatch  $\frac{\Delta k}{2}$ . In periodically poled crystals the oscillatory behavior is used so the sign of the  $d_{eff}$  is changed with a period of  $l_c/2$  in order to enhance second harmonic generation (orange).

the fundamental beam,  $P_\omega$  is the incident power in the fundamental beam,  $l$  is the length of the crystal,  $A$  is the area of the incident beam,  $n$  is the refractive index of the crystal,  $\mu_0$  is the vacuum magnetic permeability,  $\epsilon_0$  is the vacuum electrical permittivity, and  $\Delta k = k_2 - 2k_1$  is the phase mismatch between the second-harmonic beam and the fundamental beam, where  $k_1$  and  $k_2$  are the wave numbers of the fundamental and second harmonic beams.

It is worth noting that only a slight phase mismatch leads to periodic oscillation of the conversion efficiency over a distance known as the coherence length  $l_c$ . In this situation, the energy in the nonlinear medium will periodically flow back into the input signals thereby diminishing the overall efficiency. One way to avoid this is to change sign of the  $d_{eff}$  with a period of  $l_c/2$  so the second harmonic generation is enhanced which is used in periodically poled crystals, see figure 3.3.

Second harmonic generation involves the interaction of two fields with frequency  $\omega_1$  and  $\omega_2 = 2\omega_1$ , and as implied, these signals must obey conservation of energy. To achieve phase matching, the refractive index seen by the optical signals inside the crystal must be considered. Therefore the phase

matching condition can be rewritten as:

$$0 = 2\frac{n_1}{\lambda_1} - \frac{n_2}{\lambda_2} \quad (3.2)$$

The crystal is normally not phase matched due to dispersion but this can be compensated by exploiting the birefringent properties of the crystal. Phase matching can be achieved by adjusting the birefringence between the ordinary and extraordinary beams. This can be done by changing the angle between the optical axis of the crystal and the laser beam, i.e. angle phase matching. The nonlinear interaction is classified by the birefringent configuration where "o" stands for ordinary beam and "e" for extraordinary beam. The configuration in which both input beams are of the same polarization i.e. (ooe) or (eoo) is referred to as type I phase matching, and when they are different (i.e. (oeo)) it is referred to as type II phase matching.

Angle phase matching can be used over a wide range of wavelengths since the birefringence changes significantly with angle. However, the birefringence causes the energy flow (Poynting vector) of the ordinary and extraordinary beams to propagate in different directions, an effect known as walk-off. This reduces the overall efficiency since the beams must remain overlapped for the nonlinear interaction to occur and causing a progressive mismatching of the direction of propagation of the second harmonic beam along the crystal. This produces a longitudinally multi-mode second harmonic beam whose mode get worse for increasing crystal length. Walk-off does not occur if all the beams propagate at  $90^\circ$  to the optic axis of the crystal but then the birefringence must be adjusted using its temperature dependence. This type of phase matching is called noncritical phase matching or temperature phase matching. Noncritical phase matching has advantages over angle phase matching since it is more tolerant of misalignment which therefore allows stronger focusing of the beams to obtain higher efficiency. The disadvantage is that the temperature dependence of the birefringence is often rather small, and therefore the range of wavelengths that can be non-critically phase matched is usually much smaller than for angle phase matching. In the laser systems described in this thesis, periodic poling is used together with non critical and

angle phase matching.

### 3.1.2 Enhancement Cavities

Optical resonators are an important part of frequency doubling cw lasers since the process is characterized by a low efficiency scaling with the length of the crystals and the square of the power inside the crystal. External ring cavities are usually exploited to enhance the circulating power inside the non-linear crystal to increase the efficiency and limit the length of the crystal itself.

The following section presents the basic features of the frequency doubling cavities.

There are two basic types of optical resonators: the standing wave resonator and the traveling wave or ring resonator. The simplest resonator consists of two facing mirrors of which at least one is spherical. A ring resonator consists of at least three mirrors. For the light sources used in this experiment four-mirror traveling-wave resonators are used.

For simplicity an optical resonator with two mirrors separated by a distance  $L$  is considered. An electromagnetic wave with frequency  $\omega$  incident on the first mirror  $M_1$  of the resonator splits up into a reflected and a transmitted wave, with amplitudes  $E_0, E_R, E_T$ . Assuming that the reflection takes place at the surfaces of the mirrors pointing towards the inner side of the resonator the reflected wave will obtain a phase shift of  $\pi$  at this interface. The mirrors are characterized by their reflection coefficients  $r_1$  and  $r_2$  and by their transmission coefficients  $t_1$  and  $t_2$ . The transmitted wave will then again be reflected and transmitted on the second mirror thereby bouncing back and forth inside the cavity. The electromagnetic field amplitude of the wave transmitted through the resonator is given by:

$$I_T = E_T E_T^* = E_0^2 \frac{t_1^2 t_2^2}{1 + r_1^2 r_2^2 - 2r_1 r_2 \cos(2L\omega/c)} \quad (3.3)$$

which depends on the phase shift  $\Delta\phi = 2L\omega/c$  between adjacent partial

waves.

If this phase shift corresponds to an integral multiple of  $2\pi$ , all partial waves interfere constructively in contrast to all other cases where the partial waves interfere more or less destructively. The phase difference between the partial waves and the transmitted power varies with the angular frequency  $\omega$  of the incident radiation. The frequency difference that leads to a phase shift of  $2\pi$  between two consecutive round trips of the radiation inside the resonating cavity is the free spectral range (FSR).

$$FSR = \frac{c}{2L} \quad (3.4)$$

The full width at half maximum linewidth (FWHM)  $2\pi\delta\nu$  of the interference structure becomes sharper if more partial waves contribute to the transmitted amplitude, i.e. if the reflectivities  $r_1$  and  $r_2$  of the mirrors become higher.

The effective number of round-trips that a photon makes before escaping the resonator is determined by transmission or loss mechanisms. The intensity inside the resonator on resonance is:  $I = bI_0$ , where  $b$  is the build up factor and is given by:  $b = 1/\ell$  where the losses  $\ell$  are the sum of all resonator intensity losses including mirror losses, mirror transmissions and nonlinear crystals.

Frequency doubling resonators consist of mirrors and a nonlinear crystal in a variety of configurations. Figure 3.4 shows a sketch of the different cavity designs used in the experiments. All the cavities used are bow-tie configurations. A traveling wave ring resonator is generally preferred to a linear cavity for several reasons. First, no light is directly reflected back to the laser to disturb its stability. Second, only a single pass through the nonlinear crystal contributes to the round trip loss and the frequency doubled light is generated unidirectionally. Third, the fundamental and harmonic beams may be coupled to the cavity through plane optical components. The cavity has two focuses which can be adjusted independently so that the mode matching with the pump laser is easy. When an antireflection (AR) coated

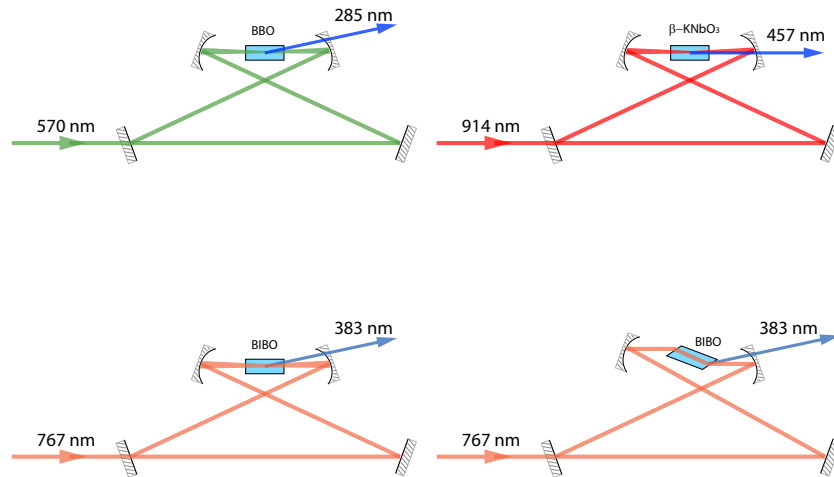


**Figure 3.4:** Illustration of the different ring cavities used. All are bow tie configurations but with different crystals. An AR-coated  $\beta$ -barium borate (BBO) crystal is used for generating light at 285 nm and has a significant walk-off (84 mrad). A potassium niobate  $\text{KNbO}_3$  crystal is used for generating light at 457 nm. The crystal is antireflection coated and has no walk-off due to non-critical phase matching. Adjustment and stabilization of its temperature is necessary. Bismuth triborate (BIBO) is used for SHG of 383 nm light both as AR-coated and as Brewster cut. Walk off is considerable but less than for BBO (69 mrad).

crystal is used at normal incidence, it typically employs a cavity with a small folding angle. Residual reflectivity from the AR coatings and possible coating damage in high power applications can be eliminated by using a Brewster-cut crystal. Most of these resonant cavities employ a partial reflector to couple the radiation into the cavity. These reflectors usually have about 95 – 99% reflectivity. The passive losses of the crystal can be made small if either the crystal is AR coated or Brewster cut.

The enhancement of power in a resonant cavity depends on the transmission of the coupling mirror and the total losses inside the cavity. These losses are due to the less than 100% reflectivity of the highly reflecting mirrors, the

absorption and scattering in the crystal, and due to the conversion of the fundamental power into second harmonic power.

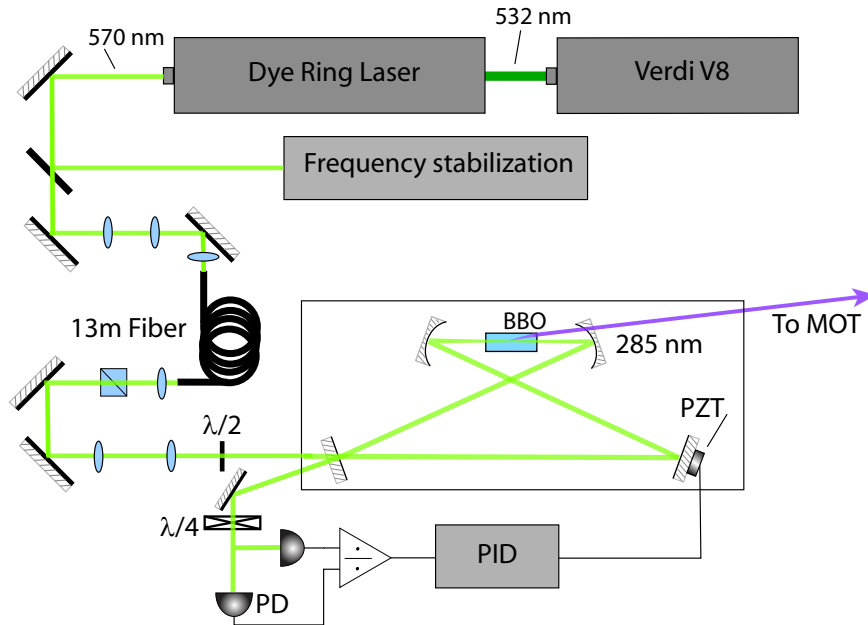


**Figure 3.5:** Illustration of the 285 nm laser setup. A 532 nm diode laser pumps a dye ring laser to generate 570 nm light. A part of the beam is split off and sent to a frequency stabilization system. The other part is fiber coupled and sent to the frequency doubling cavity which is stabilized by a Hänsch-Couillaud scheme.

### 3.1.3 285 nm Laser System

The 285 nm light used for the main cooling transition  $^1S_0 - ^1P_1$  is generated by SHG of 570 nm light. An overview of the setup can be seen in figure 3.5. The 570 nm light is made by a ring dye-laser, Coherent 899-21, using Rhodamine 560 as dye and pumped by a Verdi Coherent V8 system. The Verdi system is a diode-pumped second harmonic generation system, producing a maximal output power of 8 W at 532 nm with a linewidth of less than 5 MHz. The dye-laser is an easy-tunable system, with a range over several tens of nm

with the same dye and a linewidth of around 1 MHz when stabilized to an external Fabry-Perot cavity. Compared to more compact systems like diode lasers or fiber lasers, it requires a great deal of maintenance to be kept in optimal condition. In the usual experimental conditions, an output power of around 1.3 W at 570 nm is generated using 5.5 W of pumping power. The 570 nm laser beam is divided into two beams by a 3% beamsplitter. The more intense part of the beam is sent through a fiber to the second harmonic generation cavity. The 3% reflections are used for frequency stabilizing the system based on the polarization spectroscopy of the  $I_2$  molecule, see section 3.1.3. A telescope is used to achieve maximum coupling of  $\sim 1$  W through the fiber. Before entering the SHG cavity, an adjustable telescope optimizes the mode-matching of the primary beam inside the cavity. In this way, the 570 nm light is coupled inside a ring cavity where in the focus a  $\beta - BaB_2O_4$  (BBO) crystal is placed. The choice of the BBO crystal has been made due to its high non linearity and transparency at 285 nm. Two characteristics of this crystal needs to be pointed out. First of all, it is hygroscopic and therefore sensitive to the humidity of the air which can be reduced using an antireflection (AR) coating. A second aspect is that the walk-off is not negligible, leading to a non-gaussian SHG beam with the presence of many fringes in the horizontal direction. Details on the construction, characteristics and calculation of the SHG ring cavity can be found in [102]. The crystal is antioated for 570 nm, 5 x 3 x 3 mm in dimensions and the SHG cavity generates an output power of around 50 mW at 285 nm with an input power of 900 mW at 570 nm. The output is mainly limited by the use of an old BBO crystal which over the years has deteriorated.

### Hänsch-Couillaud Locking of Cavities

In order to have a build-up in the cavities used for frequency doubling, the traveling length in the cavity has to be an integer multiple of half the injected wavelength. This means that the intensity of the frequency doubled light is strongly sensitive to acoustic noise and changes in frequency of the injected light source. By use of a feedback system it is possible to lock the traveling length relative to the injected wavelength. A commonly used feedback system

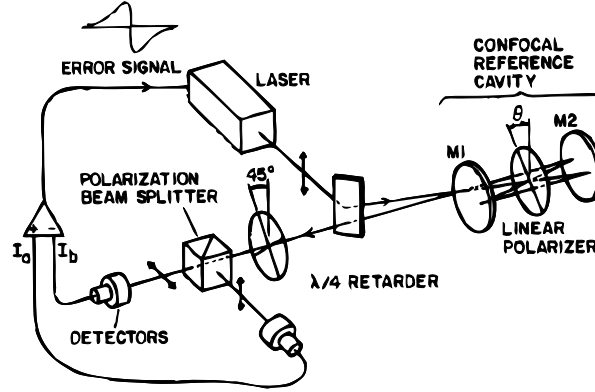


**Figure 3.6:** Illustration of the principles in a Hänsch-Couillaud scheme. The illustration is from the article [103] where the scheme was first proposed.

is the Hänsch-Couillaud locking scheme [103]. The technique is used for all the frequency doubling cavities described in this thesis.

Consider the setup shown in figure 3.6. Linearly polarized laser light is injected into a resonator. Inside the resonator a linear polarizer is tilted an angle of  $\theta$  relative to the polarization of the light. Treating the electric field as plane waves, the amplitudes inside the cavity can be decomposed into components that are parallel and perpendicular to the optical axis of the polarizer:

$$E_{\parallel}^i = E^i \cos(\theta) \quad \text{and} \quad E_{\perp}^i = E^i \sin(\theta) \quad (3.5)$$

The reflected wave components are:

$$E_{\parallel}^r = E_{\parallel}^i \left( \sqrt{R_1} - \frac{T_1}{R_1} \frac{R e^{i\phi}}{1 - R e^{i\phi}} \right) \quad (3.6)$$

$$E_{\perp}^r = E_{\perp}^i \sqrt{R_1} \quad (3.7)$$

where  $R_1/T_1$  is the reflectivity/transmissivity of the in-coupling mirror,  $\phi$  is the acquired phase difference relative to the injected electric field, and

$R$  is the loss fraction from one round-trip in the cavity.

If the resonator is on resonance with the laser light, the parallel reflected component does not acquire a phase and the total reflected light remains linearly polarized. However, if the resonator is off resonance, the parallel reflected light has acquired a phase  $\phi$  relative to the perpendicular reflected component which causes an elliptic polarization.

Linearly polarized light can be considered as a superposition of two opposite circularly polarized components of equal amplitude. If the light is elliptically polarized, the circular components have different magnitudes. Thus when the reflected beam is sent through a  $\lambda/4$  wave plate with the fast axis parallel to the optical axis of the polarizer followed by a polarizing beam splitter, the beam is split into two components. When on resonance, the light after the  $\lambda/4$ -plate is circularly polarized causing the two beams to have equal intensity. However, if not on resonance, the elliptic polarization is split into two components with different intensities. By setting up the ABCD matrix [104] of the resonator and the  $\lambda/4$ -plate followed by a polarizing beam splitter, the field amplitudes of the two outputs after the polarizing beam splitter can be calculated. Calculating the intensity difference of the two outputs results in the signal:

$$I_a^r - I_b^r = 2 \cos(\theta) \sin(\theta) \frac{T_1 R}{4(1 - R^2)R} \frac{\sin(\phi)}{\sin^2(\frac{1}{2}\phi)} I^i \quad (3.8)$$

The signal is plotted in figure 3.7 as a function of the phase difference  $\phi$ , and is seen to be ideal for use as an error signal. When on resonance, the signal is zero, however when off resonance, the signal is either positive or negative, causing the feedback signal to compensate. The signal has the maximal slope for  $\theta = \pi/4$ , in this case only half the intensity builds up inside the cavity. The angle  $\theta$  should therefore be sufficiently close to zero in order to maximize the output from the cavity while still maintaining a proper error signal. By connecting the signal to a piezo transducer attached to a mirror in the cavity, the feedback signal ensures that the resonator stays on resonance with the injected light source.

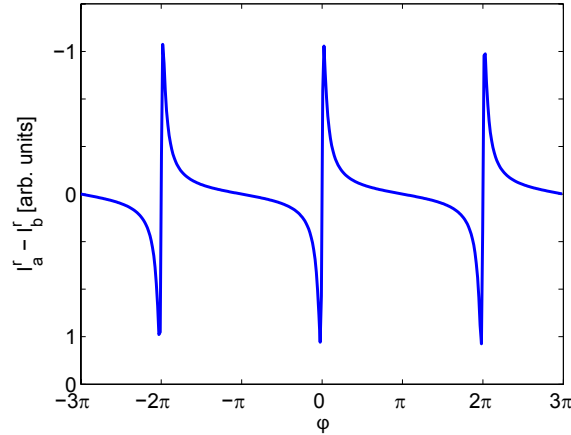


**Figure 3.7:** Plot of the ideal error signal from a Hänsch Couillaud locking scheme derived in equation (3.8).

In our case, we do not have a linear polarizer inside the cavity but instead a nonlinear crystal. However, the birefringence from the crystal ensures that the travel lengths for the two polarizations are different. The vertically polarized light from the laser is therefore tilted by a small angle  $\theta$  by a  $\lambda/2$ -plate. Setting the resonator on resonance with the parallel component causes the perpendicular component to be fully reflected. The scheme is used for all cavities. The error signal from the differential detector is sent through a proportional-integral-derivative (PID) controller to correct for both short term fluctuations and long term drifts.

### Frequency Stabilization using Polarization Spectroscopy of $I_2$

The stabilization of the 285 nm source to the  $^1S_0$ - $^1P_1$  atomic transition is performed by exploiting the hyperfine levels of the R(115)20-1 absorption line of the  $^{127}I_2$  molecule [105] which, once it has been frequency doubled, happens to overlap with the resonance of the  $^1S_0$ - $^1P_1$  ( $\lambda_{UV} = 285.234$  nm), figure 3.8.

The frequency stabilization setup is shown in figure 3.9. It is a pump probe polarization spectroscopy setup [106]. The probe beam is double-passed through an acousto-optic modulator (AOM) to make it possible to

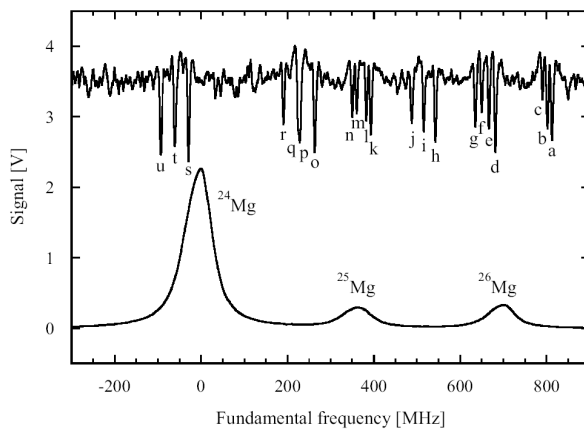


**Figure 3.8:** *Spectrum of iodine molecules together with the magnesium fluorescence as function of the fundamental frequency. The origin of the frequency axis is positioned at the maximum of the  $^{24}\text{Mg}$  fluorescence [102].*

change the frequency of the probe and thereby address different velocity classes of the iodine, resulting in a change of the position of the hyperfine peaks on the Doppler profile. The AOM is also used to modulate the signal so that a lock-in amplifier can be exploited to clean and amplify the signal.

Let two 570 nm beams counter propagate through a glass cell with a gas of  $I_2$ , as seen in figure 3.9. One of the beams has a high intensity (pump beam) and is right hand polarized,  $\sigma^+$ , while the other beam (probe beam) has a weak intensity and is vertically polarized,  $\pi$ . A photodiode ( $PD$ ), with a linear horizontal polarizer in front of it, measures the light from the probe beam that has passed through the glass cell. The ground state of the spectral line used in  $I_2$  has three degenerate hyperfine levels, here denoted by  $m_K = -1, 0, +1$ , whereas the excited state has three nondegenerate levels  $m_K = -1, 0, +1$ . For simplicity, consider only  $m_K = 0$  in the excited state as seen in figure 3.10. When on resonance, the pump beam will only induce transitions from  $m_K = -1 \rightarrow m_K = 0$  due to the atomic selection rules [87]. The state  $m_K = -1$  is therefore quickly depleted. The linear polarization of the probe is a superposition of left- and right-handed polarizations with equal weights. When the light passes through the glass cell, only the  $\sigma^-$

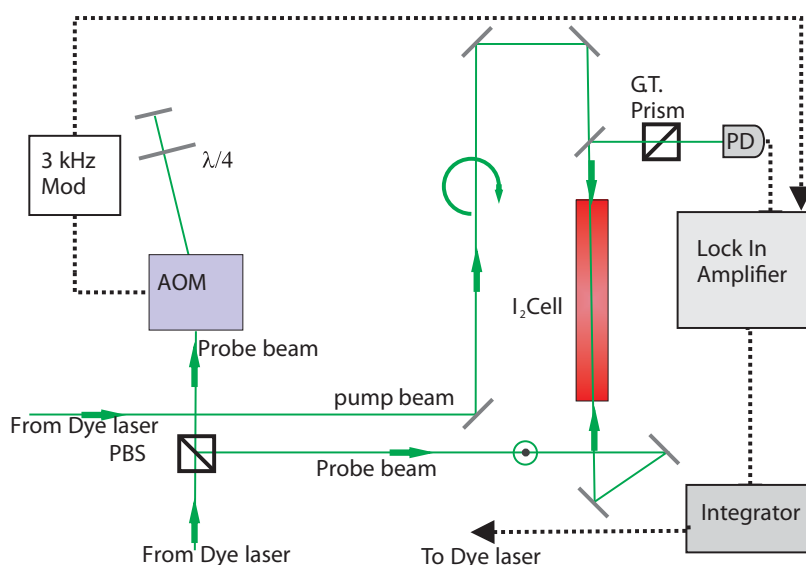


**Figure 3.9:** *Illustration of the polarization spectroscopy setup. The beam is split into two beams, pump and probe beam. The probe beam is double passed through an AOM and sent through a glass cell containing a gas of iodine. The horizontally polarized part of the probe beam is reflected on a beamsplitter and detected on a photodiode (PD). The pump beam is sent through the iodine glass cell.*

is absorbed due to the optical pumping of the pump beam. In the linear basis, the polarization has a component in the horizontal plane which is then detected by the photodiode. If the light is not on resonance, the probe beam propagates unaffected through the gas and maintains its vertical polarization. In this case, no light is detected by the photodiode.

In order to lock the laser at any frequency near the resonance, an AOM is inserted in the probe beam, see figure 3.9, and the frequency shifted beam is used for the glass cell. The procedure is exactly as described above only this time the two beams will only simultaneously interact with those molecules Doppler shifted by  $kv = 1/2\hbar\delta\omega$ , where  $v$  is the velocity component along the axis of the laser beams, and  $\delta\omega$  is the frequency shift induced by the AOM. The signal to noise ratio observed on the photodiode (PD) is too small to lock to and therefore the signal is sent to a lock-in amplifier, that removes

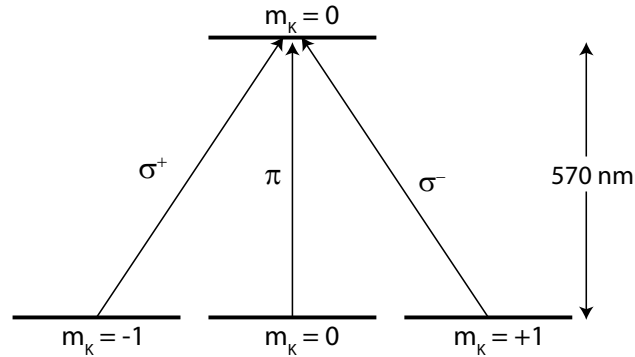


**Figure 3.10:** *The energy levels used for polarization spectroscopy.*

all high frequencies different from that of the modulation frequency of the AOM.

### 3.1.4 457 nm Laser System

The 457 nm laser system is used for the intercombination line  $^1S_0 - ^3P_1$  and thereby connecting the single to the triplet states of magnesium.

The 914 nm light source used for frequency doubling is based on a diode laser system. The system consists of a master laser and a tapered amplifier used for power amplification and known as a MOPA (Master Oscillator Power Amplifier) system. As the name implies, the master laser is the one controlling wavelength and linewidth of the 914 nm light. The laser diode is anti-reflection coated and has a typical output of 30 mW in an external cavity configuration. Diode lasers typically have very short cavity lengths ( $\sim 1 \mu\text{m}$ ) resulting in a rather broad linewidth [104]. In order to reduce the linewidth, an external cavity is set up. Setting up a mirror outside the laser diode in such a way that it reflects light back into the cavity, would result in a combined system that has an effective cavity length far bigger than the cavity length of the diode. This will effectively reduce the linewidth of the light transmitted through the mirror. Moreover, if the mirror selec-

tively reflects some frequencies and transmits others, the linewidth is further reduced. This can be realized by a grating instead of a mirror in a Littrow configuration. By properly adjusting the angle of the grating, the first order diffracted beam is coupled back into the cavity, whereas the 0'th order is used as output. Tuning the laser is now possible by changing the angle of the grating with a piezo electric element, see figure 3.11.

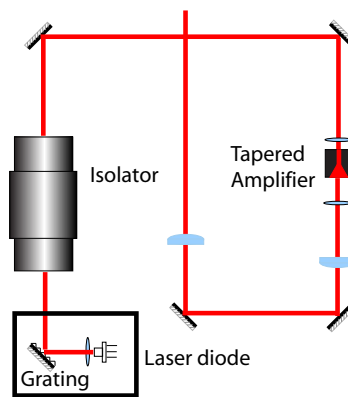


**Figure 3.11:** Schematic of the MOPA setup with a master diode laser and a tapered amplifier.

The amplification of the master laser is done by a tapered amplifier. Light from a free running tapered amplifier is typically of poor quality with multiple spatial modes and a linewidth of the order of nanometers, however they have a high output power. Injecting the master laser into the tapered amplifier dramatically improves the multiple spatial modes and reduces the linewidth of the emission to the linewidth of the master diode. The output of the tapered amplifier is up to 1 W.

After the tapered amplifier, beam shaping is done by two cylindrical lenses. The beam passes through another isolator before being coupled into a fiber to clean up the spatial mode of the beam. A small part of the infrared (IR) beam is split off by a polarizing beamsplitter cube and sent into a wave meter and to a high finesse cavity for frequency stabilization and linewidth reduction, whereas the rest is injected into the SHG cavity with an antireflection coated potassium niobate ( $\text{KNbO}_3$ ). Details of the crystal and the

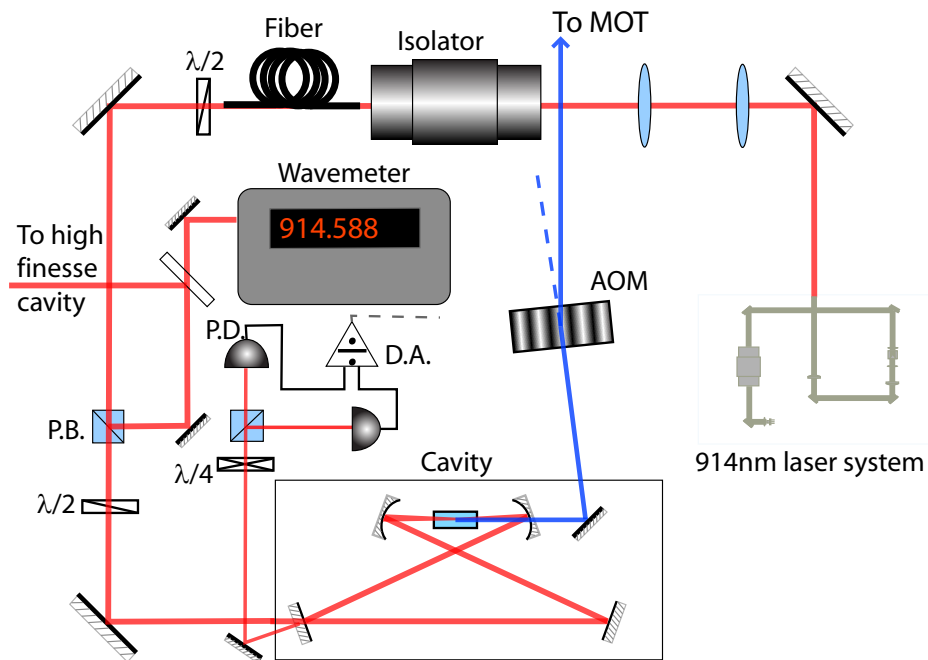


**Figure 3.12:** Illustration of the 457 nm laser setup. The 914 nm beam is sent through an isolator to avoid feedback in the tapered amplifier and a fiber to clean the mode before coupling into the SHG cavity. A small part of the beam is reflected by a polarizing beam splitter cube and used for measuring the wavelength by a wave-meter and for stabilization to a high finesse cavity. The transmitted beam is injected into the SHG cavity. Typically 70 mW of 457 nm is generated. The beam reflected from the input coupler mirror is used for locking the length of the cavity using the Hänsch-Couillaud scheme.

cavity design can be found in [107]. The phase-matching condition of  $\text{KNbO}_3$  is dependent on the temperature. In the case of 914 nm, the 457 nm non-critical phase matching condition is obtained around a temperature of  $143^\circ\text{C}$ . A stable temperature is obtained by placing the crystal inside a homemade oven consisting of a copper capsule in contact with a peltier element and a thermistor both connected to stabilization electronics which feedbacks on the peltier. The ring cavity is stabilized by the Hänsch-Couillaud locking scheme. Thanks to the non-critical phase matching condition the walk-off effect is not present and the output blue beam is characterized by a mode very close to  $TEM_{00}$ . Furthermore, the long-time stability of the diode laser path grants

a rather constant behavior of the system during multiple experimental sessions. A maximum conversion efficiency has been measured to be as high as 55 % [107], however on daily basis a conversion efficiency of  $\sim 25\%$  is obtained corresponding to around 70 mW of blue light. The 457nm output passes an AOM acting as a beam shutter before entering the vacuum chamber. It is possible to get 80% of the incoming power in the 1st order diffracted beam. The full setup is shown in figure 3.12. A telescope was also set up to generate a collimated beam with a waist diameter of about 2 mm, corresponding to the MOT dimensions.

### Stabilization to High Finesse Cavity

The 914 nm diode laser is stabilized to a high finesse cavity in order to reduce the linewidth and counteract drifts. This procedure is chosen due to different reasons. Firstly, stabilization to an atomic sample in a beam or vapor cell is quite challenging for the 457 nm  $^1S_0 - ^3P_1$  intercombination line due to the narrow linewidth of 30 Hz of this transition. In a conventional beam line setup where the atoms are excited by a laser, the fluorescence is extremely weak since it is hard to obtain a high Rabi frequency to excite the atoms, and due to the lifetime of 4 ms, it is spread over a large distance along the beam line. It can be done using single photon counting and a Ramsey interrogation scheme as in [108]. Alternatively, a 2 m long vapor cell heated to 450°C have been used [109]. Stabilization to a high finesse cavity was chosen, even though it does not provide an absolute frequency reference. But the drift is so slow that for the experimental purposes this is sufficient. Furthermore, a significant reduction in laser linewidth is obtained.

In figure 3.13 the setup is shown. The 914 nm laser beam is double passed through an AOM to have some frequency tunability with regards to the  $TEM_{00}$  mode of the high finesse cavity. Then the laser beam passes an electro optic modulator (EOM) which adds 10 MHz frequency sidebands before being coupled into the high finesse cavity, see figure 3.14. The high finesse cavity is a non-confocal and consists of two high-reflection mirrors and a ULE (Ultra Low Expansion) glass spacer. The identical mirrors have a radius of curvature of 1000 mm. The spacer is 200 mm long and has a

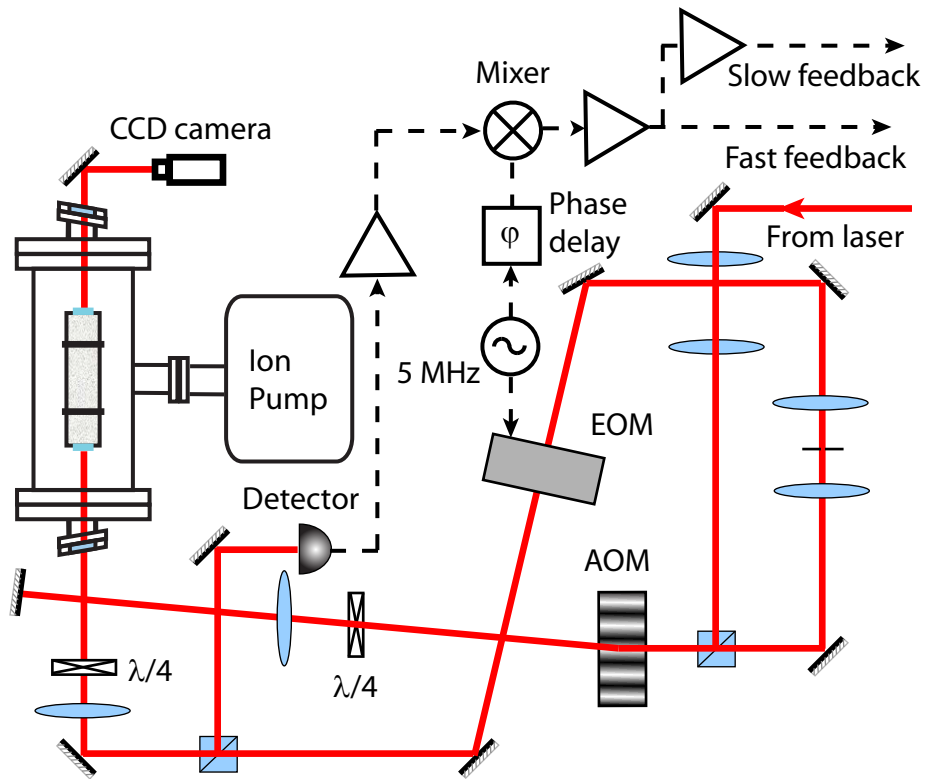


**Figure 3.13:** Setup of the Pound–Drever–Hall (PDH) stabilization to a high finesse cavity. The 914 nm laser beam is double-passed through an AOM to have some frequency tunability with regards to the  $TEM_{00}$  mode of the high finesse cavity. Then the laser beam passes an electro optic modulator (EOM) which imprints 10 MHz frequency sidebands before being coupled into the high finesse cavity. The reflected light from the cavity is detected by a photodetector. The cavity error signal is phase-sensitively detected by the coherent mixing of the amplified photocurrent and the local oscillator signal (which drives the EOM) in a mixer. The loop filter provide additional gain, filtering and integration before sending the correction signal to the laser diode current and the piezo-mounted grating in the MOPA. The required dynamic range of the servo varies from the high frequency (500 kHz) to the low frequency region and therefore the signal is divided into two negative feedback loops. A slow feedback integrating loop to the grating PZT and a faster feedback loop applied to the laser diode current.

diameter of 50 mm. Figure 3.14 shows the high finesse cavity which rests on two glass rods through a pair of Viton O-rings. The glass rods rest upon the

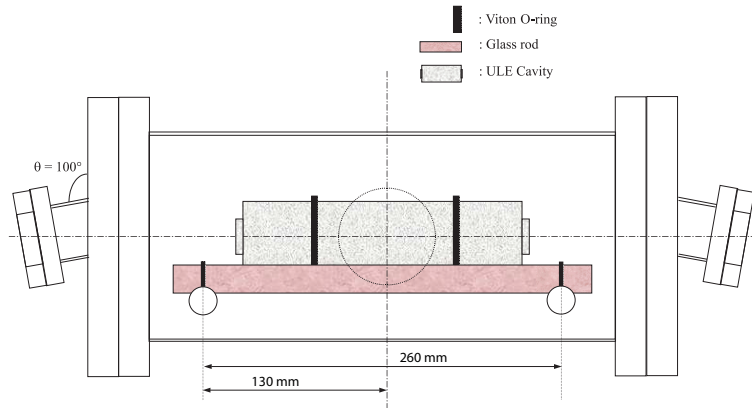


**Figure 3.14:** Overview of the high finesse cavity. The high finesse cavity is non-confocal and consists of two high-reflection mirrors and a ULE (Ultra Low Expansion) glass spacer. The identical mirrors have a radius of curvature of 1000 mm. The spacer is 200 mm long and has a diameter of 50 mm. The high finesse cavity rests on two glass rods through a pair of Viton O-rings. The glass rods rest upon the steel shell. The setup is placed in a vacuum chamber which is evacuated to  $5 \cdot 10^{-9}$  mbar by an ion pump

steel shell. The setup is placed in a vacuum chamber, which is evacuated to  $5 \cdot 10^{-9}$  mbar by an ion pump. The vacuum provides thermal and acoustic isolation of the cavity and prevents contamination of the cavity mirrors. The cavity has a finesse of about 86 000 [107] and a linewidth of 8.4 kHz, see figure 3.15.

The reflected light from the cavity is detected by a photodetector. The cavity error signal is phase-sensitively detected by the coherent mixing of the amplified photocurrent and the local oscillator signal (which drives the EOM) in a double-balanced mixer. The loop filter provide additional gain, filtering and integration before sending the correction signal to the laser diode current and the piezo-mounted grating in the MOPA. The required dynamic range of the servo varies from the high frequency (500 kHz) to the low frequency region and therefore the signal is divided into two negative feedback loops. A slow feedback integrating loop to the grating PZT and a faster feedback

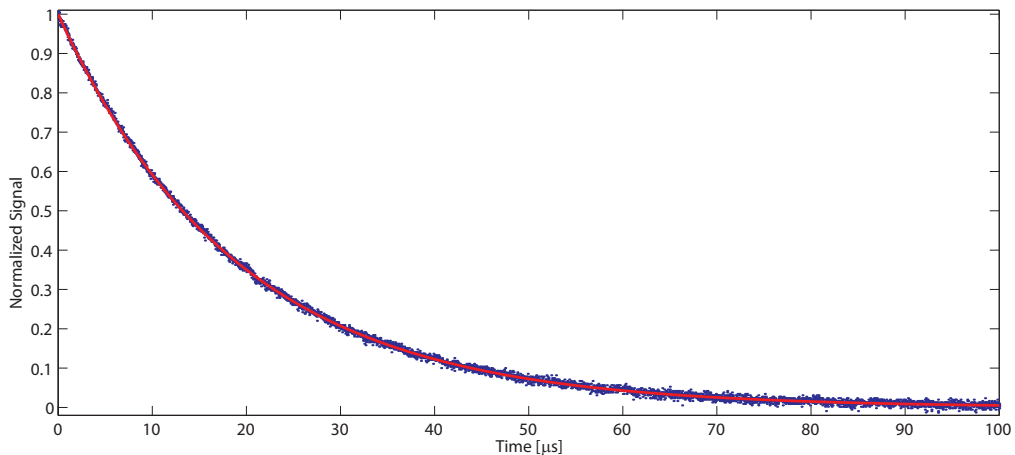


**Figure 3.15:** *Cavity ring down fitted to an exponential decay function resulting in a decay time of  $19.0 \mu\text{s}$  giving a cavity linewidth of  $8.4 \text{ kHz}$  which corresponds to the value found in [107].*

loop applied to the laser diode current.

The 914 nm laser is stabilized using the Pound–Drever–Hall (PDH) technique which is named after its inventors [110] and R. V. Pound who used a corresponding technique in the microwave regime [111]. It is a phase modulation spectroscopic method which is applied to stabilize the frequency of a laser to an optical resonator. The PDH technique is described in detail in many references (see e.g. [112]). Here a more general approach will be presented. In the Pound–Drever–Hall technique, the phase of the laser beam of angular frequency  $\omega$  is modulated by an electro-optical modulator with the angular frequency  $\omega_m$ . In the case of small modulation index  $\beta$  it suffices to take into account the carrier of angular frequency  $\omega$  and the two nearest sidebands at  $\pm\omega_m$ . Consider a frequency modulated (FM) laser beam hitting the input mirror of an optical cavity and reflecting back to a detector. After the laser beam has passed through the EOM, the incoming electric field to the cavity is:

$$E_i = E_0 \cdot e^{i(\omega t + \beta \sin(\omega_m t))} \quad (3.9)$$

$$\approx E_0 [J_0(\beta)e^{i\omega t} + J_1(\beta)e^{i(\omega + \omega_m)t} - J_1(\beta)e^{i(\omega - \omega_m)t}] \quad (3.10)$$

When the carrier and the sidebands are reflected from the high finesse cavity their amplitudes and phases are changed by a complex reflectivity coefficient [112]:

$$F(\omega) = \frac{r(e^{i2L\omega/c} - 1)}{1 - r^2 e^{i2L\omega/c}} \quad (3.11)$$

Where L is the cavity length and r is the amplitude reflection coefficient of the mirrors. The electric field of the reflected beam is then given by:

$$\begin{aligned} E_r = & E_0 [F(\omega)J_0(\beta)e^{i\omega t} \\ & + F(\omega + \omega_m)J_1(\beta)e^{i(\omega + \omega_m)t} \\ & - F(\omega - \omega_m)J_1(\beta)e^{i(\omega - \omega_m)t}] \end{aligned} \quad (3.12)$$

To separate the beam reflected back by the high finesse cavity from the incoming beam, a  $\lambda/4$  plate is employed leading to a rotation of the direction of the polarization of the laser beam, and the reflected beam is directed by a polarizing beam splitter to a photodetector. Consider a detector which is constructed such that it is sensitive only to frequencies near the modulation frequency  $\omega_m$ , i.e. for the beat note between the carrier and the side bands. Then the beat note between the high-frequency and the low-frequency side bands occurring at  $2\omega_m$  is usually suppressed. In this case only the terms oscillating with the modulation frequency are kept:

$$\begin{aligned}
P_r = |E_r|^2 &= P_c |F(\omega)|^2 + P_s [ |F(\omega + \omega_m)|^2 + |F(\omega - \omega_m)|^2 ] \\
&+ 2\sqrt{P_c P_s} \{ \text{Re} [ F(\omega) F^*(\omega + \omega_m) - F^*(\omega) F(\omega - \omega_m) ] \cos(\omega_m t) \\
&+ \text{Im} [ F(\omega) F^*(\omega + \omega_m) - F^*(\omega) F(\omega - \omega_m) ] \sin(\omega_m t) \} \quad (3.13)
\end{aligned}$$

where  $P_c = J_0^2(\beta)P_0$  and  $P_s = J_1^2(\beta)P_0$  is the power in the carrier and side bands. The photodetector signal contains contributions depending on  $\cos(\omega_m t)$  and on  $\sin(\omega_m t)$ . One can select one of the terms by comparison with the phase  $\phi$  of the modulation frequency. In the experiment (figure 3.13) the phase comparison is readily done by employing a mixer. The PDH error signal ( $\sin(\omega_m t)$  term) can be seen in figure 3.16.

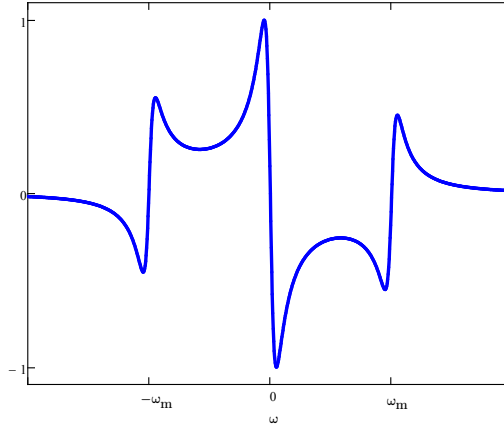


**Figure 3.16:** Plot of the ideal PDH errorsignal derived from equation 3.13.

Once stabilized to the high finesse cavity, the linewidth of the laser is estimated to be below 1 kHz. Previously the laser system was located in the basement of DFM (Danish Fundamental Metrology) in Lyngby where the linewidth was estimated to be below 100 Hz [107]. In the present location on the 4th floor of the Niels Bohr Institute there are significantly more vibration noise due to the building and the wooden floors the optical table are placed on.

### 3.1.5 881 nm Laser System

The 881nm light is used to excite the magnesium atoms from the  $^1P_1$  state to the  $^1D_2$  state, where the atoms can decay into the  $^3P_{2,1}$  states.

The 881 nm light is generated by a Ti:Saph laser, Coherent model MBR-110 pumped by a Coherent Verdi V10 which lases at 532 nm wavelength with a maximum output of 10 W. The Ti:Saph laser is highly tunable from around 700 nm - 980 nm. The cavity length can be adjusted by a birefringent filter and three sets of cavity mirrors can be interchanged to optimize the lasing at a given wavelength. The cavity resonator only sustains frequency and modes compatible with its length which in order to obtain a single frequency output is stabilized by locking to an external Fabry-Perot cavity. This counteracts slow fluctuations like temperature or pressure variations of the surroundings and reduces the linewidth of the laser. The laser linewidth of the system is specified to be below 100 kHz. The typical output power 881 nm is around 500 mW with a pump power of 8 W. Frequency stabilization at this wavelength is complicated since no lines are available in iodine or other atomic or molecular species. Many frequency stabilization schemes have been tried: polarization spectroscopy with magnesium in a cell, two-photon saturation spectroscopy on a magnesium thermal beam, 881 nm spectroscopy on a magnesium thermal beam excited to the  $^1P_1$  state by electron impact and even spectroscopy of iodine molecule, but none of these trials has really been successful [113]. After the laser, the beam is divided into two beams, a low-power one to be sent to the wavemeter for adjusting and monitoring the wavelength. The second beam is sent to the MOT setup, enlarged and collimated.

### 3.1.6 383 nm Laser Systems

The 383 nm laser systems are used to address the  $^3D$  states and to transfer atoms between the  $^3P$  states.

Currently two systems for generating 383 nm light are operational, one based on a MOPA system with a SHG cavity with a AR-coated bismuth triborate crystal (BIBO,  $BiB_3O_6$ ) and one using the Ti:Saph laser described

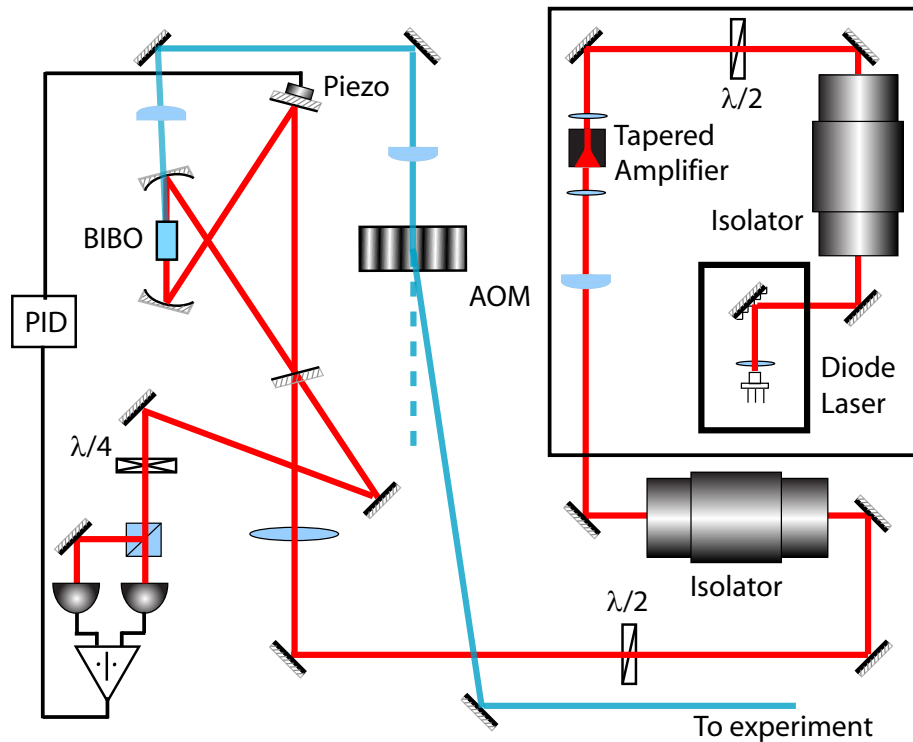


**Figure 3.17:** Illustration of the 383 nm MOPA setup. The 766 nm beam is sent through an isolator to avoid feedback from the tapered amplifier. The output from the tapered amplifier passed another isolator before being coupled into the SHG cavity and up to 150 mW of 383 nm is generated. The beam reflected from the input coupling mirror is used for locking the length of the cavity using the Hänsch-Couillaud scheme.

in section 3.1.5 with a SHG cavity containing a Brewster cut BIBO crystal.

The MOPA system resembles the MOPA system described in section 3.1.4. It consists of an external cavity laser diode in Littrow configuration with an output of 40 mW which after passing an isolator is injected into a tapered amplifier. The approximately 1 W output is after passing another isolator coupled into a SHG cavity with a 5 mm AR coated BIBO crystal. The SHG cavity has a total length of 23 cm with an input coupler of 1% and a radius of curvature (ROC) of 25 mm of the two curved mirrors. A coupling efficiency of around 50% is obtained, which is mainly limited by the poor spatial mode of the output of the tapered amplifier, and a maximum output of 150 mW

have been obtained. The cavity is stabilized using the Hänsch-Couillaud scheme previously described. An overview of the setup can be seen in figure 3.17

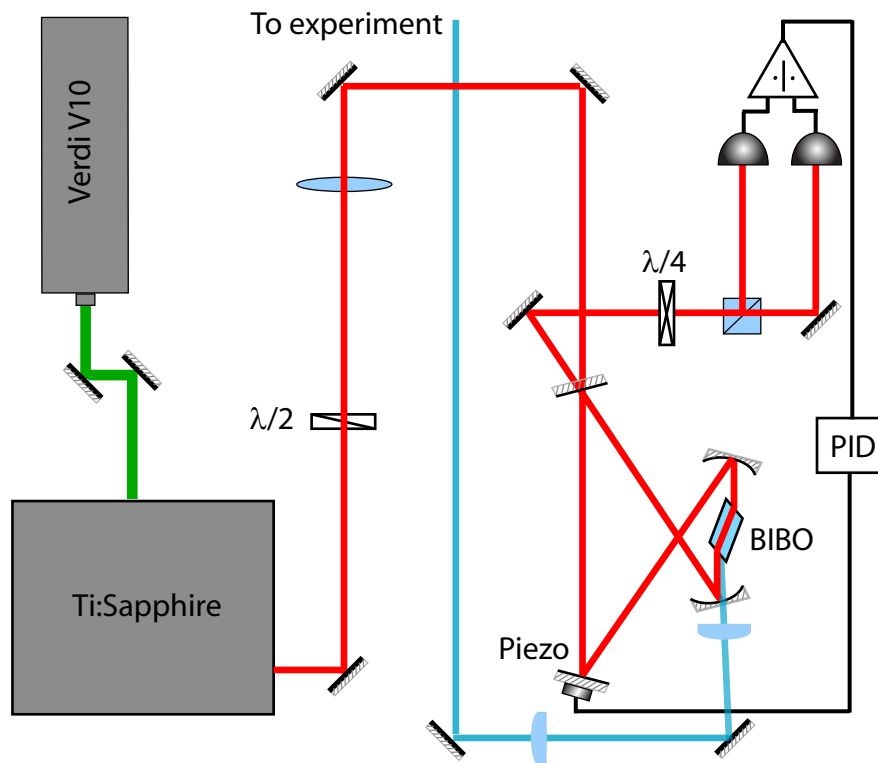


**Figure 3.18:** Illustration of the 383 nm Ti:Sapphire setup. The output from the Ti:sapphire laser is coupled into the SHG cavity and up to 50 mW of 383 nm is generated using a Brewster cut BIBO crystal. The beam reflected from the input coupling mirror is used for stabilizing the length of the cavity using the Hänsch-Couillaud scheme.

The second 383 nm setup is as mentioned based on the Ti:Saph laser described in section 3.1.5. The Ti:Saph laser delivers 500 mW output which is then coupled into the SHG cavity. The SHG cavity has a total length of 21 cm with an input coupler of 0.65% and a ROC of 25 mm of the two curved mirrors. A coupling efficiency of around 40% is obtained and the efficiency is mainly limited by poor alignment. The output of the SHG cavity is 50 mW and since this is significantly more than needed for the experiments, no

further effort has been put into optimizing the output. The laser system is located in the room next door to the main setup with the vacuum chamber and is therefore sent through a hole in the wall. An overview of the setup is seen in figure 3.18. The two 383 lasers are frequency stabilized to the metastable beamline using a side fringe locking technique as described in section 3.2.

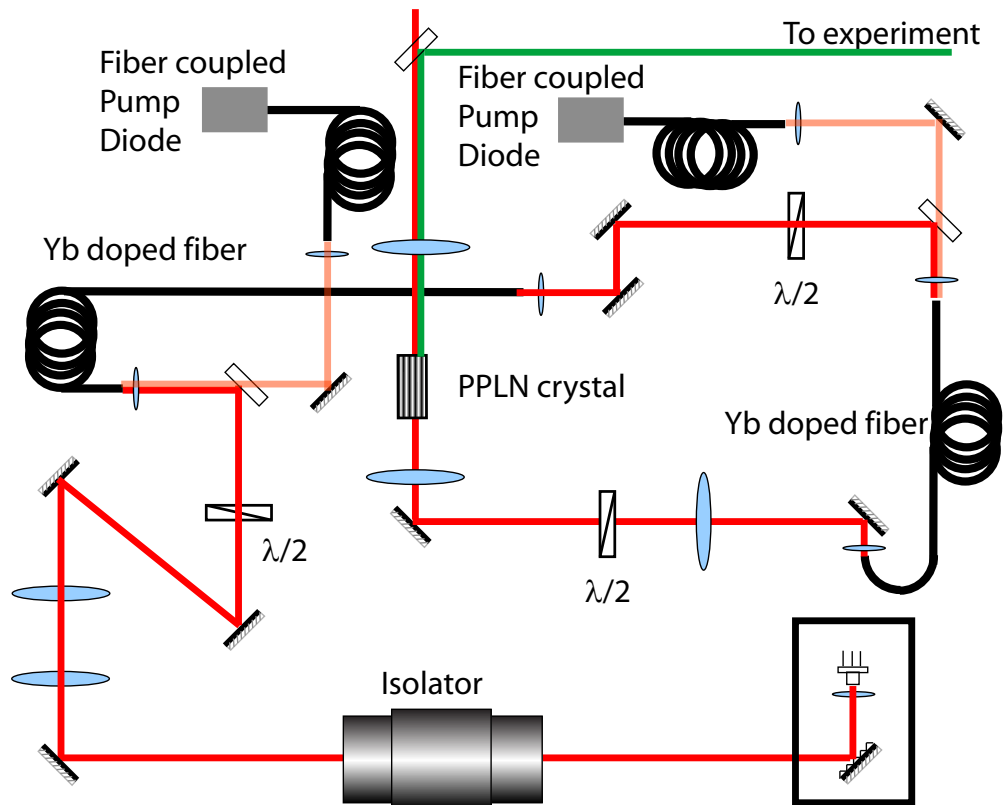


**Figure 3.19:** Illustration of the 517 nm setup. The output from the 1034 nm external cavity diode laser is amplified by a two-stage Yb-doped fiber amplifier system and single pass frequency doubled using a periodically poled lithium niobate (PPLN) crystal.

### 3.1.7 517 nm Laser System

The 517 nm laser system is used for addressing the  ${}^3P_{0,1,2} - {}^3S_1$  transitions.

The 517 nm laser is based on a 1034 nm external cavity diode laser which is amplified by a two-stage Yb-doped fiber amplifier (YDFA) system and single pass frequency doubled using a periodically poled lithium niobate (PPLN) crystal. An overview of the setup can be seen in figure 3.19.

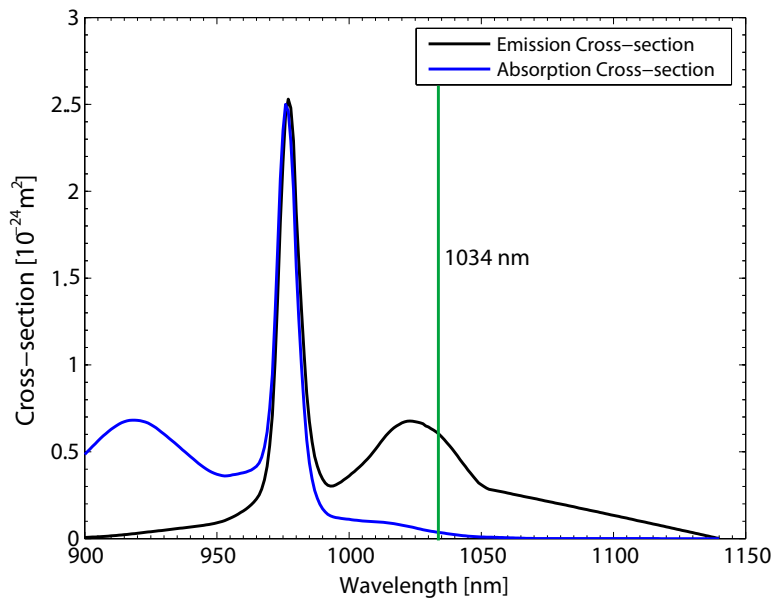


**Figure 3.20:** *The emission cross-section and absorption cross-section of ytterbium in a silica host material. At 1034 nm a non negligible absorption is present, making the fiber amplifiers sensitive to the length of the fibers.*

The seed laser is an external-cavity diode laser in Littrow configuration centered at 1034 nm. After a 40 dB optical isolator, the seed laser output is 15 mW. A telescope is used to optimize the fiber-coupling efficiency of the 1034 nm laser. The Yb-doped fiber amplifier consists of a polarization maintaining (PM) fiber (Liekki Yb1200-10/125DC-PM), providing amplification of light with wavelengths ranging from 1030 nm to 1120 nm when pumped by a fiber coupled laser diode at 976 nm. The YDFA has an Yb-doped single-mode core with a 10  $\mu\text{m}$  diameter, and a large multimode pump guiding cladding with a 125  $\mu\text{m}$  diameter. The pump absorption at 976 nm is 1200 dB/m in

the core and around 7 dB/m in the cladding. The fiber length of both the Yb-doped fibers is about 2.5 m. This is probably not the optimum length since the fiber has a significant reabsorption at 1034 nm, see figure 3.20. This indicates that shorter fiber lengths might be more favorable, but no tests have been made to support this.

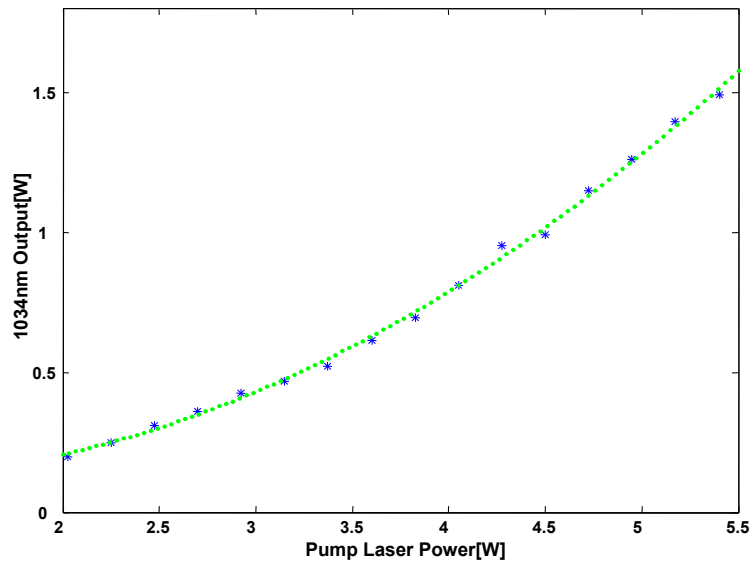


**Figure 3.21:** *1034 nm output of two-stage YDFA as a function of total pump power. 1.5 W of 1034 nm light is obtained. The green line is added as a guide for the eye.*

Dichroic Mirrors (DM) are employed to overlap and couple both 976 nm and 1034 nm lasers into the Yb-doped fibers. In order to achieve the more than 1 W of 1034 nm laser power required for the single pass frequency doubling, a two-stage YDFA is used as shown in figure 3.19. The first stage acts as an initial amplifier of the seed laser, and the second stage acts as the main amplifier to generate the powerful 1034 nm output. An interference filter (IF) transmitting 1034 nm light is placed after the two-stage YDFA, to remove the residual 976 nm pump power. 8 mW of seed laser power is coupled into the 1st YDFA stage and 200 mW, is obtained after the first amplifier stage. A maximum of 400 mW can be obtained from the first amplifier stage, however at outputs higher than 200 mW the stimulated amplification

saturates and amplified spontaneous emission (ASE) starts to dominate the output [114]. The coupling efficiency between Yb-doped cores of the 1st stage and 2nd stage YDFA is about 50%. The typical output of the two-stage YDFA is shown in figure 3.22, where a maximum output of 1.5 W at 1034 nm is reached. The setup of the second-harmonic generation (SHG) of 517 nm is shown in figure 3.19. The crystal used is a periodically poled lithium niobate (PPLN), with a size of 9.8 mm x 20 mm x 0.5 mm. It has 6 tracks of different polings with periods ranging from 6.31  $\mu\text{m}$  to 6.45  $\mu\text{m}$  in order to be able to obtain phase matching over a large wavelength range covering the three transitions between the  $^3P_{0,1,2}$  states and the  $^3S_1$  state. Originally, the laser system was meant to consist of 3 different sets of laser diodes plus fiber amplifiers, which then all should be amplified in the same PPLN crystal but in separate tracks with different poling periods. However, until now only one of the diode laser plus fiber amplifier sets has been constructed.

An oven is used to stabilize the temperature of the PPLN crystal below 0.01°C. The 1034 nm laser beam from the two-stage YDFA is collimated and then focused in the PPLN crystal, with a beam waist of approximately 40  $\mu\text{m}$ . After the single pass frequency doubling, a dichroic mirror is used to reflect the 517 nm green light and transmit the 1034 nm light. The track with a period of 6.37  $\mu\text{m}$  is used for the  $^3P_1 - ^3S_1$  transition, for optimal phase matching around 35°C. The phase matching temperature is changing corresponding to the wavelength of the incident light with a rate estimated to be 0.09 nm/°C.

Figure 3.22 shows the generated 517 nm power, where a maximum of 40 mW is obtained with 1.4 W of incident 1034 nm power. The 517 nm light generated is a TEM<sub>00</sub> Gaussian beam. A decreasing doubling efficiency can be observed, from an initial value of  $\sim 2.5\% \text{ W}^{-1}\text{cm}^{-1}$  to  $\sim 2\% \text{ W}^{-1}\text{cm}^{-1}$  at high power. This is attributed to an increase in amplified spontaneous emission (ASE) [115]. The ASE presents a fundamental source of laser amplifier noise. The ASE contributes more on the YDFA output at high-power outputs and thereby reduces the doubling efficiency.

To determine the linewidth of the 517 nm laser system, a confocal cavity

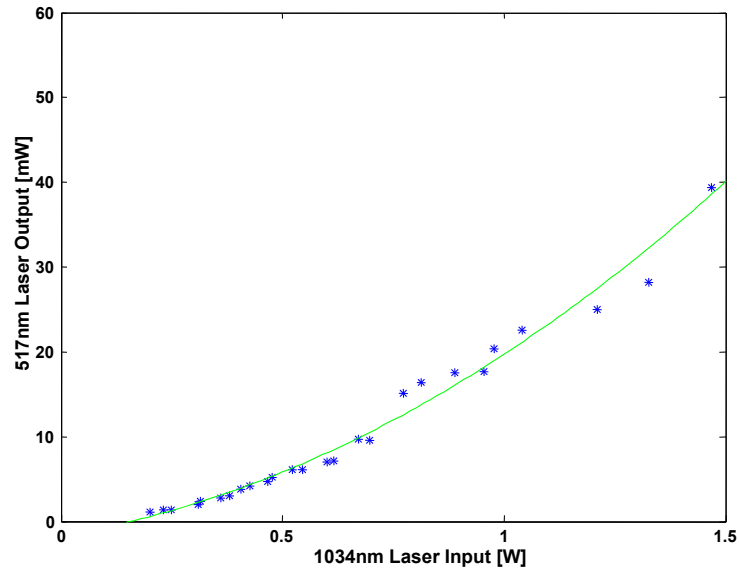


**Figure 3.22:** *517 nm SHG laser output as a function of 1034 nm input power. A maximum of 40 mW 517 nm laser power is obtained. The green line is added as a guide for the eye.*

with a linewidth of less than 1 MHz is used. 5 mW of 517 nm power is coupled into this cavity, and the transmitted signal is collected by a photodiode. The FWHM linewidth of the 517 nm system is estimated to be 3 MHz.

The 517 nm laser is frequency stabilized to the metastable beamline using a side fringe locking technique as described in section 3.2.

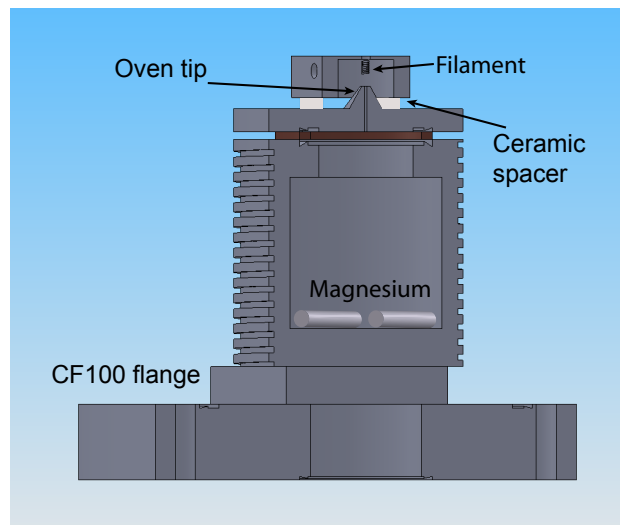


**Figure 3.23:** *The metastable source consists of an oven with a hole diameter of 2 mm and a  $\text{BaCO}_3$  coated filament approximately 10 mm above the oven aperture. The oven has grooves for the heating wire to ensure optimal thermal contact and is thermally shielded by two stainless steel cylinders. The filament is shielded by a copper piece at the same potential as the filament. The metastable source is mounted on a CF100 flange using ceramic screws.*

## 3.2 Generation of Metastable Magnesium

In this section, a metastable magnesium source is described. The two main reasons for constructing a metastable magnesium source are the need for an absolute reference for the 517 nm and 383 nm laser systems and the possible generation of a metastable Mg MOT.

Discharge beam sources have in the past been shown to be very efficient in the excitation of atomic beams of Ca [116], [117], Pb [118], Ba [120], [121], [122], Sr [123] and Mg [124], [125] into metastable beams. An efficiency of up to 40% has been obtained for the metastable magnesium source described in the following.

The metastable oven can be seen in figure 3.23. It consists of a thermal effusive oven heated by a resistive heater. The oven is made from stainless

steel. The oven lid is sealed using a titanium ring on CF40 flange. The beam exits the lid through a tip with a hole of 2 mm in diameter and 12 mm in length. Above the tip a tungsten filament with a diameter of 2.5 mm is placed inside a copper shield. The wolfram filament is coated with  $\text{BaCO}_3$  which when heated under vacuum turns into  $\text{BaO}$  which is an effective electron emitter. A voltage difference between the oven tip and the filament is necessary in order to initiate the discharge, and therefore the oven and filament are electrically isolated from each other and the vacuum chamber using ceramic spacers and screws. The vacuum chamber is pumped using a 250 l/s turbo molecular pump keeping the pressure below  $1 \cdot 10^{-7}$  mbar. Typically, the oven is operated at a temperature of around  $520^\circ\text{C}$  in order to obtain a high enough atomic density to sustain the discharge.

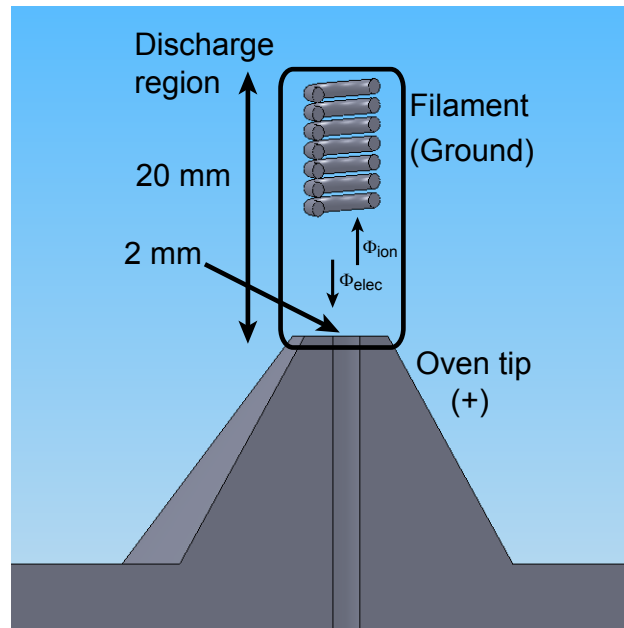


**Figure 3.24:** Details of the discharge region defined by the filament and the oven aperture.

The total flux in the  $^1S_0$  state can be estimated with the following equation [126]:

$$\Phi_0 = 1/k \frac{\alpha A_0 n_0}{2\sqrt{\pi}} \quad (3.14)$$

Where  $\alpha$  is the most probable velocity of Mg atoms inside the oven (738 m/s at 520°C),  $A_0$  is the area of the oven aperture,  $n_0$  is the atomic density in the oven ( $1.4 \cdot 10^{15}$  at 520°C [102]) and  $1/k$  is a factor which takes the aperture thickness into account and is about 1/2 for the oven described here [126]. At the typical operating temperature of 520°C the total flux is  $\Phi_0 \approx 4.5 \cdot 10^{17}$  atoms/s.

The maximum of the metastable triplet excitation cross section by electron collisions is at an energy of 4.55 eV [124] and since the ionization and singlet excitation (maximum at 17 eV) cross sections are negligible at this electron energy, this indicates that a low voltage discharge is favorable for efficiently generating metastable magnesium atoms. By establishing a discharge self sustained by the atomic flux itself the voltage difference between the oven and filament is reduced to a value lower than the ground state ionization value. In figure 3.24 a close up of the discharge region is shown. The electron flux  $\Phi_{elec}$  and ion flux  $\Phi_i$  in the discharge region are given by:

$$\Phi_{elec} = n_{elec} v_{elec} \quad (3.15)$$

$$\Phi_i = n_i v_i \quad (3.16)$$

where  $n_{elec}, n_i$  are the electron and ion densities and  $v_{elec}, v_i$  are the electron and ion velocities respectively. In order to obtain a discharge self sustained by the atomic flux, the ion generation rate has to guarantee the charge conservation in the neutral discharge region  $n_{elec} \simeq n_i$ . The charge conservation gives:

$$\Phi_{elec} = \Phi_i + I/e \quad (3.17)$$

where  $I$  is the external current and  $e$  is the electron charge. The ion generation rate is given by:

$$\Phi_i = \sigma_i n_a l I / e \quad (3.18)$$

Combining the previous equations the following condition for the atomic density is obtained in a self sustained discharge:

$$n_a \geq \frac{v_i / v_{elec}}{l \sigma_i} = \frac{\sqrt{m_e / m_i}}{l \sigma_i} \quad (3.19)$$

where  $m_e$  and  $m_i$  are the electron and ion masses. Inserting the relevant numbers into equation 3.19, the following value of the atomic density is obtained:  $n_0 \sim 5 \cdot 10^{12}$  atoms/cm<sup>3</sup> which corresponds to an oven temperature of around 520°C. The experimental curve of the voltage between the filament and oven can be seen in figure 3.25.

The discharge region is seen as a bright green region due to the fast  $^3S_1 - ^3P_{0,1,2}$  decay which is one of the most important decay channels for reaching the metastable triplet states, see figure 3.25. A circular collimator 15 cm downstream from the oven aperture reduces the beam divergence and the ground state atomic flux to  $\sim 8 \cdot 10^{13}$  atoms/s.

### 3.2.1 Theory of Metastable Excitation

The excitation of the atomic beam into the metastable triplet states  $^3P_{0,1,2}$  is mainly due to the inelastic collisions between atoms and electrons. However the elastic collisions will also play a significant role for a diffusion process affecting the velocity distribution and reducing the slow atoms in the beam. The slow atoms can easily be deflected or even stopped by the electron collisions. The fast atoms only spend a short time in the discharge region and therefore their chance of getting excited to the metastable state is reduced. Following the lines of [124] and [125], the two collision processes are treated independently in the following.

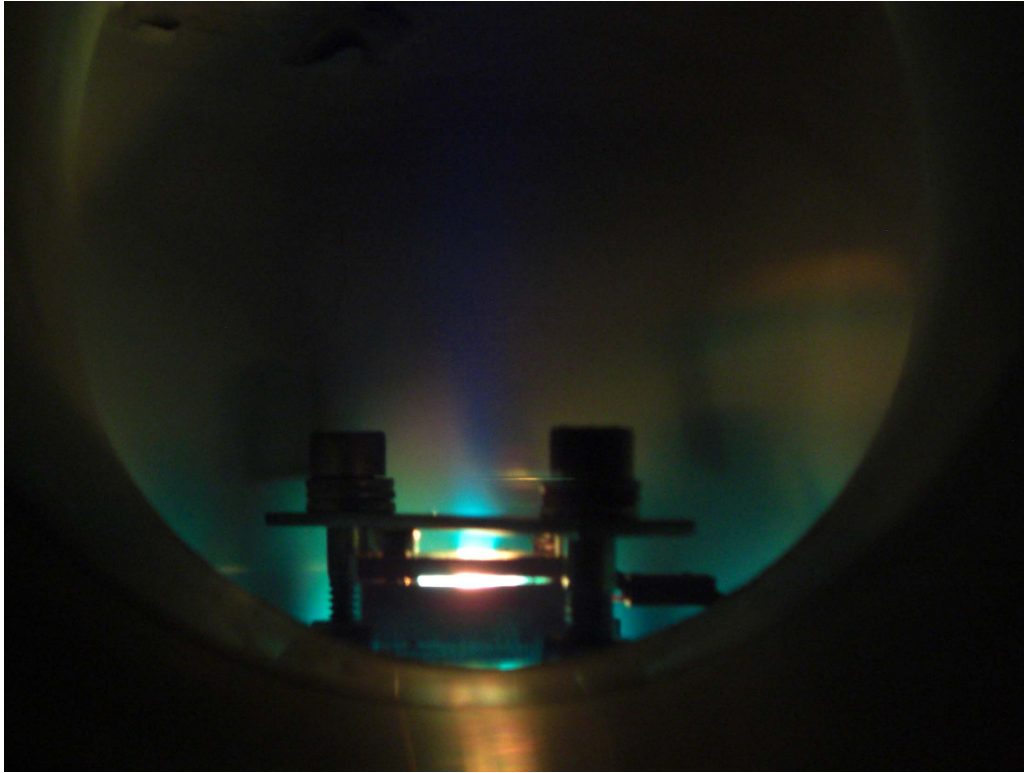


**Figure 3.25:** *Photo of the metastable oven. The green color from the  $^3S_1 - ^3P_{0,1,2}$  decay can be clearly seen. The faint blue color that can be seen is from the  $457\text{nm } ^3P_1$  decay to the ground state.*

The elastic collision effect is treated phenomenologically as in [125] by introducing a modified Maxwellian velocity distribution for the neutral atomic beam:

$$\rho_0(v) = \frac{2}{\alpha \Gamma[\frac{\gamma+1}{2}]} \left(\frac{v}{\alpha}\right)^\gamma e^{-\frac{v^2}{\alpha^2}} \quad (3.20)$$

where  $\Gamma$  is the gamma function and  $\gamma$  is a positive number.

For the inelastic collision processes, the following rate equation system

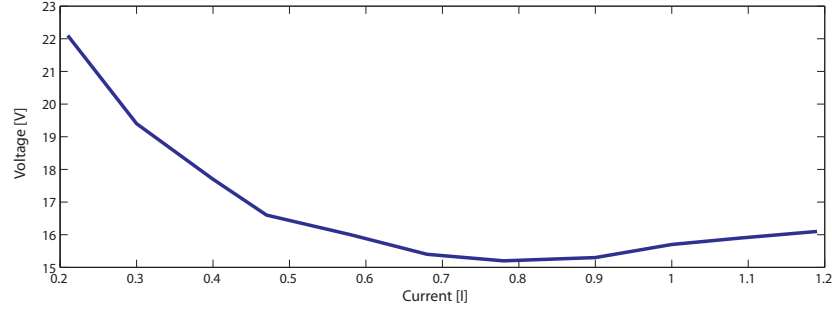


**Figure 3.26:** Anode to cathode voltage as a function of discharge current. Recorded from high current to low current with a filament current of 0 A showing that the discharge is self sustained.

for the ground and excited state atomic densities are considered:

$$\dot{n}_e = \frac{\sigma_E}{e} J n_0 - \frac{\sigma_D}{e} J n_e - \frac{\sigma_{P,ion}}{e} J n_e \quad (3.21)$$

$$\dot{n}_g = -\frac{\sigma_E}{e} J n_0 + \frac{\sigma_D}{e} J n_e - \frac{\sigma_{S,ion}}{e} J n_0 \quad (3.22)$$

where  $\sigma_{S,ion}$ ,  $\sigma_{P,ion}$  are the ionization cross sections from the ground and excited state,  $\sigma_E$ ,  $\sigma_D$  are the  $^3P$  excitation and de-excitation cross sections. It is assumed that the different cross sections are independent of the discharge current. Figure 3.26 indicates that the mean energy in the discharge region is independent of the discharge current. The solution to equation 3.21 with the initial conditions  $n_e(t=0) = 0$  and  $n_0(t=0) = n_0$  is:

$$n_e(t) = \frac{\sigma_E n_0}{p} e^{-\frac{J C_1 t}{e}} \sinh(J C_2 t / e) \quad (3.23)$$

where

$$C_1 = \frac{1}{2} (\sigma_{S,ion} + \sigma_{P,ion} + \sigma_E + \sigma_D) \quad (3.24)$$

$$C_2 = \frac{1}{2} \sqrt{(\sigma_E + \sigma_{S,ion} - \sigma_D - \sigma_{P,ion})^2 + 4\sigma_E \sigma_D} \quad (3.25)$$

and  $t = l_D/v$  is the time the atoms spend in the discharge region. The current density is given by the current over the cross section  $J = I/A_D$ . Introducing the two parameters  $H = \frac{l_D C_1}{e A_D}$  and  $K = \frac{l_D C_2}{e A_D}$  the flux of metastable atoms can be expressed as:

$$\Phi_m(v) = \Phi_0 \frac{\sigma_E}{C_2} e^{-\frac{HI}{v}} \sinh(KI/v) \rho_0(v) \quad (3.26)$$

meaning that the velocity distribution of the metastable atoms will be given by:

$$\rho_m(v) = B \left(\frac{v}{\alpha}\right)^\gamma e^{-\frac{v^2}{\alpha^2} - \frac{HI}{v}} \sinh(KI/v) \quad (3.27)$$

where B is a normalization factor. A plot of the velocity distribution can be seen in figure 3.27 with the typical fitting parameters from section 3.2.2:  $T=520^\circ\text{C}$ ,  $H=2840 \frac{\text{m}}{\text{s}\cdot\text{A}}$ ,  $H/K=0.7$ ,  $I=1\text{A}$ ,  $\gamma=4$  together with a Maxwell-Boltzmann distribution. The velocity distribution of the metastable atoms is shifted towards higher velocities consistent with the expectation that the slow atoms are lost in the discharge region.

### 3.2.2 Characterization of the Metastable Source

The main characteristics of interest of the metastable atomic beam are the excitation efficiency and the velocity distribution. These are described in the following section.

The excitation efficiency can be estimated using a 285 nm laser and quite simply monitoring the fluorescence level while the discharge is on or off, see figure 3.29. This gives an excitation efficiency of 40% and is comparable to results obtained in [125]. Meaning that the total flux 40 cm down stream from the oven is  $\sim 3 \cdot 10^{13}$  atoms/s.

The longitudinal velocity distribution of the metastable  $^3P_2$  atoms are measured using two different techniques. The first technique is a time of flight

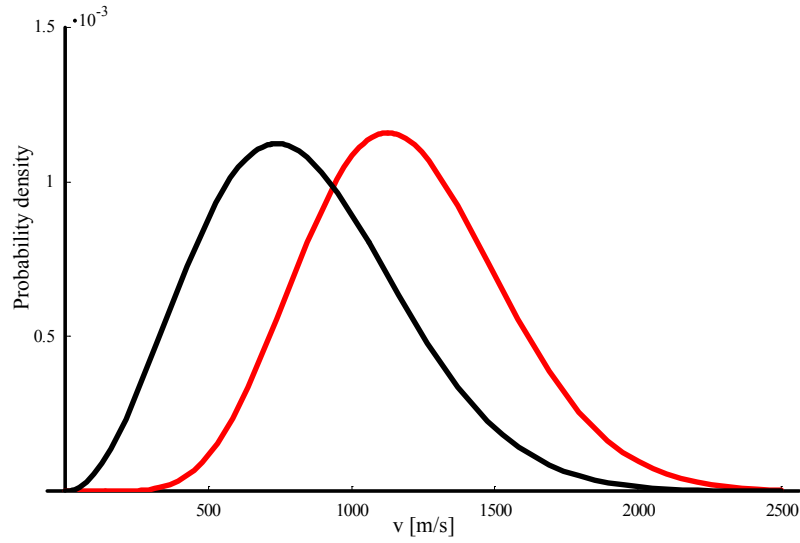


**Figure 3.27:** Maxwell-Boltzmann velocity distribution (black) and velocity distribution given by equation 3.27 (red) with the typical fitting parameters from section 3.2.2:  $T=520^{\circ}\text{C}$ ,  $H=2840 \frac{\text{m}}{\text{s}\cdot\text{A}}$ ,  $H/K=0.7$ ,  $I=1\text{A}$ ,  $\gamma=4$ . The velocity distribution of the metastable atoms is shifted towards higher velocities consistent with the expectation that the slow atoms are lost in the discharge region.

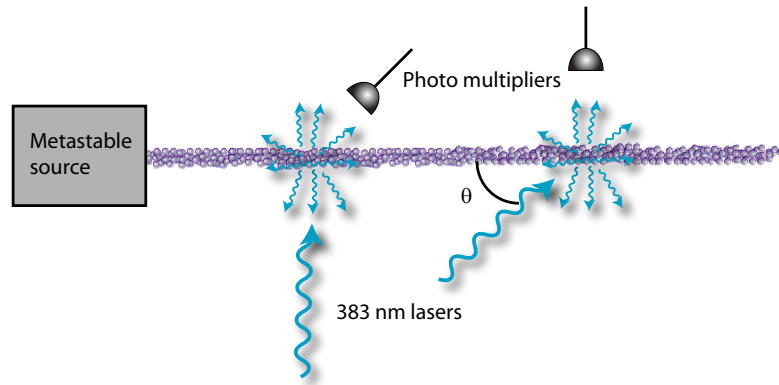


**Figure 3.28:** Metastable beamline setup. The velocity distribution of the metastable  $^3P_2$  atoms are measured using two different techniques. The first technique records the fluorescence of  $^3P_2 - ^3S_1$  transition after the discharge is switched off. The second technique measures the velocity distribution using the Doppler shift by having a non perpendicular angle between the atomic beam and the laser beam.

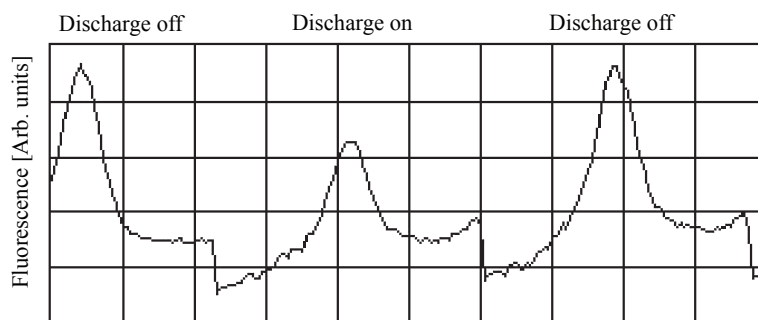


**Figure 3.29:** 285 nm fluorescence recorded while turning the metastable discharge on and off. An excitation efficiency of 40% is observed and is comparable to results obtained in [125].

(TOF) technique which records the fluorescence of  ${}^3P_2 - {}^3S_1$  transition after the discharge is switched off. The second technique measures the velocity distribution using the Doppler shift by having a non perpendicular angle between the atomic beam and the laser beam, see figure 3.28.

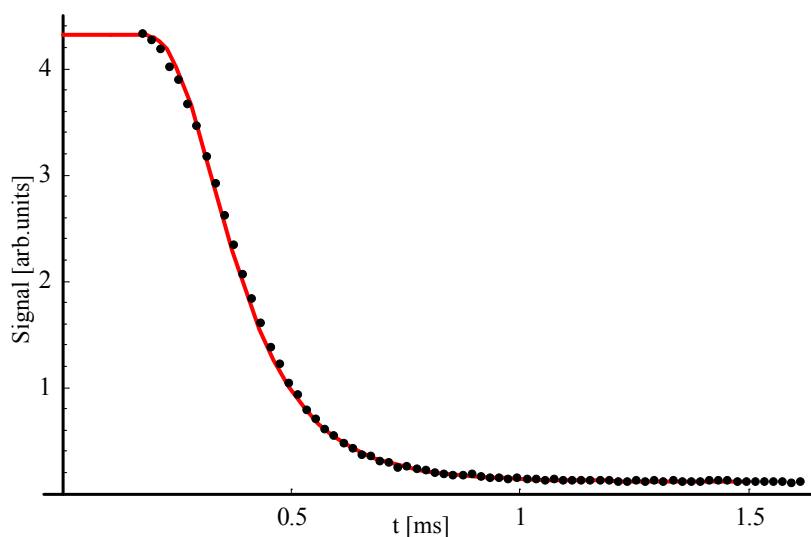


**Figure 3.30:** Signal of the photomultiplier as a function of time (black dots) and fitted to equation 3.28 giving  $T=520^\circ\text{C}$ ,  $H=2840 \frac{\text{m}}{\text{s}\cdot\text{A}}$ ,  $H/K=0.7$ ,  $I=1\text{A}$ ,  $\gamma=4$ .

The discharge is switched on in less than  $10 \mu\text{s}$  by switching the power supply that drives the discharge. After the discharge is switched off, the atoms propagate  $d=40 \text{ cm}$  before passing a  $1 \text{ mm}$  diameter  $383.9 \text{ nm}$  laser beam on resonance with the  $^3P_2 - ^3D_3$  transition. The fluorescence signal detected by the photomultiplier depends on the time each velocity class of atoms spend on traveling from the discharge to the interrogation laser and the time they spend in the laser beam. Therefore the signal is given by:

$$S_{TOF}(t) = A \int_0^\infty \frac{\rho_m(v)}{v} (1 - \Phi(t - d/v)) dv \quad (3.28)$$

where  $A$  is an amplitude factor depending on the detection efficiency of the photomultiplier and lens system. In figure 3.30 a typical time of flight signal is shown together with a fit to equation 3.28 giving the fit values:  $T=520^\circ\text{C}$ ,  $H=2840 \frac{m}{s \cdot A}$ ,  $H/K=0.7$ ,  $I=1A$ ,  $\gamma=4$ . The fitting values are comparable to those found in [124], [125].

The second method uses the Doppler shift of the atoms, so by detuning the laser it is possible to map out the velocity distribution. The signal seen by the photo multiplier is actually a convolution between the Lorentzian emission profile of an atom at rest and the velocity distribution of the atoms. But in this case the width of the emission profile is so narrow compared to the velocity distribution ( $\sim 25 \text{ MHz}/2.5 \text{ GHz}$ ) that it can be considered as a delta function. From the resonance condition  $\delta_L = \bar{k} \cdot \bar{v} = kv \cos(\theta)$  the velocity distribution can be mapped out directly if the angle  $\theta$  between the laser beam and the atomic beam is known (in these measurements  $\theta = 45^\circ$ ). The signal from the photomultiplier will be given by the convolution of the velocity distribution and the time the atoms spend in the interrogation laser:

$$S_{Doppler}(\delta) = A \frac{\rho_m\left(\frac{\delta k}{\cos(\theta)}\right)}{\frac{\delta k}{\cos(\theta)}} \quad (3.29)$$

where again  $A$  is an amplitude factor depending on the detection efficiency of the photomultiplier and lens system. In figure 3.31 typical photomultiplier

signals are shown together with a fit to equation 3.29 giving the same fit values as in 3.30:  $T=520^\circ\text{C}$ ,  $H=2840 \frac{\text{m}}{\text{s}\cdot\text{A}}$ ,  $H/K=0.7$ ,  $\gamma=4$ . As expected a clear shift of the velocity distribution as a function of current is observed.

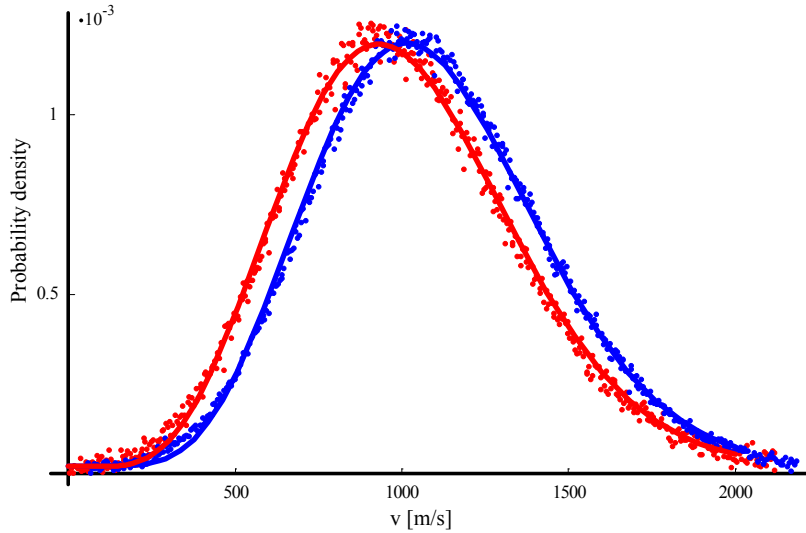


**Figure 3.31:** Photomultiplier signal as a function of velocity (detuning) for two different discharge currents  $I = 0.5 \text{ A}$  (red dots) and  $I = 1 \text{ A}$  (blue dots) and the fits (solid) to equation 3.29 with the values:  $T=520^\circ\text{C}$ ,  $H=2840 \frac{\text{m}}{\text{s}\cdot\text{A}}$ ,  $H/K=0.7$ ,  $\gamma=4$ .

The transverse velocity distribution is easily measured by scanning the detuning of a laser propagating perpendicular to the atomic beam. The transverse velocity distribution has a full width at half maximum of 70 MHz.

### 3.2.3 Frequency Stabilization

The frequency of the 517 nm and the two 383 nm lasers are stabilized to the metastable beam line using a simple side fringe locking technique. The setup is shown in figure 3.32. The fluorescence from a laser near resonance is detected and using a variable offset, the zero point is adjusted so that the slope of the gaussian fluorescence profile is used as the locking signal. After an integrator, the signal is used as feedback to the laser. The performance of the frequency stabilization is limited by the transverse velocity distribution

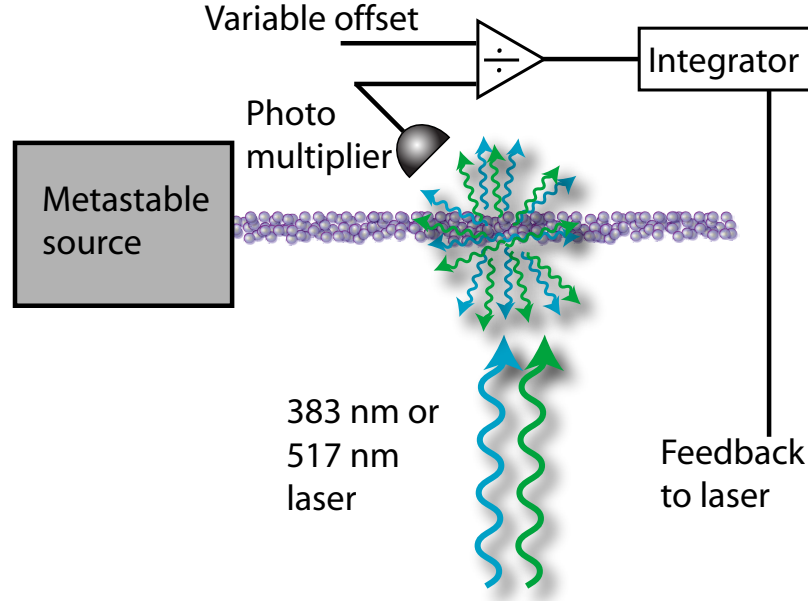


**Figure 3.32:** *Metastable beamline setup. The fluorescence from a laser near resonance is detected, and using a variable offset, the zero point is adjusted so that the slope of the gaussian fluorescence profile is used as the locking signal. After an integrator, the signal is used as feedback to the laser.*

and the signal to noise ratio (S/N). For the 517 nm and 383 nm laser systems, the S/N ratio is around 100. Under the assumption of white noise limitation [112], the linewidth of the frequency-stabilized 517 nm laser system is estimated to be:

$$\Delta\nu = \frac{\Gamma}{2S/N} \approx \frac{70MHz}{2 \cdot 100} < 0.5MHz \quad (3.30)$$

The disadvantages of the fringe locking technique is that the locking point does not coincide with the center of the resonance, but is defined by the variable offset, and as a consequence the locking point is sensitive to fluctuations in laser power. However, for the purposes in this thesis the level of stabilization is sufficient.

### 3.3 MOT Setup

In this section the remaining components needed for generation of a 285 nm MOT are described.

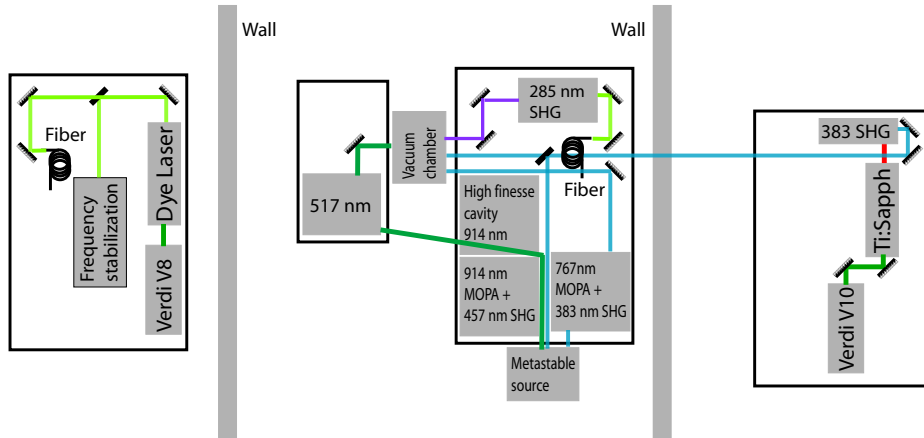


**Figure 3.33:** General overview of experimental setup. The dye and Ti:Sapphire lasers are located in different rooms than the vacuum chamber and the remaining laser systems.

Due to the evolution of the magnesium experiment and the size of the labs, the different elements of the MOT setup are not placed on the same optical table. Figure 3.33 gives an overview of the placement of the different elements of the setup. The MOT setup is sketched in figure 3.34. The vacuum chamber is mounted on a homemade steel frame standing directly on the concrete traverse of the building. The setup consists of three parts: the UV optics, an oven generating a thermal magnesium beam placed inside a vacuum chamber and an ultra high vacuum steel chamber for the MOT. The main vacuum chamber is equipped with a number of optical viewports and a set of coils in an anti-Helmholtz configuration used for generating the inhomogeneous magnetic field needed for the MOT. The two chambers are connected by a flexible flange so that the direction of the thermal beam can be adjusted with respect to the zero of the magnetic field. The distance between the oven aperture and the MOT region is 26 cm. The oven vacuum

chamber is pumped by a 250 l/s turbo pump (Edwards EXT250) keeping the pressure below  $5 \cdot 10^{-8}$  mbar. The MOT chamber is pumped by a 150 l/s Varian noble diode ionpump and maintains a pressure of  $3 \cdot 10^{-10}$  mbar. The atomic source is an effusive thermal beam of neutral magnesium atoms which is generated by a standard single chamber oven with a 1 mm orifice and is collimated by a differential pumping tube of 4 mm in diameter and 60 mm long placed 90 mm from the oven orifice between the two vacuum chambers. The actual geometry and the standard operating temperature of around 710 K gives a mean atomic velocity of around 790 m/s and a thermal beam divergence  $\theta = 13$  mrad with a beam diameter of around 7 mm in the MOT region. This also implies that only a fraction of  $10^{-5}$  of the total number of atoms reaching the MOT area have a velocity below 50 m/s which is a reasonable value for the capture velocity. The transverse Doppler width of the beam is around 90 MHz at 710 K. A mechanical shutter is placed before the differential pumping tube in order to stop the access of the thermal beam to the MOT-chamber. The measured density of the beam at an oven temperature of 710 K is around  $5 \cdot 10^7 \text{ cm}^{-3}$  corresponding to a calculated flux of atoms into the MOT area of around  $10^{12} \text{ s}^{-1}$  [102], [127].

The optical MOT setup is quite standard as can be seen from figure 3.34. A Glan-Thompson crystal is placed as the first element to ensure a clean linear polarization of the UV-beam. Afterwards, the beam is divided in three directions, and the polarization of the light is modified accordingly to the sign of the magnetic field gradient by a combination of  $\lambda/2$  and  $\lambda/4$  plates. The  $\lambda/4$  plates are placed after the last mirror before the beams pass into the MOT chamber and they ensure the needed circular polarization of the light. Due to the lack of UV-power, a configuration with three back reflected beams was chosen, and a second  $\lambda/4$  plate is placed after the output window together with a back reflecting mirror. The inhomogeneous magnetic field is generated by a set of coils in the anti-Helmholtz configuration whose construction details can be found in [128]. The coils are made of a copper hollow tube for water cooling and are formed by a number of windings with diminishing radius and numbers towards the center of symmetry. Along the axis passing through the center of the coils, conventionally named z, the field

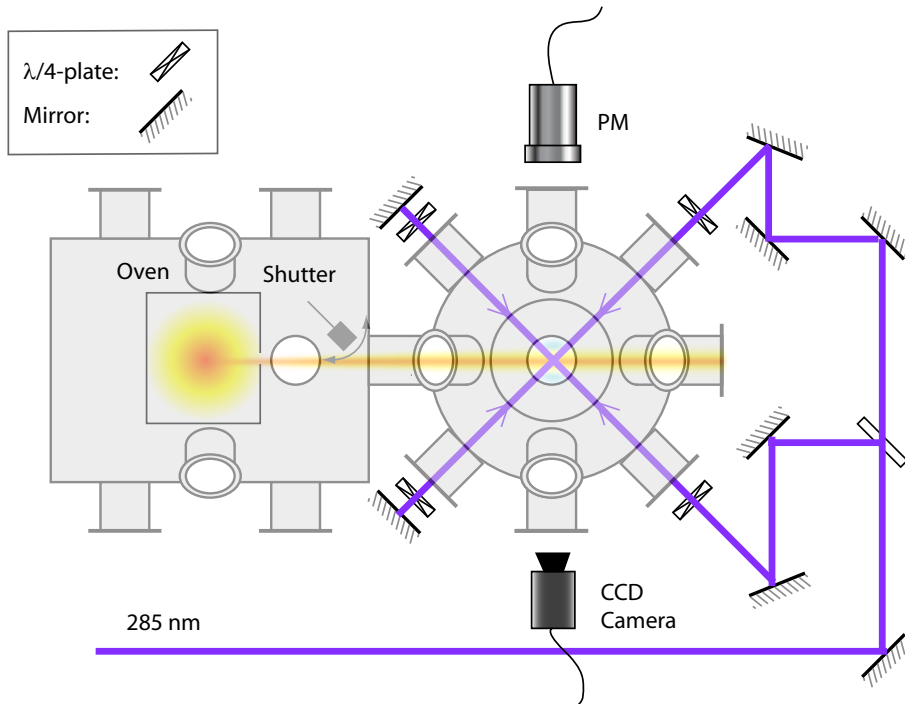


**Figure 3.34:** *The MOT setup seen from above. The oven chamber is separated from the main chamber by a differential pumping tube. The 285 nm MOT beams are retroreflected.*

gradient is approximately 1.4 gauss/(A cm). The current power supply can provide a maximum current of 200 A, granting a maximum z axis gradient of up to 280 G/cm. The MOT is usually operated with a current of 120 A. The current in the coils can be switched off in 50  $\mu$ s using a RCL circuit.

### 3.3.1 Detection

The experiments in this thesis involve essentially two types of detectors: CCD cameras and photomultiplier tubes. Both these detector types are used to monitor the fluorescence from either cold atoms or atoms in a thermal beam. We have two different CCD cameras: an EHD KamPro02 high sensitive monochrome CCD-camera (sensible to UV-light), where the chip window partially absorbing UV light has been removed and a Hamamatsu C8800-

C21 camera. A flexible lens system is integrated with the CCD cameras with the possibility of adding different interference filters. The two identical lens systems consist of two UV-lenses in a telescope configuration whose focal lenses are respectively 200 mm and 75 mm, so that the first lens is placed about 200 mm from the MOT region, and the second lens about 75 mm from the CCD chip. The EHD KamPro02 is permanently mounted on the MOT chamber for monitoring the 285 nm fluorescence from the MOT. A calibration of horizontal and vertical axis gives that one pixel in the camera corresponds to  $28 \pm 2 \mu\text{m}$  in both directions at the MOT position. Consequently the region imaged is around 13x18 mm.

The fluorescence from the MOT-cloud or from the atomic beam is measured by a UV sensitive photomultiplier tube (Hamamatsu r7400p-06) equipped with a UV-filter and a telescope identical to the system used for the cameras. The rise time has been measured to be  $\tau < 20$  ns. The calibration of the photomultiplier with no gain (no external voltage applied), of the incoming UV power  $P_{in}$  against the output voltage  $V_{out}$  of the photomultiplier, has been routinely repeated [102], [113], and it is consistent with a linear function given by  $V_{out} = 64 \text{ mV} + 29.96 \text{ mV/nW} \cdot P_{in}$ .

An estimation of the total number of atoms in the MOT is given by the simple relation:

$$N = \frac{P_{in}}{\hbar\omega_{UV}} \frac{1}{\eta} \frac{1}{\Gamma \rho_{ee}} \quad (3.31)$$

where  $\hbar\omega_{UV}$  is the photon energy,  $\eta$  is the geometrical detection efficiency (around  $4 \cdot 10^{-3}$  for the present geometry),  $\Gamma$  is the linewidth of the upper state, and  $\rho_{ee}$  the population on the excited state given by equation 2.3. Typically, in the order of  $10^7$  atoms are trapped.

### 3.3.2 MOT Characteristics

A detailed model and first characterization of the  $^{24}\text{Mg}$  MOT can be found in [102], [113]. For this reason, only an overview of the main parameters are given here.

All three isotopes of magnesium can be trapped by the present setup, but here only  $^{24}\text{Mg}$  is described. A  $^{24}\text{Mg}$  MOT-sample is observed in a [-150,-30] MHz detuning interval and for coil currents as low as 60A to the maximum obtainable with the present setup of 200A, corresponding to a magnetic field gradient from around 50 to 280 G/cm in the z direction and to a magnetic field gradient from 25 to 140 G/cm in the directions perpendicular to the z axis.

The number of atoms trapped in the MOT depends on the dimensions of the UV beams, the detuning of the UV-light and the gradient of the magnetic field, and ranges from  $10^5$  to  $10^8$  corresponding to a peak density of  $10^{12}$  atoms/cm<sup>3</sup>. The spatial distribution of the cloud shows a typical gaussian shape, and the radius has been investigated as a function of the detuning and the field gradient [102].

#### Temperature

Many attempts of characterizing the temperature has been made in the past years, from release and recapture experiments to time of flight techniques resulting in temperatures significantly higher than the Doppler limit (6-30 mK [113]). These techniques have been shown to have significant disadvantages which might account for some of the deviation from the Doppler temperature [113]. Furthermore, fluctuations of the intensity of the UV-light, together with the multiple fringes shaping the UV-beam could play a central role in the explanation of the fluctuating feature of the temperature and the difficulty getting closer to the Doppler temperature limit (1.9 mK).

A series of temperature measurements has been performed by exploiting a ballistic expansion technique consisting of recording a sequence of images of the expanding cloud at different times using a CCD camera, see figure 3.35.

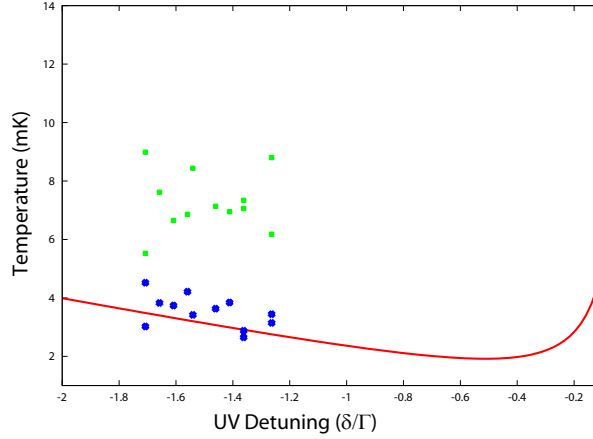


**Figure 3.35:** MOT temperature along the  $z$ -axis (green dots) and in the  $xy$ -plane (blue dots) as a function of detuning. The magnetic field is turned off  $100 \mu\text{s}$  before the UV light. The temperature in the solid line is the Doppler temperature given by equation 2.11.

The temperature of an atomic cloud can be determined by ballistic expansion, measuring the radius of the cloud at different expansion times and assuming a gaussian velocity distribution in the MOT. The radius  $\sigma(t)$  of the ballistically expanding cloud is given by (see [129], [130] for more detail)

$$\sigma^2(t) = \sigma_0^2 + v^2 t^2 \quad (3.32)$$

where  $\sigma_0$  is the radius at time  $t = 0$ , i.e. in the trap and  $v$  is the expansion velocity of the radius. This means that expansion images contain information on the density distribution, if the time-of-flight is short, and information about the temperature for long expansion times, corresponding to the two terms in the formula above. Here, we note that for expansion of thermal atoms, the expansion velocity is given by:

$$v = \sqrt{\frac{k_B T}{m}} \quad (3.33)$$

From figure 3.35 a clear difference is seen between the temperature along the z-axis and in the xy-plane probably caused by a more efficient molasses cooling in that direction when the magnetic field is turned off.

### Losses

A MOT consists of tens of millions of atoms that continuously are added and lost from the trap. A steady state is reached when losses from the trap equals additions to the trap. The rate equation can be found from the following simple arguments: The addition of atoms to the trap are solely from the atomic beam that feeds the atoms at a constant rate. The velocity distribution of the atoms coming from the oven are assumed to follow a Maxwell-Boltzmann distribution. Only a small fraction of the distribution is trapped. If an atom has too high a velocity, it will simply pass through the MOT and never return. The velocity, at which the MOT is just capable of trapping an atom, is referred to as the capture velocity, and simple calculations of the capture velocity is given in [102], [113]. The rate of atoms captured is referred to as the load of the MOT and is assumed to be independent of the number of atoms in the trap. Losses from the MOT includes those caused by collision of two trapped atoms, and those where only a single trapped atom is involved. Higher order collisions are safely neglected due to the low density of cold atoms. The first process is referred to as cold collisions. Because two atoms are involved in the process, the loss rate depends on the square of the density in the MOT. The second process is either caused by collisions of hot background atoms with the cold magnesium atoms or by photo-ionization. The latter is due to absorption of two 285 nm photons that causes excitation from  $^1P_1$  to the continuum states thereby ionizing the atom. Both processes involve only one trapped atom, and is proportional to the number of trapped atoms. The photo-ionization rate is furthermore dependent on the intensity

given by

$$\alpha_{ion}(I) = \sigma_{ion}\rho_{ee}\frac{I}{\hbar\omega} \quad (3.34)$$

where  $\sigma_{ion}$  is the photo-ionization cross section. A measurement of  $\sigma_{ion}$  is reported in [131].

Summarized, the losses and contributions result in the rate equation

$$\frac{dN(t)}{dt} = L - \alpha N(t) - \beta N^2(t) \quad (3.35)$$

where  $N(t)$  is the number of atoms in the trap at time  $t$ ,  $\alpha$  is the total rate occurring from photo-ionization and background collisions,  $\beta$  is the collision rate from cold collisions, and  $L$  is the atomic load.

From earlier experiments, it is shown that  $\beta/V_{mot}$  is of the order of  $10^{-5} \text{ s}^{-1}$  [102], where  $V_{mot}$  is the mean volume of the gas cloud. Typical values of  $\alpha$  ranges from  $0.1 \text{ s}^{-1}$  to  $2 \text{ s}^{-1}$ . The term from cold collisions can therefore safely be neglected, resulting in a total rate equation:

$$\frac{dN(t)}{dt} = L - \alpha N(t) \quad (3.36)$$

The steady state ( $\frac{dN(t)}{dt} = 0$ ) is seen to be

$$N_0 = \frac{L}{\alpha} \quad (3.37)$$

and the solution to (3.36) is easily found to be

$$N(t) = N_0 (1 - \exp(-\alpha t)) \quad (3.38)$$

with the initial condition  $N(t=0) = N_0$ .

Typical load and decay curves of the MOT can be seen in figures 3.36 and 3.37 showing a MOT lifetime of up to 5.6 s. A significant difference in the

load and decay times is observed and is attributed to collisions with atoms in the atomic beam.

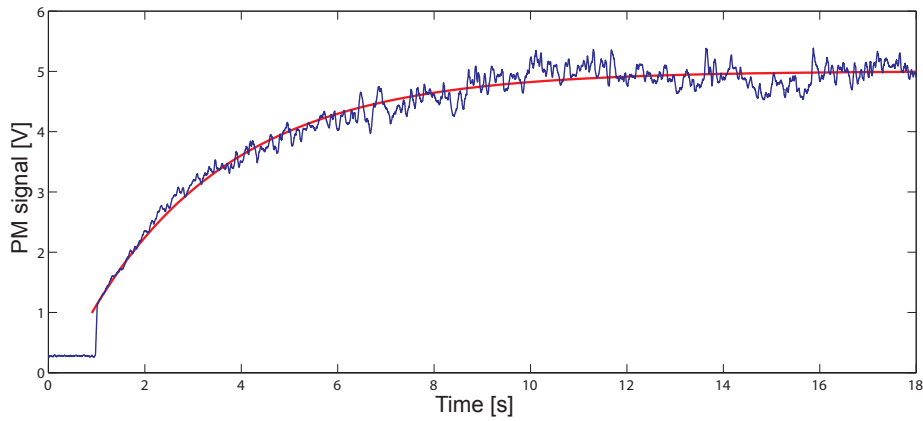


**Figure 3.36:** Typical loading curve of the MOT. Evolution of the photomultiplier signal during a load experiment together with the fit to an exponential function, resulting in a time constant  $\tau = 3.1$  s.

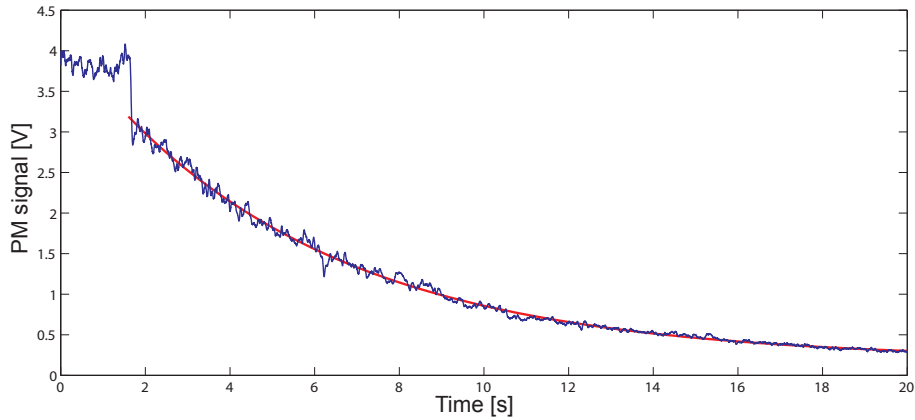


**Figure 3.37:** Typical decay curve of the MOT. Evolution of the photomultiplier signal during a decay experiment together with the fit to an exponential function, resulting in a time constant  $\tau = 5.6$  s.



---

---

## CHAPTER 4

---

# Experiments with the Metastable Source

In this chapter spectroscopy of the  ${}^3P_{0,1} - {}^3S_1$  and the  ${}^3P_{0,1,2} - {}^3D_{1,3,2}$  transitions is presented. Spectroscopy is performed in order to gain information useful for astronomical observations and for theoretical modeling of the alkaline earth atoms. Furthermore spectroscopy is performed as a preliminary investigation for future applications of the involved transitions in e.g. laser cooling.

### 4.1 Spectroscopy of the ${}^3P_{0,1} - {}^3S_1$ Transitions

In this section, improved measurements for the isotope shift and the hyperfine structure splitting of the  $(3s3p) {}^3P_{0,1} - (3s4s) {}^3S_1$  Mg I transitions at 517 nm in a metastable atomic magnesium beam, are presented. Improvements to previous measurements by up to a factor of eight for the stable isotopes  ${}^{24}\text{Mg}$  ( $I=0$ ),  ${}^{25}\text{Mg}$  ( $I=5/2$ ) and  ${}^{26}\text{Mg}$  ( $I=0$ ) are achieved. For  ${}^{25}\text{Mg}$   ${}^3S_1$  the hyperfine coefficient  $A({}^3S_1)$  is determined. Finally the  ${}^{24}\text{Mg}$   $(3s3p) {}^3P_1 - (3s4s) {}^3S_1$  transition frequency is referenced to the  ${}^{127}\text{I}_2$  R(59) (0-42) iodine line. As mentioned in section 3.2 fluorescence spectroscopy is used to stabilize the 517 nm laser system.

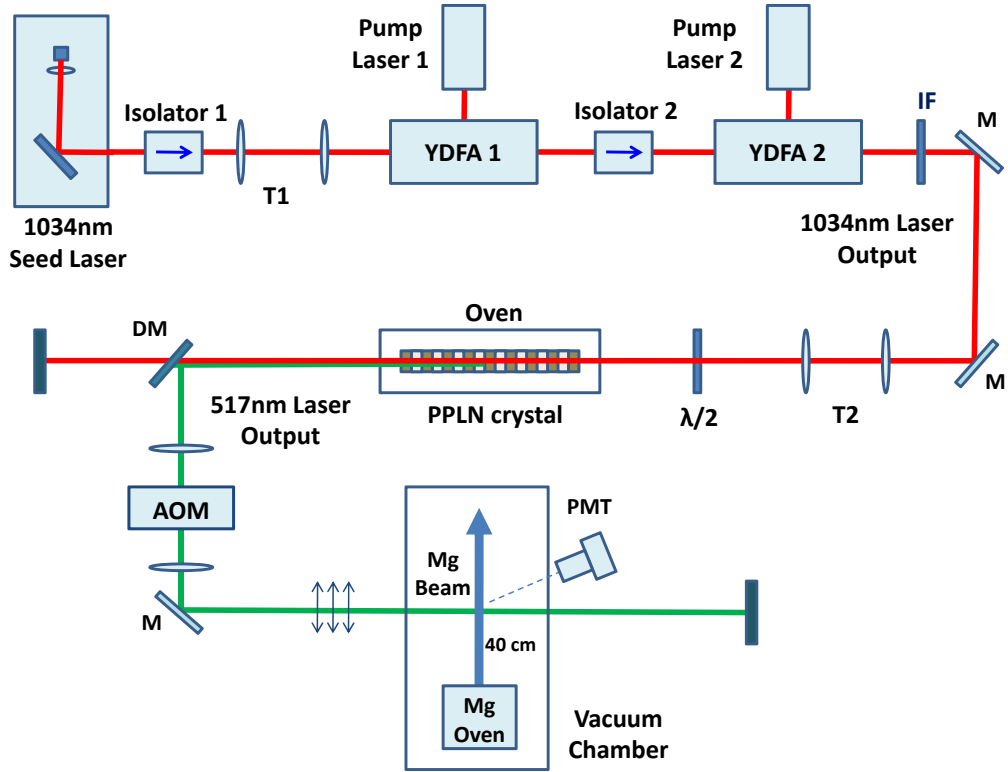


**Figure 4.1:** Schematic diagram of 517 nm laser system: *T*, telescope; *DM*, dichromatic mirror; *IF*, interference filter; *M*, mirror;  $\lambda/2$ , half waveplates; *AOM*, acousto-optic modulator; *PMT*, photomultiplier tube. A two-stage YDFA system is used for 1034 nm laser amplification, and then there is the 517 nm second harmonic generation by PPLN crystal. For absorption spectroscopy of metastable magnesium beam, the distance between oven orifice and laser beam is 40 cm.

#### 4.1.1 Experimental Setup

Figure 4.1 shows the experimental setup used for spectroscopy on metastable magnesium atoms. The oven is operated at  $T = 793$  K and produces an effusive magnesium beam with mean velocity 1000 m/s and typical intensity of  $10^{13}$  atoms/s, see section 3.2. The 517 nm light is produced from a fiber amplified diode laser which is amplified and single pass frequency doubled as described in section 3.1.7.

Spectroscopy is performed at a distance of 40 cm from the oven orifice

using linearly polarized light. The imaging system collects fluorescence from an area of about  $9 \text{ mm}^2$  within the atomic beam limiting the residual Doppler effect to about 68 MHz. Finite size of the oven orifice only give rise to an 8 MHz Doppler effect. The fluorescence is imaged onto a photomultiplier. The zero and first order of a 275 - 400 MHz AOM is overlapped and used for absolute frequency calibration. The absolute AOM frequency is determined better than 1 kHz using a precision counter. The laser beam have a radius of 0.5 mm and the intrinsic linewidth of the 517 nm light has been measured to below 3 MHz using a confocal cavity.

#### 4.1.2 Results and Discussion

The energy of a  ${}^3L_J$  level may be written in the following way [132]:

$$\hbar\omega({}^3L_J)_F = \hbar\omega_0({}^3L_J) + \hbar\omega_1({}^3L_J)_F \quad (4.1)$$

where J and F are the electronic and total angular-momentum quantum numbers,  $\omega_0({}^3L_J)$  is the energy level without nuclear spin and  $\omega_1({}^3L_J)_F$  is the first order hyperfine interaction energy, given by:

$$\omega_1({}^3L_J)_F = \frac{K}{2}A({}^3L_J) + \frac{3K(K+1) - 4IJ(I+1)(J+1)}{8IJ(2I-1)(2J-1)}B({}^3L_J) \quad (4.2)$$

where  $K = F(F+I) - J(J+I) - I(I+1)$ . Contributions from higher-order terms [132] in equations 4.1 and 4.2 are negligible and are therefore not required to interpret the measurements. The hyperfine constants for the  ${}^3P_1$  levels are necessary to extract the hyperfine constants for the  ${}^3S_1$  level from the  ${}^3P_1 - {}^3S_1$  transition and have been accurately determined in [133]. For the  ${}^3S_1$  level,  $B({}^3S_1)$  is expected to be far below the resolution of this experiment ( $\approx 10^{-5}$  MHz [134]) and is therefore assumed to be zero in the following.

In figures 4.2 and 4.3 typical spectra are seen showing the metastable

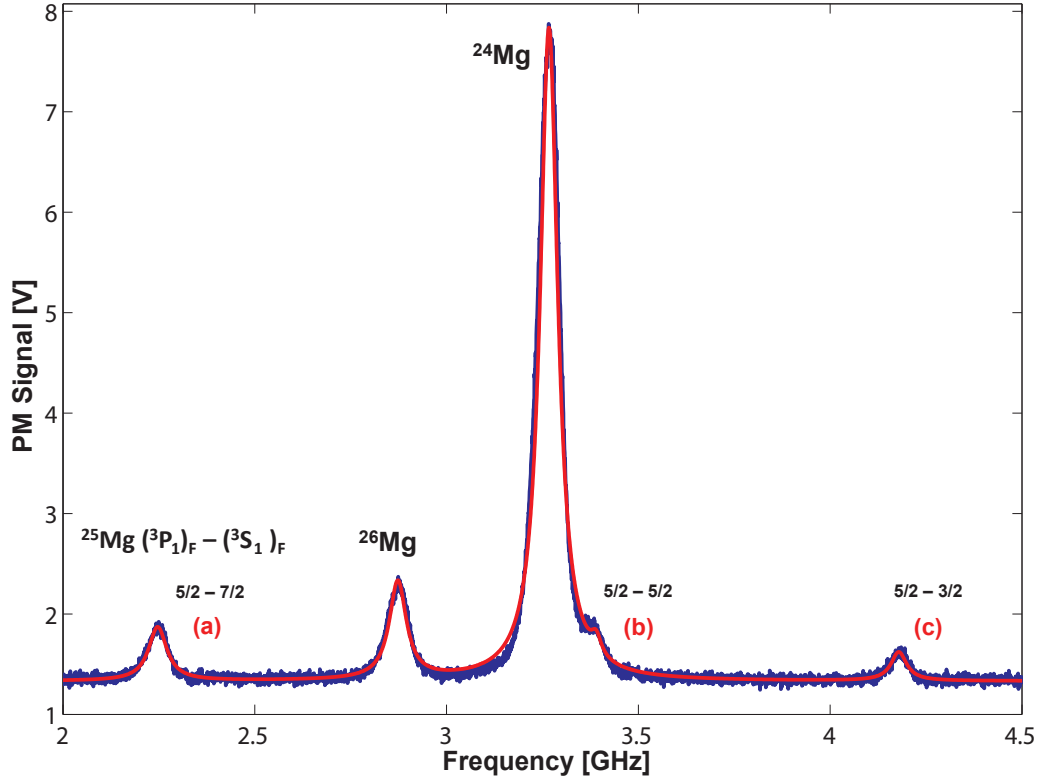


**Figure 4.2:** The fluorescence signal from the  ${}^3P_0 - {}^3S_1$  transitions. The blue curve represents the experimental data and the red curve is a fit to the data. The hyperfine transitions of  ${}^{25}\text{Mg} ({}^3P_0)_F - ({}^3S_1)_F$  are indicated as (a) - (c).

beam fluorescence as a function of laser frequency. The blue curves are the raw data and the red curves are the fits. For  ${}^{24}\text{Mg}$  a linewidth of 71 MHz is obtained in agreement with the beam and detector geometry. From the spectra, the  ${}^{24}\text{Mg}$ - ${}^{26}\text{Mg}$  isotope shifts, as well as the hyperfine  $({}^3P_1)_F - ({}^3S_1)_F$  transitions of  ${}^{25}\text{Mg}$ , are seen. From the difference in signal strength between the  ${}^{24}\text{Mg}$  and  ${}^{26}\text{Mg}$  peaks, the isotope abundance ratio is determined to be  ${}^{24}\text{Mg}/{}^{26}\text{Mg} = 6.9$ , which differ from the isotope ratio stated in [59] of 7.2. This is probably due to a difference of electron excitation cross sections between the different isotopes, which after the discharge region lead to a different isotope ratio of atoms in the excited  ${}^3P_{0,1,2}$  states.

Each spectrum showed in figures 4.2 and 4.3 is an average over eight

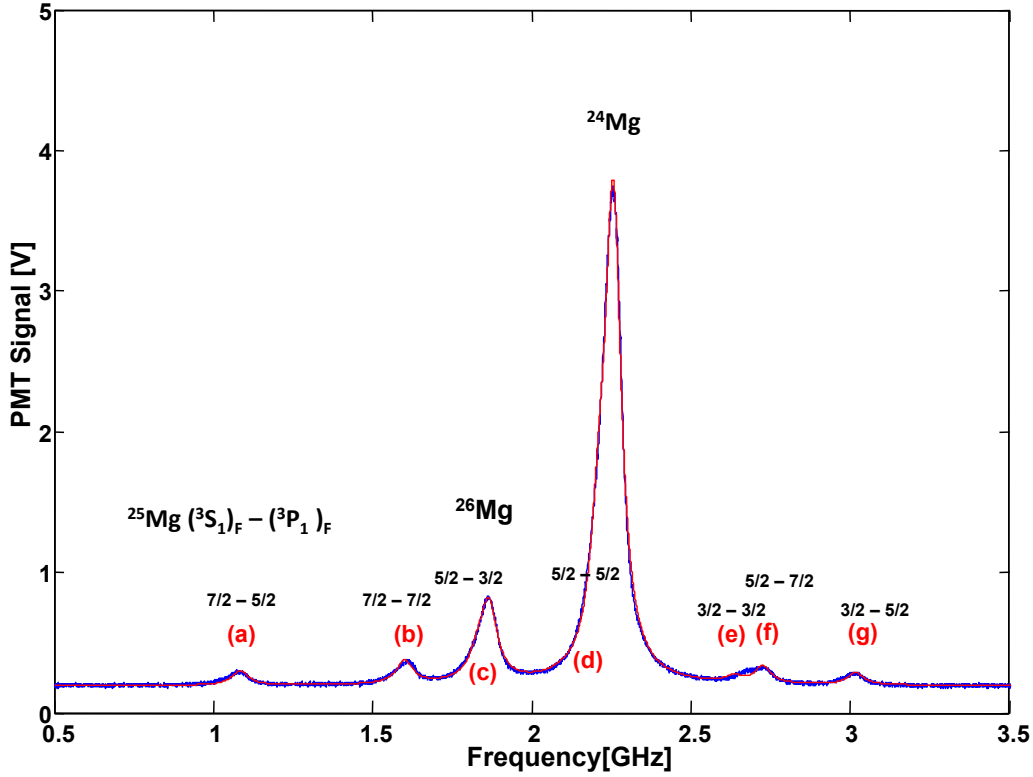


**Figure 4.3:** The fluorescence signal from the  ${}^3P_1 - {}^3S_1$  transitions. The blue curve represents the experimental data and the red curve is a fit to the data. The hyperfine transitions of  ${}^{25}\text{Mg} ({}^3P_1)_F - ({}^3S_1)_F$  are indicated as (a) - (g).

measurements. Spectra are recorded at thirty different AOM frequencies for both of the  ${}^3P_0 - {}^3S_1$  and  ${}^3P_1 - {}^3S_1$  transitions. From the data the hyperfine coefficient  $A({}^3S_1) = -321.4 \pm 1.9$  MHz is extracted. The isotope shifts of the  ${}^3P_0 - {}^3S_1$  transition are found to be  $\Delta^{24-26} = 391.3 \pm 1.7$  MHz and  $\Delta^{24-25} = 205.7 \pm 1.5$  MHz. And for the  ${}^3P_1 - {}^3S_1$  transition the isotope shifts are  $\Delta^{24-26} = 390.1 \pm 1.4$  MHz and  $\Delta^{24-25} = 209.1 \pm 1.3$  MHz. Table 4.1 summarizes the measured isotope shifts and  ${}^3S_1$  hyperfine structure constants and compare to literature. It is seen that the measurements presented here agree with the previous measurements within the stated uncertainties. Recent theoretical calculations [134] give a hyperfine coefficient of  $A({}^3S_1) = -325$  MHz, which is in excellent agreement with results obtained here.

	${}^3P_0 - {}^3S_1$		${}^3P_1 - {}^3S_1$		$A({}^3S_1)$ [MHz]
	$\Delta^{24-26}$ [MHz]	$\Delta^{24-25}$ [MHz]	$\Delta^{24-26}$ [MHz]	$\Delta^{24-25}$ [MHz]	
Ref. [135] (1949)	$414 \pm 9$		$366 \pm 45$		$-322 \pm 6$
Ref. [136] (1978)	$396 \pm 6$	$210 \pm 36$	$391 \pm 4.5$	$201 \pm 21$	$-329 \pm 6$
Ref. [137] (1990)	$391 \pm 10$	$214 \pm 10$	$393 \pm 10$	$215 \pm 10$	$-322 \pm 6$
This work (2009)	$391.3 \pm 1.7$	$205.7 \pm 1.5$	$390.1 \pm 1.4$	$209.1 \pm 1.3$	$-321.4 \pm 1.9$

**Table 4.1:** Measured isotope shifts and  ${}^3S_1$  hyperfine structure constant and comparison with previous measurements.

Figure 4.4 shows the  ${}^3P_1 - {}^3S_1$  transition and the iodine reference line  ${}^{127}\text{I}_2$  R(59) (0-42). The shift between the  ${}^{24}\text{Mg}$  absolute frequency and the center of the  $\text{I}_2$  transition is determined to be  $252 \pm 22$  MHz, in agreement with a previous measurement in [137]. In order to improve this value it will be necessary to compare to the hyperfine structure of  ${}^{127}\text{I}_2$  R(59) (0-42).

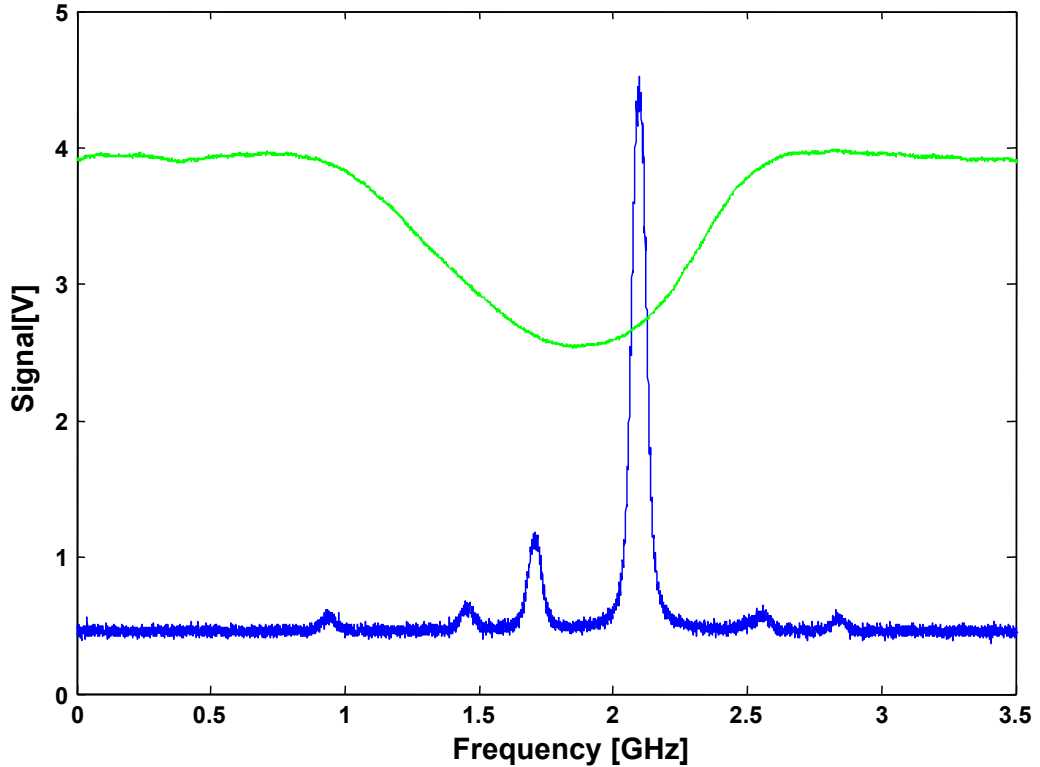


**Figure 4.4:** Spectrum of Mg  ${}^3P_1 - {}^3S_1$  transition and the iodine reference line  ${}^{127}\text{I}_2$  R(59) (0-42).

### 4.1.3 Conclusion

In this section improved data for the isotope shifts of the  ${}^3P_{0,1} - {}^3S_1$  transitions, and the hyperfine coefficient  $A({}^3S_1)$  for the  ${}^{25}\text{Mg}$  isotope, are presented. Experimental values reported here are improved by up to a factor of eight compared to previous studies. Finally the  ${}^3P_1 - {}^3S_1$  transition of  ${}^{24}\text{Mg}$  is referenced to the iodine line  ${}^{127}\text{I}_2$  R(59) (0-42).

## 4.2 Spectroscopy of the ${}^3\text{P}_{0,1,2} - {}^3\text{D}_{1,2,3}$ Transitions

In this section, preliminary spectroscopic results of the  $(3s3p){}^3\text{P}_0 - (3s3d){}^3\text{D}_1$ ,  $(3s3p){}^3\text{P}_1 - (3s3d){}^3\text{D}_{1,2}$  and  $(3s3p){}^3\text{P}_2 - (3s3d){}^3\text{D}_{1,2,3}$  transitions, are presented. The spectroscopic data presented in the following section is the first step towards a metastable  ${}^3\text{P}_J$  Mg MOT. Different possibilities for laser cooling atoms in the metastable  ${}^3\text{P}_J$  states exist. However the  ${}^3\text{P}_2 - {}^3\text{D}_3$  transition is the most obvious candidate since it is the most closed cooling transition. However, losses exist due to a non-zero excitation probability to the  ${}^3\text{D}_{1,2}$  states when the laser is red-detuned  $\sim \Gamma = 25.6$  MHz from the  ${}^3\text{P}_2 - {}^3\text{D}_3$  transition. The lifetime of a  ${}^3\text{P}_2 - {}^3\text{D}_3$  MOT is estimated to be 0.5 ms without taking optical pumping to the stretched  $m_J$  states into account. The addition of a repumper on the  ${}^3\text{P}_1 - {}^3\text{D}_2$  state increases the MOT lifetime  $\sim 100$  ms again without taking optical pumping to the stretched  $m_J$  states into account. The Doppler temperature of the  ${}^3\text{P}_2 - {}^3\text{D}_3$  MOT is 615  $\mu\text{K}$  with the possibility of sub-Doppler cooling.

### 4.2.1 Experimental Setup

The experimental setup is similar to the one presented in the previous section. Again the oven is operated at  $T = 793$  K and produces an effusive magnesium beam with mean velocity 1000 m/s and a typical intensity of  $10^{13}$  atoms/s, see section 3.2. The 383 nm light is produced by an amplified diode laser which is frequency doubled as described in section 3.1.6. The 383 nm laser beam is double-passed through an 85 - 115 MHz AOM and both the incoming beam and the double-passed beam are sent to the oven chamber. The two beams are overlapped and used to produce a spectrum of double peaks which is used for frequency calibration. Spectroscopy is performed at a distance of 40 cm from the oven orifice, using linearly polarized light. The imaging system collects fluorescence from an area of about 9 mm<sup>2</sup> within the atomic beam limiting the residual Doppler effect to about 68 MHz. The AOM is modulated with 45 kHz, and the fluorescence signal are sent through a lock-in amplifier

to increase the signal to noise ratio.

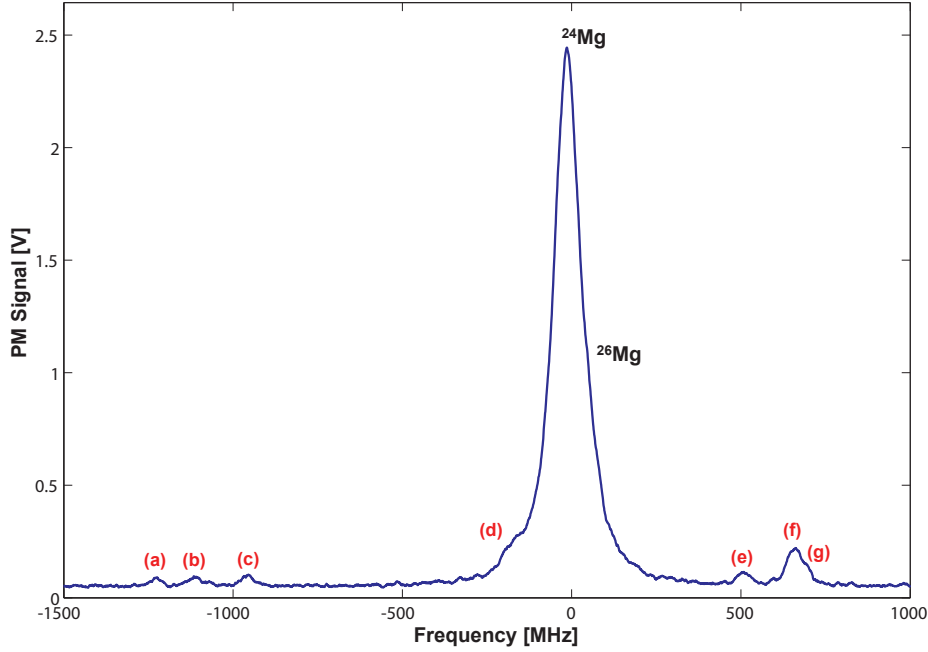


**Figure 4.5:** The fluorescence signal from the  ${}^3P_0 - {}^3D_1$  transitions. The blue curve represents the experimental data. The  ${}^{25}\text{Mg}$  transitions are indicated as (a) - (g). (d) might contain more than one peak. At least 7 peaks are seen in contrast to the expected 3 hyperfine  ${}^{25}\text{Mg}$  transitions:  ${}^3P_0)_{5/2} - ({}^3D_1)_{3/2,5/2,7/2}$ .

#### 4.2.2 Results and Discussion

Typical spectra for the  ${}^3P_0 - {}^3D_1$ ,  ${}^3P_1 - {}^3D_{1,2}$  and  ${}^3P_2 - {}^3D_{1,3,2}$  transitions can be seen in figures 4.5, 4.6 and 4.7, respectively.

Figure 4.5 show the  ${}^3P_0 - {}^3D_1$  spectrum. The main peak is asymmetric since it contains both the  ${}^{24}\text{Mg}$  and  ${}^{26}\text{Mg}$  transitions. From the asymmetry the isotope shift can be estimated to be  $\sim 65$  MHz which is consistent with previous measurements [138], [139]. From figure 4.2 in the previous section three  ${}^{25}\text{Mg}$  transitions are seen:  $({}^3P_0)_{5/2} - ({}^3S_1)_{3/2,5/2,7/2}$ . Correspondingly the following three  ${}^{25}\text{Mg}$  transitions are expected in figure 4.5:  $({}^3P_0)_{5/2} - ({}^3D_1)_{3/2,5/2,7/2}$ . However, this is not observed in figure 4.5. Instead of the expected 3 peaks at least 7 peaks are observed. This has previously been

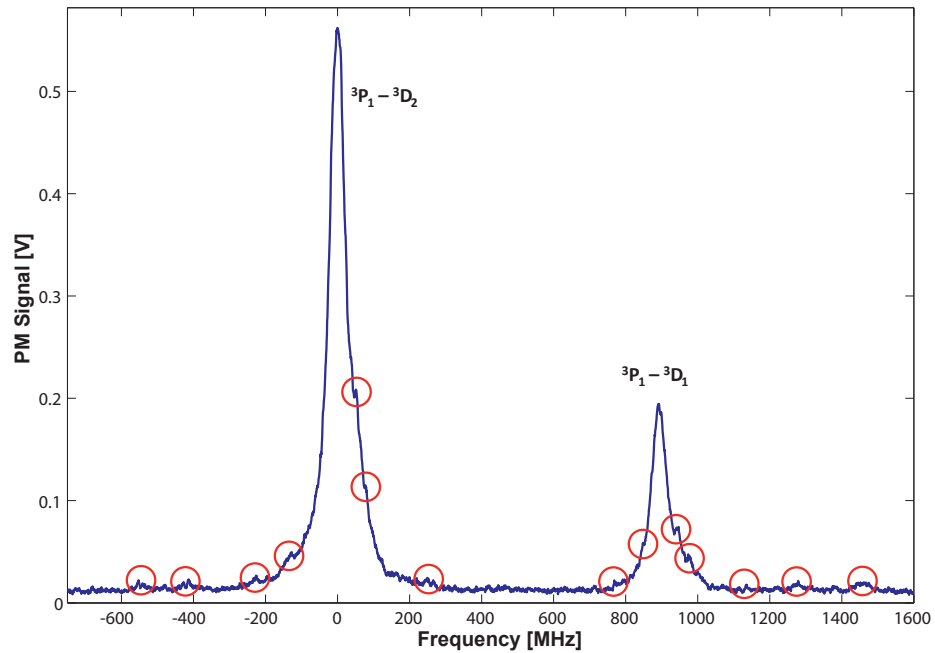


**Figure 4.6:** The fluorescence signal from the  ${}^3P_1 - {}^3D_{1,2}$  transitions. The blue curve represents the experimental data. The asymmetry of the  ${}^{24}\text{Mg}$  peaks are due to overlap with  ${}^{26}\text{Mg}$ . Possible  ${}^{25}\text{Mg}$  transitions are indicated by a red circle.

observed by [138], and was suggested to be due to the fact that the fine splitting and the hyperfine splitting of the  $(3s3d)^3D$  level are of the same order of magnitude, and therefore the usual assumption that hyperfine interaction is small and can be treated as a perturbation with respect to fine structure breaks down entirely. Under these conditions, levels with the same  $F$ , but different  $J$ , should mix, thus changing the frequency and the intensity of the transition components. However mixing with other states usually does not give rise to additional splitting of the different levels and can therefore not necessarily explain the additional transitions observed [94]. Currently we have not been able to explain this peculiar feature, and hope theoretical support on this issue.

Figure 4.7 shows the  ${}^3P_1 - {}^3D_{1,2}$  spectrum. The frequency difference between the  ${}^3D_1$  and  ${}^3D_2$  states is found to be 925 MHz which is in agreement

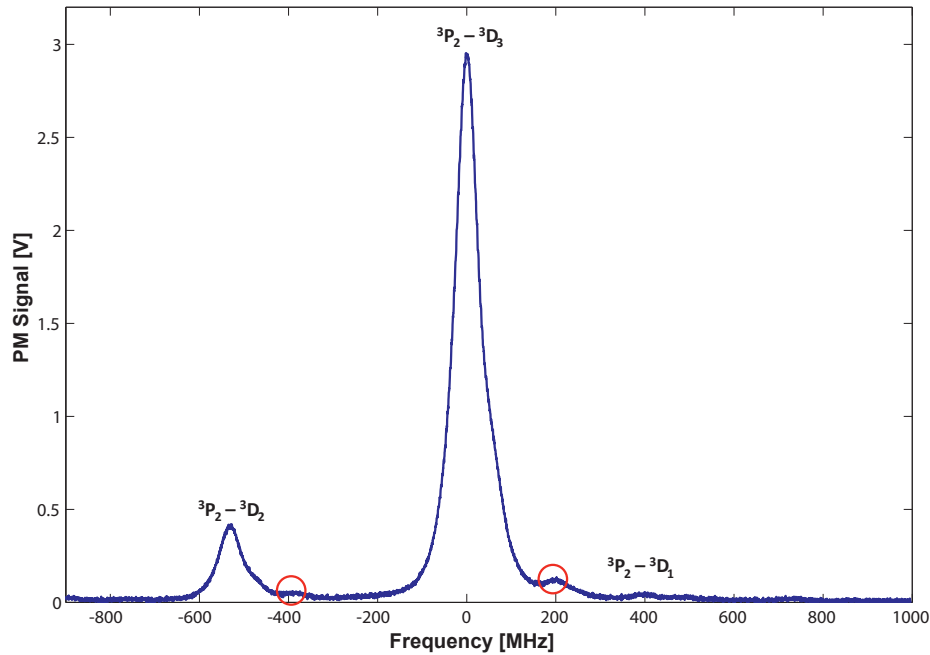


**Figure 4.7:** The fluorescence signal from the  ${}^3P_2 - {}^3D_{1,2,3}$  transitions. The blue curve represents the experimental data. The asymmetry of the  ${}^{24}\text{Mg}$  peaks are due to overlap with  ${}^{26}\text{Mg}$ . Possible  ${}^{25}\text{Mg}$  transitions are indicated by a red circle. The spectrum is recorded without the use of a lock-in amplifier.

with the value reported in [140]. From the hyperfine structure of the  ${}^{25}\text{Mg}$   ${}^3P_1 - {}^3D_{1,2}$  transitions a total of 16 transitions are expected (7 from the  ${}^3P_1 - {}^3D_1$  transition and 9 from the  ${}^3P_1 - {}^3D_2$ ). Unfortunately the resolution of figure 4.6 is not sufficient to determine if more than the 16 expected peaks are present.

Figure 4.6 show the  ${}^3P_2 - {}^3D_{1,2,3}$  spectrum which is recorded without the use of a lock-in amplifier. The asymmetry of the  ${}^{24}\text{Mg}$  peaks are due to overlap with  ${}^{26}\text{Mg}$ . The resolution of the spectrum does unfortunately allow the identification of many  ${}^{25}\text{Mg}$  transitions.

### 4.2.3 Conclusion

In this section preliminary spectroscopic results of the  ${}^3P_{0,1,2} - {}^3D_{1,3,2}$  transitions was presented. The splittings of the  ${}^3D_{1,3,2}$  levels have been measured. However, it has not been possible to explain the hyperfine transitions of  ${}^{25}\text{Mg}$ .

---

---

## CHAPTER 5

---

# Experiments with the MOT

One of the main motivations for the work described in this thesis is to find a way to obtain a sample of atoms colder than the MOT temperature of a few mK. For this purpose, several new laser systems have been developed. Previously, a two-color cooling technique has been explored [113], [141], but since it has not been possible to reduce the temperature below 1 mK [97], another approach is chosen. From the metastable  $(3s3p)^3P_{0,1,2}$  states several transitions suited for laser cooling exist, to the  $(3s3d)^3D_{1,3,2}$  and the  $(3s4s)^3S_1$  state. Therefore the main problem is to obtain a sample with a large amount of atoms in the  $^3P_{0,1,2}$  states and preferably in the  $^3P_{0,2}$  states since they have significantly longer lifetimes than the  $^3P_1$ . Using the 285 nm MOT there are two possibilities of doing this. One option is to transfer the atoms to  $^3P_1$  using the 457 nm intercombination line and optically pump the atoms to either of the  $^3P_{0,2}$  states. Alternatively, it is possible to use the spin-forbidden  $^1D_2 \rightarrow ^3P_{2,1}$  decay channel, which naturally exists in a Sr or Ca MOT, by exciting the atoms from the  $^1P_1$  to the  $^1D_2$  state. The latter case is investigated in the following section.

## 5.1 Measurement of the Spin-forbidden Decay Rate

### $(3s3d)^1D_2 \rightarrow (3s3p)^3P_{2,1}$ in $^{24}\text{Mg}$

In the following, the measurement of the spin-forbidden decay rate of the  $(3s3d)^1D_2 \rightarrow (3s3p)^3P_{2,1}$  transition in  $^{24}\text{Mg}$  is described. The two-color cascade system of the  $^1S_0$ - $^1P_1$ - $^1D_2$  states of  $^{24}\text{Mg}$  is a nearly ideal two-photon cascade system, since there are no leaks from the  $^1P_1$  state and only a small leak from the  $^1D_2$  state to the  $^3P_{0,1,2}$  states. In this section a short examination of the three level system will be done, and the Optical Bloch Equations (OBE) will be treated. Furthermore, the leak from the  $^1D_2$  will be investigated.

#### 5.1.1 The Optical Bloch Equations for the Three Level System

In figure 5.1 an ideal three level atom is depicted. The ground state of the bosonic isotope  $^{24}\text{Mg}$  can almost be considered as an ideal atom. The three states  $|a\rangle, |b\rangle, |c\rangle$  correspond to the  $^1S_0$ - $^1P_1$ - $^1D_2$  states of  $^{24}\text{Mg}$ . In figure 5.1 two lasers are considered: one near resonance of the two lowest states,  $\omega_{UV}$  and one near resonance between the middle and the upper state ( $\omega_{IR}$ ).

In figure 5.1, the notation for the various parameters is shown. The natural linewidth of the two excited states is  $\gamma_{aa}$  for the upper and  $\gamma_{bb}$  for the middle, respectively. The detuning is denoted  $\delta_{UV}$  and  $\delta_{IR}$ .

The OBE are the equations of motion for the density matrix ( $\rho$ ). From the Hamiltonian of our system the time evolution of the population of the three states  $|a\rangle, |b\rangle$  and  $|c\rangle$  can easily be calculated. In the following this is done by solving the time evolution of the density matrix [142].

$$\dot{\rho} = -\frac{i}{\hbar} [\hat{H}, \rho] \quad (5.1)$$

The Hamiltonian  $\hat{H}$  for the interaction between light and an atom can for example be found in [142]. The differential equations regarding the elements

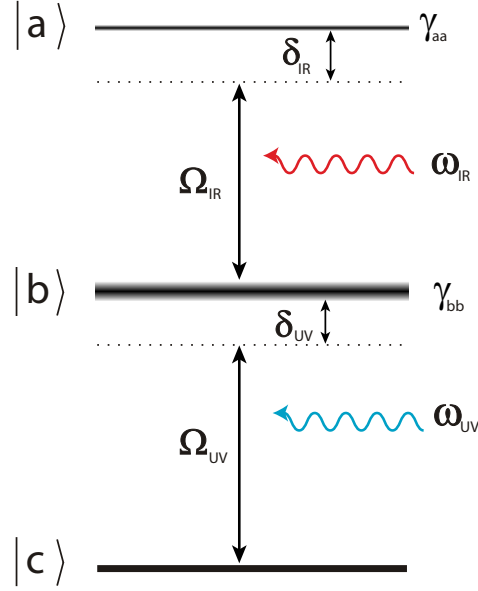


**Figure 5.1:** The energy levels of an ideal three level atom subjected to two different colors of light. The respective Rabi frequencies are denoted  $\Omega_{IR}$  and  $\Omega_{UV}$  and the detunings for the two laser beams  $\delta_{IR}$  and  $\delta_{UV}$ , with the natural linewidths denoted  $\gamma_{aa}$  and  $\gamma_{bb}$ , respectively.

of the density matrix,  $\rho_{nm}$ , can be calculated in the following way

$$\dot{\rho}_{nm} = -\frac{i}{\hbar} \langle n | [\hat{H}, \rho] | m \rangle \quad (5.2)$$

$$= \frac{i}{\hbar} \sum_k \langle n | \hat{H} | k \rangle \langle k | \rho | m \rangle - \langle n | \rho | k \rangle \langle k | \hat{H} | m \rangle \quad (5.3)$$

In the semiclassical treatment, the spontaneous decay from the excited states needs to be phenomenologically inserted as a non-conservative dispersive component. The time evolution of the density matrix can be as [142]:

$$\dot{\rho} = -\frac{i}{\hbar} [\hat{H}, \rho] - \frac{1}{2} \{\gamma, \rho\} \quad (5.4)$$

where  $\gamma$  is the decay matrix. Assuming only the diagonal entries of the decay matrix to take on nonzero values. Now the OBE of the three level system as shown in figure 5.1 becomes:

$$\dot{\rho}_{aa} = \frac{i\Omega_{IR}}{2} (\rho_{ba} - \rho_{ab}) - \gamma_{aa} \rho_{aa} \quad (5.5)$$

$$\dot{\rho}_{bb} = \frac{i\Omega_{IR}}{2} (\rho_{ab} - \rho_{ba}) + \frac{i\Omega_{UV}}{2} (\rho_{cb} - \rho_{bc}) + \gamma_{aa} \rho_{aa} - \gamma_{bb} \rho_{bb} \quad (5.6)$$

$$\dot{\rho}_{cc} = \frac{i\Omega_{UV}}{2} (\rho_{bc} - \rho_{cb}) + \gamma_{bb} \rho_{bb} \quad (5.7)$$

$$\dot{\rho}_{ab} = i\delta_{IR} \rho_{ab} + \frac{i\Omega_{IR}}{2} (\rho_{bb} - \rho_{aa}) - \frac{i\Omega_{UV}}{2} \rho_{ac} - \frac{\gamma_{aa} \rho_{ab}}{2} - \frac{\gamma_{bb} \rho_{ab}}{2} \quad (5.8)$$

$$\dot{\rho}_{ba} = -i\delta_{IR} \rho_{ba} - \frac{i\Omega_{IR}}{2} (\rho_{bb} - \rho_{aa}) + \frac{i\Omega_{UV}}{2} \rho_{ca} - \frac{\gamma_{aa} \rho_{ba}}{2} - \frac{\gamma_{bb} \rho_{ba}}{2} \quad (5.9)$$

$$\dot{\rho}_{ac} = i(\delta_{UV} + \delta_{IR}) \rho_{ac} + \frac{i\Omega_{IR}}{2} \rho_{bc} - \frac{i\Omega_{UV}}{2} \rho_{ab} - \frac{\gamma_{aa}}{2} \rho_{ac} \quad (5.10)$$

$$\dot{\rho}_{ca} = -i(\delta_{UV} + \delta_{IR}) \rho_{ca} - \frac{i\Omega_{IR}}{2} \rho_{cb} + \frac{i\Omega_{UV}}{2} \rho_{ba} - \frac{\gamma_{aa}}{2} \rho_{ca} \quad (5.11)$$

$$\dot{\rho}_{bc} = i\delta_{UV} \rho_{bc} + \frac{i\Omega_{UV}}{2} (\rho_{cc} - \rho_{bb}) + \frac{i\Omega_{IR}}{2} \rho_{ac} - \frac{\gamma_{bb}}{2} \rho_{bc} \quad (5.12)$$

$$\dot{\rho}_{cb} = -i\delta_{UV} \rho_{cb} - \frac{i\Omega_{UV}}{2} (\rho_{cc} - \rho_{bb}) - \frac{i\Omega_{IR}}{2} \rho_{ca} - \frac{\gamma_{bb}}{2} \rho_{cb} \quad (5.13)$$

These differential equations can be solved numerically, using the assumption, that no losses occur out of the three level system, meaning that:

$$\rho_{aa} + \rho_{bb} + \rho_{cc} = 1 \quad (5.14)$$

This assumption is valid even in the "real world" case, since the leaks are so small compared to the linewidth of the upper state. The OBE for the three-level cascade system has been solved and studied in great detail in [113]. The system is obviously rather complex due to the many parameters of the

equations.

For all practical purposes the three levels will be in a steady state before measurements, meaning that  $\dot{\rho} = 0$ . This means that the steady state is a sufficient description for the system.

### 5.1.2 Leaks to Metastable States

Consider the magnesium level scheme depicted in figure 5.2. When excited to the  $^1D_2$  state, there is a small probability that the atom decays to the metastable  $^3P_1$  or  $^3P_2$  state. The decay rates are denominated  $\Gamma_{22}$  for the  $^1D_2 \rightarrow ^3P_2$  decay and  $\Gamma_{21}$  for the  $^1D_2 \rightarrow ^3P_1$  decay, and they are theoretically estimated to be [143]:  $\Gamma_{21} = 144 \text{ s}^{-1}, \Gamma_{22} = 57 \text{ s}^{-1}$ .

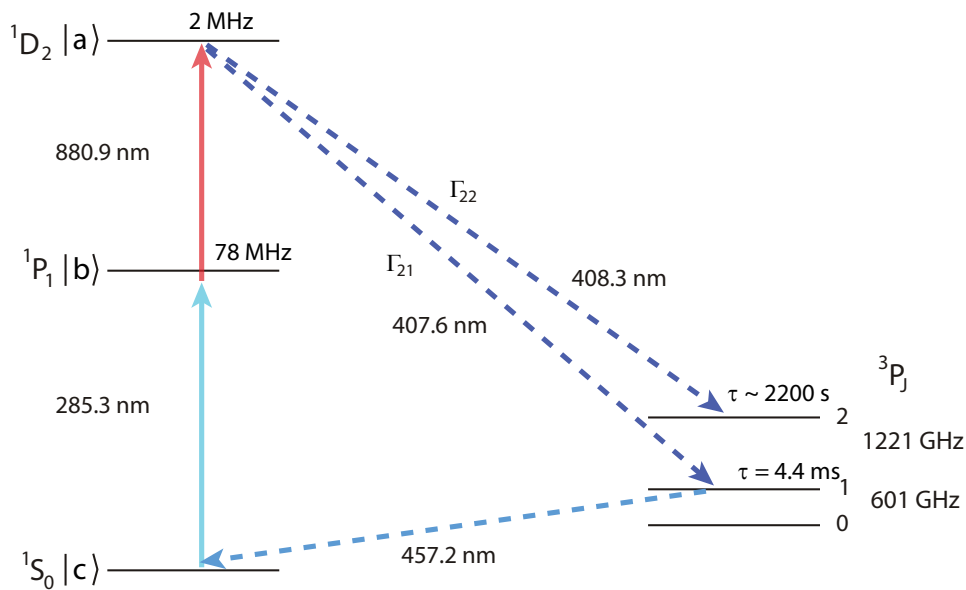


**Figure 5.2:** Overview of the magnesium atom. Solid lines illustrate transitions excited with laser light, while dotted lines denote the measured decays.

As in section 3.3.2, the rate equation for the number of atoms in a MOT exposed to a beam of 881 nm light is given by:

$$\dot{N} = L - \rho_{aa}(\Gamma_{22} + \Gamma_{21})N - \alpha N \quad (5.15)$$

$$= L - N(\rho_{aa}(\Gamma_{22} + \Gamma_{21}) + \alpha) \quad (5.16)$$

In the stationary state  $N_{st}$ , using that  $\dot{N} = 0$  and solving equation 5.16 thus gives

$$N_{st} = \frac{L}{\rho_{aa}(\Gamma_{22} + \Gamma_{21}) + \alpha} \quad (5.17)$$

When the 881 nm laser is on, and near the two-photon resonance, assuming a steady state, the signal from the emitted 285 nm photons will be:

$$S^{on} = \rho_{bb}^{on} N_{st} \Gamma_{bb} \quad (5.18)$$

$$= \rho_{bb}^{on} \Gamma_{bb} \frac{L}{\rho_{aa}(\epsilon \Gamma_{21} + \Gamma_{22}) + \alpha^{on}} \quad (5.19)$$

$$= \rho_{bb}^{on} \Gamma_{bb} \frac{\alpha^{off} N_0}{\rho_{aa}(\epsilon \Gamma_{21} + \Gamma_{22}) + \alpha^{on}} \quad (5.20)$$

with  $\alpha^{on}$  and  $\alpha^{off}$  being the loss rate for the system with IR on or off, respectively, assuming that they are not the same.  $\alpha$  is dominated by photo ionization which is dependent on the population of the  $^1P_1$  state, see section 3.3.2, which leads to  $\frac{\rho_{bb}^{on}}{\alpha^{on}} = \frac{\rho_{bb}^{off}}{\alpha^{off}}$ . This population is changed when the 881 nm laser is on.  $\epsilon$  is a factor that compensates for the fact that some of the atoms decaying to the  $^3P_1$  state are recaptured. Due to the long lifetime of the  $^3P_2$  state, which is theoretically estimated to be 2200 seconds [144] and the time scale of the experiment, being only a few seconds, we consider the atoms from this state to be lost. However, for the  $^3P_1$  states atoms in the  $|m_J = +1\rangle$  magnetic sub state will be trapped in the magnetic quadrupole field of the MOT (trap depth 1.7 mK/mm, see section 2.5), and they are most likely recaptured when decaying back to the  $^1S_0$  ground state ( $\tau = 4.4$  ms [145]). Atoms in the  $|m_J = 0, -1\rangle$  magnetic sub states are expected to

be lost, since the mean velocity of the trapped atoms around 2 m/s, leading to a mean distance of 9 mm, which is large compared to our MOT beam diameter. The total decay rate is modified to  $\epsilon \Gamma_{21} + \Gamma_{22}$ . The actual value of  $\epsilon$  depends strongly on the polarization of the 285 nm and the 881 nm beams.

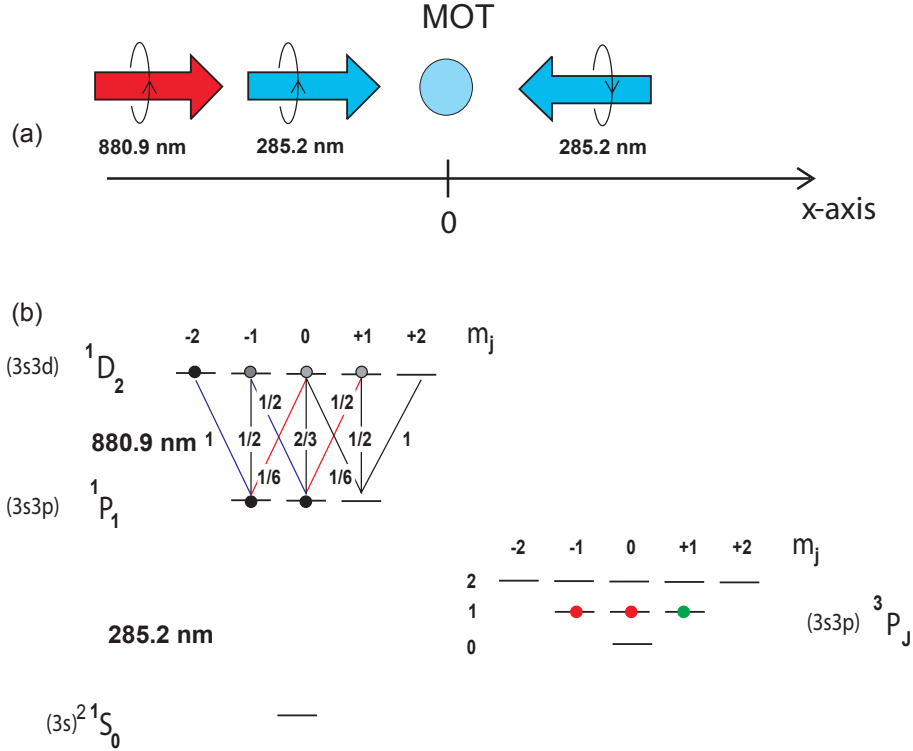


**Figure 5.3:** (a) Experimentally the 881 nm beam is co-linear with one of the MOT beams. The polarization state can be selected similar to the MOT helicity, as shown in the figure, or opposite. (b) Polarization dependent pumping of atoms in the MOT. Assuming a one dimensional representation of the MOT, the 881 nm polarization, represented by blue line (= MOT helicity) or red line, optical pumping will drive the atoms such that anisotropy in the decay rate will emerge. The green dot represents atoms trapped in the MOT quadrupole magnetic field, while red dots represent atoms in non-trapped states. The Clebsch Gordan coefficients shown will also apply to the  $(3s3d) \ ^1D_2 \rightarrow (3s3p)^3P_1$  decay.

If we assume a standard one dimensional model for the MOT, we can determine the influence of the constant  $\epsilon$ . This is a good approximation as the 881 nm beam is directed along one of the MOT beams, but not retro

reflected. Consider atoms on the  $-z$  side, see figure 5.3. These atoms will mainly populate the  $^1P_1 |m_j = 0, -1\rangle$  states. Further excitation of the co-linear 881 nm laser will drive the atoms to the left (blue line) or right (red line) depending on the helicity of the 881 nm laser. This creates an anisotropy in the decay to the  $(3s3p)^3P_1$  state. Atoms driven along the blue line, i.e., with the same polarization helicity as the MOT beams, will only populate non-trapped states. Experiments performed in this configuration are insensitive to the retrapping dynamics as described above. Using the Clebsch Gordan coefficients shown in figure 5.3 and assuming that only the  $^1P_1 |m_j = 0, -1\rangle$  states are populated with populations denoted  $n_-, n_0$  we find the rate  $(n_- \cdot 1 + n_0 \cdot (1/2 + 1/2))\Gamma_{21} = (n_- + n_0)\Gamma_{21} = \Gamma_{21}$ , as expected. For the opposite polarization, we find a reduction  $(n_- \cdot (2/3 + 1/6) + n_0 \cdot 1/2)\Gamma_{21} = (1/2 + 1/3 \cdot n_-)\Gamma_{21}$  which for equal populations in the  $^1P_1 |m_j = 0, -1\rangle$  states will be  $2/3\Gamma_{21}$ .

More generally, a case where all three magnetic sub states  $^1P_1 |m_j = +1, 0, -1\rangle$  are populated can be considered. The populations are denoted  $n_+, n_0, n_-$  and with  $n_+ + n_0 + n_- = 1$ . We find the effective decay constant as  $(1 - n_+/6)\Gamma_{21}$  for the case with the same helicity as the MOT beam. The  $n_+$  coefficient is expected to be small compared to the sum of the two other terms. However, even in an extreme case where all sub states are populated equally,  $\Gamma_{21} + \Gamma_{22}$  is effected only by about 5%.

A 881 nm helicity opposite to that of the MOT beam, marked in red color on figure 5.3, will ultimately result in a destruction of the trapping force as the 881 nm laser intensity increases. This effect is expected as a result of destructive reshuffling of the atoms into the "wrong" magnetic sub-states.

If the 881 nm laser is switched on and off, the 285 nm photomultiplier signal from the MOT is modulated. This gives the following expression, where  $S^{on}$  and  $S^{off}$  denotes the photomultiplier signal with the IR laser on and off.

$$\frac{S^{on}}{S^{off}} = \frac{S^{on}}{\rho_{bb}^{off} \Gamma_{bb} N_0} \quad (5.21)$$

$$= \frac{\rho_{bb}^{on}}{\rho_{bb}^{off}} \frac{\alpha^{off}}{\rho_{aa} \left( \gamma \Gamma_{21} + \Gamma_{22} \right) + \alpha^{on}} \quad (5.22)$$

$$= \frac{\alpha^{off} \rho_{bb}^{on} / \rho_{bb}^{off}}{\rho_{aa} \left( \gamma \Gamma_{21} + \Gamma_{22} \right) + \alpha^{off} \frac{\rho_{bb}^{on}}{\rho_{bb}^{off}}} \quad (5.23)$$

where  $\rho_{bb}^{on}$  and  $\rho_{bb}^{off}$  is the density matrix elements for the  $|b\rangle$  state with the 880 nm light on or off, and using that  $\frac{\rho_{bb}^{on}}{\alpha^{on}} = \frac{\rho_{bb}^{off}}{\alpha^{off}}$ .

Assuming that we use circularly polarized IR light, the density matrix element  $\rho_{aa}$  is changing over the area of the MOT due to the Zeeman shift that shifts the resonance in space. The linewidth of the  $^1D_2$  state is only 2 MHz, and the magnetic field results in a shift of the  $^1D_2$  level in the order of 24 MHz over the area of the MOT at a typical coil current of 120 A. The distribution of the density matrix element  $\rho_{aa}$  as a function of IR detuning is a Lorentzian distribution as can be seen in figure 5.4. The distribution of the atoms, each contributing with a part in the total matrix element  $\rho_{aa}$  over the MOT, is Gaussian. The resulting profile is a convolution between a Gaussian and a Lorentzian distribution see equation 5.24. This distribution has to be integrated over, in order to get the weighted density of atoms in the  $^1D_2$  state. The following correction has to be applied to each calculation of  $\rho_{aa}$  to calculate the modified density matrix elements used in equation 5.23.

$$\rho_{aa, \text{ modified}} = \frac{1}{\sqrt{\pi} \nu_0} \int_{-\infty}^{\infty} \frac{b}{(\nu - x_0)^2 + a^2} \exp^{-\left(\frac{\nu - x_0}{\nu_0}\right)^2} d\nu \quad (5.24)$$

With  $2a$  being the full width half maximum (FWHM) of the Lorentzian profile,  $x_0$  being the center of the distribution and  $\nu_0$  the value of the Zeeman shift. The center of the modified distribution is in our case not necessarily the center of the MOT, but may instead be the place of maximum  $\rho_{aa}$ . This point

varies at different detunings, but should remain constant at fixed detunings and varying IR Rabi frequencies. The integration is done over the size of the MOT, which typically is about 1 mm in diameter. Algorithmically the values for  $x_0$  and  $\frac{b}{a^2}$  are found as  $x_0$  is the IR detuning at max  $\rho_{aa}$ , where  $\rho_{aa}(x_0) = \frac{b}{a^2}$ . This enables calculation of  $b$ , as  $a$  is found as the half width at half maximum of the Lorentzian as depicted in figure 5.4.

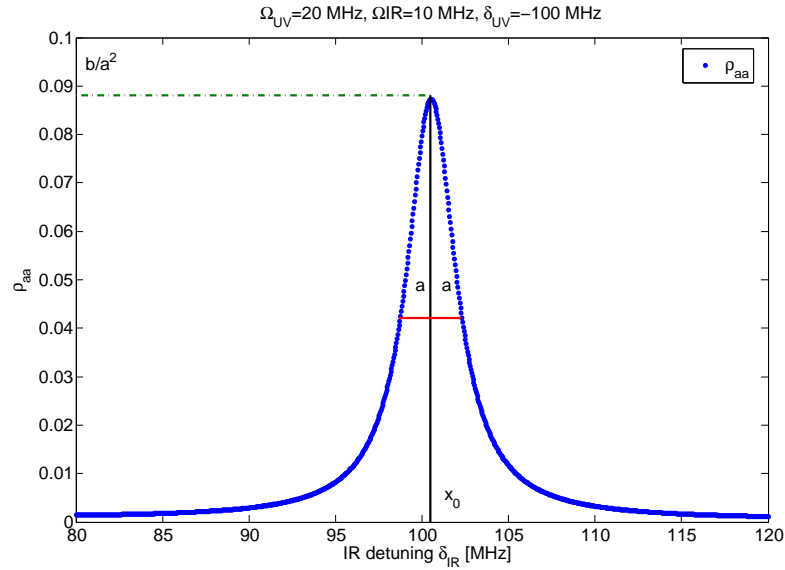


**Figure 5.4:** *The lorentzian profile of  $\rho_{aa}$  as a function of IR detuning. The frequency scale on the x-axis can readily be converted to spatial coordinates, since the field varies linearly in space, over the area of the MOT. It is the values from this kind of plot that are used for the Voigt profile (equation 5.24) describing the distribution over the Zeeman detuning of the MOT, as done in all the calculations.*

Equation 5.23 as a function of the IR Rabi frequency is shown in figure 5.5.

Note that the curve is rather sensitive in the value of  $\Gamma$ . This method of measuring decay rates is simple and robust, as its resolution is practically independent of the number of atoms, and only dependent on the ratio of the photomultiplier signal when the 881 nm laser is on and off.

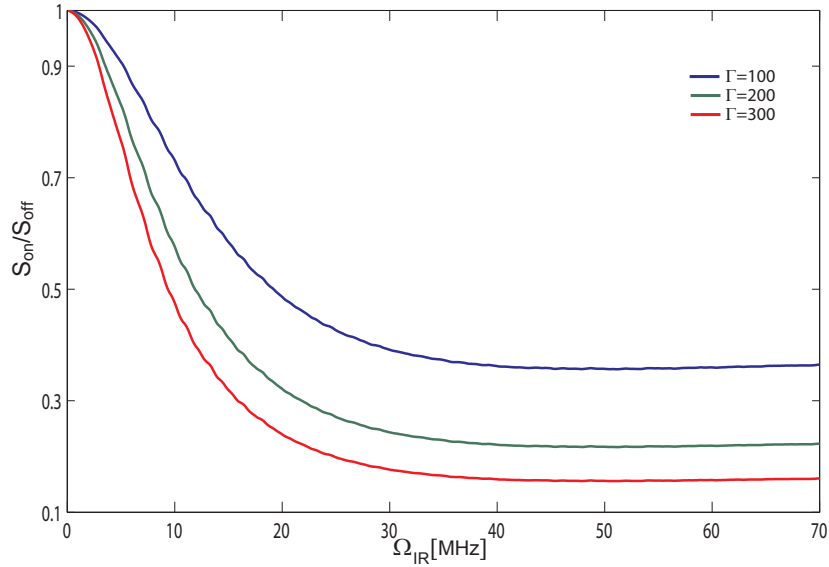


**Figure 5.5:** A simulated set of data points for  $\frac{S_{on}}{S_{off}}$  (equation 5.23), as a function of the IR Rabi frequency ( $\Omega_{IR}$ ) with the MOT loss rate  $\alpha=0.175$  and three different values for  $\Gamma$ .

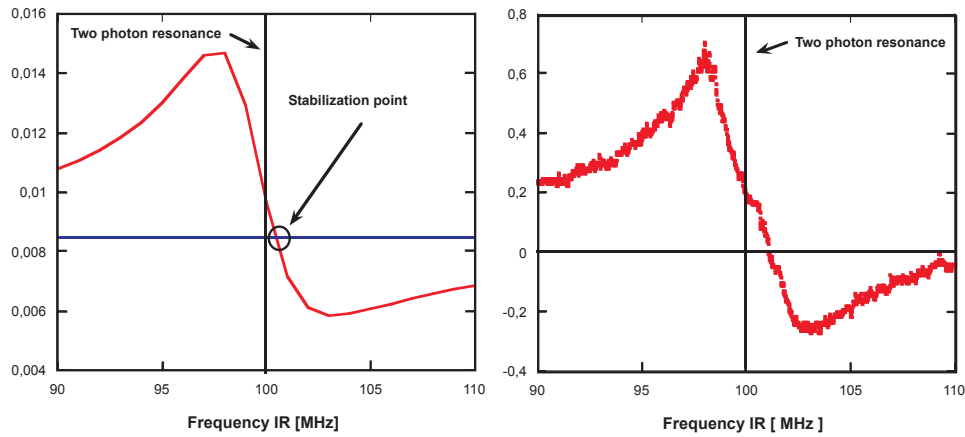


**Figure 5.6:** The 881 nm laser is frequency stabilized to the two photon resonance of the ladder system  $\nu_{881} = -\nu_{285} = 100$  MHz. This ensures a maximal population transfer to the  $(3s3d)^1D_2$ . Left part of the figure shows the  $(3s3p)^1P_1$  excited state fraction obtained from the optical Bloch equations. The right part shows the experimental photomultiplier signal.

### 5.1.3 Experimental Results

The ratio of emitted 285 nm photons, when the IR laser was on and off, was measured, for two circular polarizations and a linear polarization, as described in the following. The 881 nm light is power and frequency controlled by an AOM. A  $\lambda/4$  plate controls the helicity of the light. The presence of the 881 nm light will change the 285 nm light level recorded by the photomultiplier with a 285 nm interference filter in order to make it insensitive to 881 nm photons. This is used to stabilize the 881 nm laser frequency close to the two photon resonance  $\nu_{881} = -\nu_{285} = 100$  MHz during the experiments, see figure 5.6. Increasing the Rabi frequency of the 881 nm light causes a minor change of the lock point. In our power range, this corresponds to about 1 MHz and is not considered important at this level of accuracy.

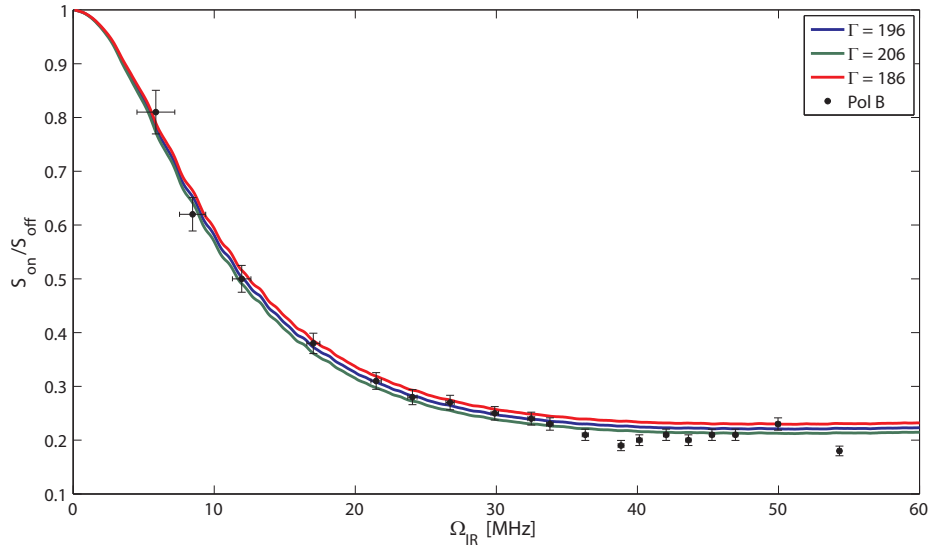


**Figure 5.7:** *Experimental results of the ratios  $\frac{S_{on}}{S_{off}}$  for various values of the IR Rabi frequency and circularly polarized light. Also plotted are the corresponding simulated curves for various values of  $\Gamma$  with  $\delta_{UV} = 100$  MHz,  $\Omega_{UV} = 20$  MHz,  $\alpha = 0.175$ , corresponding to the MOT operating conditions. The vertical errorbars shown are  $\pm 5\%$  and the horizontal errorbars correspond to an uncertainty in determination of the 881 nm power of 0.1 mW.*

The number of emitted 285 nm photons when the IR laser was on and off, respectively, was measured for each of the two circular polarizations states.

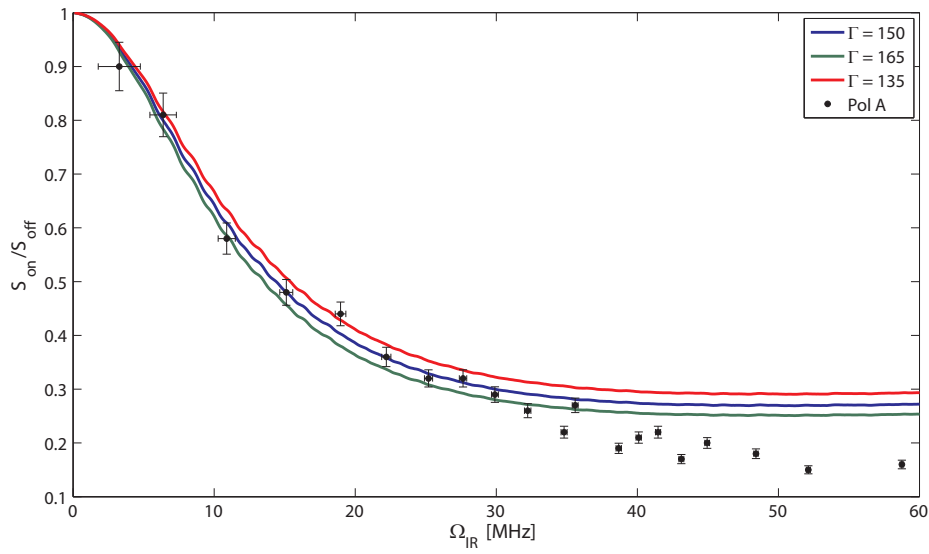


**Figure 5.8:** Experimental results of the ratios  $\frac{S_{\text{on}}}{S_{\text{off}}}$  for various values of the IR Rabi frequency and circularly polarized light. Also plotted are the corresponding simulated curves for various values of  $\Gamma$  with  $\delta_{UV} = 100$  MHz,  $\Omega_{UV} = 20$  MHz,  $\alpha = 0.175$ , corresponding to the MOT operating conditions. The vertical errorbars shown are  $\pm 5\%$  and the horizontal errorbars correspond to a uncertainty in determination of the 881 nm power of 0.1 mW.

The 881 nm light was sent through the AOM, which was modulated with a square wave at 1 kHz, with a duty cycle of 20 %. The photomultiplier signal was measured and averaged over 32 periods with the light on and off, thus providing values for  $S^{on}$  and  $S^{off}$ . At the same time these signals provided a lock of the Ti:Sapphire laser to the two photon resonance, see figure 5.6. This measurement was repeated for different IR intensities (Rabi frequencies), while the MOT was running in steady state mode.

Experimental values for the ratio  $\frac{S^{on}}{S^{off}}$  as a function of the 881 nm Rabi frequency are shown in figures 5.7 and 5.8. As expected, the fraction starts out at 1 and gradually decreases as the Rabi frequency is increased. In figure 5.7, the 881 nm polarization corresponds to the MOT helicity and in figure 5.8 a polarization opposite to the MOT helicity is shown. The solid curves are results from a simulation based on the OBE including the MOT magnetic field. Experiments with this helicity support a value of  $\Gamma_{21} + \Gamma_{22} = (196 \pm 10) \text{ s}^{-1}$  in good agreement with calculations performed in [143], where  $\Gamma_{22} + \Gamma_{21} = (57.3 + 144) \text{ s}^{-1}$ . For the opposite 881 nm polarization (red line in figure 5.3), we observe a reduced decay constant of around  $\Gamma = (150 \pm 15) \text{ s}^{-1}$ . For Rabi frequencies above  $\sim 35 \text{ MHz}$ , a steady decrease of the  $S^{on}/S^{off}$  ratio is observed, which is probably due to a break down in the MOT operation due to destructive reshuffling of the atoms into the "wrong" magnetic sub states from the strongly driven 881 nm transition.

Using values of [143] and the coefficient deduced above, we obtain  $\Gamma = \Gamma_{22} + 2/3\Gamma_{21} = 153 \text{ s}^{-1}$  in favor of the one dimensional model described above. Using the simple one dimensional model for the MOT we find the differential decay constants  $3s3d^1D_2 \rightarrow 3s3p^3P_1$ , and  $3s3d^1D_2 \rightarrow 3s3p^3P_2$  as  $\Gamma_{21} = 138 \text{ s}^{-1}$  and  $\Gamma_{22} = 57 \text{ s}^{-1}$ .

The found decay constant  $\Gamma_{22}$  to the  $^3P_2$  state leads to a load rate in the order of  $10^5 - 10^6$  atoms/s with for the current MOT characteristics. Assuming a magnetic trap lifetime in the order of 20 s this will result in a  $^3P_2$  population of  $10^6 - 10^7$  atoms which is fine starting point for laser cooling on the  $^3P_2 - ^3D_3$  transition. An increased loading rate to the  $^3P_2$  state can be obtained by increasing the MOT loading rate by adding a slowing beam, as described in [113]

#### 5.1.4 Conclusion

In conclusion, we have measured the total spin forbidden decay rate  $3s3d^1D_2 \rightarrow 3s3p^3P_{2,1}$  in  $^{24}\text{Mg}$ . We find a rate of  $\Gamma = (196 \pm 10) \text{ s}^{-1}$  supporting state of the art relativistic many-body calculations [143]. Assuming a simple one dimensional model for the MOT we find the differential decay constants  $3s3d^1D_2 \rightarrow 3s3p^3P_1$ , and  $3s3d^1D_2 \rightarrow 3s3p^3P_2$  as  $\Gamma_{21} = 138 \text{ s}^{-1}$  and  $\Gamma_{22} = 57 \text{ s}^{-1}$  supporting the above mentioned calculations.

## 5.2 Lifetime of the $^3P_1$ State

An accurate method for measuring the lifetime of long-lived metastable magnetic states using a magneto-optical trap (MOT) is demonstrated. Through optical pumping, the metastable  $(3s3p) ^3P_1$  level is populated in a standard MOT. During the optical pumping process, a fraction of the population is captured in the magnetic quadrupole field of the MOT. When the metastable atoms decay to the  $(3s^2) ^1S_0$  ground state they are recaptured into the MOT. In this system, no alternative cascading transition is possible. The lifetime of the metastable level is measured directly as an exponential load time of the MOT. The method has been tested experimentally by measuring the lifetime of the  $(3s3p) ^3P_1$  of  $^{24}\text{Mg}$ . This lifetime has been measured numerous times previously, but with quite different results. Using this method the  $(3s3p) ^3P_1$  lifetime is found to be  $4.4 \pm 0.2$  ms.

### 5.2.1 Introduction

Compared to alkali elements, collision and spectroscopic properties of the alkaline earth elements are less understood. In particular, the lack of high precision radiative data prevents decisive conclusions on new accurate *ab initio* many-body calculations and models for two electron atoms [143]. Pioneering experiments on neutral Ca and Sr have provided new accurate data of the  $^1P_1$ ,  $^3P_1$  and  $^3P_2$  lifetimes down to a 1% level [146,147,148,149]. These methods and the method presented in this paper are to some extent a variation of the well known electron shelving experiments carried out with ions [150,151]. With photoassociation studies, lifetime measurements have greatly improved, yet the results are somewhat model dependent. Here we demonstrate the use of a MOT for precision measurements of long lived magnetic metastable lifetimes, by studying the metastable  $(3s3p) ^3P_1$  state of  $^{24}\text{Mg}$ . For this state we only consider decay to the ground state as the 0.5 mHz transition  $(3s3p) ^3P_1 \rightarrow (3s3p) ^3P_0$  is strongly forbidden and suppressed. The lifetime of the  $(3s3p) ^3P_1$  state has been measured several times, however, the various ex-

perimental results differ significantly, and they range from 4 ms to about 5 ms for the most recent measurement in 1992 [152, 153, 154, 155]. Theoretical calculations support a value in the range 2.8 to 3.6 ms [143], [156, 157, 158], however, not all theories were targeting high precision for this particular lifetime.

### 5.2.2 Theory of the Experiment

In figure 5.9, the relevant energy levels and transitions for our experiment are shown. The 285 nm transition is used for cooling the atoms, while the 457 nm transition is used to populate the metastable  $(3s3p) ^3P_1$  state. Having cooled the atoms close to the Doppler temperature limit of approximately 2 mK, we expose the atoms to a millisecond pulse of 457 nm light. During this pulse, most of the cold ensemble is transferred to the  $(3s3p) ^3P_1$  state. Statistically about 1/3 of these can be transferred into the magnetically trapped  $^3P_1$  state  $|J = 1, m_j = +1\rangle$  and held by the MOT quadrupole magnetic field. Experimentally, we transfer as much as 85 % of the ground state population by aligning the MOT to a point of non-zero magnetic field parallel to the propagation direction of the 457 nm light. In this case, optical pumping with circularly polarized light will only populate one of the magnetic substates  $|J = 1, m_j = \pm 1\rangle$  depending on the helicity of the 457 nm light and the direction of the magnetic field.

To model the system, the optical Bloch equations have been solved for the three level scheme shown in figure 5.9. Special care must be taken in solving the equations numerically as the difference in the two upper state lifetimes differ by about a factor one million. Figure 5.10 displays the calculated 285 nm fluorescence, monitored in the experiment, as a function of time. Part A is normal MOT operation, whereas in part B, the MOT is flashed with the 457 nm pulse, and a steady state population of the  $(3s3p) ^3P_1$  state is prepared. It can be shown that the 285 nm fluorescence during part B decays exponentially [113]. The time constant of this decay is controlled by the Rabi frequencies  $\Omega_1$  and  $\Omega_2$ , as well as the lifetimes of the  $(3s3p) ^1P_1$  and  $(3s3p) ^3P_1$  states, with 2 ns and a few ms, respectively. In principle, this

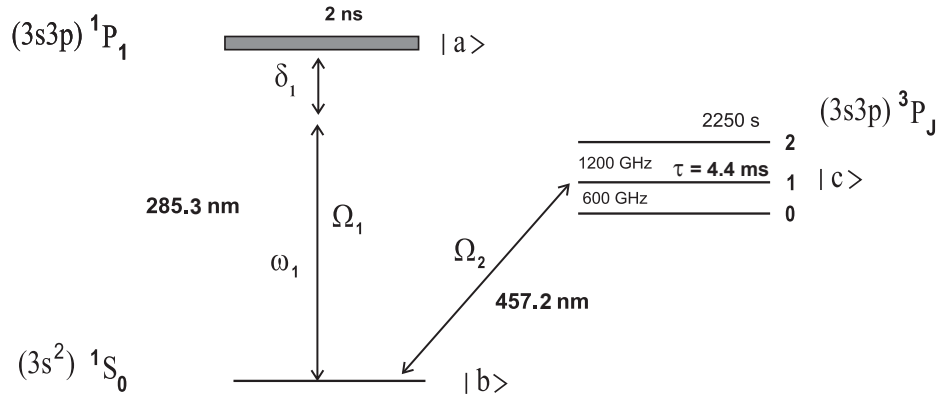


**Figure 5.9:** Energy levels relevant for the lifetime measurement of the metastable  $(3s3p) \ ^3P_1$  state of the  $^{24}\text{Mg}$  isotope. The involved levels are labeled  $|a\rangle$ ,  $|b\rangle$  and  $|c\rangle$  respectively.

may be used to obtain the lifetime of the  $(3s3p) \ ^1P_1$  state as part C yields the metastable lifetime. Determining the lifetime in this way is difficult as it requires precise knowledge of the involved Rabi frequencies, i.e., laser intensities at the MOT region.

In part C of figure 5.10 the 285 nm fluorescence signal rises exponentially according to section 3.3.2

$$S(t) = N_0(1 - e^{-t/\tau}), \quad (5.25)$$

with a time constant  $\tau$  of the  $(3s3p) \ ^3P_1$  lifetime. In the experiment,  $(3s3p) \ ^3P_1$  atoms decaying to the  $(3s^2) \ ^1S_0$  ground state are recaptured in the MOT. Here we monitor them as they emit fluorescence at 285 nm. Three important time scales control the dynamics of the system: the metastable state lifetime of about 4 ms, the MOT lifetime 4 s, and finally the magnetic trap lifetime of more than 20 s. However, the time scale of interest to this experiment is only about 40 ms ( $\sim 10 \cdot \tau$ ), and contributions to the signal from a finite magnetic trap lifetime may safely be disregarded. By including the linear losses from the MOT  $\alpha$  due to collisions with background atoms and photo-ionization [131] etc. (as mentioned in section 3.3.2, higher order

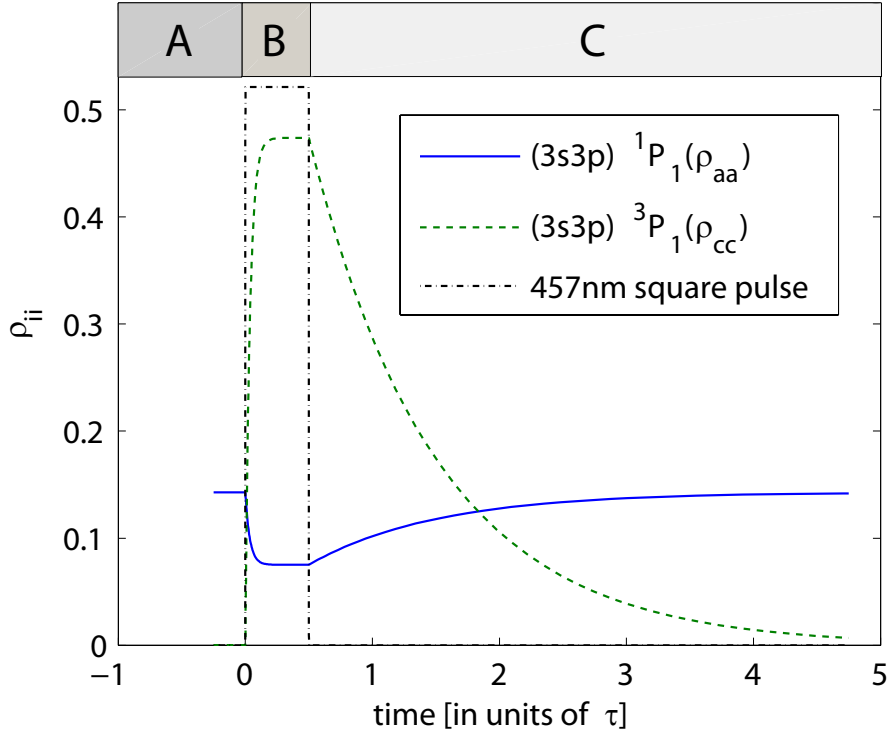


**Figure 5.10:** The number of atoms in the excited  $(3s3p) \ ^1P_1$  ( $\rho_{aa}$ ) and  $(3s3p) \ ^3P_1$  ( $\rho_{cc}$ ) states during the pulsed experiment. Time is in units of  $\tau$ . The signal monitored in our experiment is proportional to the fluorescence determined by  $(\rho_{aa})$ .

terms can be neglected), the following is obtained:

$$\dot{N} = \frac{N_0}{\tau}(e^{-t/\tau}) - \alpha N(t) + L, \quad (5.26)$$

where  $N_0$  is the number of metastable atoms trapped in the magnetic trap, and  $L$  is the load rate from the atomic beam. The solution of equation (5.26) becomes:

$$N(t) = \frac{\gamma_{cc}}{\gamma_{cc} - \alpha} N_0 (e^{-\alpha t} - e^{-\gamma_{cc} t}) + \frac{L}{\alpha} (1 - e^{-\alpha t}) \quad (5.27)$$

with  $\gamma_{cc} = 1/\tau$ . In the case where the atomic beam shutter is blocking the beam, the last term is equal to zero. As  $\gamma_{cc}$  is a factor 1000 larger than

$\alpha$ , linear losses of the magnetic trapped atoms during the time interval of the measurement  $\sim 10 \cdot \tau$  is neglected. For time scales longer than 40 ms this is no longer true as seen in figure 5.12.

### 5.2.3 Experimental setup

The parts of the experimental setup have been described in chapter 3. A standard magneto optical trap is intersected by a circularly polarized 457 nm light beam. The beam is overlapped with a MOT beam in the plane perpendicular to the MOT coil symmetry axis (xy-plane). The 457 nm laser is free running during the experiment (effective linewidth below 1 MHz), and it is tuned to resonance manually by minimizing the 285 nm fluorescence. In free running mode, the 457 nm laser is stable for minutes, however, it is nevertheless tuned before each individual decay experiment. The combined power broadening of 457 nm and the Doppler effect, makes the metastable state easily populated without the need for a narrow-linewidth 457 nm laser. In order to control the pulse of the blue light, the beam is sent through an AOM. The 457 nm beam has a diameter comparable to the MOT (1.5 mm), and it is sent through one of the UV mirrors overlapping the UV beam. Experiments were performed for both a single and a retro-reflected beam, with no detectable difference on the outcome.

The experiment is fully controlled by computer using a sequence program in Labview. Our main parameters for this experiment include: 457 nm pulse time 0.1-5 ms, coil current, corresponding to a magnetic field gradient of 108 gauss/cm - 216 gauss/cm and atomic beam shutter. Just before the blue 457 nm pulse the atomic beam shutter can be closed during period C to prevent loading from the thermal beam source. Due to significantly lower observed lifetimes with the atomic beam on, possibly due to collisions between atoms in the atomic beam and in the  $^3P_1$  state [159, 154], experiments were performed with the atomic beam shutter closed. The experimental sequence can be seen in figure 5.11. Typically,  $10^7$  atoms are captured in the MOT (load rate  $3 \cdot 10^6 \text{ s}^{-1}$ ), with a rms diameter of 1 mm and temperatures from 3-5 mK.

In the experiment, the  $|J = 1, m_j = +1\rangle$  atoms are captured in the MOT

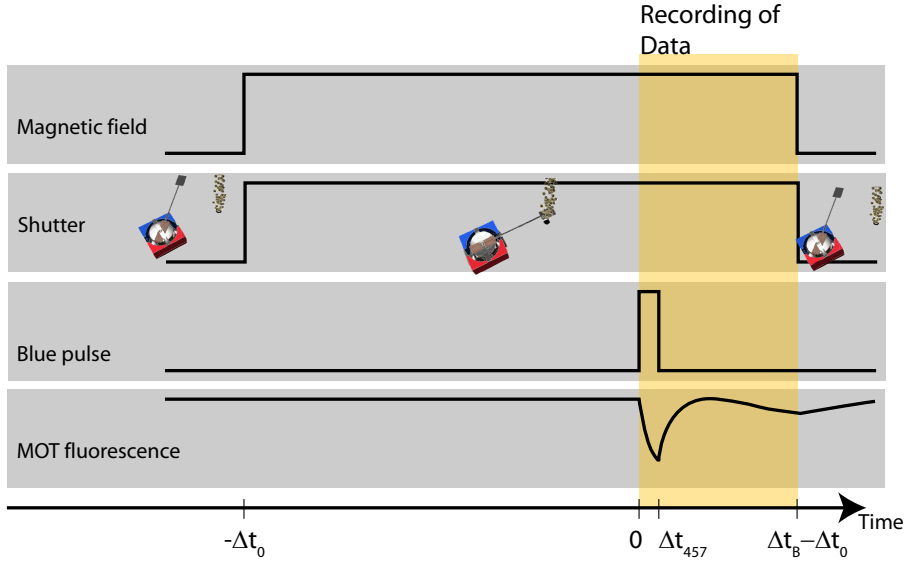


**Figure 5.11:** *Time-line of an experiment. The signals controlling the magnetic field and the shutter are started simultaneously. Due to the response time of the shutter, the blue pulse is not initiated before a few hundred milliseconds after the shutter signal. The time of the pulse, controlling the magnetic field and the shutter, is typically 500 ms, while the blue pulse lasts 0.1 – 5 ms. The time of recording is 100 ms.*

magnetic quadrupole field. The Zeeman energy shift yields  $g_j \mu_B m_j / k_B = 100.8 \mu\text{K}/\text{gauss}$  ( $g_j = 3/2$ ) giving 1.7 mK/mm at 172.8 gauss/cm, which is our typical operating gradient for the MOT on the coil symmetry axis. As the MOT temperature is 3-5 mK and the UV laser beam radius is 3 mm ( $1/e^2$ ), most  $|J = 1, m_j = +1\rangle$  atoms remain trapped within the MOT volume. Different degrees of recapture can be seen in the experiment, due to the alignment of the MOT. Due to the large cooling force for the  $^1S_0 - ^1P_1$  state in Mg, the MOT can be aligned away from the zero of the magnetic field, resulting in a spin polarized sample of atoms and thereby a higher fraction of atoms excited to the  $^3P_1, m_j = +1$  state.

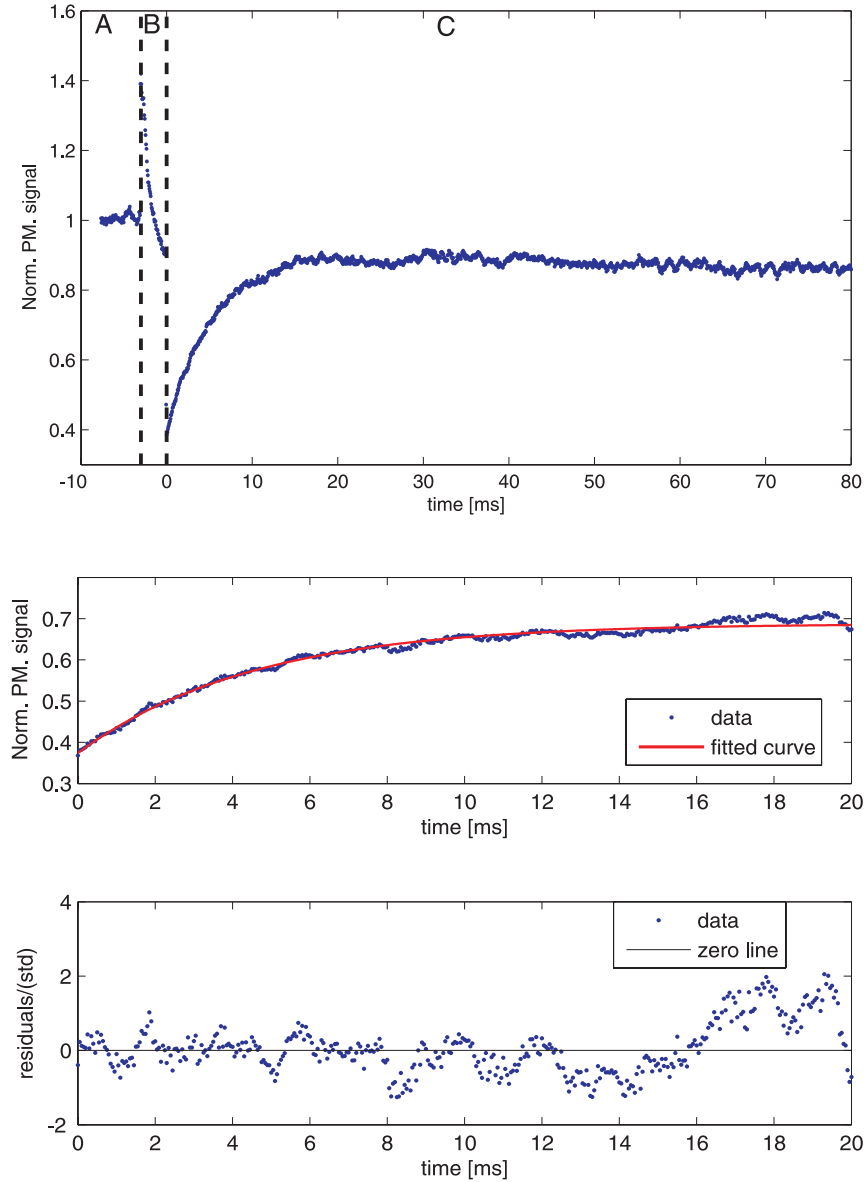


**Figure 5.12:** Typical MOT fluorescence measurement, here normalized to the UV power level. The interval marked with dashed lines show the 457 nm pulse. As the 457 nm light is turned on, additional background photons are observed. After a load period of about 10 ms, the signal slowly decays due to the 4-5 second MOT lifetime. Lower two graphs: the red curve is a fit to equation (5.27), results in a lifetime of 4.4 ms. The lower part shows the residuals of the fit.

### 5.2.4 Experimental Results and Discussion

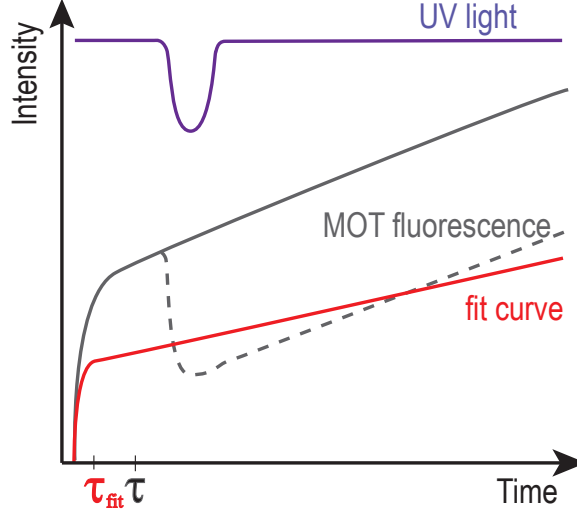
In figure 5.12, a typical experimental result with MOT operation, 457 nm flash, and reload is seen. Small oscillations in the fluorescence signal are visible and are due to a poor servo loop of the UV cavity. To minimize these oscillations, the observed fluorescence signal is divided with a normalizing power signal taken from one of the UV beams. The dashed lines show when the 457 nm pulse is on. During this period, an overall increased signal due to scattered 457 nm photons on vacuum windows etc. not coated for this wavelength is observed. In the reload period, we recover 85% of the atoms. The last 15% may be lost due to imperfect spin polarization of the MOT or due to that the MOT temperature is outside our recapture range. Hot atoms trapped magnetically may decay outside the MOT capture region defined by the laser beams, here 3 mm. Our maximal range is 5.1 mK/mm (2.6 mK/mm perpendicular to the symmetry axis of the coils) which is barely sufficient for a 5 mK MOT temperature. After about 10 ms, a weak decay of the reloaded signal is noticed. This is due to linear loss mechanisms reducing the MOT lifetime to 4-5 s, limited mainly by two photon ionization induced by the 285 nm MOT light. The lifetime of the magnetic trap is estimated to be about 20 seconds at our present background pressure of  $10^{-9}$  mbar.

Figure 5.12, lower panel, shows data from the reload period. The red curve is equation (5.27) fitted to the data giving a lifetime of  $\tau = 4.4$  ms.

A total of 80 measurements were performed at different settings, exploring systematic effects, such as magnetic field gradient, power of the 457 nm pulse, pulse duration and polarizations as well as maximum signal-to-noise ratio and recapture fraction. The experiments turned out to be insensitive to the duration and intensity of the 457 nm pulse. A clear difference could be seen in the recapture fraction when changing the polarization of the 457 nm beam.

The measurements at the maximum field gradient of 216 gauss/cm gave the best signal to noise ratio and only these 34 measurements are used in the quoted lifetime. Our measurements gave a final value of  $(4.4 \pm 0.2)$  ms here quoted with the statistical uncertainty being the standard deviation divided

$\sqrt{N}$ , where  $N=34$ . A standard deviation of 0.9 ms for the 34 measurements, which gives an uncertainty of 0.16 ms, here rounded to 0.2 ms, is found.



**Figure 5.13:** Illustration of the effect of having a drop in intensity of the UV light (violet) after a period of a few lifetimes. When the intensity drops, the MOT fluorescence (gray) drops as well and hereafter stays low (dashed gray), as the loading of the MOT takes the time of the order of  $\alpha^{-1}$  to reload. The fitted curve (red) is affected by this by giving a smaller value for  $\tau_{fit}$  (red) relative to the lifetime (black  $\tau$ ).

Looking at the fit in figure 5.12 middle panel, a better uncertainty than the quoted 0.2 ms is expected. However, shot to shot fluctuations result in a standard deviation of 0.9 ms for the 34 measurements. Noise fluctuations on the same timescale as the lifetime can give shot to shot fluctuations. This could be caused by fluctuations in the laser intensity, as seen in figure 5.13, but we rather believe that this effect is due to the dynamics of the atoms in the trap, which however is indirectly linked to the laser intensity fluctuations. Atoms excited to the  $|J = 1, m_j = +1\rangle$  state experiences an attractive potential, and performs an oscillating motion with a characteristic frequency determined by the gradient of the magnetic field and the initial temperature of the MOT, while atoms in the  $|J = 1, m_j = 0\rangle$  state will expand at constant velocity, and the atoms in the  $|J = 1, m_j = -1\rangle$  state

will be accelerated away from the zero of the magnetic field. The initial temperature of the MOT is sensitive to intensity fluctuations of the laser. Simple 1D numerical simulations of the classical motion of the atoms show, for our setup with an estimated MOT temperature of about 3-5 mK, that shot to shot fluctuations of the temperature and the degree of spin-polarization of the MOT leads to fluctuations in the lifetime [159], see figure 5.14.

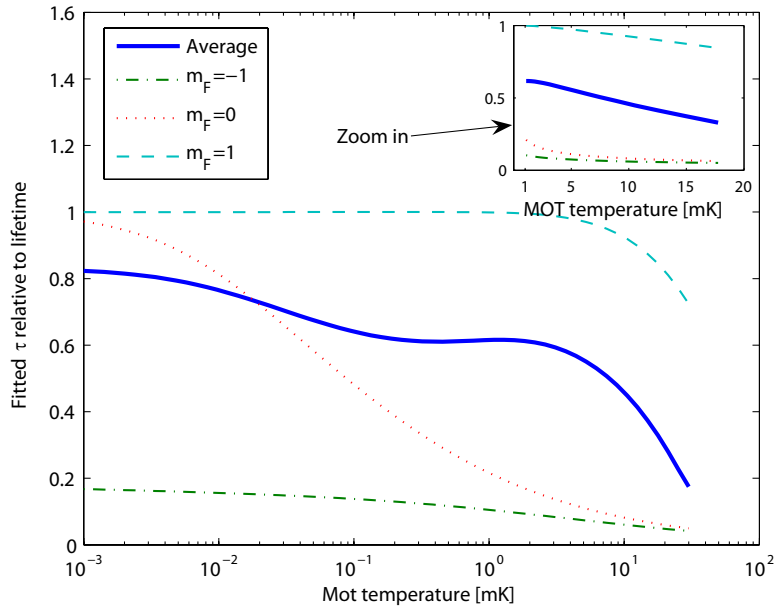


**Figure 5.14:** Plot of the fitted values of the lifetime  $\tau$  relative to the "true" lifetime (here set to 5 ms) based on the 1D simulation of the classical motion of the  $^3P_1$  atoms as a function of the MOT temperature. The inset shows a zoom of the plot on a linear temperature scale [159]. It is seen that both for  $m_F = 0$  and  $m_F = -1$ , the measurements are only about one tenth of the true lifetime. This leads to a measurement of  $\tau$  made on the average signal of the three levels (assuming equal populations of the three magnetic substates), which is still significantly lower than the true lifetime.

Figure 5.14 shows that the accuracy of the lifetime depends strongly on the degree of spin-polarization of the MOT, since only a minor fraction of the atoms in the  $|J = 1, m_j = 0, -1\rangle$  states are recaptured in the MOT. Figure 5.15 shows the dependence of the found value for the lifetime of the magnetic field gradient and indicates that the lifetime tends to be overestimated for

lower magnetic field gradients for highly spin polarized samples, a behavior that is also seen from the experimental data. Therefore the best thing to do experimentally is to have a high recapture fraction, which indicates a highly spin-polarized sample with a low enough temperature to get recaptured, at a high magnetic field gradient. A high recapture fraction also indicates that there was not any severe dips in fluorescence within the time scale of the fit. However, according to the figures 5.14 and 5.15, the measured value for the lifetime must be assumed to be a lower limit. The 34 measurements quoted above are performed at those conditions with an average recapture fraction of 65% and the highest magnetic field gradient achievable at that time<sup>1</sup> of 216 gauss/cm.

In Table 5.2.4, the experimental and theoretical investigations of the  $(3s3p) \ ^3P_1$  lifetime are collected. Experimentally, there is a good agreement between the different methods. The latest experimental value [152] seems somewhat higher compared to the present work, but still overlapping at the one sigma level. More recent theoretical calculations point towards a lower value for the lifetime. The difference seems not to be linked to a particular experimental or theoretical method, but appears as a general trend.

Theoretical			Experimental		
Reference	Year	$\tau$ [ms]	Reference	Year	$\tau$ [ms]
[156]	2004	2.8(1)	This work	2006	4.4(2)
[157]	2002	3.8	[152]	1992	5.3(7)
[143]	2001	3.6	[153]	1982	4.8(8)
[158]	1979	4.60(4)	[154]	1975	4.5(5)
			[155]	1975	4.0(2)

**Table 5.1:** Collection of most recent calculated and measured  $(3s3p) \ ^3P_1$  lifetimes.

Possible errors, which could explain this trend, could be an accidental resonance to other excited states. For the magnesium energy levels, no resonant transitions are present at the half or the double of the 457 nm wavelength.

<sup>1</sup>The coils generating the magnetic field have been changed, since the experiments were performed, to a new set with a gradient approximately 33% higher than the ones used here, see section 3.3.2.

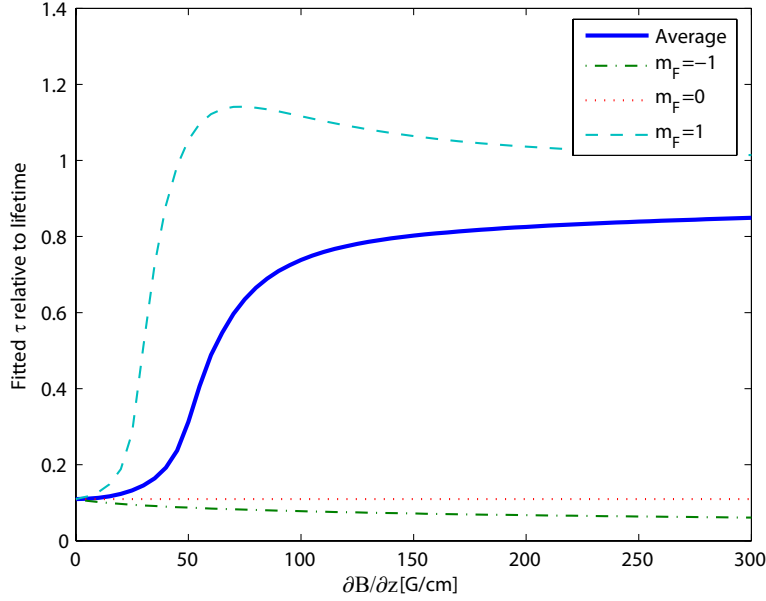


**Figure 5.15:** Plot of the fitted values of  $\tau$  relative to the lifetime as a function of the gradient of the magnetic field for a MOT temperature of 5 mK [159]. It is seen that both for  $m_F = 0$  and  $m_F = -1$ , the measurements are only about one tenth of the true lifetime. This leads to a measurement of  $\tau$  made on the average signal of the three levels, that is still significantly lower than the true lifetime. For  $m_F = 1$ , the measured  $\tau$  is in good agreement with the true lifetime for gradients larger than 200 G/cm.

The closest transitions found are the  $3s4p\ ^1P_1 \rightarrow 3s10d\ ^1D_2$  at 901.6 nm and  $2p^63s^2\ ^1S_0 \rightarrow 3s4p\ ^1P_1$  at 202.6 nm, which both can be ruled out here. Another possible mechanism could be magnetic field induced mixing to nearby P states. Using first order perturbation theory, we write the  $^3P_1$  state in terms of  $^1P_1$  and  $^3P_J$  contributions [160]:

$$|^3P'_1\rangle = \alpha|^3P_0\rangle + \beta|^3P_1\rangle + \gamma|^3P_2\rangle + \delta|^1P_1\rangle \quad (5.28)$$

Evaluating the involved matrix elements gives,  $\alpha = (3/2)^{1/2}\mu_B B/\hbar\Delta_0$ ,  $\beta = 1$ ,  $\gamma = (3/2)^{1/2}\mu_B B/\hbar\Delta_1$  and  $\delta = (6)^{1/2}\mu_B B/\hbar\Delta_2$ . Here  $\Delta_0$  is the energy difference  $^3P_0$ - $^3P_1$ ,  $\Delta_1$  is the energy difference  $^3P_1$ - $^3P_2$  etc,  $\mu_B$  is the Bohr magneton and  $B$  the magnetic field. The  $\Delta$ -values are:  $\Delta_0 = 600$  GHz,  $\Delta_1 = 1200$  GHz and  $\Delta_2 = 395.3$  THz, see figure 5.9. However, our magnetic

field is below 22 gauss within the atom cloud giving coefficients of magnitude  $10^{-4}$  to  $10^{-6}$  and the mixing effect can therefore be neglected here.

### 5.2.5 Conclusion

In conclusion we have measured the metastable 24 magnesium ( $3s3p$ )  $^3P_1$  lifetime using a Magneto-Optical trap by loading the metastable atoms into a magnetic quadrupole trap. The value  $(4.4 \pm 0.2)$  ms is the most accurate to date and in good agreement with recent experimental work on a one sigma level. Theoretically, several recent calculations point towards a significantly lower value and the general discrepancy between theory and experiment is presently not understood.

---

---

## CHAPTER 6

---

# Outlook

### 6.1 Outlook

The work presented in this thesis is a part of the way towards realizing an atomic clock with Mg. Some essential steps further down the road together with an estimate of the performance of a future atomic clock, are presented in the following section.

#### 6.1.1 Determination of the Magic Wavelength

As mentioned in section 2.6, the calculation of the magic wavelength relies on accurate information of the involved atomic states. The calculated value for the  $^3P_0$  magic wavelength is 464 nm. This is a wavelength area where it is difficult to generate high output powers. Before construction of a specific laser system, the position of the magic wavelength can be narrowed down by measuring the light shift at different wavelengths near the presumed position. For this purpose an old Ar-ion laser operated in single line mode at 514 nm, 488 nm and 476 nm can be used. Alternatively, the lifetimes of the  $^1P_1$ ,  $^3S_1$  and  $^3D_1$  could be measured directly, resulting in a better theoretical determination of the magic wavelength. A more accurate determination of the  $^3S_1$  lifetime will together with the information of the isotope shifts and hyperfine coefficients, determined in section 4.1, be of use for astronomical

observations as mentioned in section 1.3.

### 6.1.2 Optical Trapping

There are different routes to obtain a sample of Mg cold atoms in an optical trap. Either the atoms need to be cooled further before being loaded into the optical trap, or one can select the coldest atoms from the MOT and load them into the optical trap.

As mentioned earlier, different approaches such as quench cooling [45] and two-color cooling [97], to cool a sample of Mg atoms below the  $^1S_0 - ^1P_1$  Doppler temperature of 1.9 mK have been tested. Unfortunately, none of these have yet been successful in reducing the temperature below 1 mK.

The atomic drain method, used for Sr in Paris [98], uses repumping lasers overlapped with a cavity enhanced 1D-lattice trapping laser to transfer atoms from the MOT into a dark optically trapped state. A similar technique could be implemented for Mg, where atoms could be transferred to the optically trapped  $^3P_0$  state using the 457 nm intercombination line and repumpers from the  $^3P_{1,2}$  states to either the  $^3S_1$  or the  $^3D_1$  state. Simple calculations taking the geometric overlap and the trap depth into account show that a loading rate of a few percent of the MOT loading rate is achievable, see figure 6.1.

This simple argument shows that it should be possible to obtain loading rates into the dipole trap comparable to those reported in [98] of  $10^5$  atoms/s. A trap depth of 0.5 mK at a beam waist of  $60 \mu\text{m}$  ( $1/e^2$  radius), can be realized with 200 mW laser power in an enhancement cavity with a buildup of a factor 70. In order to achieve this, it is necessary with a build up cavity inside the vacuum chamber which is technically challenging. This procedure would generate a sample of atoms in a 1D-lattice which can be sideband cooled using the intercombination line.

A different approach which can be pursued, is a MOT with metastable atoms like in Ca [161]. Either loaded from a  $^1S_0 - ^1P_1$  MOT, as for Ca, or directly using a metastable source, as described in section 3.2, in combination with a Zeeman slower. There are different options for MOT operation, see

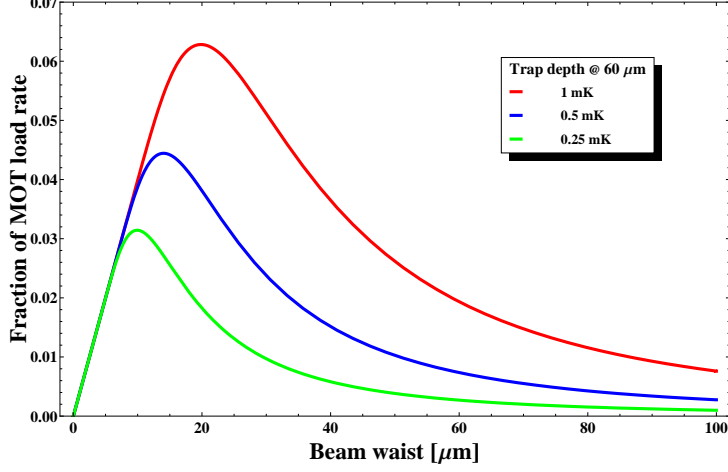


**Figure 6.1:** Load rate into the optical trap given as a fraction of the MOT load rate as a function of beam waist.

Transition	Wavelength [nm]	Linewidth [MHz]	Lifetime [ns]	$I_{sat}$ [mW/cm <sup>2</sup> ]	$T_{Doppler}$ [ $\mu$ K]	$T_{recoil}$ [ $\mu$ K]
$^3P_0 \rightarrow ^3S_1$	516.876	1.8	88.5	1.7	43	2.97
$^3P_1 \rightarrow ^3S_1$	517.413	5.4	29.7	5.1	129	2.96
$^3P_2 \rightarrow ^3S_1$	518.505	8.9	17.8	8.4	214	2.95
$^3P_0 \rightarrow ^3D_1$	383.044	14.3	11.1	33.3	343	5.40
$^3P_1 \rightarrow ^3D_1$	383.339	10.7	14.8	24.9	257	5.39
$^3P_1 \rightarrow ^3D_2$	383.339	19.3	8.3	44.7	462	5.39
$^3P_2 \rightarrow ^3D_1$	383.938	0.7	223.2	1.6	17	5.37
$^3P_2 \rightarrow ^3D_2$	383.938	6.4	24.8	14.8	154	5.37
$^3P_2 \rightarrow ^3D_3$	383.938	25.6	6.2	59.2	615	5.37

**Table 6.1:** Data for the transitions originating from the  $^3P_{0,1,2}$  states.

figure 6.1, but the obvious candidate is the  $^3P_2 - ^3D_3$  transition with a Doppler temperature of 615  $\mu$ K with the possibility of sub-Doppler cooling. Due to non-zero excitation probability to the  $^3D_2$  state, there is a need for repumping on the  $^3P_1 - ^3D_2$  transition in order to close the cooling cycle. A sample of

$^3P_2$  atoms can then be repumped into the  $^3P_0$  state and transferred into an optical trap, ready for probing at the clock transition.

### 6.1.3 Expected Performance of a Mg Atomic Clock

Recently, the optical atomic clocks have improved beyond the performance of the Cs microwave clocks. The recent performances of different atomic clocks are listed in table 6.2. The two parameters characterizing the performance of an optical clock are, as mentioned in section 1.2, the stability and accuracy. The stability is described by equation 1.2 and depends on the transition quality, signal to noise ratio and the probe time to cycling time ratio. For Mg it should be possible to obtain a signal to noise ratio  $\sim 10$  and a cycling time to probe time ratio comparable to what is reported in [41]. The natural linewidth of the  $^1S_0 - ^3P_0$  transition for  $^{25}\text{Mg}$  is  $70 \mu\text{Hz}$  [162], which is significantly narrower than the same transition in  $^{87}\text{Sr}$  (1 mHz), and it denotes the highest obtainable quality factor. However, the effective quality factor obtained depends on the conditions under which the atoms are interrogated and the linewidth of the interrogation laser. The linewidth of the interrogation laser is becoming limiting for the performance of the best atomic clock. For an optical lattice clock a stability as low as  $10^{-17}$  are expected from equation 1.2.

Clock Type	Stability at 1 s	Accuracy
Cs fountain (9.2 GHz) [163]	$3 \cdot 10^{-13}$	$5 \cdot 10^{-16}$
Cs fountain (9.2 GHz) [164]	$1.6 \cdot 10^{-14}$	$4 \cdot 10^{-16}$
Al <sup>+</sup> ion (267 nm) [62]	$3.9 \cdot 10^{-15}$	$2.3 \cdot 10^{-17}$
Hg <sup>+</sup> ion (282 nm) [62]	$3.9 \cdot 10^{-15}$	$1.9 \cdot 10^{-17}$
Yb Lattice clock (578 nm) [165]	$5.5 \cdot 10^{-15}$	$1.5 \cdot 10^{-15}$
Sr Lattice clock (689 nm) [41]	$3 \cdot 10^{-15}$	$1.5 \cdot 10^{-16}$

**Table 6.2:** *Current performances of different types of atomic clocks.*

The current limitation of the Sr atomic clock accuracy is the black body radiation (BBR) shift. On this point, Mg has a clear advantage compared to Sr. In table 6.3, the BBR shifts are listed for different elements, and it is

seen that the expected BBR shift for Mg is an order of magnitude lower than for Sr. The BBR shift is currently the main limitation [41] for the Sr lattice clock, so from that point of view, it should be possible to reach an accuracy below  $10^{-17}$ .

Clock Transition	BBR shift
Hg $^1S_0 - ^3P_0$ (266 nm) [166]	$-1.6 \cdot 10^{-16}$
Mg $^1S_0 - ^3P_0$ (458 nm) [61]	$-3.9 \cdot 10^{-16}$
Yb $^1S_0 - ^3P_0$ (579 nm) [61]	$-2.6 \cdot 10^{-15}$
Sr $^1S_0 - ^3P_0$ (698 nm) [41]	$-5.2 \cdot 10^{-15}$

**Table 6.3:** *Black body radiation shifts.*

The work presented in this thesis represents a step in the way of realizing a sample of ultra cold atoms. A Mg frequency standard in an optical lattice at the magic wavelength has the potential of reaching an accuracy below  $10^{-17}$  and a stability of  $10^{-17}$  at 1 s.



---

## Appendix: Publications

The following publications are produced during this ph.d. and can be seen on the following pages.

- Measurement of the Spin-forbidden Decay rate  $(3s3d)^1D_2 \rightarrow (3s3p)^3P_{2,1}$  in  $^{24}\text{Mg}$   
K. T. Therkildsen, B. B. Jensen, C. P. Ryder, N. Malossi, and J. W. Thomsen  
arXiv:0812.3800v1, accepted for publication in Physical Review A (December 2008).
- Measurement of the  $3s3p\ ^3P_1$  lifetime in magnesium using a magneto-optical trap  
P. L. Hansen, K. T. Therkildsen, N. Malossi, B. B. Jensen, E. D. van Ooijen, A. Bruschi, J. H. Müller, J. Hald, and J. W. Thomsen  
Physical Review A **77**, 062502 (2008).
- Characterization of a magnetic trap by polarization dependent Zeeman spectroscopy  
C.V. Nielsen, J.K. Lyngsø, A. Thorseth, M. Galouzis, K.T. Therkildsen, E.D. van Ooijen, and J.W. Thomsen  
Eur. Phys. J. D **48**, 111119 (2008).
- Amplification and ASE suppression in a polarization-maintaining ytterbium-doped all-solid photonic bandgap fibre  
C. B. Olausson, C. I. Falk, J. K. Lyngsø, B. B. Jensen, K. T. Therkildsen, J. W. Thomsen, K. P. Hansen, A. Bjarklev and J. Broeng  
Optics Express **16**, 13657 (2008).

# Measurement of the Spin-forbidden Decay rate $(3s3d)^1D_2 \rightarrow (3s3p)^3P_{2,1}$ in $^{24}\text{Mg}$

K. T. Therkildsen,\* B. B. Jensen, C. P. Ryder, N. Malossi, and J. W. Thomsen

*The Niels Bohr Institute, Universitetsparken 5, 2100 Copenhagen, Denmark*

(Dated: December 19, 2008)

## Abstract

We have measured the spin-forbidden decay rate from  $(3s3d)^1D_2 \rightarrow (3s3p)^3P_{2,1}$  in  $^{24}\text{Mg}$  atoms trapped in a magneto-optical trap. The total decay rate, summing up both exit channels  $(3s3p)^3P_1$  and  $(3s3p)^3P_2$ , yields  $(200 \pm 10) \text{ s}^{-1}$  in excellent agreement with recent relativistic many-body calculations of [S.G. Porsev et al., Phys. Rev. A. **64**, 012508 (2001)]. The characterization of this decay channel is important as it may limit the performance of quantum optics experiments carried out with this ladder system as well as two-photon cooling experiments currently explored in several groups.

PACS numbers: Valid PACS appear here

---

\*Electronic address: kaspertt@fys.ku.dk

## I. INTRODUCTION

The interest in alkaline earth systems has increased significantly over the past years. One of the main interests in these systems is their applications to high resolution spectroscopy and atomic frequency standards, as they offer very narrow electronic transitions [1]. Another attractive feature of the two-electron systems is their very simple energy level structure, for bosonic isotopes, free of both fine and hyperfine structure. This simple structure opens for detailed comparison between theory and experiment [2]. Recent advances in *ab initio* relativistic many-body calculations of two-electron systems have provided very accurate values for atomic structure and properties such as the electric-dipole transitions of Mg, Ca, and Sr[3]. However, in the case of Mg relatively few experiments have been reported in literature motivating the studies in this Brief Report.

In a series of papers two photon cooling in ladder schemes have been proposed to lower the temperature below the doppler limit of alkaline earth elements [4, 5, 6]. The magnesium and calcium systems are of particular interest since cooling is limited to a few mK. Experimental evidence for two-photon cooling has been established, but the effect is rather modest contrary to theoretical predictions [7, 8]. One important mechanism to take into account in these studies are leaks from the ladder system, limiting the number of atoms that eventually can be cooled.

In this this Brief Report we present the first measurements of the spin forbidden decay from the magnesium  $(3s3d)^1D_2$  state to  $(3s3p)^3P_1$  and  $(3s3p)^3P_2$ . Using atoms trapped in a magneto-optical trap we optically prepare the atoms in the  $(3s3d)^1D_2$  state and measure the decay to  $(3s3p)^3P_{2,1}$  manifold by trap loss measurements. This enables us to deduce the absolute decay rate for these transitions and compare our results to state of the art theoretical calculations.

## II. TRAP LOSS MEASUREMENTS

In figure 1, we show the relevant energy levels and transitions in our experiment. The 285 nm transition is used for cooling and trapping the atoms while the 881 nm transition is used to populate the  $(3s3d)^1D_2$  state. From this state the atoms may decay to the  $(3s3p)^3P_1$

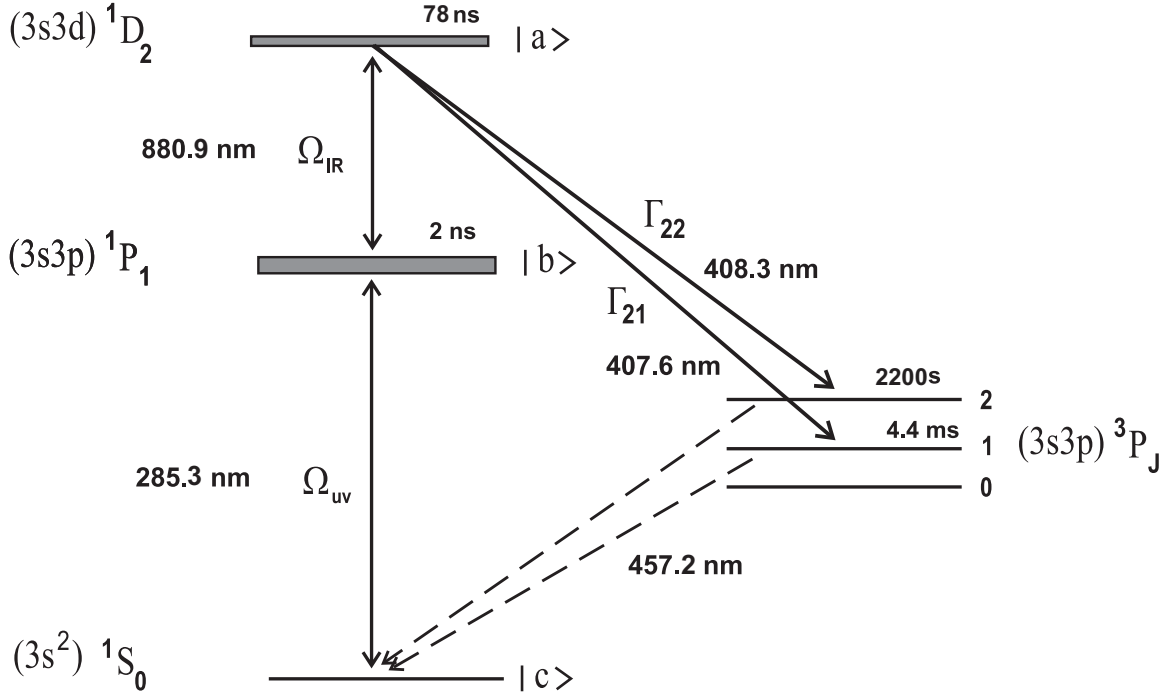


FIG. 1: Energy levels relevant for the  $(3s3d) \ ^1D_2 \rightarrow (3s3p) \ ^3P_{2,1}$  decay measurement in  $^{24}\text{Mg}$ .

state (407.6 nm) with rate  $\Gamma_{21}$  or to the  $(3s3p) \ ^3P_2$  state (408.3 nm) with rate  $\Gamma_{22}$ , or simply back to  $(3s3p) \ ^1P_1$ . By neglecting decay to the  $(3s3p) \ ^3P_0$  state, which is weaker by orders of magnitude, no other decay channels are open. When the 881 nm laser is switched off we express the steady state number of atoms  $N_0$  as the ratio of the load rate to linear losses  $L/\alpha$ . Here we neglect intra-MOT collisions since we are working at relative low atom densities. The equation for the number of atoms trapped in the MOT with 881 nm light present can be written as:

$$\dot{N} = L - \rho_{aa} (\Gamma_{22} + \Gamma_{21})N - \alpha N. \quad (1)$$

Experimentally we determine the total loss rate  $\Gamma_{22} + \Gamma_{21}$ . In our case the linear loss rate  $\alpha$  is dominated by resonant photo-ionization of  $(3s3p) \ ^1P_1$  at 285 nm [9]. Photo-ionization from the  $(3s3d) \ ^1D_2$  level is below 1 Mb and will not be considered here[10]. The steady state becomes

$$N^{on} = \frac{L}{\rho_{aa} (\Gamma_{22} + \Gamma_{21}) + \alpha^{on}}, \quad (2)$$

and

$$N^{off} = \frac{L}{\alpha^{off}}. \quad (3)$$

The ratio of signal with 881 nm turned on and off is proportional to  $\rho_{bb}^{on}$ ,  $\rho_{bb}^{off}$  respectively.

We find finally

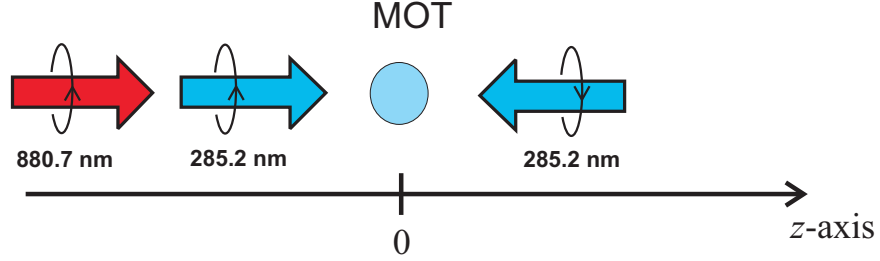
$$\frac{S^{on}}{S^{off}} = \frac{\alpha^{off} \rho_{bb}^{on} / \rho_{bb}^{off}}{\rho_{aa} \left( \Gamma_{21} + \Gamma_{22} \right) + \alpha^{off} \frac{\rho_{bb}^{on}}{\rho_{bb}^{off}}}, \quad (4)$$

as the  $\alpha$ -coefficient is dominated by resonant photo-ionization and thus proportional to the fraction of atoms in the  $(3s3p)^1P_1$  state. So far we assumed that all atoms decaying to the  $(3s3p)^3P_J$  manifold are lost. This is indeed the case for the  $(3s3p)^3P_2$  final states due to their long lifetime exceeding 2200 seconds [11]. On the time scale of the experiment, being only a few seconds, we consider the atoms from this state lost. However, for the  $(3s3p)^3P_1$  states atoms in the  $|J = 1, m_j = +1\rangle$  magnetic sub state will be trapped in the magnetic quadrupole field of the MOT and most likely be recaptured when decaying back to the  $(3s^2)^1S_0$  ground state. Atoms in  $|J = 1, m_j = 0, -1\rangle$  magnetic sub states are expected to be lost since the rms velocity of the trapped atoms exceed 1 m/s leading to a rms travelled distance of more than 5 mm, which is large compared to our MOT beam diameter of only a few mm. The total decay rate will thus be modified to  $\gamma\Gamma_{21} + \Gamma_{22}$ . The actual value of  $\gamma$  depend strongly on the polarization of the 285 nm beam and the 881 nm beam.

If we assume a standard one dimensional model for the MOT we can determine the influence of the constant  $\gamma$ . This is a good approximation as the 881 nm beam is directed along one of the uv MOT beams, but not retro reflected. Consider atoms on the  $-z$  side, see figure 2. These atoms will mainly populate the  $|J = 1, m_j = 0, -1\rangle$  state. Further excitation of the collinear 881 nm laser will drive the atoms to the left (blue line) or right (red line) depending on the helicity of the 881 nm laser. This creates an anisotropy in the decay to the  $(3s3p)^3P_1$  state. Atoms driven along the blue line, i.e., with same polarization helicity as the MOT beams, will only populate non-trapped states. Experiments performed in this configurations is thus insensitive to the re-trapping dynamics as described above. Using the Clebsch Gordan coefficients shown in figure 2 we find the rate  $(1/2 \cdot 1 + 1/2 \cdot (1/2 + 1/2))\Gamma_{21} = \Gamma_{21}$ , as expected. For the opposite polarization we find a reduction  $(1/2 \cdot 1/2 + 1/2 \cdot (2/3 + 1/6))\Gamma_{21} = 2/3\Gamma_{21}$ . We now Consider a more general case where all three magnetic sub states  $|J = 1, m_j = +1, 0, -1\rangle$  are populated. The populations are denoted  $n_+$   $n_0$  and with  $n_+ + n_0 + n_- = 1$ . We find the effective decay constant as  $(1 - n_+/6)\Gamma_{21}$  for MOT polarization. The  $n_+$  coefficient is expected to be small compared to the sum of the two other terms. However, even in an extreme case where all sub states

are populated equally  $\Gamma_{21}$  is effected only by about 5%.

(a)



(b)

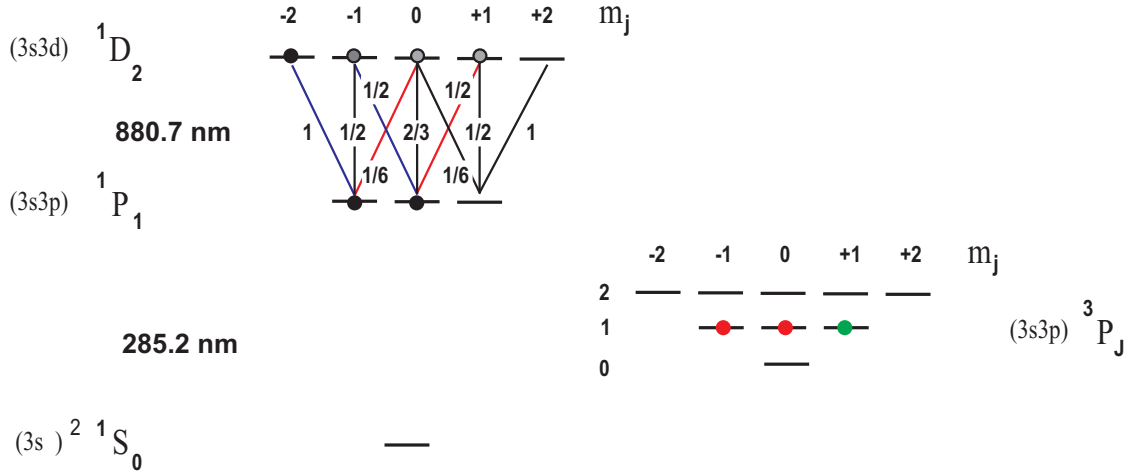


FIG. 2: (color online)(a) Experimentally the 881 nm beam is co-linear with one of the MOT beams. The polarization state can be selected similar to the MOT helicity, as shown in the figure, or opposite. (b) Polarization dependent pumping of atoms in the MOT. Assuming a one dimensional representation of the MOT the 881 nm polarization, represented by blue line (= MOT helicity) or red line, optical pumping will drive the atoms such that anisotropy in the decay rate will emerge. The green dot represents atoms trapped in the MOT quadrupole magnetic field, while red dots represents atoms in non-trapped states. The Clebsch Cordan coefficients shown will also apply to the  $(3s3d) \ ^1D_2 \rightarrow (3s3p) \ ^3P_1$  decay.

With a 881 nm helicity opposite to that of the MOT beam, marked in red color on figure 2, will ultimately result in a destruction of the trapping force as the 881 nm laser intensity increases. This effect is expected as a result of destructive reshuffling of the atoms into "wrong" magnetic sub states.

### III. EXPERIMENTAL SETUP AND RESULTS

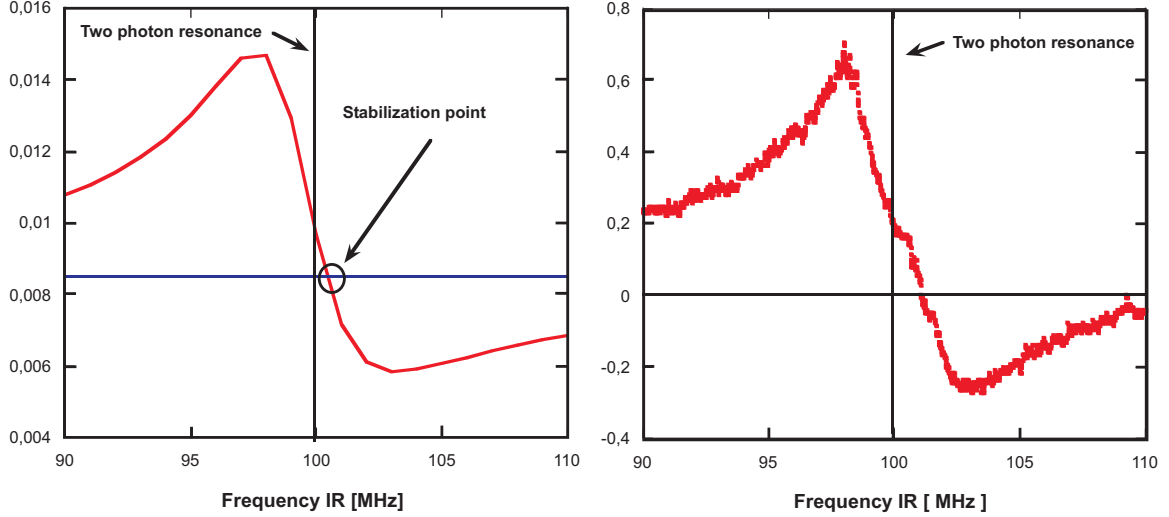


FIG. 3: (color online) The 881 nm laser is frequency locked to the two photon resonance of the ladder system  $\nu_{881} = -\nu_{285} = 100$  MHz. This ensures a maximal transfer of population to the  $(3s3d) \ ^1D_2$ . Left part of the figure shows the  $(3s3p) \ ^1P_1$  excited state fraction obtained from the optical Bloch equations. Right part shows the experimental lock signal.

The main part of the experimental setup has been described in [12]. In our experiment the 285 nm MOT is probed by 881 nm light produced by a Ti:Sapphire laser. The 881 nm light is power and frequency controlled by an AOM. A  $\lambda/4$  plate controls the helicity of the light. Presence of the 881 nm light will change the 285 nm light level recorded by a PM (not sensitive to 881 nm light). This we use to lock the 881 nm laser frequency close to the two photon resonance  $\nu_{881} = -\nu_{285} = 100$  MHz during the experiments, see figure 3. Increasing the rabi frequency of the 881 nm light causes a minor change in the locking point. In our power range this corresponds to about 1 MHz and not considered important at this level of accuracy.

Typically  $10^7$  atoms are captured in the MOT, with a rms diameter of 1 mm and temperatures from 3 to 5 mK. The Doppler cooling limit for the MOT is 2 mK as sub-Doppler cooling is not supported in this system.

The number of emitted 285 nm photons when the IR laser was on and off respectively, was measured for each of the two circular polarizations states. The 881 nm light was sent through the AOM, which was modulated with a square wave at 1 kHz, with a duty cycle

of 20 %. The photomultiplier signal was measured and average over 32 periods with the light respectively on and off, thus providing values for  $S^{on}$  and  $S^{off}$ . At the same time these signals provided a lock of the Ti:S laser to the two photon resonance, see figure 3. This measurement was repeated for different IR intensities (Rabi frequencies), while the MOT was running in steady state mode.

Experimental values for the ratio  $\frac{S^{on}}{S^{off}}$  as a function of the 881 nm Rabi frequency are show in figure 4. As expected the fraction starts out at 1 and gradually decreases as the Rabi frequency is increased. In figure 4 the 881 nm polarization corresponds to the MOT helicity (blue line in figure 2) and polarization opposite to the MOT helicity. The solid curves are results from a simulation based on the optical Bloch equations including the MOT magnetic field. Experiments with this helicity clearly supports a value of  $\Gamma = (200 \pm 10) \text{ s}^{-1}$  in good agreement with calculations performed in [3], where  $\Gamma = \Gamma_{22} + \Gamma_{21} = (57.3 + 144) \text{ s}^{-1}$ . For the opposite 881 nm polarization (red line in figure 2) we observe a reduced decay constant of  $\Gamma = (150 \pm 10) \text{ s}^{-1}$  as substates . Using values of [3] and the coefficient deduced above we obtain  $\Gamma = \Gamma_{22} + 2/3\Gamma_{21} = 153 \text{ s}^{-1}$  in favor of the one dimensional model described above.

#### IV. CONCLUSION

In conclusion we have measured the total spin forbidden decay rate  $(3s3d)^1D_2 \rightarrow (3s3p)^3P_{2,1}$  in  $^{24}\text{Mg}$ . We find a rate of  $\Gamma = (200 \pm 10) \text{ s}^{-1}$  supporting state of the art relativistic many-body calculations. Assuming a simple one dimensional model for the MOT we find the differential decay constants  $(3s3d)^1D_2 \rightarrow (3s3p)^3P_1$ , and  $(3s3d)^1D_2 \rightarrow (3s3p)^3P_2$  as  $\Gamma_{21} = 150 \text{ s}^{-1}$  and  $\Gamma_{22} = 50 \text{ s}^{-1}$  supporting the above mentioned calculations.

#### Acknowledgments

We wish to acknowledge the financial support from the Lundbeck Foundation and the Carlsberg Foundation.

---

[1] T. P. Heavner, S. R. Jefferts, E. A. Donley, J. H. Shirley, T. E. Parker, Metrologia **42**, 411 (2005).

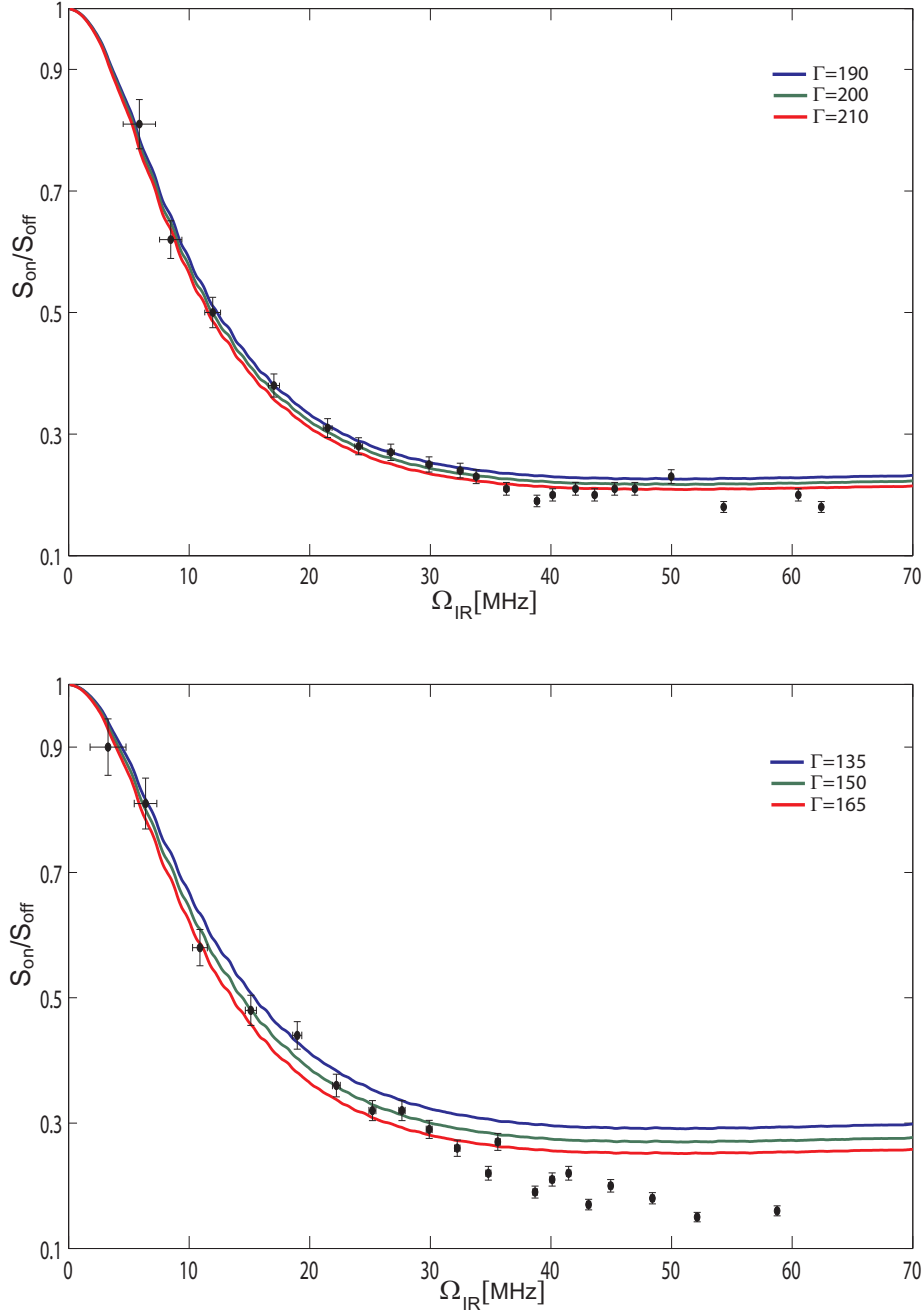


FIG. 4: (color online) Experimental values for the ratio  $\frac{S_{on}}{S_{off}}$  as a function of the 881 nm rabi frequency. (top) Here the circular polarization corresponds to the MOT helicity (blue lines in figure 2). The solid curves are results from a simulations based on the optical Bloch equations, including the magnetic field of the MOT, at different decay constants  $\Gamma = \Gamma_{22} + \Gamma_{21} = 190 \text{ s}^{-1}$ ,  $200 \text{ s}^{-1}$ ,  $210 \text{ s}^{-1}$ . Experiments with this circular helicity supports a value of  $\Gamma = (200 \pm 10) \text{ s}^{-1}$ . (bottom) Experiment with 881 nm polarization opposite to the MOT helicity. At a Rabi frequency of about 30 MHz the MOT is being destroyed by the destructive optical pumping effects of the 881 nm laser. Only data points below 30 MHz should be considered.

- S. Bize et al., J. Phys. B **38**, S449 (2005)
- L. Hollberg et al., J. Phys. B **38**, S469 (2005)
- M. M. Boyd et al., Science **314**, 1430 (2006)
- W. H. Oskay et al., Phys. Rev. Lett. **97**, 020801 (2006)
- [2] Mette Machholm, Paul S. Julienne and Kalle-Antti Suominen. Phys. Rev. A. **59**, R4113 (1999)
- [3] Porsev, S. G. and Kozlov, M. G. and Rakhlina, Yu. G. and Derevianko, A. Physical Review A **64**, 012508 (2001)
- [4] Wictor C. Magno, Reinaldo L. Cavasso Filho, and Flavio C. Cruz. Phys. Rev. A **67**, 043407 (2003)
- [5] Josh W. Dunn, J. W. Thomsen, Chris H. Greene, and Flavio C. Cruz. Phys. Rev. A **76**, 011401 (2007)
- [6] Giovanna Morigi and Ennio Arimondo. Phys. Rev. A **75**, 051404 (2007)
- [7] N. Malossi, S. Damkjr, P. L. Hansen, L. B. Jacobsen, L. Kindt, S. Sauge, J. W. Thomsen, F. C. Cruz, M. Allegrini, and E. Arimondo. Phys. Rev. A **72**, 051403 (2005)
- [8] T. E. Mehlstäubler, K. Moldenhauer, M. Riedmann, N. Rehbein, J. Friebe, E. M. Rasel, and W. Ertmer. Phys. Rev. A **77**, 021402 (2008)
- [9] Madsen D. N. and Thomsen J. W. J. Phys. B **33**, 4981 (2000)
- [10] T. K. Fang and Kozlov, T. N. Chang Physical Review A **61**, 052716 (2000)
- [11] Sergey G. Porsev and Andrei Derevianko. Phys. Rev. A **69**, 042506 (2004)
- [12] Loo F. Y., Bruschi A., Sauge S., Allegrini M., Arimondo E., Andersen N., Thomsen J. W. J. Opt. B: Quantum Semiclass. Opt. **6**, 81 (2004)

# Measurement of the $3s3p\ ^3P_1$ lifetime in magnesium using a magneto-optical trap

P. L. Hansen,<sup>1</sup> K. T. Therkildsen,<sup>1</sup> N. Malossi,<sup>1</sup> B. B. Jensen,<sup>1</sup> E. D. van Ooijen,<sup>1</sup> A. Bruschi,<sup>1</sup> J. H. Müller,<sup>1</sup> J. Hald,<sup>2</sup> and J. W. Thomsen<sup>1,\*</sup>

<sup>1</sup>The Niels Bohr Institute, Universitetsparken 5, 2100 Copenhagen, Denmark

<sup>2</sup>Danish Fundamental Metrology, Ltd., Matematiktorvet 307, DK-2800 Lyngby, Denmark

(Received 30 October 2007; published 2 June 2008)

We demonstrate an accurate method for measuring the lifetime of long-lived metastable magnetic states using a magneto-optical trap (MOT). Through optical pumping, the metastable  $(3s3p)\ ^3P_1$  level is populated in a standard MOT. During the optical pumping process, a fraction of the population is captured in the magnetic quadrupole field of the MOT. When the metastable atoms decay to the  $(3s^2)\ ^1S_0$  ground state they are recaptured into the MOT. In this system no alternative cascading transition is possible. The lifetime of the metastable level is measured directly as an exponential load time of the MOT. We have experimentally tested our method by measuring the lifetime of the  $(3s3p)\ ^3P_1$  of  $^{24}\text{Mg}$ . This lifetime has been measured numerous times previously, but with quite different results. Using our method we find the  $(3s3p)\ ^3P_1$  lifetime to be  $(4.4 \pm 0.2)$  ms. Theoretical values point toward a lower value for the lifetime.

DOI: 10.1103/PhysRevA.77.062502

PACS number(s): 32.70.Jz, 78.20.Ls, 32.70.Cs, 37.10.De

## I. INTRODUCTION

In many spectroscopic experiments, beam line and cell measurements have played an important role, however, the workhorse of today is atom traps such as the magneto-optical trap (MOT), magnetic traps or various types of dipole traps. In these traps large numbers of atoms or molecules ( $10^9$ – $10^{12}$ ) can be stored with lifetimes exceeding 300 s at submilli-K temperatures [1–7]. Following this development a large amount of new high precision spectroscopic data on atoms and molecules has emerged. Parallel to these achievements theory has been developing new accurate models of atoms and molecules and single species and mixed species [8,9].

Compared to alkali elements collision and spectroscopic properties of the alkaline earth elements are less understood. In particular the lack of high precision radiative data prevents decisive conclusions on new accurate *ab initio* many-body calculations and models for two electron atoms [10]. Pioneering experiments on neutral Ca and Sr have provided new accurate data of the  $^1P_1$ ,  $^3P_1$ , and  $^3P_2$  lifetimes down to a 1% level [11–14]. These methods and the method presented in this paper are to some extent a variation of the well-known electron shelving experiments carried out with ions [15,16]. With photoassociation studies, lifetime measurements have greatly improved, yet the results are somewhat model dependent. Here we demonstrate the use a MOT for precision measurements of long-lived magnetic metastable lifetimes, by studying the metastable  $(3s3p)\ ^3P_1$  state of  $^{24}\text{Mg}$ . For this state we only consider decay to the ground state as the 0.5 mHz transition  $(3s3p)\ ^3P_1 \rightarrow (3s3p)\ ^3P_0$  is strongly forbidden and suppressed. The lifetime of the  $(3s3p)\ ^3P_1$  state has been measured several times, however, the various experimental results differ significantly and range from 4 ms to about 5 ms for the most recent measurement in 1992 [17–20]. Theoretical calculations support a value in the range 2.8 to 3.6 ms [10,21–23], however, not all theories were targeting high precision for this particular lifetime.

## II. THEORY OF MEASUREMENT

In Fig. 1, we show the relevant energy levels and transi-

tions for our experiment. The 285 nm transition is used for cooling the atoms, while the 457 nm transition is used to populate the metastable  $(3s3p)\ ^3P_1$  state. Having cooled the atoms close to the Doppler temperature limit of approximately 2 mK, we expose the atoms to a millisecond pulse of 457 nm light. During this pulse most of the cold ensemble is transferred to the  $(3s3p)\ ^3P_1$  state. Statistically about 1/3 of these can be transferred into the magnetically trapped  $^3P_1$  state  $|J=1, m_j=+1\rangle$  and held by the MOT quadrupole magnetic field. Experimentally, we transfer as much as 85% of the ground state by aligning the MOT to a point of nonzero magnetic field parallel to the propagation direction of the 457 nm. In this case optical pumping with circularly polarized light will only populate one of the magnetic substates  $|J=1, m_j=\pm 1\rangle$  depending on the helicity of the 457 nm light and the direction of the magnetic field.

To model our system we have solved the optical Bloch equations for the three level scheme shown in Fig. 1. Special care must be taken in solving the equations numerically as the difference in the two upper state lifetimes differ by about a factor of 1000000. Figure 2 displays the calculated 285 nm fluorescence, monitored in the experiment, as a function of time. In Fig. 2(A) we have normal MOT operation, whereas in Fig. 2(B) we flash the MOT with the 457 nm pulse, and prepare a steady state population in the  $(3s3p)\ ^3P_1$  state. It

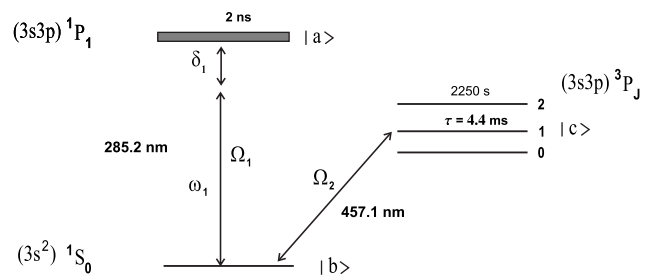


FIG. 1. Energy levels relevant for the lifetime measurement of the metastable  $(3s3p)\ ^3P_1$  state of the 24 magnesium isotope. The involved levels are labeled  $|a\rangle$ ,  $|b\rangle$ , and  $|c\rangle$  respectively.

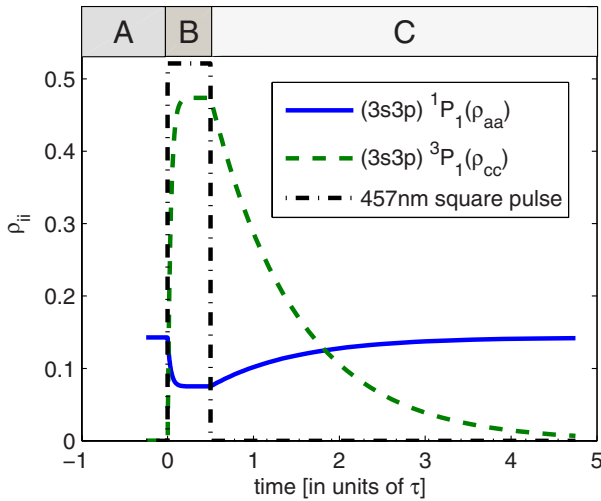


FIG. 2. (Color online) The number of atoms in the excited  $(3s3p) \ ^1P_1 (\rho_{aa})$  and  $(3s3p) \ ^3P_1 (\rho_{cc})$  states during the pulsed experiment. Time is in units of  $\tau$ . The signal monitored in our experiment is proportional to the fluorescence determined by  $(\rho_{aa})$ .

can be shown that the 285 nm fluorescence in Fig. 2(B) decays exponentially. The time constant of this decay is controlled by the Rabi frequencies  $\Omega_1$  and  $\Omega_2$  as well as the lifetimes of the  $(3s3p) \ ^1P_1$  and  $(3s3p) \ ^3P_1$  states, with 2 ns and a few ms, respectively. In principle this may be used to obtain the lifetime of the  $(3s3p) \ ^1P_1$  state as Fig. 2(C) yields the metastable lifetime. Practically determining the lifetime in this way is difficult as it requires precise knowledge of the involved Rabi frequencies, i.e., laser intensities at the MOT region.

In Fig. 2(C) the 285 nm fluorescence signal rises exponentially according to

$$S(t) = N_0(1 - e^{-t/\tau}), \quad (1)$$

with a time constant of the metastable lifetime  $\tau$ . In the experiment  $(3s3p) \ ^3P_1$  atoms decaying to the  $(3s^2) \ ^1S_0$  ground state are recaptured in the MOT. Here we monitor them as they emit fluorescence at 285 nm. Three important time scales control the dynamics of the system, the metastable state lifetime of about 4 ms, the MOT lifetime 4 s and finally the magnetic trap lifetime of more than 20 s. However, the time scale of interest to this experiment is only about 40 ms ( $\sim 10\tau$ ), and contributions to the signal from a finite magnetic trap lifetime may safely be disregarded. By including the linear losses from the MOT due to collisions with background atoms, photoionization [24], etc., here described by  $\alpha$ , we obtain

$$\dot{N} = \frac{N_0}{\tau}(e^{-t/\tau}) - \alpha N(t), \quad (2)$$

where  $N_0$  is the number of metastable atoms trapped in the magnetic trap. The solution of Eq. (2) becomes

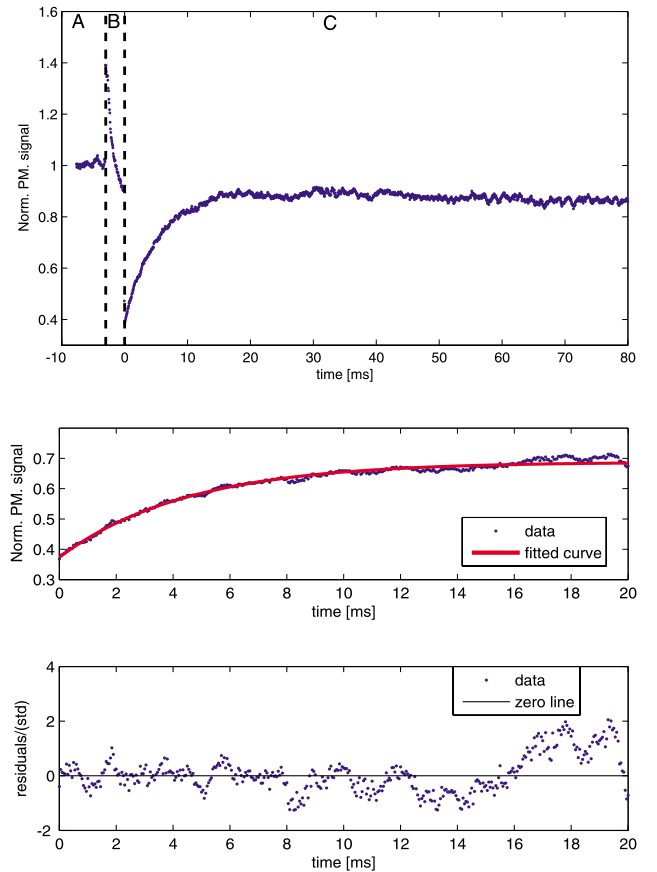


FIG. 3. (Color online) Typical MOT fluorescence measurement, here normalized to the uv power level. The interval marked with dashed lines show the 457 nm pulse. As the 457 nm light is turned on additional background photons are observed. After a load period of about 10 ms the signal is slowly decays due to the 4–5 s MOT lifetime. Lower two graphs: the red curve is a fit to Eq. (3), giving 4.4 ms. The lower part shows the residuals of the fit.

$$N(t) = \frac{\gamma_{cc}}{\gamma_{cc} - \alpha} N_0 (e^{-\alpha t} - e^{-\gamma_{cc} t}), \quad (3)$$

with  $\gamma_{cc} = 1/\tau$ . As  $\gamma_{cc}$  is a factor 1000 larger than  $\alpha$  we neglect linear losses of the magnetic trapped atoms during the time interval of the measurement  $\sim 10\tau$ . For time scales longer than 40 ms this is no longer true as seen in Fig. 3.

### III. EXPERIMENTAL SETUP

The main part of the experimental setup has been described in Ref. [25]. A standard magneto-optical trap is intersected by a circularly polarized 457 nm light beam. The beam is overlapped with a MOT beam in the plane perpendicular to the MOT coil symmetry axis. An amplified 914 nm diode is used for generation of 457 nm light by frequency doubling in  $\text{KNbO}_3$  in a standard four mirror cavity [26]. The 914 nm diode is antireflection coated with feedback from an external grating in a Littrow configuration, and it provides an output of approximately 40 mW. The amplifier consist of an AR coated broad-area laser diode (BAL). Normally we have

about 350 mW output from the 914 nm system and 125 mW of 457 nm light. The 457 nm laser is free running during the experiment (effective linewidth 1 MHz) and is tuned to resonance manually by minimizing the 285 nm fluorescence. In free running mode the 457 nm laser is stable for minutes, however, it is nevertheless tuned before each individual decay experiment. The combined power broadening of 457 and 285 nm transitions, added with the Doppler effect, makes the metastable state easily populated without the need for a narrow-linewidth 457 nm laser. In order to control the pulse of the blue light, the beam is sent through an AOM. The 457 nm beam has a diameter comparable to the UV beams (1.5 mm) used for the MOT and is sent through one of the UV mirrors overlapping the UV beam. Experiments were performed for both a single and a retro reflected beam, with no detectable difference on the outcome.

The experiment is fully controlled by computer using a sequence program in LABVIEW. Our main parameters for this experiment include: 457 nm pulse time 0.1–5 ms, coil current 100–200 A, corresponding to a coil symmetry gradient of 108–216 Gauss/cm. Just before the blue 457 nm pulse is sent we close the atomic beam shutter which remains closed during period  $C$  to prevent loading from the thermal beam source. Typically  $10^7$  atoms are captured in the MOT (load rate  $3 \times 10^6\ \text{s}^{-1}$ ), with a rms diameter of 1 mm and temperatures from 3–5 mK. The Doppler cooling limit for the MOT is 2 mK as sub-Doppler cooling is not supported in this system.

In our experiment, the  $|J=1, m_j=+1\rangle$  atoms are captured in the MOT magnetic quadrupole field. The Zeeman energy shift yields  $g_j \mu_B m_j / k_B = 100.8\ \mu\text{K}/\text{Gauss}$  ( $g_j=3/2$ ) giving 1.7 mK/mm at 172.8 Gauss/cm, our typical operating gradient on the coil symmetry axis. As the MOT temperature is 3–5 mK and the laser beam diameter a 3 mm ( $1/e^2$ ), most  $|J=1, m_j=+1\rangle$  atoms remain trapped within the MOT volume.

#### IV. EXPERIMENTAL RESULTS AND DISCUSSION

In Fig. 3 we present a typical experimental result with MOT operation, 457 nm flash, and reload clearly visible. Small oscillations in the fluorescence signal are visible and are due to a poor servo loop of the UV cavity. To minimize these oscillations we divide the observed fluorescence signal with a normalizing power signal taken from one of the uv beams. The dashed lines show when the 457 nm pulse is on. During this period we observe an overall increased signal due to scattered 457 nm photons on vacuum windows, etc., not being coated for this wavelength. In the reload period we recover 85% of the atoms. The last 15% may be lost due to imperfect polarization of the 457 nm light or possibly if the MOT temperature is outside our recapture range. Hot atoms trapped magnetically may decay outside the MOT capture region defined by the laser beams, here 3 mm. Our maximal range is 5.1 mK/mm (2.6 mK/mm perpendicular to the symmetry axis of the coils) and barely sufficient for a 5 mK MOT temperature. After about 10 ms we notice a weak decay of the reloaded signal. This is due to linear loss mechanisms reducing the MOT lifetime to 4–5 s, limited mainly by

two photon ionization induced by the 285 nm MOT light. The lifetime of the magnetic trap is estimated to be about 20 s at our present background pressure of  $10^{-9}$  mbar.

Figure 3, lower panel shows data from the reload period. The red curve is Eq. (3) fitted to the data giving  $\tau=4.4$  ms. A total of 80 measurements were taken at different settings, exploring systematic effects (magnetic field gradient, power of the 457 nm pulse, pulse duration and polarizations) and maximum signal-to-noise ratio and recapture fraction. The measurements at maximum field gradient 200 Gauss/cm gave the best signal to noise ratio and only these 34 measurements are used in the quoted lifetime. Our measurements gave a final value of  $(4.4 \pm 0.2)$  ms here quoted with the statistical uncertainty being the standard deviation divided  $\sqrt{N}$ ,  $N=34$ . We found the standard deviation of 0.9 ms for the 34 measurements and thus an uncertainty of 0.16 ms, here rounded to 0.2 ms.

Looking at the fit in Fig. 3 middle panel, we would expect a better uncertainty than the quoted 0.2 ms. However, noise fluctuations on the same time scale as the lifetime will give shot to shot fluctuations. This could be caused by fluctuations in the laser intensity, but we rather attribute this effect to the dynamics of the atoms in the trap, however, indirectly linked to the laser intensity fluctuations. Atoms exited to  $|J=1, m_j=+1\rangle$  state, experiencing an attractive potential, would perform an oscillating motion with a characteristic frequency determined by the gradient of the magnetic field and the initial temperature of the MOT. The latter is sensitive to intensity fluctuation of the laser. Simple 1D numerical simulations show, that for our setup with an estimated MOT temperature of about 3–5 mK corresponding to a mean velocity of close to 2 m/s, this would induce oscillations in the observed fluorescence peaking on time scales close to the lifetime. The amplitude of the oscillations is proportional to the number of atoms in the  $|J=1, m_j=+1\rangle$ , which explains why these oscillations are not observed at times much later than the lifetime. Improving the uv intensity stability by a lock, servoed using, e.g., an AOM, could to some extent lower the MOT temperature to improve the accuracy of the measurements.

In Table I we have collected experimental and theoretical investigations of the  $(3s3p)\ ^3P_1$  lifetime. Experimentally, there is a good agreement between the different methods. The latest experimental value [17] seems somewhat higher compared to the present work, but still overlapping at the  $1\sigma$  level. More recent theoretical calculations point toward a lower value for the lifetime. The difference seems not to be linked to a particular experimental or theoretical method, but appear as a general trend. Possible errors could be caused by accidental resonance to other excited states. For the magnesium energy levels no resonant transitions is present at half or double of the 457 nm wavelength. Closest we find  $3s4p\ ^1P_1 \rightarrow 3s10d\ ^1D_2$  at 901.6 nm and  $2p^63s^2\ ^1S_0 \rightarrow 3s4p\ ^1P_1$  at 202.6 nm which both can be ruled out here. Another possible mechanism could be magnetic field induced mixing to near by  $P$  states. Using first order perturbation theory we write the  $^3P_1$  state in terms of  $^1P_1$  and  $^3P_J$  contributions [27]

TABLE I. Collection of most recent calculated and measured ( $3s3p$ )  $^3P_1$  lifetimes.

Theoretical			Experimental		
Reference	Year	$\tau$ [ms]	Reference	Year	$\tau$ [ms]
[21]	2004	2.8(1)	This work	2006	4.4(2)
[22]	2002	3.8	[17]	1992	5.3(7)
[10]	2001	3.6	[18]	1982	4.8(8)
[23]	1979	4.60(4)	[19]	1975	4.5(5)
			[20]	1975	4.0(2)

$$|{}^3P_1'\rangle = \alpha|{}^3P_0\rangle + \beta|{}^3P_1\rangle + \gamma|{}^3P_2\rangle + \delta|{}^1P_1\rangle. \quad (4)$$

Evaluating the involved matrix elements gives  $\alpha = (3/2)^{1/2} \mu_B B / \hbar \Delta_0$ ,  $\beta = 1$ ,  $\gamma = (3/2)^{1/2} \mu_B B / \hbar \Delta_1$ , and  $\delta = (6)^{1/2} \mu_B B / \hbar \Delta_3$ . Here  $\Delta_0$  is the energy difference  ${}^3P_0 - {}^3P_1$ ,  $\Delta_1$  is the energy difference  ${}^3P_1 - {}^3P_2$ , etc,  $\mu_B$  is the Bohr magneton and  $B$  the magnetic field. The  $\Delta$  values are  $\Delta_0 = 600$  GHz,  $\Delta_1 = 1200$  GHz, and  $\Delta_2 = 395.3$  THz, see Fig. 1. However, our magnetic field is below 22 Gauss within the atom cloud giving coefficients of magnitude  $10^{-8}$  to  $10^{-10}$  and the mixing effect can be neglected here.

## V. CONCLUSION

In conclusion we have measured the metastable II4 magnesium ( $3s3p$ )  $^3P_1$  lifetime using a magneto-optical trap by

loading the metastable atoms into a magnetic quadrupole trap. Our value ( $4.4 \pm 0.2$ ) ms is the most accurate to date and in good agreement with recent experimental work on an  $1\sigma$  level. Theoretically, several recent calculations point toward a significantly lower value and the general discrepancy between theory and experiment is presently not understood.

## ACKNOWLEDGMENTS

We would like to thank Gretchen K Campbell for stimulating discussions and for a careful reading of the manuscript. We wish to acknowledge the financial support from the Lundbeck Foundation and the Carlsberg Foundation.

- 
- [1] R. Grimm, M. Weidemuller, and Y. B. Ovchinnikov, *Adv. At., Mol., Opt. Phys.* **42**, 95 (2000).
- [2] J. Doyle, B. Friedrich, R. V. Krems, and F. Masnou-Seeuws, *Eur. Phys. J. D* **31**, 149 (2004).
- [3] J. D. Weinstein, R. deCarvalho, T. Guillet, Br. Friedrich, and J. M. Doyle, *Nature (London)* **395**, 921 (1998).
- [4] D. Egorov, W. C. Campbell, B. Friedrich, S. E. Maxwell, E. Tsikata, L. D. van Buuren, and J. M. Doyle, *Eur. Phys. J. D* **31**, 307 (2004).
- [5] S. V. Nguyen, S. Doret, C. B. Connolly, R. A. Michniak, W. Ketterle, and J. Doyle, *Phys. Rev. A* **72**, 060703(R) (2005).
- [6] H. L. Bethlem, G. Berden, and G. Meijer, *Phys. Rev. Lett.* **83**, 1558 (1999).
- [7] K. M. R. van der Stam, E. D. van Ooijen, R. Meppelink, J. M. Vogels, and P. van der Straten, *Rev. Sci. Instrum.* **78**, 013102 (2007).
- [8] J. Weiner, V. S. Bagnato, S. Zilio, and P. S. Julienne, *Rev. Mod. Phys.* **71**, 1 (1999).
- [9] K. M. Jones, E. Tiesinga, P. D. Lett, and P. S. Julienne, *Rev. Mod. Phys.* **78**, 1041 (2006).
- [10] S. G. Porsev, M. G. Kozlov, Yu. G. Rakhlina, and A. Derevianko, *Phys. Rev. A* **64**, 012508 (2001).
- [11] G. Zinner, T. Binnewies, F. Riehle, and E. Tiemann, *Phys. Rev. Lett.* **85**, 2292 (2000).
- [12] M. Yasuda and H. Katori, *Phys. Rev. Lett.* **92**, 153004 (2004).
- [13] P. G. Mickelson, Y. N. Martinez, A. D. Saenz, S. B. Nagel, Y. C. Chen, T. C. Killian, P. Pellegrini, and R. Cote, *Phys. Rev. Lett.* **95**, 223002 (2005).
- [14] T. Zelevinsky, M. M. Boyd, A. D. Ludlow, T. Ido, J. Ye, R. Ciurylo, P. Naidon, and P. S. Julienne, *Phys. Rev. Lett.* **96**, 203201 (2006).
- [15] W. Nagourney, J. Sandberg, and H. Dehmelt, *Phys. Rev. Lett.* **56**, 2797 (1986).
- [16] J. C. Bergquist, R. G. Hulet, W. M. Itano, and D. J. Wineland, *Phys. Rev. Lett.* **57**, 1699 (1986).
- [17] A. Godone and C. Novero, *Phys. Rev. A* **45**, 1717 (1992).
- [18] H. S. Kwong, P. L. Smith, and W. H. Parkinson, *Phys. Rev. A* **25**, 2629 (1982).
- [19] P. S. Furcinitti, J. J. Wright, and L. C. Balling, *Phys. Rev. A* **12**, 1123 (1975).
- [20] C. J. Mitchell, *J. Phys. B* **8**, 25 (1975).
- [21] R. Santra, K. V. Christ, and C. H. Greene, *Phys. Rev. A* **69**, 042510 (2004).
- [22] I. M. Savukov and W. R. Johnson, *Phys. Rev. A* **65**, 042503 (2002).
- [23] C. Laughlin and G. A. Victor, *Astrophys. J.* **234**, 407 (1979).
- [24] D. N. Madsen and J. W. Thomsen, *J. Phys. B* **33**, 4981 (2000).
- [25] F. Y. Loo, A. Bruschi, S. Sauge, M. Allegrini, E. Arimondo, N. Andersen, and J. W. Thomsen, *J. Opt. B: Quantum Semiclassical Opt.* **6**, 81 (2004).
- [26] V. Ruseva and J. Hald, *Appl. Opt.* **42**, 5500 (2003).
- [27] I. I. Sobelman, *Atomic Spectra and Radiative Transitions* (Springer-Verlag, Berlin, 1992).

# Characterization of a magnetic trap by polarization dependent Zeeman spectroscopy

C.V. Nielsen, J.K. Lyngsø, A. Thorseth, M. Galouzis, K.T. Therkildsen, E.D. van Ooijen, and J.W. Thomsen<sup>a</sup>

The Niels Bohr Institute, Universitetsparken 5, 2100 Copenhagen, Denmark

Received 18 July 2007 / Received in final form 18 January 2008

Published online 18 April 2008 – © EDP Sciences, Società Italiana di Fisica, Springer-Verlag 2008

**Abstract.** This paper demonstrates a detailed experimental study of our cloverleaf magnetic trap for sodium atoms. By using polarization dependent Zeeman spectroscopy of our atomic beam, passing the magnetic trap region, we have determined important trap parameters such as gradients, their curvatures and corresponding trap frequencies. Experimental findings are compared to theoretical calculations as well as complementary methods of characterizing the trap.

**PACS.** 32.60.+i Zeeman and Stark effects – 42.30.-d Imaging and optical processing – 07.55.Ge Magnetometers for magnetic field measurements

## 1 Introduction

The interest in cooling and magnetic trapping of neutral atoms and molecules has accelerated significantly during the past ten years. The workhorse in most cases is the magneto-optical trap (MOT) [1], in which atoms can be cooled and confined to a temperature of typically 100  $\mu$ K at densities of the order of  $10^{11}$   $\text{cm}^{-3}$ . The temperature is mainly limited by photon rescattering [2] and therefore other trapping and cooling schemes must be used to circumvent this problem. Most commonly used techniques are optical dipole trapping [3,4] or magnetic trapping. In the latter case, one exploits the interaction between the permanent dipole moment of paramagnetic atoms or molecules with a magnetic field gradient. Several coil geometries have been developed to generate a magnetic field with a local minimum, like a TOP trap [5], Quick trap [6], Baseball trap and a Ioffe-Pritchard trap [7]. All these traps possess a non-zero magnetic field minimum,  $B_0$ , to prevent Majorana losses [8].

Atoms trapped in such magnetic traps (low field seekers) can be cooled further by applying evaporative cooling techniques [9,10]. Here the most energetic atoms are removed by spin-flipping to a high-field seeking state by applying a resonant radio frequency field. The remaining atoms rethermalize to lower temperatures.

For optimal transfer from MOT to magnetic trap and for optimizing the process of forced evaporation [5], where the radio frequency field is continuously lowered with a certain rate, it is desirable to know trapping parameters such as the magnetic field gradient and  $B_0$ . Furthermore, at low temperatures and high densities, where degeneracy

is reached, it is essential to know the trapping frequencies in order to determine important experimental parameters such as the critical temperature ( $T_c$ ).

Measuring the magnetic field with Hall probes is usually performed, but as the actual trap region to be analyzed is in vacuum and relatively small, *in situ* characterization with this method is difficult. Numerical calculation of the coil geometry can easily be performed at high accuracy, but do not account for possible defects in the field caused by magnetized elements, possible short-cuts between windings, changes in geometry, etc.

The motivation of this work was the need for a fast and accurate determination of the trap parameters. Previous work on magnetic field cartography have been done using the mechanical Hanle effect [11]. However, this method lacks spatial resolution and works best at low magnetic fields. A more sophisticated method of measuring magnetic fields with high sensitivity and resolution have been demonstrated using imaging of Bose-Einstein condensed atoms [12,13]. Our method follows suggestions put forward in Courteille et al. [14], which presents a fast and accurate determination of the trap parameters prior to Bose-Einstein condensation. In this paper we present a detailed experimental investigation of our magnetic cloverleaf trap for sodium atoms. Essentially, we image the polarization dependent fluorescence of thermal atoms passing the magnetic trap monitored by a thin sheet of near resonant light. Experimental findings are compared to the theory presented in [14] and to complementary experimental methods of obtaining trap parameters.

The paper is organized as follows. A short introduction of the experimental setup is given, where the properties of the magnetic trap is emphasized. Subsequently, the polarization dependent Zeeman spectroscopy method

<sup>a</sup> e-mail: jwt@fys.ku.dk

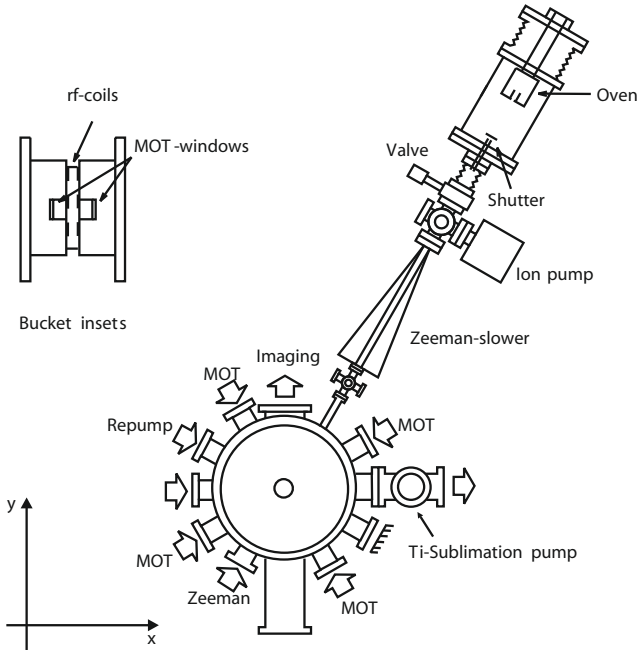


**Fig. 1.** Schematic overview of the experimental apparatus used for cooling sodium atoms.

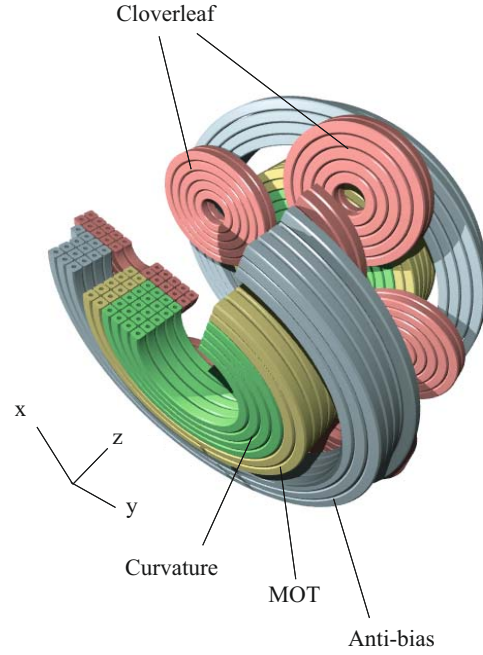


**Fig. 2.** (Color online) Coil configuration of the clover leaf magnetic trap.

is introduced and the experimental results are compared with complementary methods and discussed. In the final section we conclude on the method described in this paper.

## 2 Experimental setup

Figure 1 shows a schematic drawing of the setup used to cool and trap sodium atoms [15]. The oven produces a sodium beam with an average velocity of  $\sim 900$  m/s and a flux of  $\sim 10^{12}$  s $^{-1}$ . For cooling experiments, a fraction of the atoms are slowed using a Zeeman slower to  $\sim 30$  m/s and captured in the magneto-optical trap (MOT), where  $\sim 1.2 \times 10^9$  atoms are trapped at a temperature around  $200 \mu\text{K}$ . One third of the atoms are in the low field seeking state and can be transferred to the magnetic trap, where evaporative cooling is applied. The lifetime of the atoms in the trap is  $\sim 70$  s, where the vacuum in the trapping region is roughly  $3 \times 10^{-11}$  mbar. With our magnetic trap we have recently achieved BEC of  $\sim 5 \times 10^5$  sodium atoms.

For magnetic trapping we use a cloverleaf trap [16], which is a Ioffe-Pritchard like trap (Fig. 2). This kind of trap allows full  $360^\circ$  optical access, while the close distance between the sets of coils (25 mm) provides relatively high magnetic field gradients. The coils are wound using rectangular copper tubes with cooling water going through and operated with a current of 400 A through the cloverleaf coils and 344 A through the pinch and anti-bias coils.

The magnetic field close to the center is given by:

$$\mathbf{B}(x, y, z) = B_0 \begin{pmatrix} 0 \\ 0 \\ 1 \end{pmatrix} + B'_\rho \begin{pmatrix} x \\ -y \\ 0 \end{pmatrix} + \frac{B''_z}{2} \begin{pmatrix} -xz \\ -yz \\ z^2 - \frac{1}{2}(x^2 + y^2) \end{pmatrix}. \quad (1)$$

The trap is characterized by the three parameters  $B_0$ ,  $B'_\rho$  and  $B''_z$ . The trap shape can be altered from cigar shaped to spherical by adjusting the bias field  $B_0$ . When  $B_0$  is small the trap gives the tightest confinement. This magnetic field gives rise to a trapping potential that is proportional with the magnetic field strength  $|\mathbf{B}(x, y, z)|$ . To the lowest order in the coordinates the magnetic field strength is given by:

$$B(x, y, z) = \sqrt{(B'_\rho)^2(x^2 + y^2) + (B_0 + \frac{1}{2}B''_z z^2)^2}. \quad (2)$$

In the tight cigar mode (small  $B_0$ ) the trap has two regimes, depending on the temperature of the trapped atoms. In the high temperature regime ( $k_B T \gg \frac{1}{2}\mu_B B_0$ ) the magnetic field is given by

$$B(x, y, z) \approx \sqrt{B'_\rho{}^2(x^2 + y^2) + \left(\frac{1}{2}B''_z z^2\right)^2} + B_0, \quad (3)$$

where  $k_B$  is Boltzmann's constant and  $\mu_B$  the Bohr magneton. The trap is then dominantly linear in the radial directions and harmonic in the axial direction. In the low

temperature regime ( $k_B T \ll \frac{1}{2} \mu_B B_0$ ) the magnetic field is approximated by:

$$B(x, y, z) \approx \frac{1}{2} B''_\rho \rho^2 + \frac{1}{2} B''_z z^2 + B_0. \quad (4)$$

Here, the trap is harmonic in both the axial and the radial directions and the potential is given by a three dimensional anisotropic harmonic potential with an axial curvature proportional to  $B''_z$  and a radial curvature proportional to  $B''_\rho$ , where

$$B''_\rho \approx \frac{B'_\rho{}^2}{B_0}. \quad (5)$$

The trap characteristics are conveniently expressed in the form of trap frequencies (assuming trapping in the  $|1, -1\rangle$  state):

$$\omega_z^2 = \frac{\mu_B}{2m} B''_z, \quad \omega_\rho^2 = \frac{\mu_B}{2m} \frac{B'_\rho{}^2}{B_0}. \quad (6)$$

for the longitudinal and radial direction, respectively.

Both the minimum of the magnetic field ( $B_0$ ) and the curvature of the trap in the radial direction can be controlled with the current through the anti-bias coils. The latter is used to optimize the mode matching when transferring the MOT atoms to the magnetic trap for maximal phase-space overlap after which the trap is compressed until  $B_0$  is around 2 Gauss. The current is provided by power supplies (Delta SM15-400) with an accuracy of  $10^{-4}$  and the coil current can be switched off fast ( $\sim 300 \mu\text{s}$ ) for quick release of the trapped atoms enabling, e.g., temperature measurements.

### 3 Polarization dependent Zeeman spectroscopy

The basic idea of the method is to probe the thermal atoms by a polarized near resonant sheet of light. Polarization sensitive fluorescence measurements allow for hyperfine state selective mapping of the energy levels in the  $(x, z)$  plane, where the equipotential lines of the trap are imaged. Energy levels are converted into magnetic field values  $B(x, z)$  using a general calculated Zeeman shift as a function of the  $B$ -field. To obtain a Doppler-free signal the light sheet is directed perpendicular to the atomic beam. Polarization of the sheet laser is circular right/left or linear parallel or perpendicular to the atomic beam, see Figure 3. For analysis we use a linear polarizer in front of a CCD camera.

#### 3.1 Experimental conditions

In the experiments involving the tomography only a thermal beam is used. The laser light used is generated by a ring dye laser (Coherent 899-21), pumped by a Coherent Verdi V-8 solid state laser. The frequency of the light is

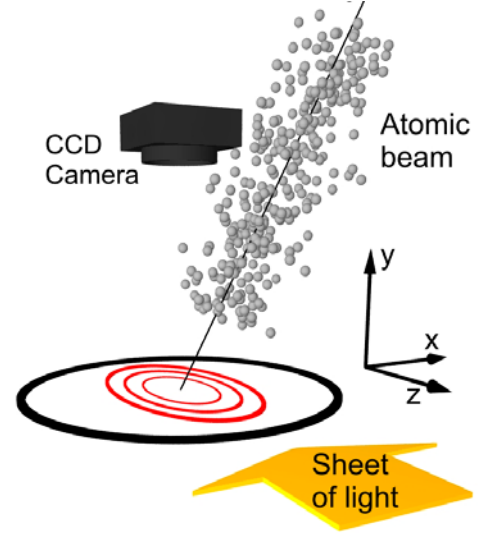


**Fig. 3.** (Color online) Schematic of the tomography experiment showing the equipotential lines of the trap (red) and the sheet of light in the  $x-z$  plane (detection plane). The atomic beam enters at a 30 degree angle with the  $y$ -axis. For analysis a linear polarizer is used parallel or perpendicular to the light sheet direction.

locked to the  $F = 2 \rightarrow F' = 3$  transition using saturation spectroscopy. The detuning with respect to this transition can be controlled several hundreds MHz by double passed AOM's. The light is guided to the setup by use of optical fibers and is expanded by a telescope to a beam diameter of 20 mm and finally directed through a 0.5 mm slit. The sheet of light ( $2 \text{ mW/cm}^2$ ) is launched in the  $x-z$  plane of the setup (see Figs. 1, 3) and crosses the center of the trap perpendicular to the thermal atomic beam. The obtained fluorescence is imaged on a CCD-camera (Prosilica, EC1380) after passing a linear polarizer.

The measurements described in this section are all performed with the fully compressed trap, with detunings between  $-180 \text{ MHz}$  and  $-50 \text{ MHz}$  (with respect to the  $|2, 2\rangle \rightarrow |3, 3\rangle$  transition at zero magnetic field) and magnetic fields between 40 G and 130 G.

#### 3.2 Basic principle of the experiment

The magnetic field will change the resonance condition of the atom due to the Zeeman effect. For a given state (labeled by  $i$ ) of the atom, the frequency shift  $\delta_i$  of this state is:

$$\delta_i = \mu_i B(\mathbf{r}), \quad (7)$$

where  $\mu_i$  is the magnetic moment<sup>1</sup>. This means that for a specific atomic transition and a specific detuning of the laser beam, the atoms are resonant at a specific magnetic field magnitude. By imaging the fluorescence, we can directly relate  $B$ -field magnitude and position, and when

<sup>1</sup> Notice that we have assumed adiabatic following of the magnetic field, which is well justified even for a thermal beam except for the center of the trap.

changing the laser detuning, we can map out different equipotential lines of the magnetic trap.

For a maximal magnetic field gradient of approximately 250 G/cm the adiabatic condition:

$$\omega_L \gg \frac{1}{B} \frac{dB}{dt}, \quad (8)$$

is satisfied with the thermal beam in the region of the trap, with  $\omega_L$  the Larmor-frequency. Furthermore, the Rabi-frequency (typically 20 MHz) is small compared to the Larmor-frequency (few GHz), which means that the atoms will align according to the local magnetic field lines. This makes it a good candidate as the quantization axis. Because the atoms are imaged from the  $y$ -direction perpendicular to pump light vector  $\mathbf{k}$ , all the light collected by the camera is assumed to originate from spontaneous emission. Unless otherwise noted the pump light is linear polarized along  $\hat{\mathbf{e}} = \hat{\mathbf{x}}$ .

A prerequisite of the method is the precise knowledge of the frequency shift as a function of magnetic field. This is addressed theoretically in next section.

## 4 Theoretical model

This section describes the theoretical model used to analyze the tomography data. In contrast to the work of Courteille et al we have put up a multilevel model adapted for the measurements presented here. The model has two steps: the basic calculation of the energy shift of the energy levels and transitions involved in analysis. The second step, models the relative strengths of the different transitions. We can thus determine which transitions are significant and furthermore the emitted fluorescence intensity can be modelled accurately.

### 4.1 Energy calculations

Energy levels in the presence of a magnetic field, as in the magnetic trap, can be calculated by diagonalizing the Hamiltonian:

$$\hat{H} = \hat{H}_0 + \left(\frac{\mu_B}{\hbar}\right) B_z (\hat{L}_z + 2\hat{S}_z) - g_I \left(\frac{\mu_N}{\hbar}\right) B_z \hat{I}_z, \quad (9)$$

where  $\hat{H}_0$  describes the isolated atom. The nuclear interaction with the magnetic field is vanishing in our case and has been neglected in the calculations. The effect of the applied magnetic field is to mix  $|F, m_F\rangle$  — states of different  $F$ , meaning that  $F$  is a good quantum number only at low magnetic fields. However, the interaction conserves the  $F_z$  component and thus only states of same  $m_F$  will mix. Consequently, the selection rule  $\Delta m_F = 0, \pm 1$  still holds. Therefore the possible transition frequencies may be calculated and the result is shown in Figure 4.

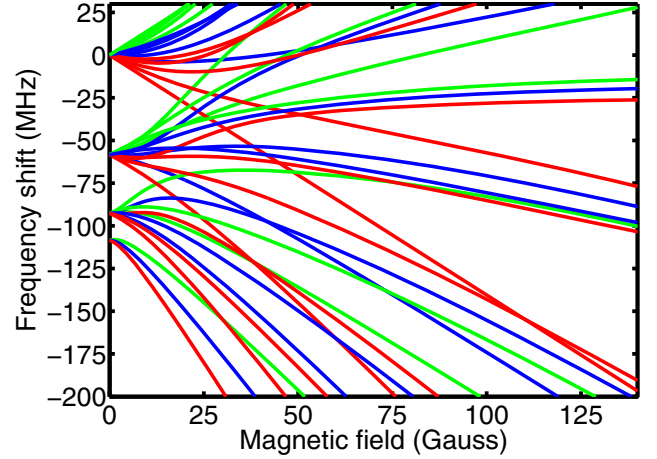


**Fig. 4.** (Color online) Frequency shifts of allowed transitions from the  $F = 2$  ground state to the excited manifold calculated from equation (9). Frequencies are relative to the  $F = 2 \rightarrow F' = 3$  transition at zero magnetic field. Colors represent the helicity of the transition: green ( $\sigma^+$ ), blue ( $\pi$ ), red ( $\sigma^-$ ).

### 4.2 Transition strengths

The complicated structure presented in Figure 4 is not fully adapted for analysis of measurements. Below we calculate the strength of each transition as a function of magnetic field. Later we combine those and the energy shift calculations in a simple model well suited for analysis of data.

Since the effect of the magnetic field is to mix states of different  $F$ , we will still use the  $|F, m_F\rangle$  — basis to describe the new eigenstates. We name the eigenstates  $|\psi_{F_0, m_{F_0}}\rangle$  of  $\hat{H}$  according to their original state at low magnetic fields and expand the states  $|\psi_{F_0, m_{F_0}}\rangle = \sum_F c_{F, m_{F_0}}(B) |F, m_{F_0}\rangle$  on the appropriate basis. Here  $c_{F, m_{F_0}}(B)$  are the field-dependent expansion coefficients determined by the diagonalization of  $\hat{H}$ . For a specific transition,  $\alpha = \{F'_0, m'_{F_0}, F_0, m_{F_0}\}$ , the absorption cross section is given by:

$$\sigma_\alpha = \frac{2\omega_0}{c\epsilon_0\Gamma\hbar} |\hat{\mathbf{e}} \cdot \mathbf{d}_\alpha|^2, \quad (10)$$

where  $\hat{\mathbf{e}}$  is a unit polarization vector. The dipole matrix elements in the presence of the magnetic field is easily described in terms of the matrix elements at zero magnetic field by:

$$\begin{aligned} \langle \psi_{F'_0, m'_{F_0}} | \hat{\mathbf{d}} | \psi_{F_0, m_{F_0}} \rangle &= \sum_{F, F'} c_{F', m'_{F_0}}(B)^* c_{F, m_{F_0}}(B) \\ &\times \langle F', m'_{F_0} | \hat{\mathbf{d}} | F, m_{F_0} \rangle. \end{aligned} \quad (11)$$

In turn, the matrix elements at zero magnetic field are evaluated in terms of the relevant Clebsch-Gordan

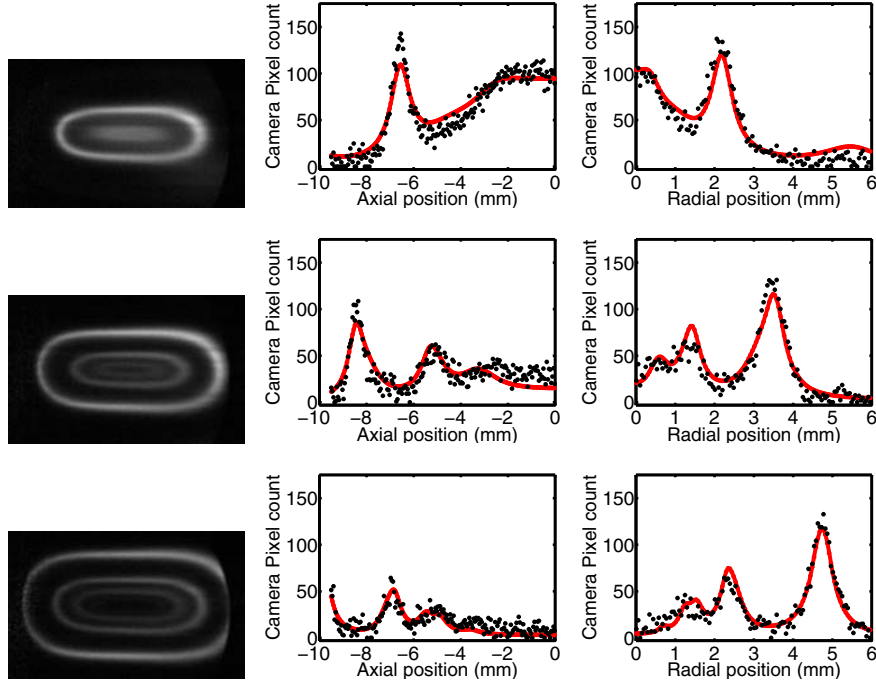


**Fig. 5.** (Color online) Imaging the trap at three different red detunings  $\delta_L/2\pi$   $-68$  MHz,  $-108$  MHz, and  $-148$  MHz. Fits to radial and axial cuts are shown in red.

coefficients<sup>2</sup>:

$$\begin{aligned} \langle F', m'_F | \hat{\mathbf{d}} | F, m_F \rangle &\propto (-1)^{1+L'+S+J+I-M'_F} \\ &\times \sqrt{(2J+1)(2J'+1)(2F+1)(2F'+1)} \\ &\times \begin{Bmatrix} L' & J' & S \\ J & L & 1 \end{Bmatrix} \begin{Bmatrix} J' & F' & I \\ F & J & 1 \end{Bmatrix} \\ &\times \begin{pmatrix} F & 1 & F' \\ M_F & q & -M_F \end{pmatrix}. \end{aligned} \quad (12)$$

Finally, to calculate the total absorption cross section, we sum over all possible transitions including their individual detunings:

$$\sigma_{eff}(B) = \sum_{\alpha} \frac{\sigma_{\alpha}(B)}{1 + \left(\frac{2\delta_{\alpha}(B)}{T}\right)^2}. \quad (13)$$

Obviously, power and Doppler broadening may be included. In our experiments only the Doppler broadening was corrected for, as laser powers generally was below saturation. Please note that  $\sigma_{eff}$  depends strongly on the magnetic field through the expansion coefficients  $c_{F,m_{F_0}}(B)$ .

### 4.3 Analysis of images

The basic assumption in the analysis is that intensity of the emitted light can be described by the calculated absorption cross section, meaning that the model does not

<sup>2</sup> Primed quantum numbers represent excited states and non-primed represent ground states. Curly braces are 6j symbols and normal parentheses are 3j symbols.

include optical pumping effects. However, a quick calculation will show that an atom with the average velocity will spend approx. 700 ns in the laser beam equivalent of roughly 10 optical pump cycles of the  $|2, -2\rangle \rightarrow |3, -3\rangle$  transition at the intensity used. On the other hand optical pumping effects are reduced at moderate magnetic fields since energy level spacings are significantly larger compared to the natural line width.

For each detuning the images are analyzed along two directions, vertical( $x$ ) and horizontally( $z$ ) and the data is fitted with

$$S(x) = k_1 \cdot \sigma_{eff}(B_0 + B'_\rho x), \quad (14)$$

$$S(z) = k_1 \cdot \sigma_{eff}\left(B_0 + \frac{1}{2}B''_z z^2\right), \quad (15)$$

where  $k_1$  is a global scaling of the data. The quantities  $B'_\rho$  and  $B''_z$  are extracted from these fits. However the method is not optimized for extracting  $B_0$ , but  $B_0$  can be accurately determined from the method presented in Section 5.

Figure 5 shows radial and axial fits at three different detunings  $\delta_L/2\pi = -68$  MHz,  $-108$  MHz, and  $-148$  MHz. The model predicts the peaks very well, but slightly underestimates the fluorescence of the outer circle. We will return to this in the next section.

Since every detuning provides a value of both  $B'_\rho$  and  $B''_z$  we present the average values:  $B'_\rho = (218 \pm 2)$  G/cm and  $B''_z = (212 \pm 3)$  G/cm<sup>2</sup>. The quoted errors are only statistical.

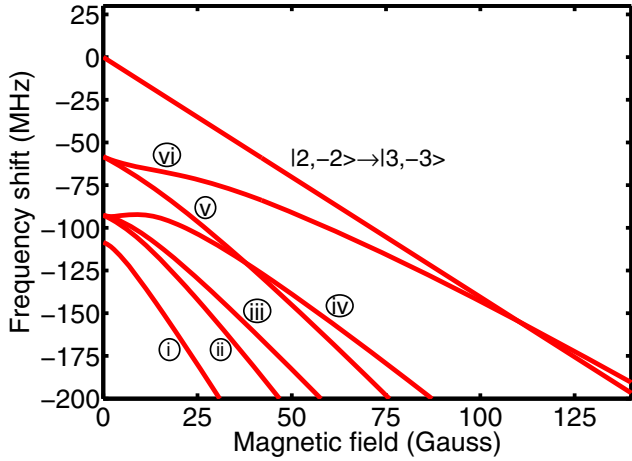


**Fig. 6.** (Color online) Strong transitions allowed by experimental polarization. All transitions are  $\Delta m_F = -1$ . Notice the pure  $|2, -2\rangle \rightarrow |3, -3\rangle$  transition.

#### 4.4 A simple model

The number of contributing transitions in Figure 4 is immediately reduced by noting that the polarization of the sheet of light (along  $\hat{x}$ ) does not allow  $\Delta m_F = 0$  transitions in the regions of analysis (axial and radial direction), since the local magnetic field is perpendicular to the  $\hat{x}$ -axis. Furthermore, we may analyze the relative transition strengths according to equations (11) and (12) and find that all  $\Delta m_F = +1$ -transitions are very weak except at zero magnetic field. The contributing transitions are shown in Figure 6.

A much simpler analysis can be performed by tracking only the most prominent transition, namely the  $|2, -2\rangle \rightarrow |3, -3\rangle$  transition. The advantage is that both states involved remain pure in the presence of the magnetic field and the Clebsch-Gordan coefficient is maximal.

This transition corresponds to the outermost of the rings in the CCD images of Figure 5. According to Figure 6 the ring is made up of two transitions: (vi) and  $|2, -2\rangle \rightarrow |3, -3\rangle$ , where  $|2, -2\rangle \rightarrow |3, -3\rangle$  is by far the strongest. Tracking the peak center position of the outer ring and equating the detuning with the Zeeman shift of the transition

$$\hbar\delta = \mu_B (g'_F m'_F - g_F m_F) B = \mu_B B, \quad (16)$$

we can determine the relation between position and magnetic field. The result is shown in Figure 7 which can then be fitted to find the radial gradient and the axial curvature. The result  $B'_\rho = (217 \pm 3) \text{ G/cm}$  and  $B''_z = (212 \pm 3) \text{ G/cm}^2$  agree very well with the more complicated analysis and the statistical errors are similar.

## 5 Measuring the bias field

### 5.1 Split trap method

The bias field is controlled by the current in the anti-bias coils. When the anti-bias coils overcompensate the field

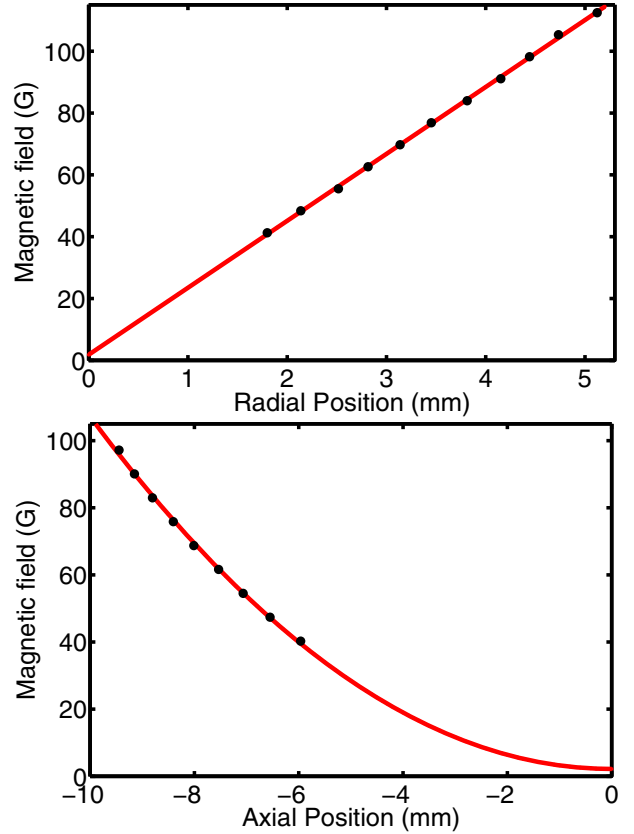


**Fig. 7.** (Color online) Tracking the radial (a) and axial (b) position of the outer fluorescence ring and the energy shift of the  $|2, -2\rangle \rightarrow |3, -3\rangle$  transition we can extract the radial gradient and axial curvature. The result is  $B'_\rho = 217 \pm 3 \text{ G/cm}$  and  $B''_z = 212 \pm 3 \text{ G/cm}^2$ .

from the curvature coils there are two points on the symmetry axis, where the magnetic field is zero. Tracking the movement of these two minima as a function of the current in the anti-bias coils reveals the bias field dependence of the anti-bias current. This can be used to determine the bias field using the tomography method.

We set the tomography laser beam on resonance with the  $F = 2 \rightarrow F' = 3$  transition for zero magnetic field. This way, we can find the region with zero magnetic field simply as the most fluorescent region. Using a simple two level approach, this can be described by an absorption cross section in the axial direction as

$$\sigma = \frac{\sigma_0}{1 + s_0 + \left( \frac{2\delta_L}{\Gamma} + \frac{\mu_B(B_0 + \frac{1}{2}B''_z z^2)}{\hbar\Gamma} \right)^2}, \quad (17)$$

where the detuning has contributions from both laser and magnetic detuning  $\delta = \delta_L + \Delta(B)$ , where  $\delta_L = 0$  in our case. This means that we will have maximum fluorescence where the magnetic field is zero, i.e. when

$$B_0 = -\frac{1}{2}B''_z z^2. \quad (18)$$

Although this two-level approach is not exact, we will still adopt it, motivated by the success of the simpler approach in last section.

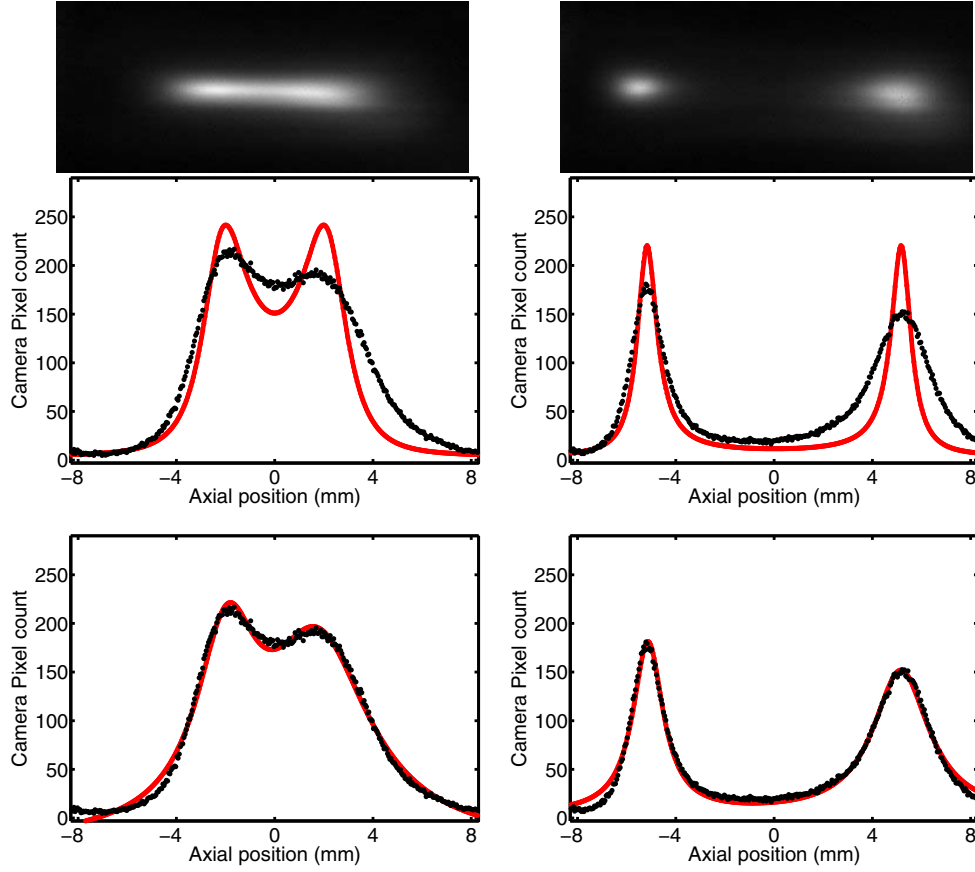


**Fig. 8.** (Color online) Axial positions of the split trap for extra anti-bias currents of 21 A (left) and 34 A (right). The top shows the CCD image, below fits according to equation (17) and the bottom shows two-peak Lorentzian fits to determine the peak centers accurately.

Figure 8 shows two of the analyzed images of the split trap. The left is taken at an extra-bias current of  $I_{EAB} = 21$  A just as the trap is splitting. The right is taken at  $I_{EAB} = 34$  A with two well separated clouds. From the axial position of the peaks, we can infer the bias field in the center of the trap from equation (18).

This way we can determine the central bias field as a function of current in the extra-bias coils. The result is shown in Figure 9 with a linear fit giving:

$$B_0(G) = (37.3 \pm 0.4)G - (1.902 \pm 0.022)G/A \cdot I_{EAB}(A). \quad (19)$$

Thus for  $I_{EAB} = (19.6 \pm 0.2)$  A we have  $B_0 = (0 \pm 0.4)$  G giving an indication of how well we can determine the central bias field using this method.

## 5.2 Central fluorescence method

Another method to determine the current at which there is zero bias field in the center of the trap, simply relies on recording the fluorescence in the central part. The position of the center of the trap is very well-known from the split trap measurements, exploiting the symmetry of the system. Since the tomography laser is on resonance with the  $F = 2 \rightarrow F' = 3$  transition the atoms will fluoresce

the most when they experience no Zeeman shift, i.e., when the bias field is zero. So by measuring the fluorescence for several currents as the trap splits the zero bias field can be determined. If this is done for several currents as the trap splits, we can find zero bias field as the current with maximum fluorescence in the central region.

Figure 9 shows the central fluorescence for different anti-bias currents. The fit is Lorentzian and peaking at  $I_{EAB} = (19.74 \pm 0.03)$  A and a with  $FWHM$  of  $(10.6 \pm 0.1)$  A.

## 6 Comparison

We compare the results from the tomography experiments with two additional methods: a direct way to measure the trap frequency by sloshing of cold atoms combined with Hall probe measurements of the coils. These methods, however, only give partial answers or are not directly related to the actual experimental situation as in-situ probing is virtually impossible. Using the first alternative method we observe the oscillation of a cold atomic cloud. To prevent excessive damping of the harmonic motion a cloud of  $100 \mu K$  is used. In Figure 10 the position of the cloud center is plotted versus the oscillation time.

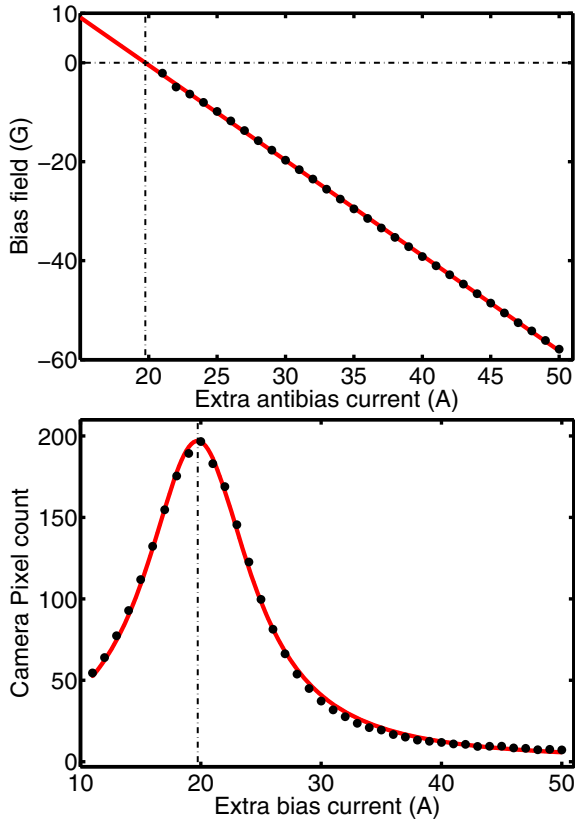


**Fig. 9.** Top: central bias field as a function of current using the split trap method. Error bars from the statistical uncertainty in the determination of  $B_z''$  are small and not shown. The solid red line is a linear fit from which we can extrapolate the current for zero bias field to  $I_{EAB} = (19.6 \pm 0.2)$  A. Bottom: fluorescence from the center of the trap as a function extra anti-bias current.

The dots are the data points, and the solid line is a fit based on a damped oscillator. This yields an axial trap frequency of:  $\omega_z = 2\pi(25.0 \pm 0.1)$  Hz, with a current of  $I_C = I_{Abias} = 344$  A running in the curvature and anti-bias coils. A small damping is still observed, even with the cold cloud. We interpret this as atoms probes some anharmonic region of the trap. This could introduce a small systematical error that causes the measured trap frequency to be lower than the real value for the trap frequency. At higher temperatures the damping ratio increases fast supporting our interpretation. The anharmonic behavior will be the subject of a forthcoming paper.

Furthermore the magnetic field produced by the coils is calculated by integrating the Bio-Savart law and measured in a test bench. Table 1 shows a summary of the results.

The sloshing and tomography method are in very good agreement as expected. For calculated and coil measurements performed on a bench, before installation, numbers differs about 10–15%. However, calculated values are performed for ideal circular geometries and positions, and usually tend to disagree by about 10%, as in the present case. Bench measurements may also be difficult to compare to on a more detailed level, since exact reproduction of coil positions in the actual experiment are virtually impossible due various mechanical constrains. Never the less

**Table 1.** Comparison of the different methods for a current through the anti-bias coils of  $I_{Antibias} = 344$  A. T: tomography experiments, S: sloshing experiments, C: calculation, CM: coil measurements on bench.

	T	S	C	CM
$B_z''$ (G cm <sup>-2</sup> A <sup>-1</sup> )	0.65		0.95	0.77
$B_\rho'$ (G cm <sup>-1</sup> A <sup>-1</sup> )	0.55		0.58	0.62
$B_0$ (G A <sup>-1</sup> )	–		0.38	0.21
$\omega_\rho/2\pi$ (Hz)	274		285	–
$\omega_z/2\pi$ (Hz)	26.2	25.0	32	–

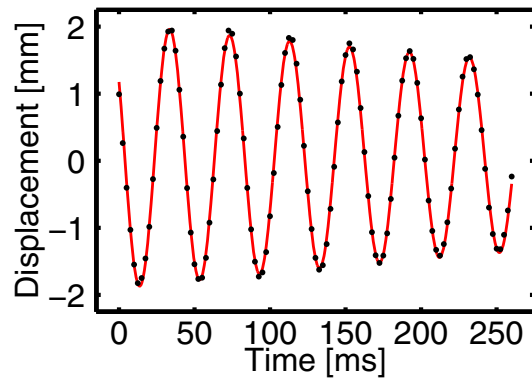


**Fig. 10.** Oscillatory axial movement of a cloud with a temperature  $T \approx 100$   $\mu$ K in the magnetic trap.

we observe convincing agreement between coil measurements and tomography experiments.

## 7 Conclusion

This paper demonstrates a fast and reliable method for accurate measurements of important trap parameters in a magnetic cloverleaf trap. By use of polarization dependent Zeeman spectroscopy we have determined the bias field, gradients and trap frequencies. The values obtained using spectroscopy is in excellent agreement with supplementary methods based of sloshing cold atoms in the trap or direct measurements of field gradient of the coils. The method presented here is simple in nature and can easily be extended to other alkali atoms and trap geometries.

We acknowledge financial support from the Niels Bohr Institute, Danish Natural Research Council and the Carlsberg Foundation.

## References

1. E.L. Raab, M. Prentiss, A. Cable, S. Chu, D.E. Pritchard, Phys. Rev. Lett. **59**, 2631 (1987)
2. T. Walker, D. Sesko, C.E. Wieman, Phys. Rev. Lett. **64**, 408 (1990)
3. S. Chu, J.E. Bjorkholm, A. Ashkin, A. Cable, Phys. Rev. Lett. **57**, 314 (1986)

4. M.D. Barrett, J.A. Sauer, M.S. Chapman, *Phys. Rev. Lett.* **87**, 010404-1 (2001)
5. M.H. Anderson, J.R. Ensher, M.R. Matthews, C.E. Wieman, E.A. Cornell, *Science* **269**, 198 (1995)
6. T. Esslinger, I. Bloch, T.W. Hänsch, *Phys. Rev. A* **58**, 2664 (1998)
7. T. Bergeman, G. Erez, H.J. Metcalf, *Phys. Rev. A* **35**, 1535 (1987)
8. W. Petrich, M.H. Anderson, J.R. Ensher, E.A. Cornell, *Phys. Rev. Lett.* **74**, 3352 (1995)
9. H. Hess, *Phys. Rev. B* **34**, 3476 (1986)
10. O.J. Luiten, M.W. Reynolds, J.T.M. Walraven, *Phys. Rev. A* **53**, 381 (1996)
11. R. Kaiser, N. Vansteenkiste, A. Aspect, E. Arimondo, C. Cohen-Tannoudji, *Z. Phys. D.* **18**, 17 (1991)
12. S. Wildermuth, S. Hofferberth, I. Lesanovsky, S. Groth, I. Bar-Joseph, P. Krüger, J. Schmiedmayer, *Appl. Phys. Lett.* **88**, 264103 (2006)
13. S. Wildermuth, S. Hofferberth, I. Lesanovsky, E. Haller, L. Mauritz Andersson, S. Groth, I. Bar-Joseph, P. Krüger, J. Schmiedmayer, *Nature* **435**, 440 (2005)
14. Ph.W. Courteille, S.R. Muniz, K. Magalhães, R. Kaiser, L.G. Marcassa, V.S. Bagnato, *Eur. Phys. J. D* **15**, 173 (2001)
15. E.W. Streed, A.P. Chikkatur, T.L. Gustavson, M. Boyd, Y. Torii, D. Schneble, G.K. Campbell, D.E. Pritchard, W. Ketterle, *Rev. Sci. Instrum.* **77**, 023106 (2006)
16. M.-O. Mewes, M.R. Andrews, N.J. van Druten, D.M. Kurn, D.S. Durfee, W. Ketterle, *Phys. Rev. Lett.* **77**, 416 (1996)

# Amplification and ASE suppression in a polarization-maintaining ytterbium-doped all-solid photonic bandgap fibre

C. B. Olausson<sup>1,2\*</sup>, C. I. Falk<sup>3</sup>, J. K. Lyngsø<sup>1,2</sup>, B. B. Jensen<sup>3</sup>, K. T. Therkildsen<sup>3</sup>, J. W. Thomsen<sup>3</sup>, K. P. Hansen<sup>1</sup>, A. Bjarklev<sup>2</sup> and J. Broeng<sup>1</sup>

<sup>1</sup>Crystal Fibre A/S, Blokken 84, DK-3460 Birkerød, Denmark

<sup>2</sup>DTU Fotonik, Ørstedes Plads, building 343, 2800 Kgs. Lyngby, Denmark

<sup>3</sup>Niels Bohr Institute, Universitetsparken 5, 2100 København, Denmark

\*Corresponding author: [cbo@crystal-fibre.com](mailto:cbo@crystal-fibre.com)

**Abstract:** We demonstrate suppression of amplified spontaneous emission at the conventional ytterbium gain wavelengths around 1030 nm in a cladding-pumped polarization-maintaining ytterbium-doped all-solid photonic crystal fibre. The fibre works through combined index and bandgap guiding. Furthermore, we show that the peak of the amplified spontaneous emission can be shifted towards longer wavelengths by rescaling the fibre dimensions. Thereby one can obtain lasing or amplification at longer wavelengths (1100 nm – 1200 nm) as the amount of amplification in the fibre is shown to scale with the power of the amplified spontaneous emission.

©2008 Optical Society of America

**OCIS codes:** (060.2280) Fiber design and fabrication; (060.2270) Fiber characterization; (060.2400) Fiber properties; (060.2420) Fibers, polarization-maintaining; (060.5295) Photonic crystal fibers; (060.3510) Lasers, Fiber.

---

## References and links

1. G. Bouwmans, L. Bigot, Y. Quiquempois, F. Lopez, L. Provino, and M. Douay, "Fabrication and characterization of an all-solid 2D photonic bandgap fiber with a low-loss region (< 20 dB/km) around 1550 nm," *Opt. Express* **13**, 8452-8459 (2005).
2. G. Canat, J. C. Mollier, J. P. Bouzinac, G. L. M. Williams, B. Cole, L. Goldberg, G. Kulcsar, Y. Jaouen, "Power limitations of fiber lasers at 1.5  $\mu\text{m}$  by parasitic lasing effects," in *Conference on Lasers and Electro-Optics/Quantum Electronics and Laser Science and Photonic Applications Systems Technologies*, Technical Digest (CD) (Optical Society of America, 2004), paper CMK6.
3. A. Shirakawa, J. Ota, H. Maruyama, and K. -I. Ueda, "Linearly-Polarized Yb-Doped Fiber Laser Directly Operating at 1178 nm for 589-nm Generation," in *Advanced Solid-State Photonics*, OSA Technical Digest Series (CD) (Optical Society of America, 2007), paper MD1.
4. S. Sinha, C. Langrock, M. Dignonnet, M. Fejer, and R. Byer, "Efficient yellow-light generation by frequency doubling a narrow-linewidth 1150 nm ytterbium fiber oscillator," *Opt. Lett.* **31**, 347-349 (2006).
5. N. Malossi, S. Damkjaer, P. L. Hansen, L. B. Jacobsen, L. Kindt, S. Sauge, J. W. Thomsen, F. C. Cruz, M. Allegrini, and E. Arimondo, "Two-photon cooling of magnesium atoms," *Phys. Rev. A* **72**, 051403 (2005).
6. A. Wang, A. K. George, and J. C. Knight, "Three-level neodymium fiber laser incorporating photonic bandgap fiber," *Opt. Lett.* **31**, 1388-1390 (2006).
7. V. Pureur, L. Bigot, G. Bouwmans, Y. Quiquempois, M. Douay, and Y. Jaouen, "Ytterbium-doped solid core photonic bandgap fiber for laser operation around 980 nm," *Appl. Phys. Lett.* **92**, 061113 (2008).
8. R. Goto, K. Takenaga, K. Okada, M. Kashiwagi, T. Kitabayashi, S. Tanigawa, K. Shima, S. Matsuo, and K. Himeno, "Cladding-Pumped Yb-Doped Solid Photonic Bandgap Fiber for ASE Suppression in Shorter Wavelength Region," in *Optical Fiber Communication Conference and Exposition and The National Fiber Optic Engineers Conference*, OSA Technical Digest (CD) (Optical Society of America, 2008), paper OTuJ5.
9. T. Birks, F. Luan, G. Pearce, A. Wang, J. Knight, and D. Bird, "Bend loss in all-solid bandgap fibres," *Opt. Express* **14**, 5688-5698 (2006).
10. K. P. Hansen, C. B. Olausson, J. Broeng, K. Mattsson, M. D. Nielsen, T. Nikolajsen, P. M. W. Skovgaard, M. H. Sørensen, M. Denniger, C. Jakobsen, and H. R. Simonsen, "Airclad fiber laser technology," *Proc. SPIE* **6873**, 687307 (2008).

11. W. J. Wadsworth, R. M. Percival, G. Bouwmans, J. C. Knight, T. A. Birks, T. D. Hedley, and P. S. J. Russell, "Very High Numerical Aperture Fibers," *IEEE Photonics Tech. Lett.* **16**, 843-845 (2004).
12. A. Cerqueira S. Jr., F. Luan, C. Cordeiro, A. George, and J. Knight, "Hybrid photonic crystal fiber," *Opt. Express* **14**, 926-931 (2006).
13. J. K. Lyngsø, B. J. Mangan, and P. J. Roberts, "Polarization Maintaining Hybrid TIR/Bandgap All-Solid Photonic Crystal Fiber," in *Conference on Lasers and Electro-Optics/Quantum Electronics and Laser Science Conference and Photonic Applications Systems Technologies*, OSA Technical Digest (CD) (Optical Society of America, 2008), paper CThV1.
14. N. M. Litchinitser, S. C. Dunn, B. Usner, B. J. Eggleton, T. P. White, R. C. McPhedran, and C. Martijn de Sterke, "Resonances in microstructured optical waveguides," *Opt. Express* **11**, 1243-1251 (2006).

## 1. Introduction

In photonic bandgap (PBG) fibres light is confined within a low-index core by a microstructured cladding typically formed by silica and air. In this work an all-solid PBG fibre is used in which the PBG cladding is made by a triangular lattice of germanium-doped high-index micro-rods in a silica background, which raise the overall cladding index as in [1], while the core consists of a single ytterbium-doped micro-rod as gain medium. Combining the wavelength filtering effect of PBG confinement with an ytterbium-doped core results in efficient suppression of amplified spontaneous emission (ASE) at the conventional ytterbium gain wavelengths around 1030 nm and thus a reduction in parasitic lasing outside the bandgap, which typically limits the operation of long wavelength fibre lasers and amplifiers [2]. Frequency doubled fibre lasers and amplifiers around 1180 nm [3,4] are of interest for yellow light generation in medical and astronomical application, while frequency quadrupling of fibre lasers can generate narrow linewidth UV light in the range 255 nm – 295 nm for applications in atomic physics [5]. Previous work on the use of the photonic bandgap filtering effect for shorter wavelength laser operation at 907 nm and 980 nm is reported in [6,7].

In this paper, we demonstrate suppression of ASE for two different all-solid PBG fibres with different bandgap positions. We show that the ASE peak can be shifted towards longer wavelengths by rescaling the dimensions of the fibre and thereby moving the bandgap. It has been shown that the ASE peak of an all-solid PBG fibre can be shifted towards longer wavelengths by reducing the coiling diameter [8], however, this method works by and suffers from significant bend losses [9]. With the present approach, we show that tight coiling of the fibre is not necessary in order to shift towards longer wavelengths. Furthermore, we demonstrate that the amplification in the fibres scales with the ASE power for a given wavelength.

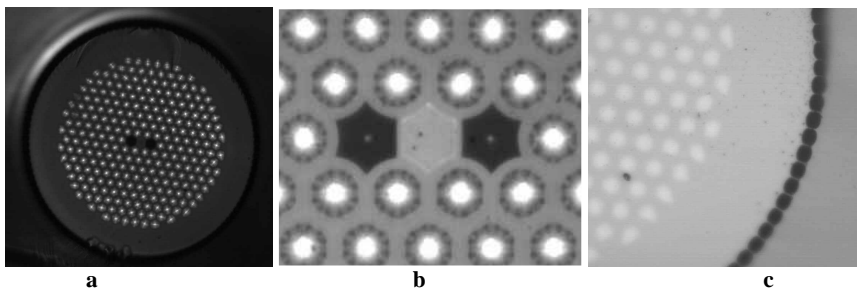


Fig. 1. (a) Microscope image of the fibre structure. The lighter regions are the germanium-doped rods constituting the pump-cladding, while the two darker regions are the boron rods. (b) Microscope image of the core region. (c) Microscope image of the airclad surrounding the pump-cladding structure.

## 2. Fibre properties

Two all-solid photonic PBG fibres were fabricated with a cladding pitch of 9.45  $\mu\text{m}$  and 9.80  $\mu\text{m}$ , respectively. The signal core consists of an ytterbium-doped rod, which is index matched to the silica background. The core is surrounded by the PBG pump-cladding structure made

by an eight period triangular lattice structure of high-index germanium-doped rods. For the two fibres we measured the diameter of the cladding to 214  $\mu\text{m}$  and 220  $\mu\text{m}$ , respectively. Both fibres have pump absorption of 1.1 dB/m at 976 nm. Furthermore, the PBG pump cladding is surrounded by an airclad structure providing the pump guide with a large numerical aperture of 0.57, allowing for efficient high-power cladding-pumping [10,11].

The polarization-maintaining properties of the fibre are obtained by incorporating two low index boron-doped rods on either side of the core. The boron-doped rods act as stress applying parts, inducing high birefringence in the fibre while the lower index results in confinement by total internal reflection (TIR) in one direction and bandgap guiding in other directions [12]. The birefringence is on the order of  $10^{-4}$ .

Microscope images of the fibre structure, the core and the airclad structure surrounding the pump cladding are shown in Fig. 1. The lighter regions are the germanium-doped rods, while the two darker regions near the core are the boron rods.

Core properties of the fibre have been determined by performing measurements on a fibre which is identical to the fibre in question in terms of pump cladding and core properties, but without the surrounding airclad. Near-field measurements at 1150 nm yield a  $1/e^2$  mode field diameter of 10.0  $\mu\text{m}$  in the axis parallel to the stress rods, a mode field diameter of 10.8  $\mu\text{m}$  in the axis perpendicular to the stress rods and an average numerical aperture of 0.1. A near field image taken in the third order bandgap using 1150nm light is shown in Fig. 2. The lack of an anti-resonant tail of light in the boron-doped stress rods on either side of the core is evidence of index guiding in the direction of the stress rods and bandgap guiding in the other direction. A passive version of this type of hybrid TIR / bandgap fibre has been reported in [13].

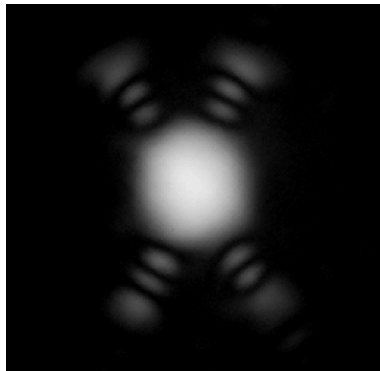


Fig. 2. Near field CCD image taken in the third order bandgap using 1150 nm light, where the stress rods are in the horizontal direction. An anti-resonant tail of light is visible in the surrounding high-index germanium-doped rods, but not in the boron-doped stress rods.

Recently, ASE suppression in an ytterbium-doped all-solid photonic PBG fibre for long wavelength applications has been demonstrated [8]. The present fibre design is polarization-maintaining and holds potential for higher power due to the airclad surrounding the pump cladding.

### 3. Suppression of amplified spontaneous emission

The transmission spectrum of the fibres is measured using the setup in Fig. 3(a). In order to only transmit light in the core, light from a white light source is launched into 1 m of single-mode large mode area (LMA) fibre with a core size of 10  $\mu\text{m}$ , which is then butt-coupled to the 10  $\mu\text{m}$  core of 30 m of the ytterbium-doped all-solid PBG fibre. The light from the core of the PBG fibre is subsequently collected by a high NA 10  $\mu\text{m}$  core fibre in order to limit light collected by the optical spectrum analyzer (OSA) to the core region.

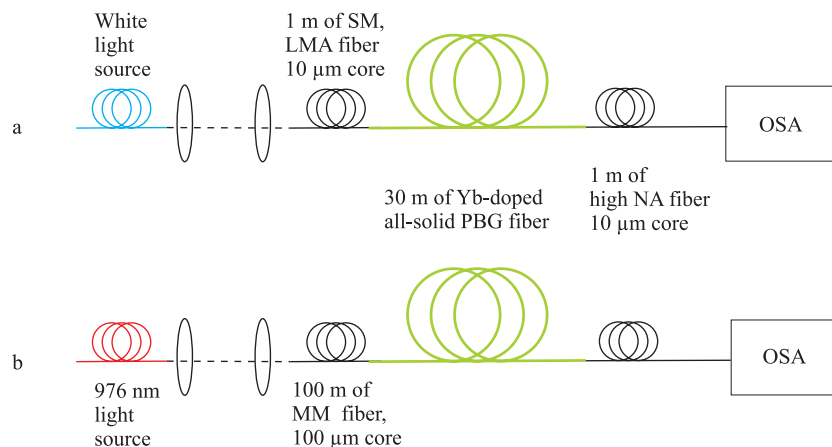


Fig. 3. (a) Experimental setup for measuring the bandgap transmission spectrum and (b) setup for measuring the ASE spectrum.

The ASE spectrum in the core is measured using the setup shown in Fig. 3(b). The 976 nm pump light is launched into the pump cladding of the PBG fibre using a multi-mode fibre with a core size of 100 μm and the output core light is collected by the same high NA fibre and detected by the optical spectrum analyzer.

Figure 4 shows the ASE spectrum (red) of a PBG fibre with a bandgap centered around 1140 nm (grey). Compared to the ASE spectrum of an index-guiding photonic crystal fibre (black), the PBG fibre shows significant suppression of ASE outside the bandgap.

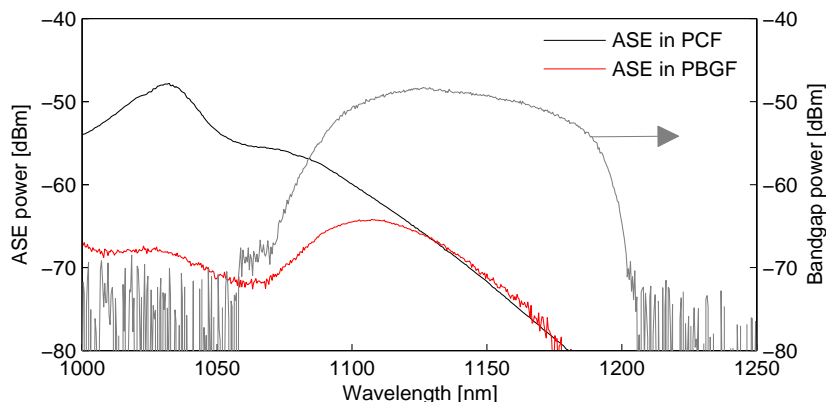


Fig. 4. ASE spectrum of an ytterbium-doped all-solid PBG fibre (red) showing suppression of ASE outside the bandgap (grey) compared to the ASE spectrum of an index guiding photonic crystal fibre (black).

Figure 5 shows the ASE spectra of the two different ytterbium-doped all-solid PBG fibres, one designed with a bandgap centered at 1140 nm (red) and another designed with a bandgap centered at 1180 nm (black). Results show that the peak of the ASE spectrum can be shifted towards longer wavelengths by moving the bandgap position in the fibre. This is done by rescaling the fibre dimensions in the drawing process.

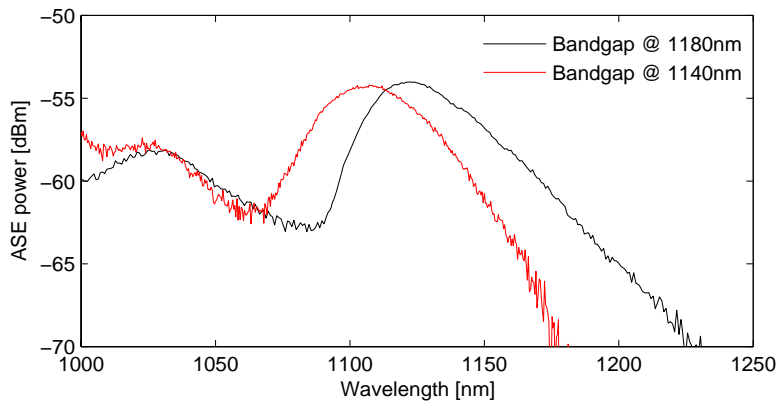


Fig. 5. ASE spectra of two ytterbium-doped all-solid PBG fibres with bandgap positions centered at 1140nm (red) and 1180nm (black). The peak of the ASE spectrum is shifted towards longer wavelengths by moving the bandgap.

#### 4. Amplification and laser properties

The amplification properties of the fibres are measured using the forward seeded amplification setup depicted in Fig. 6. The PBG fibre is pumped with up to 3 W of 980 nm light and seeded with 2 mW of 1080 nm – 1145 nm light from a laser cavity created from 30 m of the same PBG fibre and a laser dispersing prism. The seed laser cavity is tuned using a mirror. Furthermore, the pump light is launched at an angle in order to reduce guidance in the high-index rods and obtain maximum pump absorption.

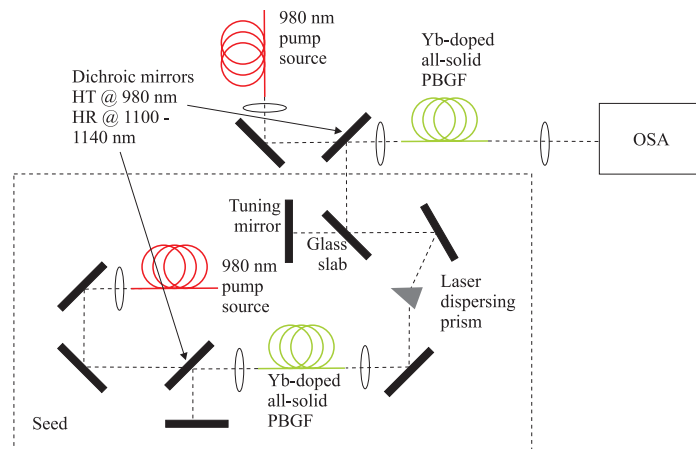


Fig. 6. Amplification setup using forward seeding with a seed setup tunable in the range 1080 nm – 1145 nm.

The amplification results for the two PBG fibres are presented in Fig. 7. For both fibres results show that the amplification for a given wavelength scales with the ASE power. For the specified pump power an amplification of up to 15dB is obtained in both fibres. Peak amplification occurs at the wavelengths that experience the least loss due to the bandgap combined with the highest gain due to their emission cross section. Increasing the pump power will shift the ASE peak, and hence also the peak amplification, towards the left bandgap edge.

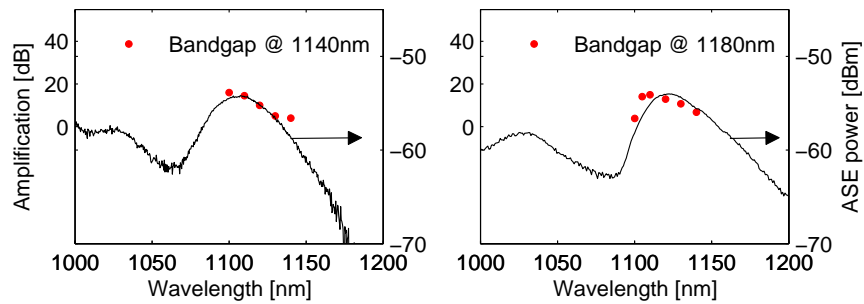


Fig. 7 The amplification properties of the fibres (red dots) are seen to follow the ASE profiles (black).

Laser properties of the fibres are presented in Fig. 8. The fibre with the bandgap centered at 1140 nm is pumped with 1.1 W of 980 nm light while the fibre with the bandgap centered at 1180 nm is pumped with 2.5 W. Approximately 17 dB of pump light is absorbed at 980 nm while 2 dB of pump light is trapped in the high-index rods due to imperfect angled incoupling. The fibres are tunable as shown in Fig. 8(a) with optimum wavelengths at approximately 1100 nm and 1120 nm for the two fibres. These wavelengths lie at the top of the left bandgap edge. The bandgap widens as the cladding pitch is increased [14], which causes the left bandgap edge to shift less than the bandgap center and hence reduces the shift of the optimum lasing wavelength to 20 nm compared to the 40 nm shift of the bandgap center. Furthermore, in Fig. 8(b) the ASE suppression is apparent in the output power spectrum outside the bandgap, when the fibre with a bandgap centered at 1180 nm is lasing at exactly the edge of the bandgap. Comparing the level of ASE inside the bandgap to the level of ASE outside the bandgap, we measure an ASE suppression of 15dB at the bandgap edge.

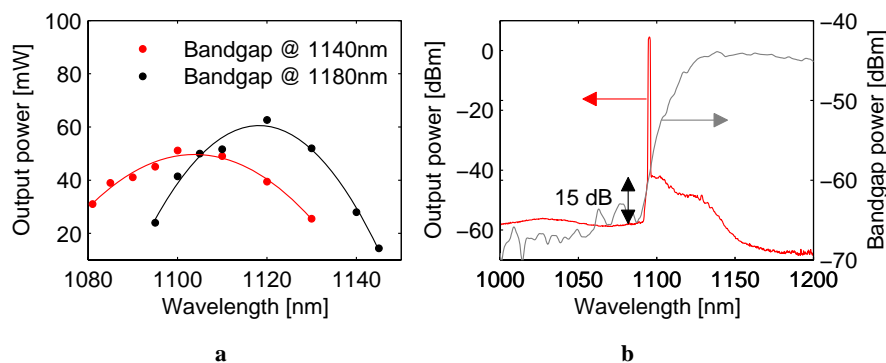


Fig. 8. (a) Laser properties of the two fibres. (b) Power spectrum of the PBG fibre with a bandgap centered at 1180nm (red) lasing at the edge of the bandgap (grey). ASE suppression of 15 dB is apparent in the power spectrum outside the bandgap.

## 5. Conclusion

Experimental results show ASE suppression in two different ytterbium-doped all-solid PBG fibres and the ability to shift the ASE peak towards longer wavelengths by rescaling of the fibre design. In addition to the control of the ASE suppression, amplification measurements for the two fibres have shown that also the amplification properties can be controlled by design as the amplification is seen to scale with the ASE power. These features can be useful when designing fibres with potential for even longer wavelength lasing and amplification and can open new possibilities for high-power ytterbium-doped fibre lasers and amplifiers lasing at longer wavelengths above the conventional ytterbium gain wavelengths.



---

## Bibliography

- [1] T. W. Hänsch and A. L. Schawlow, *Optics Communications*, **13**, 68 (1975).
- [2] D. Wineland and H. Dehmelt, *Bull. Am. Phys. Soc.*, **20**, 637 (1975).
- [3] W. D. Phillips and H. Metcalf, *Phys. Rev. Lett.*, **48**, 596 (1982).
- [4] Steven Chu, L Hollberg, J. E. Bjorkholm, Alex Cable, and A. Ashkin. *Physical Review Letters*, **55**, 48 (1985).
- [5] Steven Chu, J. E. Bjorkholm, A. Ashkin, and Alex Cable. *Physical Review Letters*, **57**, 314 (1986).
- [6] A. L. Migdall, J. V. Prodan, W. D. Phillips, T. H. Bergeman, and H. J. Metcalf. First observation of magnetically trapped neutral atoms. *Phys. Rev. Lett*, **54**, 2596 (1985).
- [7] E. L. Raab, M. Prentiss, Alex Cable, Steven Chu, and D. E. Pritchard. *Phys. Rev. Lett.*, **59**, 2631 (1987).
- [8] R. Blatt, W. Ertmer, and J.L. Hall. *Prog. Quant. Electr.*, **8**, 237 (1984).
- [9] M. Kasevich, E. Riss, S. Chu, and R. De Voe. *Physical Review Letters*, **63**, 612 (1989).
- [10] K. Gibble and S. Chu. *Metrologia*, **29**, 201 (1992).
- [11] A. Clairon, C. Salomon, S. Guellati, and W. Phillips. *Europhys. Letters*, **16**, 164 (1991).

- [12] C. Cohen-Tannoudji. Proceedings of the International School of Physics Enrico Fermi -Laser Cooling of Atoms an Ions. Elsevier Science Publishers B.V, 1991.
- [13] W. D. Philips. Proceedings of the International School of Physics Enrico Fermi -Laser Cooling of Atoms an Ions. Elsevier Science Publishers B.V, 1991.
- [14] Harold J. Metcalf and Peter van der Straten. Laser Cooling and trapping. Springer, second edition, 2001.
- [15] M. H. Anderson, J. R. Ensher, M.R. Matthews, C. E. Wieman, and E. A. Cornell. Observation of bose-einstein condensation in a dilute atomic vapor. *Science*, **269**, 198 (1995).
- [16] K. B. Davis, M. O. Mewes, M. R. Andrews, N. J. van Druten, D. S. Durfee, D. M. Kurn, and W. Ketterle. Bose-einstein condensation in a gas of sodium atoms. *Physical Review Letters*, **75**, 3969 (1995).
- [17] C. C. Bradley, C.A. Sackett, J. J. Tollett, and R. G. Hulet, *Phys. Rev. Lett.* **75**, 1687 (1995).
- [18] D. G. Fried, T. C. Killian, L. Willmann, D. Landhuis, S. C. Moss, D. Kleppner, and T. J. Greytak, *Phys. Rev. Lett.* **81**, 3811 (1998).
- [19] G. Modugno, G. Ferrari, G. Roati, R. J. Brecha, A. Simoni, and M. Inguscio, *Science* **294**, 1320 (2001).
- [20] A. Robert, O. Sirjean, A. Browaeys, J. Poupard, S. Nowak, D. Boiron, and C.W. A. Aspect, *Science* 292, 461 (2001).  
F. Pereira Dos Santos, J. Leonard, J.Wang, C. J. Barrelet, F. Perales, E. Rasel, C. S. Unnikrishnan, M. Leduc, and C. Cohen-Tannoudji, *Phys. Rev. Lett.* **86**, 3459 (2001).
- [21] T. Weber, J. Herbig, M. Mark, H.-C. Nägerl, and R. Grimm, *Science* **299**, 232 (2003).

- 
- [22] Y. Takasu, K. Maki, K. Komori, T. Takano, K. Honda, M. Kumakura, T. Yabuzaki, and Y. Takahashi, Phys. Rev. Lett. **91**, 040404 (2003).
- [23] Axel Griesmaier, Jörg Werner, Sven Hensler, Jürgen Stuhler, and Tilman Pfau, Phys. Rev. Lett. **94**, 160401 (2005)
- [24] J. Weiner, V. S. Bagnato, S. Zilio, and P. S. Julienne. Experiments and theory in cold and ultracold collisions. Reviews of Modern Physics, **71**, 1 (1999).
- [25] P. S. Julienne and F. H. Mies. Collisions of ultracold trapped atoms. J.Opt.Soc.Am. B, **6**, 2257 (1989).
- [26] M. Kasevich and S. Chu. Atomic interferometry using stimulated raman transitions. Physical Review Letters, **67**, 181 (1991).
- [27] B. DeMarco and D.S. Jin, Science **285**, 1703 (1999).
- [28] S. Jochim, M. Bartenstein, A. Altmeyer, G. Hendl, S. Riedl, C. Chin, J. Hecker Denschlag, and R. Grimm Science **302**, 2101 (2003);
- [29] C. A. Regal, C. Ticknor, J. L. Bohn, and D. S. Jin, Nature **424**, 47 (2003).
- [30] S. A. Diddams, J. C. Bergquist, S. R. Jefferts, and C. W. Oates. Nature, **306**, 1318 (2002).
- [31] J. I. Cirac and P. Zoller. Physical Review Letters, **20**, 4091 (1995).
- [32] J. I. Cirac and P. Zoller. Journal of Physics B, **38**, 567 (2005).
- [33] S. G. Porsev and A. Derevianko. Phys. Rev. A, **65**, 020701 (2002).
- [34] M.Machholm, P. S. Julienne, and K.-A. Souminen. Physical Review A, **65**, 23401 (2002).
- [35] Timothy P. Dinneen, Kurt R. Vogel, Ennio Arimondo, John L. Hall, and Alan Gallagher. Physical Review A, **59**, 1216 (1999).

- [36] G. Zinner, T. Binnewies, F. Riehle, and E. Tiemann. *Physical Review Letters*, **85**, 2292 (2000).
- [37] Robin Santra, Kevin V. Christ, and Chris H. Greene. *Physical Review A*, **69**, 042510 (2004).
- [38] S. G. Porsev, M. G. Kozlov, Yu. G. Rakhlina, and A. Derevianko. *Physical Review A*, **64**, 012508 (2001).
- [39] Th. Udem, R. Holzwarth, and T. W. Hänsch. *Nature*, **416**, 233 (2002).
- [40] Xinye Xu, Thomas H. Loftus, Matthew J. Smith, John L. Hall, Alan Gallagher, and Jun Ye. *Physical Review A (Atomic, Molecular, and Optical Physics)*, **66**, 011401 (2002).
- [41] A. D. Ludlow, T. Zelevinsky, G. K. Campbell, S. Blatt, M. M. Boyd, M. H. G. de Miranda, M. J. Martin, J. W. Thomsen, S. M. Foreman, Jun Ye, T. M. Fortier, J. E. Stalnaker, S. A. Diddams, Y. Le Coq, Z. W. Barber, N. Poli, N. D. Lemke, K. M. Beck, and C. W. Oates, *Science* **319**, 1805 (2008)
- [42] Hidetoshi Katori, Tetsuya Ido, Yoshitomo Isoya, and Makoto Kuwata-Gonokami. *Physical Review Letters*, **82**, 1116 (1999).
- [43] Xinye Xu, Thomas H. Loftus, John L. Hall, Alan Gallagher, and Jun Ye. *Journal of the Optical Society of America B: Optical Physics*, **20**, 968 (2003).
- [44] R. L. Cavasso Filho, D. A. Manoel, D. R. Ortega, A. Scalabrin, D. Pereira, and F.C.Cruz. *Applied Physics B*, **78**, 49 (2004).
- [45] T. Binnewies, G. Wilpers, U. Sterr, F. Riehle, J. Helmcke, T. E. Mehlstaubler, E. M. Rasel, and W. Ertmer. *Physical Review Letters*, **87**, 123002 (2001).
- [46] K. Sengstock, U. Sterr, J. H. Müller, V. Rieger, D. Bettermann, and W. Ertmer. *Applied Physics B*, **59**, 99 (1999).

- [47] E. A. Curtis, C. W. Oates, and L. Hollberg. *Physical Review A*, **64**, 031403 (2001).
- [48] J. R. Guest, N. D. Scielzo, I. Ahmad, K. Bailey, J. P. Greene, R. J. Holt, Z.-T. Lu, T. P. OConnor, and D. H. Potterveld. *Physical Review Letters*, **98**, 093001 (2007).
- [49] S. De, U. Dammalapati., K. Jungmann and L. Willmann, arXiv:0807.4100
- [50] K. Sengstock, U. Sterr, J. H. Müller, V. Rieger, D. Bettermann, and W. Ertmer. *Appl. Phys. B.*, **59**, 99 (1994).
- [51] C.W. Oates, F. Bondu, R.W. Fox, and L. Hollberg. *European Physical Journal D*, **7**, 449 (1999).
- [52] U. Sterr, C. Degenhardt, H. Stoehr, C. Lisdat, H. Schnatz, J. Helmcke, F. Riehle, G. Wilpers, Ch. Oates, and L. Hollberg. *C. R. Physique*, **5**, 845 (2004).
- [53] H. Katori, M. Takamoto, V. G. Palchicov, and V. D. Ovsiannikov. *Physical Review Letters*, **91**, 173005 (2003).
- [54] A. D. Ludlow, M. M. Boyd, T. Zelevinsky, S. M. Foreman, S. Blatt, M. Notcutt, T. Ido, and J. Ye. *Phys. Rev. Lett.*, **96**, 033003 (2006).
- [55] R. Le Targat, X. Baillard, M. Fouch, A. Bruschi, O. Tcherbakoff, G. D. Rovera, and Pierre Lemonde. *Phys. Rev. Lett.*, **97**, 130801 (2006).
- [56] Z. W. Barber, C. W. Hoyt, C. W. Oates, L. Hollberg, A. V. Taichenachev, and V. I. Yudin. *Phys. Rev. Lett.*, **96**, 083002 (2006).
- [57] X. Baillard, M. Fouch, R. Le Targat, P. G. Westergaard, A. Lecallier, Y. Le Coq, G. D. Rovera, S. Bize, and Pierre Lemonde. *Optics Letters*, **32**, 1812 (2007).
- [58] G. Breit and L. A. Wills, Hyperfine structure in intermediate coupling, *Physical Review* **44**, 0470 (1933).

- [59] J. R. de Laeter, J. K. Böhlke, P. De Bivre, H. Hidaka, H. S. Peiser, K. J. R. Rosman and P. D. P. Taylor, *Pure Appl. Chem.*, Vol. **75**, 683 (2003).
- [60] M. G. Mayer, *Physical Review* **78**, 16 (1950).
- [61] S. G. Porsev and A. Derevianko, *Physical Review A* **74**, 020502 (2006).
- [62] T. Rosenband, D. B. Hume, P. O. Schmidt, C. W. Chou, A. Brusch, L. Lorini, W. H. Oskay, R. E. Drullinger, T. M. Fortier, J. E. Stalnaker, S. A. Diddams, W. C. Swann, N. R. Newbury, W. M. Itano, D. J. Wineland, and J. C. Bergquist, *Science*, **319**, 1808 (2008).
- [63] D. W. Allan. *Proc. IEEE*, **54**, 221 (1966).
- [64] J. L. Hall, *Optical Frequency Measurement: 40 Years of Technology Revolutions*, *IEEE Journ. Sel. Top. Quant. Electr.* **6**, 1136 (2000).
- [65] D. J. Jones, S. A. Diddams, J. K. Ranka, A. Stentz, R. S. Windeler, J. L. Hall, and S. T. Cundiff, *Science* **288**, 635 (2000).
- [66] S. A. Diddams, D. J. Jones, J. Ye, S. T. Cundiff, J. L. Hall, J. K. Ranka, R. S. Windeler, R. Holzwarth, T. Udem, and T. W. Hänsch, *Phys. Rev. Lett.* **84**, 5102 (2000).
- [67] *Femtosecond Optical Frequency Comb: Principle, Operation, and Applications*, edited by J. Ye and S. T. Cundiff, Springer, New York, (2004).
- [68] P. A. M. Dirac. The cosmological constants. *Nature*, **264**, 323, (1937).
- [69] Oskar Klein. Quantentheorie und fünfdimensionale Relativitätstheorie. *Z. Phys.*, **37**, 895 (1926).
- [70] William J. Marciano. *Phys. Rev. Lett.*, **52**, 489 (1984).
- [71] T. Damour. Equivalence principle and clocks. In J. D. Barrow, editor, *Proceedings of the 34th Rencontres de Moriond, Gravitational waves and Experimental Gravity*, pages 16, gr-qc/9711084, 1999.

- [72] J. K. Webb, M. T. Murphy, V. V. Flambaum, V. A. Dzuba, J. D. Barrow, C.W. Churchill, J. X. Prochaska, and A. M. Wolfe. Phys. Rev. Lett., **87**, 09130114 (2001).
- [73] J. G. Williams, X. X. Newhall, and J. O. Dickey. Phys. Rev. D, **53**, 6730 (1996).
- [74] A. I. Shlyakther. Nature, **264**, 340 (1976).
- [75] Thibault Damour and Freeman Dyson. Nucl. Phys. B, **480**, 37 (1996).
- [76] J. K. Webb, V. V. Flambaum, Ch. W. Churchill, M. J. Drinkwater, and J. D. Barrow. Search for time variation of the fine structure constant. Phys. Rev. Lett., **82**, 884 (1999).
- [77] V. A. Dzuba, V. V. Flambaum, and J. K. Webb. Phys. Rev. Lett., **82**, 888 (1999).
- [78] V. A. Dzuba, V. V. Flambaum, and J. K. Webb. Calculations of the relativistic effects in many-electron atoms and space-time variation of fundamental constants. Phys. Rev. A, **59**, 230 (1999).
- [79] H. Marion, F. Pereira Dos Santos, M. Abgrall, S. Zhang, Y. Sortais, S. Bize, I. Maksimovic, D. Calonico, J. Grünert, C. Mandache, P. Lemonde, G. Santarelli, Ph. Laurent, A. Clairon, and C. Salomon. Search for variations of fundamental constants using atomic fountain clocks. Phys. Rev. Lett., **90**, 15080114 (2003).
- [80] S. Bize, S. A. Diddams, U. Tanaka, C. E. Tanner, W. H. Oskay, R. E. Drullinger, T. E. Parker, T. P. Heavner, S. R. Jefferts, L. Hollberg, W. M. Itano, and J. C. Bergquist. Testing the stability of fundamental constants with the  $^{199}\text{Hg}^+$  single-ion optical clock. Phys. Rev. Lett., **90**, 15080214 (2003).
- [81] Kaufmann & Freedman, Universe, 5th ed., W.H. Freeman, (1998)
- [82] Gratton, R. G., Carretta, E., Matteucci, F., & Sneden, C., Astronomy & Astrophysics, **358**, 671 (2000)

- [83] Matteucci, F., Ponzone, R., & Gibson, B. K., *Astronomy & Astrophysics*, **335**, 855 (1998)
- [84] J. V. Prodan, W. D. Phillips, and H. Metcalf. *Physical Review Letters*, **49**, 1149 1982.
- [85] J. V. Prodan and W. D. Phillips. *Prog. Quant. Elect.*, **8**, 231 (1984).
- [86] P. D. Lett, W. D. Phillips, S. L. Rolston, C. E. Tanner, R. N. Watts, and C. I. Westbrook. *Optical molasses. J. Opt. Soc. Am. B*, **6**, 2084, (1989).
- [87] B. H. Bransden and C. J. Joachain, *Physics of Atoms and Molecules*, Pearson Education Limited, second edition ed., 2003.
- [88] W.H. Wing. On neutral particle trapping in quasistatic electromagnetic fields. *Prog. Quant. Electr.*, **8**, 181 (1984).
- [89] W. Ketterle and D.E. Pritchard. Trapping and focusing ground state atoms with static fields. *Appl. Phys. B*, **54**, 403 (1992)
- [90] J. J. Sakuri, *Modern Quantum Mechanics* (Addison Wesley Longman, New York, 1994).
- [91] Ralchenko, Yu., Kramida, A.E., Reader, J., and NIST ASD Team (2008). NIST Atomic Spectra Database (version 3.1.5), [Online]. Available: <http://physics.nist.gov/asd3> [2008, December 31]. National Institute of Standards and Technology, Gaithersburg, MD.
- [92] S. Friebe, C. D'Andrea, J. Walz, M. Weitz, and T. W. Hänsch, CO<sub>2</sub>-laser optical lattice with cold rubidium atoms, *Phys. Rev. A* **57**, R20 (1998).
- [93] H. Katori, M. Takamoto, V. G. Palchikov, and V. D. Ovsiannikov, Ultrastable Optical Clock with Neutral Atoms in an Engineered Light Shift Trap, *Phys. Rev. Lett.* **91**, 173005 (2003).
- [94] Martin M. Boyd, Tanya Zelevinsky, Andrew D. Ludlow, Sebastian Blatt, Thomas Zanon-Willette, Seth M. Foreman, and Jun Ye *Phys. Rev. A* **76**, 022510 (2007)

- [95] R. Santra, K. V. Christ, and Ch. H. Greene: Properties of meta-stable alkaline-earth-metal atoms calculated using an accurate effective core potential. *Phys. Rev. A* **69**, 042510 (2004).
- [96] M. Takamoto and H. Katori, *Phys. Rev. Lett.* **91**, 223001 (2003).
- [97] T. E. Mehlstäubler, K. Moldenhauer, M. Riedmann, N. Rehbein, J. Friebe, E. M. Rasel, and W. Ertmer. *Phys. Rev. A* **77**, 021402 (2008)
- [98] Anders Brusich. Horloge a reseau optique a atomes de strontium, et etude des effets d'hyperpolarisabilite dus au pieges laser. These de doctorat de l'universite paris IV.
- [99] P. A. Franken, A. E. Hill, C. W. Peters and G. Weinreich. *Phys. Rev. Lett.*, **7**, 118 (1961).
- [100] K. Schneider, S. Schiller, J. Mlynek, M. Bode and I. Freitag. *Opt. Lett.*, **21**, 1999 (1996).
- [101] Yariv. *Optical Electronics*, Saunders, Philadelphia, 1991.
- [102] Dorthe Nørgård Madsen. *Experimental Studies of Cold Magnesium Atoms*. PhD thesis, Niels Bohr Institute, (2001).
- [103] T. W. Hänsch. Laser frequency stabilization by polarization spectroscopy of a reflecting reference cavity. *Optics Communications*, **35** (1980).
- [104] P. W. Milonni and J. H. Eberly, *Lasers*, Wiley-Interscience, 1988.
- [105] S. Gerstenkorn and P. Luc. *Atlas du Spectre d'Absorption de la Molécule d'Iode, 14800 - 20000 cm<sup>-1</sup>*. Laboratoire Aim Cotton, CNRS II, Orsay, 1978.
- [106] Wolfgang Demtröder. *Laser Spectroscopy*. Springer-Verlag GmbH, second edition, 1995.

- [107] Valentina Ruseva. Design of high-power frequency-doubled diode laser systems for experiments on laser cooled Magnesium. PhD thesis, Niels Bohr Institute, 2005.
- [108] F. Ruschewitz, J. L. Peng, H. Hinderthür, N. Schaffrath, K. Sengstock, and W. Ertmer, *Phys. Rev. Lett.* **80**, 3173 (1998)
- [109] Bagayev S.N.; Baraulya V.I.; Bonert A.E.; Goncharov A.N.; Seydaliev M.R., *Optics Communications*, **196**, 201 (2001)
- [110] R. W. P. Drever, J. L. Hall, F. V. Kowalski, J. Hough, G. M. Ford, A. J. Munley, and H. Ward. Laser phase and frequency stabilization using an optical resonator. *Appl. Phys. B*, **31**, 97 (1983).
- [111] R. V. Pound. Electronic frequency stabilization of microwave oscillators. *Rev. Sci. Instrum.*, **17**, 490 (1946).
- [112] *Frequency Standards - Basics and Applications*, F. Riehle, Wiley (2004)
- [113] Nicola Malossi. Studies of cold magnesium atoms in a magneto-optical trap: towards a novel optical frequency standard. PhD thesis, Niels Bohr Institute, 2008.
- [114] H. M. Pask, R. J. Carman, D. C. Hanna, A. C. Tropper, C. J. Mackechinie, P. R. Barber, and J. M. Dawes, Ytterbium-doped silica fiber lasers: Versatile sources for the 1-1.2 $\mu$ m region, *IEEE Journal of Selected Topics in Quantum Electronics*, 2-12 (1995)
- [115] M. Dekker, *Rare-Earth-Doped Fiber Lasers and Amplifier* (M. J. F. Digonnet, Editor), New York, 2nd Edition (2001)
- [116] U. Brinkmann, J. Goschler, A. Steudel and H. Walther, *Z. Phys. A*, **228**, 427 (1969)
- [117] U. Brinkmann, J. Kluge, and K. Pippert, *J. Appl. Phys.* **51**, 4612 (1980)

- [118] S. Garpman, G. Lidö, S. Rydberg and S. Svanberg, *Z. Phys. A*, **241**, 217 (1971)
- [119] S. Svanberg, *Phys. Scr.* **5**, 73 (1972)
- [120] S. Ishii and W. Ohlendorf, *Rev. Sci. Instrum.* **43**, 1632 (1972)
- [121] P. E. Jessop and F. M. Pipkin, *Phys. Rev. A* **20**, 269 (1979)
- [122] G. Brink, A. glassman and R.gupta, *Opt. Commun.* **33**, 17 (1980)
- [123] L. Pasternack and P.J. Dagdigian, *Rev. Sci. Instrum.* **48**, 226 (1977)
- [124] G. Giusfredi, P. Minguzzi, F. Strumia and M. Tonelli, *Z. Phys. A*, **274**, 279 (1975)
- [125] G. Giusfredi, A. Gondone, E. Bava and C. Novero, *J. Appl. Phys.* **63**, 1279 (1987)
- [126] *Atomic and Molecular Beam Methods*, volume 1, edited by G. Scoles, Oxford University Press, (1988).
- [127] F. Y. Loo, A. Bruschi, S. Sauge, M. Allegrini, E. Arimondo, N. Andersen, and J.W. Thomsen. Investigations of a two-level atom in a magneto-optical trap using magnesium. *Journal of Optics B: Quantum and Semi-classical Optics*, **6**, 81 (2004).
- [128] Alessandro Cosci. Raffreddamento e confinamento di atomi di magnesio in trappola magneto-ottica. Masters thesis, Università degli Studi di Firenze, Facoltà di Scienze Matematiche Fisiche e Naturali, (2006).
- [129] M. Inguscio, S. Stringari, and C. E. Wieman, editors. *Making, Probing and Understanding Bose-Einstein Condensates* (1999). Proceedings of the International School of Physics Enrico Fermi, Course CXL.
- [130] L. You and M. Holland. Ballistic Expansion of Trapped Thermal Atoms. *Phys. Rev. A* **53**, R1 (1996).

- [131] D.N. Madsen and J.W. Thomsen. Measurement of absolute photoionization cross sections using magnesium magneto-optical traps. *J. Phys. B.*, **35**, 2173 (2002).
- [132] A. Lurio, Hyperfine Structure of the  $^3P$  States of  $Zn^{67}$  and  $Mg^{25}$ , *Phys. Rev.* **126**, 1768 (1962)
- [133] Godone, A., Bava, E., Giusfredi, G.: *Z. Phys. A - Atoms and Nuclei* **318**, 13 (1984)
- [134] Sergey Porsev, private communication.
- [135] M. F. Crawford, F. M. Kelly, A. L. Schawlow, W. M. Gray, *Phys. Rev.* **76**, 1527 (1949)
- [136] L. Hallstadius and J. E. Hansen, Experimental Determination of Isotope Shifts in Mg I, *Z. Phys. A* **285**, 365 (1978)
- [137] C. Novero and A. Godone, *Z. Phys. D* **17**, 33 (1990)
- [138] N. Beverini, G. L. Genovesi, E. Maccioni, A. M. Messina, F. Strumia. *Appl. Phys. B* **59**, 321 (1994)
- [139] L. Hallstadius. *Z. Physik A* **291**, 203 (1979)
- [140] S. Isaksen, A. Andersen, T. Andersen and P. S. Ramanujam, *J. Phys. B: Atom. Molec. Phys.*, **12**, 893, (1979)
- [141] N. Malossi, S. Damkjær, P. L. Hansen, L. B. Jacobsen, L. Kindt, S. Sauge, J. W. Thomsen, F. C. Cruz, M. Allegrini, and E. Arimondo, *Phys. Rev. A* **72**, 051403 (2005)
- [142] O. Scully and S. Zubairy, *Quantum Optics*, Cambridge University Press, 1997.
- [143] S. G. Porsev, M. G. Kozlov, Y. G. Rakhlina and A. Derevianko. Many-body calculations of electric-dipole amplitudes for transitions between low-lying levels of Mg, Ca, and Sr. *Physical Review A*, **64**, 012508 2001

- [144] Sergey G. Porsev and Andrei Derevianko. Hyperfine quenching of the metastable  $^3P_{0,2}$  states in divalent atoms. *Physical Review A* **69**, 042506 (2004)
- [145] P. L. Hansen, K. T. Therkildsen, N. Malossi, B. B. Jensen, E. D. van Ooijen, A. Bruschi, J. H. Müller, J. Hald, and J. W. Thomsen. Measurement of the  $3s3p\ ^3P_1$  lifetime in magnesium using a magneto-optical trap. *Phys. Rev. A* **77**, 062502 (2008)
- [146] G. Zinner, T. Binnewies, F. Riehle, and E. Tiemann, *Phys. Rev. Lett.* **85**, 2292 (2000).
- [147] M. Yasuda and H. Katori, *Phys. Rev. Lett.* **92**, 153004 (2004).
- [148] P. G. Mickelson, Y. N. Martinez, A. D. Saenz, S. B. Nagel, Y. C. Chen, T. C. Killian, P. Pellegrini, and R. Cote. *Physical Review Letters* **95** 223002 (2005).
- [149] T. Zelevinsky, M. M. Boyd, A. D. Ludlow, T. Ido, J. Ye, R. Ciurylo, P. Naidon, and P. S. Julienne. *Physical Review Letters* **96** 203201 (2006)
- [150] W. Nagourney, J. Sandberg, and H. Dehmelt. *Physical Review Letters* **56** 2797, (1986)
- [151] J. C. Bergquist, R.G. Hulet, W. M. Itano, D. J. Wineland. *Physical Review Letters* **57** 1699, (1986)
- [152] A. Godone and C. Novero. *Physical Review A* **45** 1717 (1992)
- [153] H. S. Kwong and Peter L. Smith and W. H. Parkinson. *Physical Review A*. **25** 2629 (1982)
- [154] Remeasurement of the Mg  $^3P_1$ -state lifetime P. S. Furcinitti, J. J. Wright, and L. C. Balling. *Phys. Rev. A* **12**, 1123 (1975)
- [155] C. J. Mitchell. *J. Phys. B* **8** 25 (1975)
- [156] Robin Santra and Kevin V. Christ and Chris H. Greene. *Physical Review A* **69** 042510 (2004)

- [157] I. M. Savukov and W. R. Johnson. *Physical Review A* **65** 042503 (2002)
- [158] C. Laughlin and G. A. Victor. *The Astrophysical Journal* **234** 407 (1979)
- [159] Per Lunnemann Hansen. Experimental determination of metastable  $^3P_1$ . Master thesis, Niels Bohr Institute, 2006.
- [160] I. I. Sobelman, *Atomic Spectra and Radiative Transitions* (Springer-Verlag, Berlin, 1992).
- [161] C. Y. Yang, P. Halder, O. Appel, D. Hansen, and A. Hemmerich, *Phys. Rev. A* **76**, 033418 (2007)
- [162] S. G. Porsev and A. Derevianko: Hyperfine quenching of the metastable  $^3P_{0,2}$  states in divalent atoms. *Phys. Rev. A* **69**, 042506 (2004).
- [163] Jefferts, S. R., Heavner, T. P., Parker, T. E., and Shirley, J. H. (2007). Nist cesium fountains - current status and future prospects. *Proceedings of 2007 SPIE Conference*, 6673:9.
- [164] Chapelet, F., Guena, J., Rovera, D., Laurent, P., Rosenbusch, P., Santarelli, G., Bize, S., Clairon, A., Tobar, M., and Abgrall, M. (2007). Comparisons between 3 fountain clocks at Ine-syrte. *Frequency Control Symposium, 2007 Joint with the 21st European Frequency and Time Forum. IEEE International*, pages 467-472.
- [165] Poli, N., Barber, Z. W., Lemke, N. D., Oates, C. W., Ma, L. S., Stalnaker, J. E., Fortier, T. M., Diddams, S. A., Hollberg, L., Bergquist, J. C., Brusch, A., Jefferts, S., Heavner, T., and Parker, T. Frequency evaluation of the doubly forbidden  $^1S_0 \rightarrow ^3P_0$  transition in bosonic  $^{174}\text{Yb}$ . *Physical review A*, **77**, 050501 (2008)
- [166] Hachisu, H., Miyagishi, K., Porsev, S. G., Derevianko, A., Ovsianikov, V. D., Pal'chikov, V. G., Takamoto, M., and Katori, H. Trapping of neutral mercury atoms and prospects for optical lattice clocks. *Phys. Rev. Lett.*, **100**, 053001 (2008)